2018

2D Monolithic silicon detectors for dosimetry in Small beam radiotherapy (Stereotactic Radiotherapy)

Khalsa Ali Al Shukaili
University of Wollongong

University of Wollongong

2D Monolithic silicon detectors for dosimetry in Small beam radiotherapy (Stereotactic Radiotherapy)

A Thesis Submitted in Fulfilment of the

requirements for the award of the degree of

Doctor of Philosophy

from

UNIVERSITY OF WOLLONGONG

by

Khalsa Ali Al Shukaili

4520087

Centre for Medical Radiation Physics
Faculty of Engineering and Information Sciences

January/ 2018

DECLARATION OF ORIGINALITY

I, Khalsa Ali Al Shukaili, declare that this thesis, submitted in fulfilment of the requirements for the award of Doctor of Philosophy, in the Centre for Medical Radiation Physics, Engineering and Information Sciences, University of Wollongong, is wholly my own work, unless otherwise referenced or acknowledged. The document has not been submitted for qualification at any other academic institution.

Sign

Khalsa Al Shukaili

04.01.2018

TABLE OF CONTENTS

LIST OF FIGURES

LIST OF TABLES

LIST OF ABBREVIATIONS

2-D	Two-dimensional
3-D	Three-dimensional
ANSTO	Australian Nuclear Science and Technology Organisation
ADC	Analog to digital converter
AFE	Analog front-end
CAX	Central axis
CCE	Charge collection efficiency
CF	Correction Factors
CMRP	Centre for Medical Radiation Physics
CoP	Code of Practice
COR	Centre Of Rotation
CPE	Charged particle equilibrium
CRT	Conformal radiotherapy
CT	Computed tomography
C-V	Capacitance-voltage
DAC	Digital to analog converter
DAQ	Data acquisition
DMG	Dose Magnifying Glass (detector)
DPP	Dose per pulse
DVH	Dose volume histogram
EBRT	External beam radiotherapy
EPI	Epitaxial

FPGA	Field-programmable gate array
FF	Flattening Filter
FFF	Flattening Filter Free
FWHM	Full width at half maximum
GRCs	Generation and recombination centres
GUI	Graphical user interface
IBICC	Ion beam induced charge collection
IC	Ionisation chamber
I-V	Current-voltage
IMRT	Intensity modulated radiotherapy
LINAC	Linear accelerator
MRI	Magnetic resonance imaging
MLC	Multi-leaf collimator
MP512	MagicPlate-512 (detector)
MU	Monitor unit
MV	Megavoltage
NIEL	Non-ionising energy loss
NSWE	North South West East
OF	Output factor
OSL	Optically stimulated luminescence
PCB	Printed circuit board
PDD	Percentage depth dose
PMMA	PolyMethylMethAcrylate
QA	Quality assurance
RF	Radio-frequency

ROI	Region of interest
RT	Radiotherapy
SAD	Source to axis distance
SBRT	Stereotactic body radiotherapy
SD	Standard deviation
SFD	Stereotactic Field Diode
SNR	Signal-to-noise ratio
SRS	Stereotactic radiosurgery
SRT	Stereotactic radiotherapy
SSD	Source to surface distance
SWNE	South West North East
UOW	University of Wollongong
VMAT	Volumetric modulated arc therapy

ABSTRACT

Radiation Therapy is one type of cancer's treatment, which aims to kill or control tumour cells by using high energy radiation. However, it can affect both normal and tumour cells. Due to that, scientists worked to develop a new treatment technique of radiation delivery that focuses the high prescribed dose on the small localized area of tumour cells and protects the normal cells. This focal irradiation technique is called Stereotactic Radiosurgery (SRS). Using SRS allows the treatment of hard-to-reach lesions where surgery is not possible because of the risks resulting in the surgical procedures. The commissioning and Quality Assurance of SRS/SRT is complex and requires special dosimetry tools. Poor dosimetry of small-field characteristics may lead to reduced treatment efficacy, whether by under-dosage of targeted tumours or over-irradiation of adjacent healthy tissues. Poor measurements of the small field characteristics, such as FWHM, penumbra width, output factors and percentage depth dose may result in pernicious health consequences, such as radiation-induced carcinogenesis. Hence, the dosimetry tool plays an important role in the SRS/SRT accuracy and precise delivery. Recently, silicon detectors have increased in popularity because they have high spatial resolution, small sensitive volume, high sensitivity to radiation, reasonable uniformity and provides real time measurements. The Centre for Medical Radiation Physics (CMRP) has developed two innovative monolithic silicon array detectors, DUO and OCTA, to be used in SRS/SRT for pre-treatment quality assurance dosimetry. Therefore, the aim of this thesis is to characterise these two monolithic silicon detectors for small radiation field dosimetry employed in stereotactic radiotherapy.

DUO monolithic silicon array is based on bulk substrate and consists of 505 diodes arranged in two perpendicular arrays. The total size of DUO is 52 x 52 mm^2 with a very high resolution of 0.2 mm. It has been studied in terms of its suitability as a QA dosimeter for small field techniques. OCTA silicon array is a step further from DUO, made of Epitaxial substrate and it

contains 512 diodes arranged in four arrays, two perpendicular and the other two are 45^0 from the centre in both directions (diagonals). The resolution of the two perpendicular axes is 0.3 mm and the resolution of the diagonals is 0.43 mm. OCTA has been characterised in this study, electrically and clinically. Both detectors are a suitable choice for SRS/SRT QA dosimetry, as they have high resolution on-time measurements. However, DUO shows a charge sharing effect and volume averaging effect due to the bulk substrate and very small pitch size, which is required to be corrected. Therefore the Epitaxial substrate was chosen for the next generation of DUO and OCTA monolithic silicon detectors for SRS/SRT dosimetry.

ACKNOWLEDGEMENTS

I would like to acknowledge all those who supported and helped me to do my work for my PhD research.

First of all, I would like to thank my three supervisors: Professor Anatoly Rosenfeld, Dr. Stephanie Cord and Dr. Marco Petasecca, for their time and energy that they spent supporting me in my research.

Professor Anatoly Rosenfeld is a great supervisor and without his continuous support and encouragement, this thesis would not be possible. He consistently offered me significant advice and guidance to my research. While he has many students, he still has time to explain to me the questions I asked about the basics of solid-state dosimetry and correct my papers. I would like to thank Professor Rosenfeld for giving me opportunities to undertake training at Prince of Wales Hospital and to present this work at a number of conferences. I would also thank him for his financial support by providing me with an International Postgraduate Tuition Award for my final session to finalise my thesis.

Many thanks to Dr. Stephanie Corde for her great support of this project and myself. She was always a kind supporter and adviser who helped me in every step of this research. She spent long hours during weekends to do the experimental sessions and really many thanks, Stephanie. Her extensive clinical experience and vast knowledge taught me a lot of knowledge about clinical medical physics and conducting research.

I would like to thank Dr. Marco Petesecca for all his support that he gave me from the first week I had started my research until the last step. Thanks Dr. Petesecca for your time and energy that you spent in order to provide me with the detectors and their

electronic readout systems. He also helped me to do my measurements at Illawarra Cancer Care Centre and Prince of Wales Hospital, which was impossible to be done without his great knowledge of electronics and programming. His supervision and advice allowed this project to be completed.

During my research, I had the opportunity to participate in training at POWH, so many thanks to Simon and his team for the training they provided me. I would also like to thank Karen Ford for her administrative assistance. I would like to thank my colleagues at CMRP who taught and supported me through my research. Thanks Matthew Newell, Ziyad Alrowaili, Abdullah Aldosari, Anthony Espinoza, Claudui Porumb and Mitchel Duncan.

My thanks to my Omani government for their financial support and special thanks for his majesty Sultan Qaboos Bin Said for supporting the new generation in continuing their education.

To my husband and kids: Special thanks for your encouragement, support, love and patience during all of my research, over the past years. I am so glad that you are with me all the time. I will never forget your kind support and help.

To my family: mam, brothers and sisters, thank you for your kind encouragement and prayers to complete my research.

LIST OF CONFERENCE PRESENTATIONS AND PUBLICATIONS

1. **Al Shukaili, K.,** Pettasecca, M., Corde, S., Lerch, M., Rosenfeld, A. (2015). *High spatial resolution silicon based dosimeter for small field quality assurance*. Oral presentation at MedPhy15. University of Sydney, Sydney, Australia.
2. **Al Shukaili, K.,** Corde, S., Pettasecca, M., Lerch, M., Rosenfeld, A. (2016). *A monolithic silicon detector array for small field dosimetry in Stereotactic Radiotherapy: DUO*. Oral presentation at MedPhy16. University of Sydney, Sydney, Australia.
3. **Al Shukaili, K.**, Corde, S., Pettasecca, M., Lerch, M., Rosenfeld, A. (2016). *A monolithic silicon detector array for small field dosimetry in Stereotactic Radiotherapy: DUO*. Oral presentation at Engineering & Physical Science in Medicine. Sydney, Australia.
4. M. Petasecca, **K. Al Shukaili**, M. K. Newall, M. Duncan, I. Fuduli, S. Corde, M. L. F. Lerch, V. Perevertaylo, A. B. Rosenfeld. (2016). *DUO: a monolithic silicon detector array for small field dosimetry in Stereotactic Radiotherapy*. Poster presented at 18th International Conference on Solid State Dosimetry (SSD), Munich**,** Germany.
5. **Al Shukaili, K.,** Pettasecca, M., Corde, S., Lerch, M., Rosenfeld, A. (2017). *Charge sharing effect on silicon detector array called DUO*. Poster presented at Innovation in Radiation Application. University of Wollongong, Wollongong, Australia.

6. **Al Shukaili, K.,** Corde, S., Pettasecca, M., Lerch, M., Rosenfeld, A. (2017). *A monolithic silicon detector array Stereotactic Radiotherapy Quality Assurance*. Oral presentation at 13th International Stereotactic Radiosurgery Society Congress (ISRS2017). Montreux, Switzerland.
7. **Al Shukaili KA,** Petasecca M, Newall M, Espinoza A, Perevertaylo VL, Corde S, Lerch M, Rosenfeld AB. *A 2D silicon detector array for quality assurance in small field dosimetry: DUO*. Medical Physics. 2017 Feb 1; 44 (2):628-36.
8. **Al Shukaili KA,** Corde S, Petasecca M, Perevertaylo VL, Lerch M, Jackson M, Rosenfeld AB. *Characterization of ELEKTA SRS cone collimator using high spatial resolution monolithic silicon detector array*. Submitted for JACMP.
9. **Al Shukaili KA**, Corde S, Petasecca M, Perevertaylo VL, Lerch M, Jackson M, Rosenfeld AB. *Clinical SRS treatment*. In preparation to submit for Medical Physics journal.
10. M K Newall M Petasecca, M Duncan, I Fuduli, **K Al shukaili**, J T Booth, P Keall , S Corde, V Pereveratylo, M Lerch, A B Rosenfeld. Innovative detectors for quality assurance dosimetry in SBRT of stationary and movable targets. In Journal of Physics: Conference Series 2017 Jan (Vol. 777, No. 1, p. 012014). IOP Publishing.

CHAPTER 1: INTRODUCTION

1.1 Introduction

The body is programmed to control the cell growth and new cells are normally produced to replace the old ones or to perform a specific function of organs or tissues. However, sometimes the balance control of cell growth and death fails due to different effects, resulting in excessive cells division in the body, causing what is widely known as a tumour. This tumour may be benign or malignant, where the malignant tumour is called cancer.

Currently, cancer is the second leading causes of death in Australia, with recent data indicating that the annual number of cases will reach to 21.6 million by 2030 (WHO (2017).

There are different types of cancer treatment including surgery, chemotherapy and radiotherapy. The aim of radiation therapy treatment is to deliver the prescribed dose to kill the tumour, while trying to spare the surrounding organs and tissues from the irradiated dose as much as possible. To reach the radiotherapy aims, the treated area should be restricted to the tumour (Fraass, Doppke et al. 1998).

Currently, the external beam therapy with small high-energy photon beams are used mostly and especially in intensity modulated radiation therapy (IMRT), stereotactic radiotherapy (SRS/SRT), and volumetric modulated arc therapy (VMAT). Accurate measurements of the dose characterizing the treatment beams (percentage depth dose, beam profiles and output factors) are required to model them in the treatment planning systems in order to ensure the highest precision of patient treatment. However, the complexity of this type of delivery have the challenges of small field measurements that

are difficult to be measured and characterized (Aspradakis, Byrne et al. 2010). Therefore, these techniques require the use of specific dosimetry for more accurate and precise measurements; which can be achieved by using 1D dosimetry such as ion chambers, 2D dosimetry such as EBT3, silicon array detectors and 3D dosimetry such as gel. The inaccurate measurements can lead to under dosing the target or over dosing the surrounding normal tissues, both cases compromising the clinical outcomes of the patient treatment.

1.2 Project aims

The main objective of this research is to characterise two recently developed silicon arrays detectors to be used for small field dosimetry in external beam radiotherapy. Both detectors are designed by the Centre for Medical Radiation Physics (CMRP) at the University of Wollongong (UOW) and they are monolithic p-type silicon detectors. The first detector is called 'Bulk DUO' which consists of 505 pixels that are arranged in two orthogonal axes. The resolution of DUO is excellent (0.2 mm), compared to the available commercial dosimeters for SRS/SRT QA. The second detector called 'Epitaxial OCTA' contains 512 pixels arranged in four arrays. The resolution of the perpendicular axis is 0.3 mm and the resolution of the diagonals is 0.43 mm. Both detectors have been characterised and their response improved to counterbalance the effect of silicon density on over-response in small radiation fields by introducing an air gap above them. In addition, the charge sharing corrections have been applied for Bulk DUO. They show very good agreement with EBT3 Gafchromic^{TM} films for SRS/SRT dosimetry.

1.3 The structure of the present study

This thesis consists of 10 chapters. After this introduction chapter, chapter 2 provides a background about the radiotherapy and the new techniques that use small field, such as SRS/SRT. There is a discussion about the difficulties of SRS dosimetry by using the current commercial detectors and concludes with the use of silicon detector arrays as QA dosimetry for SRS. As silicon detectors are the smallest detectors available with very high resolution, the next section in chapter 2 was to discuss the advantages, limitations and how silicon detectors work.

Chapter 3 describes the instrumentation used in this work; hardware, software and rotatable cylindrical phantom. It begins by describing the hardware, DUO and OCTA silicon array detectors and then the software used as data acquisition system and interfaces software. Both DUO and OCTA consists of many diodes, connection of each diode (routing) to corresponding pin in a socket on PCB is important for correct interpretation of the detector spatial response. In addition, there is a description about the cylindrical phantom and the inclinometer that was used for the SRS plan delivery.

The following chapter of this thesis, chapter 4, focuses on the effect of different air gap thickness upstream DUO silicon array. In this part, square field sizes delivered by Varian LINAC were studied in terms of their output factors and beam profile parameters. The minimum air gap used in this study is 0.5 mm, to avoid the physical damage to the bonding wires, which are necessary to connect the chip to the flexible carrier. The air gap above DUO silicon array essentially effects DUO response, causing a decrease in the output factors and increase in the FWHM and penumbra width as the air gap thickness increases. DUO with the addition of 0.5 mm air gap above it shows very good agreement with the standard dosimetry tools used.

Chapter 5 focuses on the charge sharing effect of Bulk DUO and Epitaxial OCTA silicon detector arrays. The effect of charge sharing mainly affects the penumbra width. A mathematical analysis has been used to study the effect of charge sharing in detectors with very small pitch size. The analytic approach shows there is no charge sharing effect, where the pixels considered as a point and the dose gradient is constant. However, this is not the case in very small field sizes where a steep gradient exists. The experimental analysis shows that there is a higher dose gradient in Bulk DUO measurements than ion chambers by about 15%, while there is negligible difference in the Epitaxial OCTA measurements. The higher dose gradient measured by Bulk DUO is mostly due to volumetric effect, resulting from longitudinal and radial volumetric effect where the pixel size is large due to the thick 0.47 mm Bulk silicon substrate. Therefore, Bulk DUO needed to be correct in order to get a good agreement with EBT3 at the penumbra region. Epitaxial OCTA doesn't show volumetric effect or charge sharing where its sensitive volume is much better than Bulk DUO due to the thin 0.038 mm epitaxial layer from which charge is collected.

Chapter 6 is aimed to characterise Bulk DUO as a QA tool for small field dosimetry by measuring uniformity, beam profiles and percentage depth dose of small square field sizes and compare it with EBT3 films and ionisation chamber (PDD). Bulk DUO shows a good agreement with EBT3 and IC.

Chapter 7 studies the full clinical characteristics of ELEKTA SRS cone collimator by using DUO (charge sharing CF are applied) and compared with EBT3 films and IBA Stereotactic Field Diode (SFD). DUO shows excellent agreement with EBT3 in terms of OF, beam profiles and PDD for cone sizes from 5 to 50 mm diameter.

In chapter 8, the potential of using DUO as a pre-treatment QA tool was assessed by comparing the calculated SRS treatment plan to the one measured during treatment delivery with the LINAC. In this part of the study, DUO was placed in a cylindrical phantom in two different positions, horizontal and vertical, and used to evaluate the SRS treatment plan delivery. The results were compared with treatment planning system (TPS) and EBT3 films and a good agreement was found in terms of distance to agreement. DUO was used to test the mechanical isocentre shift of LINAC and it shows a shift up to ±1 mm, normalized to gantry rotation of 0^0 at the horizontal axis when the phantom was positioned horizontally. There was an offset in the cone centre about ±0.6 mm when exchange cones at the same setup. DUO is a good tool to test the centre shift in the SRS/SRT treatment as it provides accurate data in real time measurements.

The last work that was done on this study is in chapter 9. It focuses on characterising the next generation monolithic detector array Epitaxial OCTA. Firstly, the electrical characterisation including I-V, C-V and radiation hardness are studied. OCTA follows the trend of p-n silicon detectors behaviour in the electrical characterisation. Secondly, OCTA is fully characterised by using SRS cone collimator in terms of uniformity, dose linearity, OF, beam profiles in four directions, PDD and centre of LINAC rotation. OCTA agrees with the EBT3 measurements in terms of output factors, beam profiles and PDD. OCTA provides more information than DUO as it gives data in four directions. Also, Epitaxial OCTA shows that there is an isocentric mechanical shift in the ELEKTA LINAC within ±1 mm in all four directions.

At the end of the thesis, chapter 10 concludes the work that was done on this study for both Bulk DUO and Epitaxial OCTA as a dosimetry tool for SRS/SRT quality assurance. Some recommendations were given in order to improve the next generation of monolithic silicon detectors by chosen Epitaxial substrate instead of Bulk and to

continue to test OCTA by using different modalities of small field techniques used by different types of LINACs.

CHAPTER 2: LITERATURE REVIEW

2.1 Radiation therapy

Radiation therapy is one main type of cancer treatment and it uses high energy ionizing radiation to shrink the tumour and kill the cancer cells. Radiotherapy can be applied from a distance outside the body, called external radiotherapy, or from radioactive material placed inside the body called brachytherapy. However, if radiotherapy does kill the cancer cells, it also has side effects on the surrounding normal tissue. Therefore, the aim of radiotherapy is to maximize the dose required to the tumour cells and minimize the dose to the normal tissue ideally, making the dose as low as possible. The therapeutic window is extremely narrow, between the normal tissue complication and tumour control probability. To ensure the aim is achieved, the dose delivered to the target and normal tissues need to be measured accurately and precisely. Failure to do so may results in under dosage to the tumour and/or over dosage of normal tissues, which may lead to radiation-induced complications. Thus, the dose measurement is one of the utmost important challenges in radiation therapy.

2.1.1 X-ray interactions within the patient

High-energy X-ray photons and electrons from the medical linear accelerator (LINAC) are the most common source of ionizing radiation in external radiotherapy. By using the microwave technology, the electrons that are produced from an electron gun are accelerated in a wave-guide. At exit, electrons are focused by bending magnets into heavy metal targets in order to produce high energy X- rays. These high energy X-rays are shaped geometrically by using flattening filters and different collimators at the exit

of the LINAC head and then the customized beam is directed to the patient's tumour (Khan 2010).

High energy X-rays interact with matter by three main interactions: photoelectric, Compton and pair production effects. The predominant interaction for the cancer treatment is the Compton scattering effect. In this case, high-energy photons scattered with 'free electrons', transfer part of their energy to an electron. The scattered photons can continue to make more interactions, with electrons until all energy is dissipated. Electrons lose their energy via ionisation and excitation of atoms. These reactions determine the absorbed dose (or energy deposited per unit mass) to the patient, which needs to be measured.

2.1.2 Measuring X-ray dose

The dose delivered by a LINAC is calibrated by following international absolute dosimetry protocols (Andreo, Huq et al. 2002). This is generally done by using a reference ionisation chamber whose calibration is traceable to a primary standard in a water phantom, mimicking patient's tissues. The radiation causes ionizations in the cavity of the ionisation chamber. This ionisation can be collected and measured as a current, where it is related to the absorbed dose in the detector. In megavoltage radiotherapy, absolute dosimetry is only performed in reference standard condition, as per protocol (e.g. 100 cm SSD, 10 x 10 cm^2, and 10 cm depth). Relative dosimetry is then used to measure doses in non-reference conditions and access relative parameters such as percentage depth dose (PDD), tissue maximum ratio (TMR), tissue phantom ratio (TPR), beam profiles and field output factors (OF) (Almond, Biggs et al. 1999). All these measurements allow a full characterisation of the treatment beam and it's modelling in the treatment planning system.

2.1.3 Bragg-Gray cavity theory

To measure the dose in a medium, a measuring dosimeter need to be introduced in the medium. Usually, the sensitive medium of the dosimeter is not the same material as the medium embedded on it. Hence, cavity theory relates the absorbed dose in the dosimeter cavity medium to the absorbed dose in the surrounding medium. This theory works only in specific conditions. Firstly, the cavity should be very small in comparison to the range of charged particle incident on it, so no perturbation and charged particle equilibrium must exist. However, the presence of a cavity in the medium always causes some fluence perturbations, which needs to be corrected. Secondly, the absorbed dose in the cavity is deposited solely by charged particles crossing it (Mayles, Nahum et al. 2007). Therefore, no secondary electrons are produced inside the cavity and no electrons stop inside it.

Under these conditions, the dose to medium can be calculated as:

$$\mathbf{D_{med}} = \mathbf{D_{cav}} \left[\frac{\bar{\mathbf{S}}}{\boldsymbol{\rho}}\right]_{\mathbf{med,cav}}$$

where ($S/r_{(med,cav)}$) is the ratio of mass collision stopping power of the medium and cavity.

2.2 Small field dosimetry

With the developments of image guidance and delivery techniques of modern radiation therapy, small beams are now being more frequently used in the advanced techniques such as Intensity Modulated Radiation Therapy (IMRT), Image Guided Radiation Therapy (IGRT), Stereotactic Radiation Therapy (SRS/SRT & SBRT) and Volumetric Arc Therapy (VMAT). The use of small beams aims to reduce the dose to the healthy normal tissue, so minimizing the negative side effects of radiotherapy treatment.

However, the use of small treatment fields have added more difficulties and challenges to the accuracy of treatments (Aspradakis, Byrne et al. 2010, Das, Sauer et al. 2013). A small field is defined as a field with dimensions less than the lateral range of electrons; which is about field size less than 3 x 3 cm^2 (Das, Ding et al. 2008, Charles, Cranmer-Sargison et al. 2014). The three main challenges of small field dosimetry are:

1. Effects of radiation source size

The medical linear accelerators radiation source is a combination of the bremsstrahlung photon fleunce generated in the target (direct beam radiation) and the photons scattered at LINAC structures below the target (indirect beam radiation). In small radiation field, the indirect beam radiation is less important in the determination of dose and the direct beam source is shielded partially by the collimator. This block of direct beam causes a reduction in the primary photons reaching the point of measurement at the centre of the beam, and this is directly proportional to the size of the source (focal spot size) as shown in figure 2.1. Thus, source occlusion becomes a very important factor in the dose measurements at the small fields (Zhu and Bjärngard 1994). Some studies show that the output factors can be significantly affected by the collimator setting to achieve small fields (Sharpe, Jaffray et al. 1995, Ding, Duggan et al. 2006).

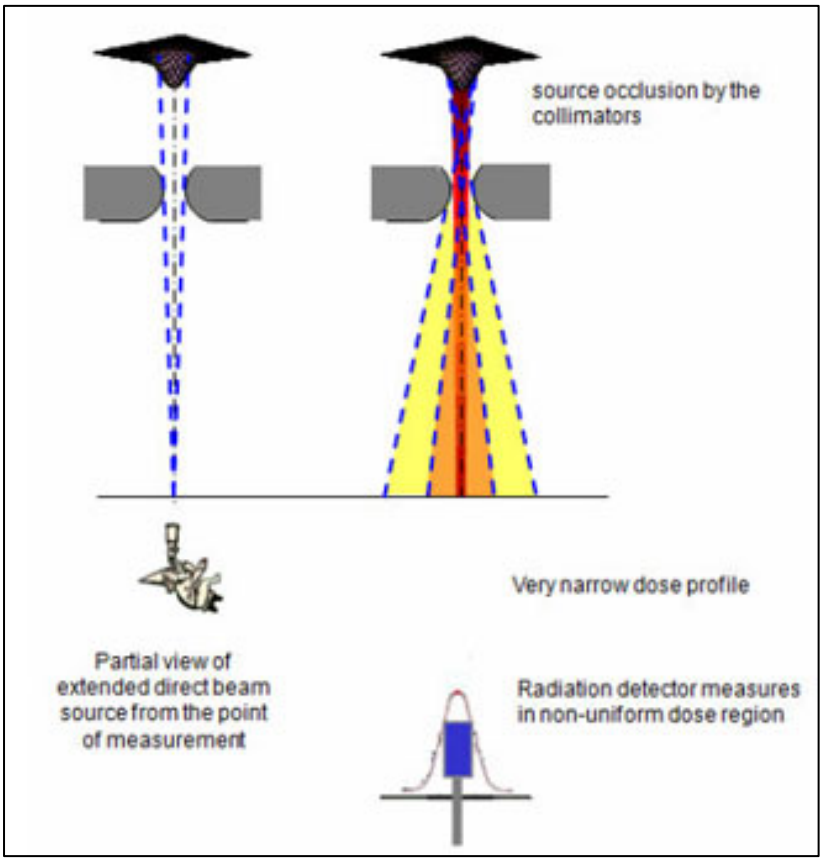

Figure 2.1: The effect of source occlusion with small field sizes(Aspradakis, Byrne et al. 2010).

2. Electron ranges and loss of charged particle equilibrium

When irradiated photon beam interact with a tissue through different types of interactions (photoelectric, Compton and pair production), some secondary electrons are produced. These electrons have a finite range in which they deposit energy in the medium. When the radius of the beam (small fields) becomes smaller than the maximum range of the secondary electrons, the lateral charged particle disequilibrium will occur. This happens at the higher beam energies and narrow field sizes. As a result, small fields can be problematic because the absorbed doses as well as the beam profile parameters are affected as shown in figure 2.2. Furthermore, the density of the medium

also affects the strength of the disequilibrium, hence for low density medium the disequilibrium is increased (Seuntjens , Das, Ding et al. 2008).

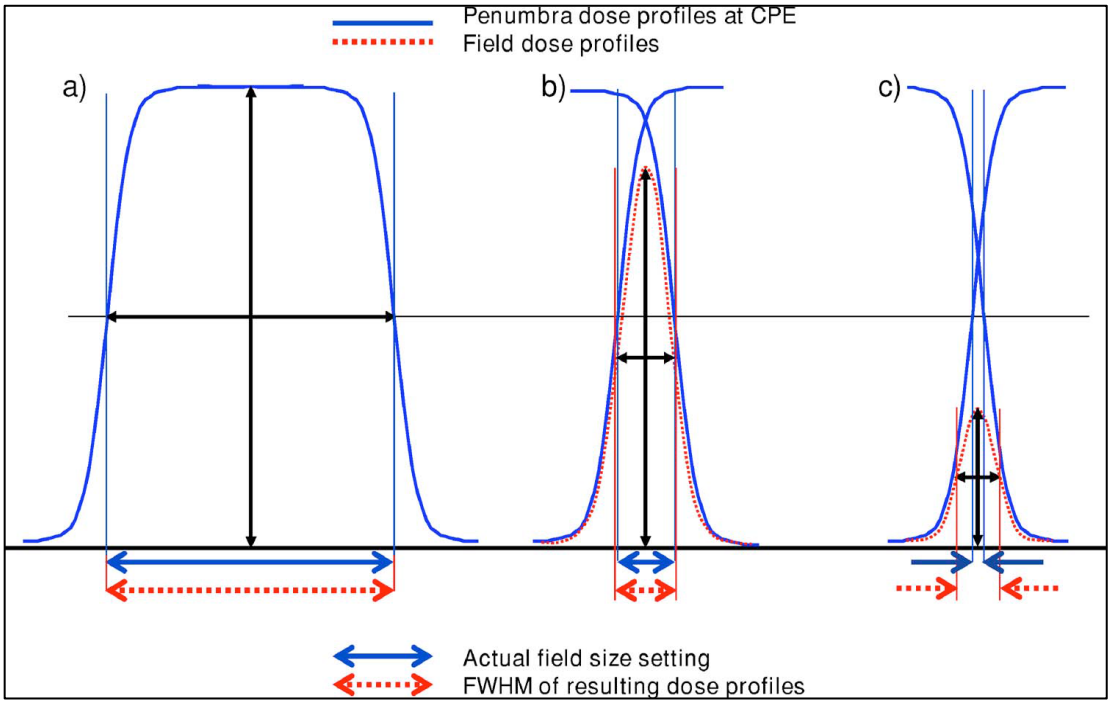

Figure 2.2: The FWHM measurements as a function of charged particle equilibrium, (a) larger field size, (b) comparable field size, (c) smaller field size (Das, Sauer et al. 2013).

3. Measurements and size of the detector

Dose measurements with ionization chambers are explained by the cavity theory. When the size of the cavity is smaller than the range of the charged particle the cavity will not perturb the beam. However, with decreasing the field size where charged particle disequilibrium exists, the presence of the detector can produce perturbation effects. These effects depend on the type of detectors (size and design). The use of relatively large detectors in small fields can cause volume-averaging effect, because the signal is averaged over its volume as in the example shown in figure 2.3. This results in a reduction in the dose intensity at the centre and so lowers the apparent beam output (Seuntjens , Aspradakis, Byrne et al. 2010).

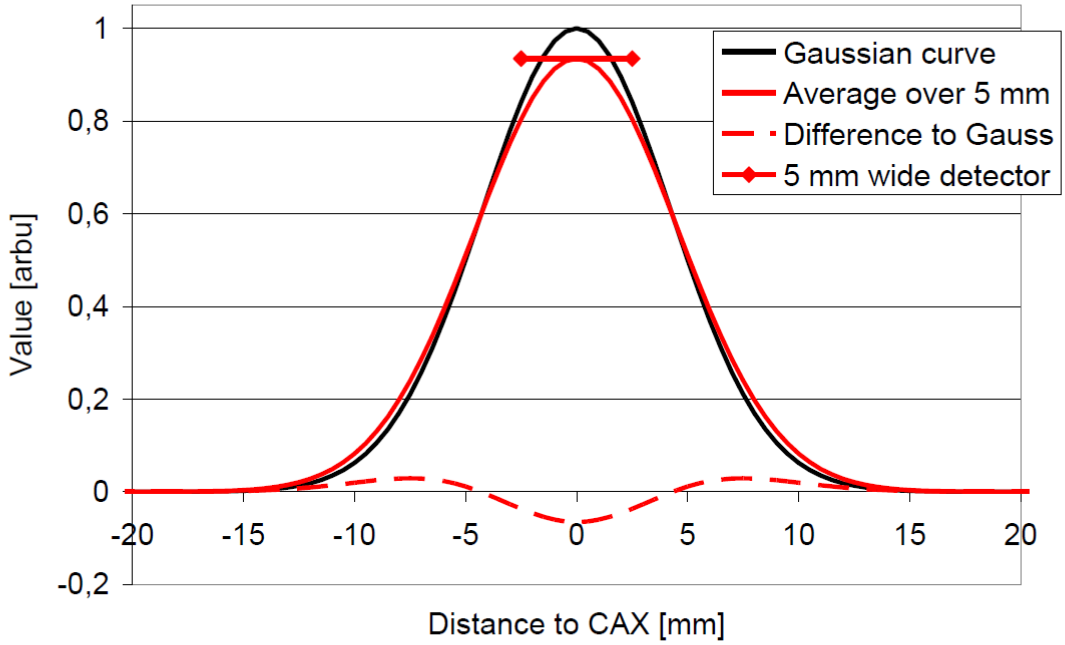

Figure 2.3: A depiction of the volume averaging effect. This example shows a comparison of Gaussian field with an ionisation chamber (Semiflex 0.125 cm^3), where IC don't have a small enough sensitive volume to accurately measure the 1.4 x 1.4 cm^2 field, resulting in underestimation of the dose at the central axis (CAX) and an overestimation at the penumbra region (Würfel 2013).

2.3 Stereotactic Radiosurgery and Stereotactic Radiotherapy

Stereotactic is a special radiotherapy technique that is used to treat small lesions (usually less than 4 cm) with a very high focused dose, to precisely target the small tumour. It can be delivered in single fraction called SRS (8-24 Gy) or multiple fractions called SRT (40-50 Gy) (Grosu, Kneschaurek et al. 2006, Benedict, Schlesinger et al. 2014). Since the 1950s, the stereotactic principle has been adopted by the Swedish neurosurgeons Leksell (Leksell 1987) . He initially used Orthovoltage X-rays to deliver a high radiation dose in one fraction to destroy tumours in the brain. He focused the dose on the target by using several beams from different directions to reduce the dose in the surrounding normal tissues. Traditionally, it was delivered for brain tumours; but by

improving and developing imaging systems and patient motion management, stereotactic radiotherapy and radiosurgery has been employed to extra cranial regions such as the lung, prostate and spinal cords, referred to as stereotactic body radiotherapy (SBRT) (Benedict, Schlesinger et al. 2014). Lesions suitable to be treated with stereotactic techniques require accurate determination of volume and location because the prescribed doses delivered per fraction are very high and the surrounding margins are small.

There are different techniques that are used in stereotactic radiotherapy. The first type that was used is Gamma Knife, which contains 201 ^{60}Co sources housed in a helmet at the centre of the machine. These sources are arranged in 160^0 sectored array to produce 201 collimated beams directed to a single focused point that define treatment spheres between 4 and 18 mm diameter. Its high cost and finite life time (5-10 years) are their disadvantages. The most frequently used system is LINAC based radiosurgery. During the last years, LINAC manufacturers have found specialized modifications capable of more precise treatment delivery, comparable in accuracy to the Gamma Knife, but offer more flexibility for different treatment options. The modifications are simple and consist of a remote control motorized couch and two types of supplementary collimations which either use a set of circular cone collimators to define small diameter circular beams or micro-multileaf collimator (MLC) to define small area of irregular shape (Brady, Perez et al. 2013).

2.4 Quality assurance requirements for SRS/SRT

While stereotactic radiosurgery was implemented more than sixty-five years ago, its clinical implementation remains challenging due to the use of the high prescribed doses in small field sizes, where the dose gradient at the penumbra become steeper and the

electronic equilibrium doesn't exist. Thus, high geometric precision and accurate measurements of dose characterization are required to deliver this type of treatment. There are some protocols that deal with the requirements and process of the SRS/SRT quality assurance such as AAPM TG-68, AAPM TG-135, and AAPM TG-101 (Lightstone, Benedict et al. 2005, Benedict, Yenice et al. 2010, Dieterich, Cavedon et al. 2011). The main important issue being the dosimetric measurements of small field parameters with confidence, in particular accurate measurements such as dose profiles, percentage depth-dose and output factors; for input into the clinical treatment planning software for dose calculation.

2.5 The ideal dosimetry for SRS/SRT

Due to the use of a high focused dose in small radiation beams with a small number of fractions in stereotactic radiotherapy, the accuracy of the measurements and calculation is an important key for the successful outcome of stereotactic treatment delivery. The measurements are done by using radiation dosimeters (detectors). These are devices, instruments or systems that measure the absorbed or equivalent dose, exposure or kerma or other related radiation quantities. The incorrect choice of dosimeter for the measurement can lead to radiation accidents as it may cause a difference in the relative output factors of up to 30% (Morales, Crowe et al. 2014). Thus, it is very critical to use the suitable dosimetry to measure the characteristic of the stereotactic radiation beams, where the penumbra measurement is critical to achieve that. IPEM report No. 103 (2010) has discussed the ideal detector parameters, which include:

- Stability: the detector response over the irradiation history has to be stable for hundreds of kGy exposures. (<0.1%)
- Tissue equivalent: the material of the detector has to be tissue equivalent so that it doesn't cause beam perturbation.

- Sensitive volume: the detector should have a small sensitive volume to avoid volume-averaging effect.
- Dose linearity: the reading of the detector should be proportional linearly to the dose over a wide range. (<0.1%)
- Dose rate linearity: the dose rate range depends on the integration time of the detector and the saturation limit of its electronics. (<0.1%)
- Dose per pulse linearity: the detector response with changing dose per pulse needs to remain stable. (<0.1%)
- Spatial resolution: it should be high enough to resolve the steep dose gradient at the penumbra region (typically 100 μm)
- Energy response: the detector should have a useful range of energies from ^{60}Co to 30 MV for photons.
- Orientation: the detector response should not be affected by the orientation of the detector with respect to the radiation beam. (<±0.5% at ±60^0 angle)
- Perturbation: By decreasing the radiation field size, neither the Bragg-Gray cavity nor the charged particle equilibrium conditions are fulfilled due to the change in the lateral scattering conditions. The perturbation produced by the detector mainly depends on the detector geometry and the medium in terms of composition and density. Therefore, the presence of the detector in small fields leads to difficulties in quantifying the perturbation effects, as the modification of the particle fluence is the main cause of this effect. Corrections of the perturbation effects resulted from the experimental conditions need to be applied to the measurements.

In addition, detectors need to demonstrate a wide dynamic range, real time measurements and high mechanical reliability and robustness. Different detectors have

different advantages to be used for small fields. However, currently there is no ideal detector that follows all the above parameters until now. Hence, the use of more than two detectors to compare the small field characterisations (beam profiles, output factors, and percentage depth dose) is recommended.

2.6 The current available dosimetry for SRS/SRT

A number of commercial detectors are available for SRS/SRT treatment verification. These detectors have been characterised and its suitability to be used for SRS measurements have been discussed by different groups. These detectors include point dosimetry, 2D dosimetry and 3D dosimetry. The following section explores some of the detectors that have been studied for small field dosimetry.

2.6.1 Point dosimetry

The point dosimetry aims to measure a single point of dose, usually at high dose low gradient region. This type includes:

2.6.1.1 Ionisation chamber

Ionisation chambers are the gold standard dosimeter for the radiotherapy departments due to their near independence of energy, dose and dose rate. In addition they are inexpensive, readily available, easily calibrated and can be found in various shapes (cylindrical, spherical and parallel plate) as well as different sizes for various applications (Das, Ding et al. 2008).

Ionisation chambers consist of gas filled cavities with two electrodes called anode and cathode. The electrodes could be in the form of parallel plates or cylindrical with internal anode wire. The electrodes are connected to a voltage source, to create electric field in the cavity. When ionizing radiation irradiated on the gas cavity, it will result in

ion-pairs production, where the number of pairs depends on the energy absorbed by the gas. This results in the current being proportional to the incident ionisation dose, measured by an electrometer circuit.

In special procedures where small fields are used such as SRS/SRT, they are not suitable because of the limited spatial resolution and the lack of electronic equilibrium (Czarnecki and Zink 2013, Tyler, Liu et al. 2013). However, the large volume of the ionisation chamber can cause a volume averaging effect which results in an overestimation of penumbra and underestimation of central axis dose (Das, Ding et al. 2008, Pappas, Maris et al. 2008). Therefore, it may not detect the areas with high dose gradient penumbra accurately (Massillon-JL, Cueva-Prócel et al. 2013).

Several micro- and mini- ionisation chambers have been developed to solve the issue of the volume limitation in small field dosimetry. Low, Parikh et al. (2003) have studied the use of a micro-chamber, Farmer chamber and waterproof scanning chamber in small fields and found that the larger in volume, the higher under-response at the centre of the field. A study of a new parallel-plate micro-chamber has showed that it under-responded as the field size decreased by comparison with Monte Carlo (Francescon, Cora et al. 1998). *Martens, De Wagter et al. (2000)* have showed that the PinPoint type ionisation chamber caused a reduction in the output factors which resulted from its over-response to the low energy Compton scattered photons and its use was limited to field sizes above 2 x 2 cm^2 (Martens, De Wagter et al. 2000).

All these works indicate that the applicability of ionisation chambers to small field measurements is limited and a combination of different measurement modalities may be appropriate.

2.6.1.2 Scintillation detectors

With the increasing complexity of radiotherapy treatment, scintillation detectors have been used for quick and accurate measurements. They offer advantages of small sensitive volume, good flexibility and stability, real time measurements, excellent signal-to-noise ratio and high spatial resolution.

When a photon beam hits a scintillation detector, it excites the atoms and the decay of these excited atoms produces photons in the visible part of spectrum. These photons are guided to the photodetector, collected and then converted to an electric signal.

Optical stimulated luminescence dosimeters (OSLDs) have been used in recent years as dosimeters for in-vivo dosimetry in radiation therapy (Jursinic 2007). These are commercially available as InLight/OSL Nanodots (Jursinic and Yahnke 2011). OSLDs have been successfully used as a reference dosimetry check for small fields. However, these dosimeters have showed energy dependence, so need to be evaluated and corrected to be used successfully in non-referenced conditions (Scarboro and Kry 2012).

Plastic scintillation detectors (PSD) have a lot of advantages over other types of detectors, including water equivalency, high spatial and temporal resolution, energy and dose rate independence, minimal perturbation of the beam and capability of providing instantaneous reading (Beddar, Mackie et al. 1992). PSD had tested to be used for stereotactic radiosurgery dosimetry and showed comparable results with the other detectors in the dose distribution and output factors (Jang, Cho et al. 2007, Lee, Jang et al. 2008, Morin, Béliveau-Nadeau et al. 2013). On the other hand, PSD had suffered from temperature effects, which changes the scintillation light output (Buranurak, Andersen et al. 2013, Wootton and Beddar 2013, Lee, Shin et al. 2015). The major

disadvantage is the generation of Cherenkov signal in the light guide that results in strong cable irradiation effects (Beddar 2006, Liu, Suchowerska et al. 2011, Würfel 2013). This can be resolved by subtracting the Cerenkov noise by using an adjacent background fibre. Also, they are suffering from the system degradation due to radiation damage.

2.6.1.3 Diamond detectors

Diamond detectors have been used as relative dosimeters for small fields because they have many advantages such as water equivalency, energy and temperature independence, stability and resistance to radiation (Würfel 2013, Ralston, Tyler et al. 2014). Diamonds have high sensitivity compared to ionization chambers and high spatial resolution; which make them suitable for small field dosimetry such as IMRT and SRS/SRT.

However, diamonds have high mass density which could cause an over-response of the dose in small fields reaching up to 9.3% in 4 mm equivalent field (Scott, Kumar et al. 2012, Ralston, Tyler et al. 2014). Diamonds are also expensive and exhibits dose rate dependence which needs to be corrected during measurements e.g. depth dose (Laub, Kaulich et al. 1999, Pappas, Maris et al. 2008). They have been successfully used in square small fields as 10 mm (Haryanto, Fippel et al. 2002), but for smaller fields they are underestimating the output factor due to their volume (Sauer and Wilbert 2007, Francescon, Cora et al. 2008). Diamond detectors need to be pre-irradiated prior each use to stabilise their response, and so reduce the polarisation effect (Podgorsak 2005).

2.6.2 2-D dosimetry

The use of 2-D dosimetry becomes more usable especially with the new complicated radiotherapy treatment techniques such as SRS/SRT. The aim of using 2-D dosimetry is

to increase the accuracy and confidence of the dose measurements. Hence, there are many 2D detector arrays that can provide the dose in different locations in the field. Some of these are real time measurements and/or can perform plan dose comparison at the same time (Distance to agreement and gamma analysis). The commercial 2D dosimeters include:

2.6.2.1 Radiochromic™ film

Radiochromic™ films is recommended for small field dosimetry (Aspradakis, Byrne et al. 2010). They consist of 7 to 23 μm ultrathin, radiosensitive leuco dye, sandwiched between two bases made of polyester. The ionizing radiation causes a change in the chemical of the film (colour) due to the polymerization process. The films don't need physical, chemical or thermal processing, but they develop by themselves with time. They can be analysed by using software after scanning. However, radiochromic™ films require calibration to get the relationship between optical density and dose (calibration curve), as recommended by AAPM Task Group 55 (Niroomand-Rad, Blackwell et al. 1998).

They are widely used in high energy radiotherapy and it becomes more popular in the dosimetry of new radiotherapy techniques such as IMRT, SRS/SRT and IGRT because they have high spatial resolution, near tissue equivalent, dose rate independent and self-developing (Butson, Peter et al. 2010, Devic, Tomic et al. 2016). They are insensitive to visible light and nearly water resistance, so they can be used for measurements in a water phantom.

In addition, they have the capability to offer two-dimensional dose mapping which is very useful for small fields dosimetry (Gagnon, Thériault et al. 2012, Ralston, Liu et al. 2012). Hence, AAPM Task Group 42 (Schell, Bova et al. 1995) recommend their use

for the measurement of profiles for GammKnife^{R} and linear accelerator dosimetry. Many authors have used these films in small beam dosimetry and report accurate measurements (Wilcox and Daskalov 2007, Pantelis, Antypas et al. 2008, Tyler, Liu et al. 2013, Miura, Ozawa et al. 2016). However, one of their disadvantages is that they require long processing which increases the probability of the errors as well as not allow on-line dose measurements (Pai, Das et al. 2007, Aland, Kairn et al. 2011). They also can't be used for absolute dose measurements to verify monitor unit outputs (Low, Moran et al. 2011). In addition, radiochromic^{TM} films can't be re-used after irradiation and are rather expensive.

2.6.2.2 IBA I'mRT MatriXX (Scanditronix Wellhofer)

This is an ionization chamber array consisting of 1020 single air vented plane-parallel cylindric ionoization chambers (4.5 mm diameter, 5 mm height and 0.08 cm^3 volume) arranged in 32 x 32 grid matrix (with pixel distance 7.62 mm center-to-center). The active area is 24.4 x 24.4 cm^2. The electrometer is based on 16 TERA ASICs, that reads out each chamber seperately. The minimum read out time is 20 ms.

The dosimetric characterisation and the clinical application of MatriXX array have been studied by different groups (Amerio, Boriano et al. 2004, Stasi, Giordanengo et al. 2005, Lin, Veltchev et al. 2015, Chung, Kang et al. 2016, Durmus and Atalay 2017). MatriXX shows good reproducibility, dose rate independence, energy independence and the dose linearity showed to be good down to 2cGy (within 1% of local dose), then the deviation increases with decreasing the dose (Han, Ng et al. 2010). MatriXX showed a percentage difference in the output measurements up to 5 % for small field sizes and penumbra width up to 50% due to the volume averaging effect (Alashrah, Kandaiya et al. 2010). Han, Ng et al. (2010) found four main negative feedbacks when using MatriXX, which are positive bias, over-response of scattered dose, angular dependence

and round-off error that can contribute significant dose measurements inaccuracies, hence they have suggested to use correction factors when it has to be used (Wolfsberger, Wagar et al. 2010).

2.6.2.2 Octavius 1000 SRS (PTW-Freiburg, Germany)

Octavius detector 1000 SRS is the first 2D liquid filled ionisation chamber array, consisting of 977 detectors with active volume of 0.003 cm^3 and arranged in 11 x 11 cm^2 field. The detector spacing centre-to-centre is 2.5 mm at the inner area (5.5 x 5.5 cm^2) and 5 mm at the outer area (11 x 11 cm^2). It has been characterised to be used in small field dosimetry. It showed excellent stability and reproducibility, dose linearity. It showed 3% dose rate dependance and up to 2.6% deviations in the output factor measurements for 6 MV photon beam at 1 x 1 cm^2 field size due to the volume effect, detector's material and positioning accuracy. Also, there is a small but not negligible field size, depth and energy dependance (Poppe, Stelljes et al. 2013, Markovic, Stathakis et al. 2014).

2.6.3 3-D dosimetry

Gel dosimeters are extremely convenient as they can be manufactured in any size and shape, therefore allowing absorbed dose measurements in full 3D geometry. There are two types of gel dosimeters: Fricke gels and polymer gels. When Fricke gels are irradiated, Fe^{+2} ions are converted to Fe^{+3} ions with changes in the paramagnetic features measurable by magnetic resonance imaging. Fricke gels are limited in use because of the resulted blurred dose distribution due to the continuous post-irradiation diffusion in the gelatine.

The second type, polymer gel monomers (usually acrylamide) are dispersed in gelatine. There are various different types of gel such as BANG^{TM} gel and MAGIC gel. When polymer gel is irradiated a polymerization process takes place and results in 3D polymer gel matrix as a function of the absorbed dose. This is measured by Nuclear Magnetic Resonance (NMR), x-ray, Computed Tomography (CT) or Ultrasound (Podgorsak 2008). Polymer gel has several advantages for measuring small-field dose distribution including its high spatial resolution, good tissue equivalence (around 94% water), 3D dose distribution, energy independence, and its ability to be prepared in different shapes (Pappas, Maris et al. 2009, Baldock, De Deene et al. 2010, Lee, Wu et al. 2014). There are many literature reviews that have showed the successful use of gel dosimeters in determining SRS/SRT dosimetric parameters measurements (Cosgrove, Murphy et al. 2000, Seimenis, Moutsatsos et al. 2009, Wong, Ackerly et al. 2009, Kairn, Taylor et al. 2012, Lee, Wu et al. 2014). On the other hand, gels have some limitations such as their sensitivity to oxygen, which cause polymerization and hence minimize the sensitivity of the gel to radiation and they are also hard to use in clinical environment due to their preparation require chemical processing (Hassani, Nedaie et al. 2014).

2.7 Silicon dosimetry for SRS/SRT

Silicon detectors have been used as radiation dosimeters for more than three decades and they have been used as in vivo dosimeters since the 1980s (Lutz 1995, Knoll 2010). They are available as 1D, 2D and 3D and have many advantages for use as a dosimeter in radiotherapy, especially in the new complicated techniques that requires real time measurements and high spatial resolution such as IMRT, IGRT, SRS/SRT and SBRT.

2.7.1 Advantages of silicon dosimetry

There are many advantages in the use of silicon detectors for megavoltage photon beam dosimetry; especially for small photon beam dosimetry. Silicon detectors have higher sensitivity to radiation than ion chambers of the same volume (18000 times more) due to their higher density (2.33 g/cm^3) and the lower ionization energy compared to gas (3.6 eV) (Attix 2008). Therefore, the sensitive volume of the diode can be small and so easily defined with the effective point of measurement within 1 mm from the outer surface of the detector (Rikner and Grusell 1987). This leads to very high spatial resolution without affecting the sensitivity of the detector (Rosenfeld 2006). Silicon diodes can be arranged as an array to cover all or most of the irradiated field area. They can be arranged easily into different configurations (shape, volume and dimensions) depending on what is required, and they have excellent reproducibility and ease of use. Silicon detectors can be available in shielded (cap) and unshielded designs, depending on the manufacturers and the aim of its use. The aim of the cap is to ensure mechanical protection and act as build-up material for photon beams (Marinello 2007). In addition, silicon detectors can works in passive mode (as TLDs) or in active mode (as ICs) (Rosenfeld 2006). Moreover, silicon detectors provide high signal-to-noise ratio and they characterise with the constancy of silicon to water stopping power ratio for the mega voltage energy that is used in radiation therapy, which makes it suitable relative dosimeter.

2.7.2 Limitations of silicon dosimetry

However, silicon detectors have some known limitations; which need to be characterized in order to derive appropriate correction factors or minimize these effects. Some silicon detectors exhibit dose rate, temperature, energy, angular dependence

and/or need to apply correction factors due to their extra-cameral components, electron density different to water and volumetric effect. In addition, their sensitivity is degraded by radiation defects produced in silicon during irradiation damage.

The sensitivity (charge collected per unit absorbed dose) of diodes increases by increasing the instantaneous dose rate (dose rate within each radiation pulse from LINAC) due to the direct recombination in the diode. This effect can be significantly minimized by selecting p-type, pre-irradiating by large doses, using heavy platinum doping or epitaxial guarded silicon (Wilkins, Li et al. 1997, Shi, Simon et al. 2003).

Another factor that can affect silicon diodes is the temperature, which could affect the level of recombination and hence the sensitivity (Podgorsak 2008). At very small irradiation levels, the detector sensitivity increases linearly with the temperature, in the clinical temperature range (20 – 40 ^{0}C). This variation depends on the previous history of the diode and the type of material (Grusell and Rikner 1986). It can affect the accuracy of the dosimetry, as reported by Sun Nuclear, PTW and Scanditronics it reached up to 0.28%/ ^{0}C (Rosenfeld 2006). The variation in sensitivity with temperature change could be cancelled by the pre-irradiation of the diode to high dose.

The silicone diode energy dependence is related to the material surrounding the die; which usually has higher atomic number compared to water. This causes an energy dependence at low photon energies below 100 keV (Tavernier 2009). This is because of higher ionization rate per unit volume of silicon compare to water that results from the large photoelectric cross section, which is proportional to the material's atomic number (Z^{n}, where n is between 4 and 5 depending on the energy) (Griessbach, Lapp et al. 2005). The energy dependence is related to the construction of the diode geometry and the build-up material. Therefore, each diode should be used with caution depending on the energy range it is designed for. The previous studies showed that the energy

dependence related to the thickness of the build-up material (shielding) (Rikner and Grusell 1985, Saini and Zhu 2007).

In addition, silicon diodes have been reported to show angular dependence when used in rotational beam measurements (Low, Moran et al. 2011). This depends on the design properties of the diode. Several research groups have studied the angular dependence of diode arrays due to the asymmetrical nature of the junction and found that it was possible to get an over-response up to 30% for 6 MV photon beams at $90^0 \pm 10^0$ and $270^0 \pm 10^0$ (Wolff, Carter et al. 1998, Jursinic, Sharma et al. 2010, Li, Deng et al. 2010, Jin, Keeling et al. 2014). The angular dependence can be eliminated by using different techniques, such add halfpipe-shaped boluses (Zhang 2010), filling air gaps with sheets of Lucite and pieces of copper (Jursinic, Sharma et al. 2010) or by applying angular correction factors (Zhou and Wu 2011).

The silicon diode arrays also have some perturbation effects due to their atomic composition and electron density properties, extra-cameral components and finite volume of the detector cavity. These perturbations affect the measurements of small fields, especially in the output factor measurements. Different scientific papers have focused on finding proper correction factors by using different beam qualities, field sizes, LINACs and detectors (Cranmer-Sargison, Weston et al. 2011, Francescon, Cora et al. 2011, Cranmer-Sargison, Weston et al. 2012, Francescon, Kilby et al. 2012, Ralston, Liu et al. 2012). Scott, Kumar et al. (2012) have indicated that the density of the detector is the main cause of over-responding in small field dosimetry, in addition to volume averaging effects. Also, Bouchard, Seuntjens et al. (2015) have pointed out that the density of the detector, extra-cameral components and volume averaging were the main cause of perturbations. The presence of high Z and density material increases the photon interactions compared to water equivalent material, which adds extra electrons

that reach the detector's sensitive volume and so cause perturbations in the electron fluence in the detector. Therefore, in order to minimize the problem of over-responding in small beam measurements, correction factors need to be applied, which could be LINAC, beam quality, field size and detector dependent. However, the performance of the detector can be improved by removing the high atomic number and density materials near the sensitive volume or by adding low atomic number and density materials around the sensitive volume to compensate for the spectral difference of high Z material (Benmakhlouf and Andreo 2017).

The irradiation of the diode for long term (high accumulated dose) can cause radiation defects and reduction in the diffusion length, which results in reduction of detector's sensitivity. This reduction is related to the irradiated energy; the higher the energy, the more degradation. To overcome this effect, the diode needs to be pre-irradiated before use (radiation hardness) or the lifetime of the charge carriers needs to be reduced by doping the diode's base (Moll 1999, Rosenfeld 2006, Ahmed 2007).

2.7.3 Radiation damage in silicon

The usefulness of silicon detectors comes from the p-n junction principle, as silicon itself is a poor conductor (IV element) when it is pure crystal. The p-n junction is obtained by joining p-substrate and n-substrate to high pure silicon to form intrinsic diodes. These can be made by using a small quantity of silicon doped with n-type diodes from V group (mostly phosphorus) or p-type diodes from III group (mostly boron). The doping level depends on the number of doping atoms per unit volume of silicon crystal (Rikner and Grusell 1987). Both types are available commercially, but p-type silicon dosimeters are suitable for radiotherapy measurements, since it has smaller dark current and is less prone to radiation damage (Ahmed 2007, Podgorsak 2008).

In the intrinsic material, Fermi level is between the conduction and valence bands, where there is an equal number of electrons and holes. The Fermi level is located closer to the valence band in p-substrate silicon, while it is closer to the conduction band in the n-substrate silicon, as shown in figure 2.4. In p-type, holes are the majority carriers and the electrons are the minority carriers, it is the opposite in n-type of silicon.

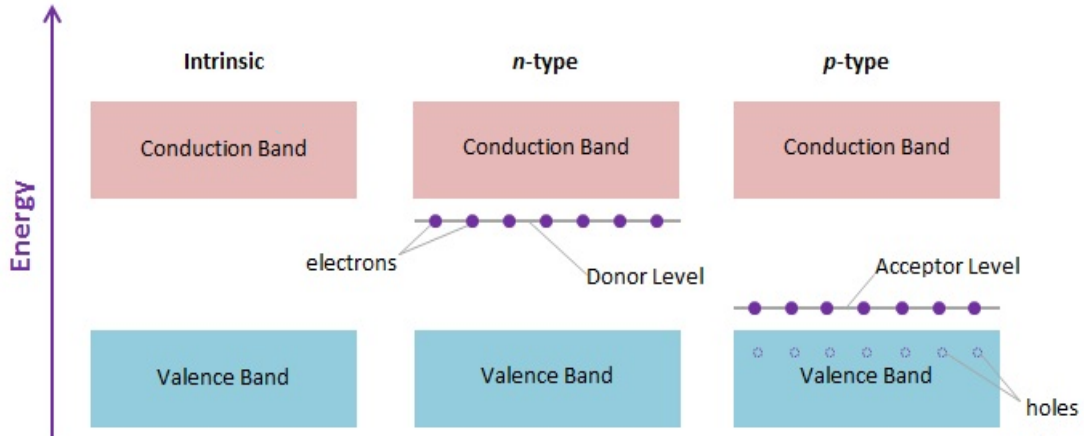

Figure 2.4: the electron energy band for intrinsic, n-type and p-type silicon.

At the equilibrium conditions, when the p- and n- regions join together results in p-n junction. Then, the carriers start moving due to diffusion across the interface, where electrons drift from n- to p- region producing negatively charged region while holes drift from p- to n- region producing positively charged region, as shown in figure 2.5. When the electric field generated by the majority carriers is strong enough the dynamic equilibrium is created and total current through diffusion and drift through p-n junctions is absent. Hence, a built in potential Ψ_0 created due to the distribution of the carriers in the junction, which prevents the continuation of diffusion of charges across the junction. This charged region is called the 'depletion layer', W, where its length depends on the impurity concentration. In non-equilibrium conditions, the current flow at the p-n junction depends on the polarity of the applied voltage.

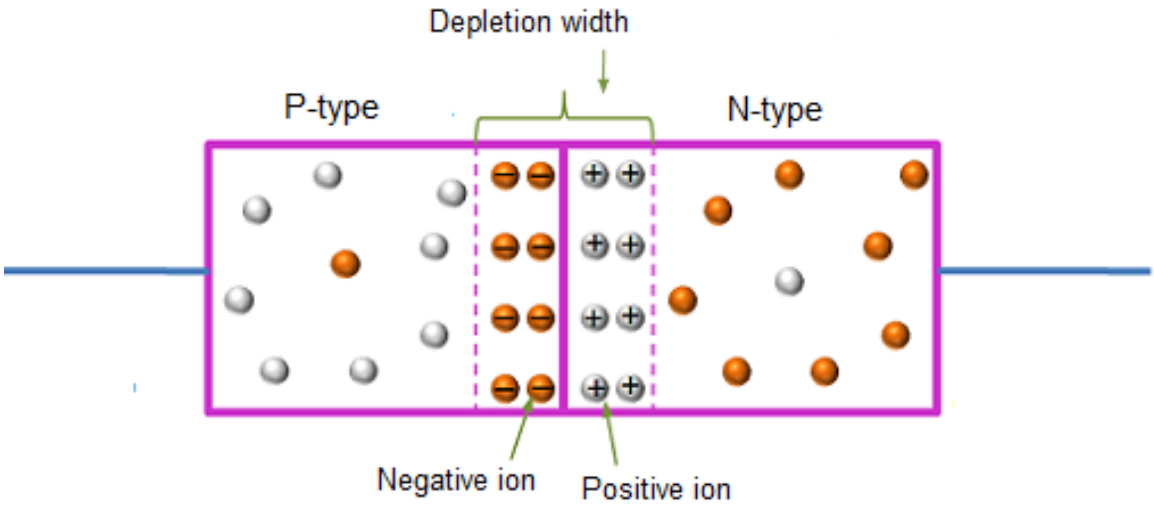

Figure 2.5: p-n silicon diode during unbiased condition.

The p-n junction works as a diode and the external bias (forward or reverse) across it affects its current as shown in figure 2.6. By applying forward bias (usually within 0.7 V), the current increases rapidly with the applied voltage (Rikner and Grusell 1987). Using a reverse bias, which could be thousands of volts, causes an increase in the width of the depletion region due to the majority of carriers moved to the electrodes and away from the junction. By increasing the reverse bias, the reverse current which is called the leakage current, rises slightly until reverse bias reaches critical value, called breakdown voltage (Sze and Ng 2006).

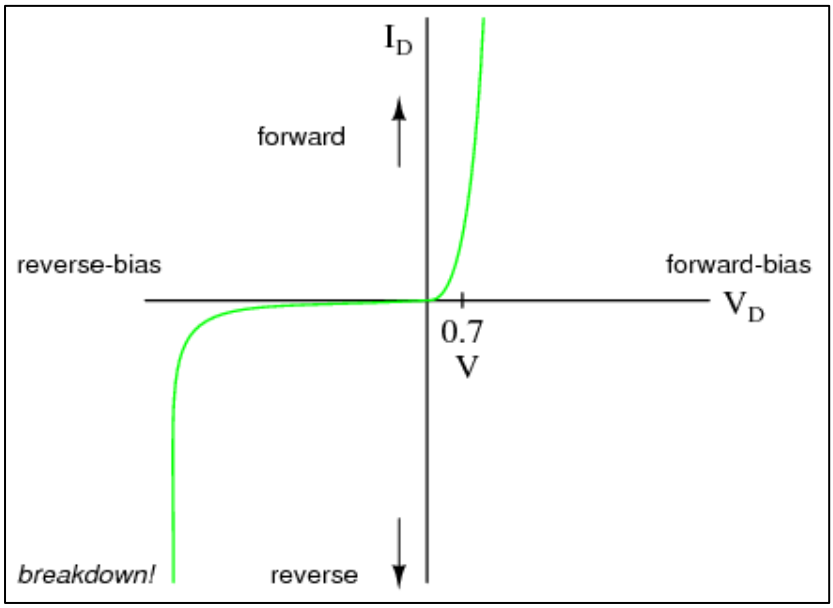

Figure 2.6: I-V characteristic of a particular Si diode.

The p-n diode is known to be operating in a passive mode (no voltage applied), so no current flows in the external circuits. When the diode is irradiated with ionising radiation as shown in figure 2.7, electron-hole pairs are produced in the diode, with average energy required to produce electron-hole pairs in the silicon is 3.6 eV. Produced minority charged carriers (electrons in p-type and holes in n-type) diffused toward the depleted region. They are swept across the depletion region by electric field due to the built in potential, Ψ_0 (Shi, Simon et al. 2003). These charged carriers detected on the electrodes by an electrometer are only those, which were produced within the diffusion length from both sides of p-n junction. (Sze and Ng 2006, Metcalfe, Kron et al. 2012).

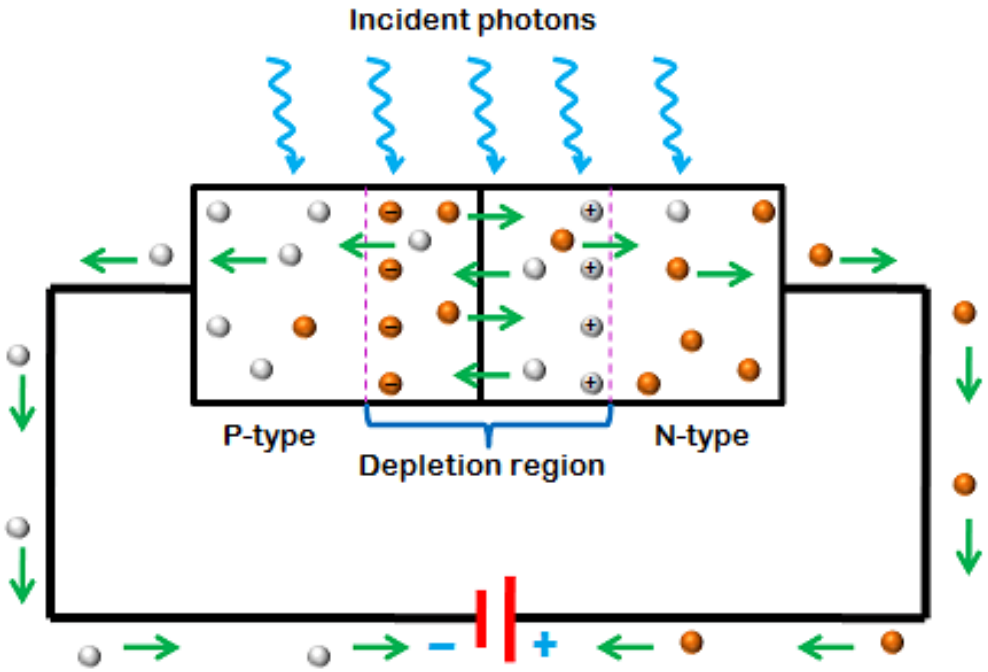

Figure 2.7: Schematic of p-n diode irradiated with photons.

If the junction region is used to detect radiation, the sensitivity is affected by with the radiation. The sensitivity of the silicon detector in the passive mode is determined by its active volume, V. This volume is the product of the detector area and the minority charged carriers diffusion length (L_n for electrons in p-Si and L_p for holes in n-Si), where L is defined as

$L = \sqrt{D\,\tau}$;

Where D is a diffusion constant (D_n for electrons, D_p for holes) and τ is the minority carrier lifetime (Sze and Ng 2006). The minority charged carrier lifetime is reduced with accumulated dose due to radiation defects, which produce recombination deep level centres in a forbidden gap. (Li 2009). Radiation damage in silicon diode causes an increase in the leakage current and change in the sensitivity with the accumulated dose due to reducing of the diffusion length. There are two main types of radiation

damage that effect the performance of silicone detectors; these are the bulk and surface damages (Dalal, Bhardwaj et al. 2014).

Firstly, bulk damage results from the displacement of a silicon atom from its physical place to an interstitial place, causing a Frenkel defect. It is based on non-ionising energy loss (NIEL) caused by protons, neutrons, electrons and high energy photons, with a minimum required energy of 25 eV (Moll 1999). The bulk damage depends on the radiation type and its energy as shown in figure 2.8. This type of damage affects the detector by increasing the leakage current, inverting the substrate type (in n-type Si) and reducing the collection efficiency. The leakage current rises due to the formation of generation–recombination centres (GRCs) in the diode. Increase in leakage current causes reduction in the signal to noise ratio (Moscatelli, Passeri et al. 2016). To minimize this issue, a diode is used in passive mode. The inversion of n-type substrate is due to radiation defects producing acceptor levels in a forbidden gap leading to the alterations in the effective doping concentration and the depletion voltage or region with built in electric field in a passive mode of operation. To control this effect, oxygen doping is used to reduce the effect of donor removal (Moll, Fretwurst et al. 2000). The third effect of bulk damage, the decrease of charge collection efficiency (CCE) which is also due to the GRCs creation in the substrate, is determined by the lifetime of minority carriers as mentioned above, the electric field distribution and the physical size of the detector (Moll and Collaboration 2006, Lalwani, Jain et al. 2016).

The second type of damage in silicone diodes is the surface damage, which results from the accumulation of trapped positive charge in the SiO_2/Si interface. It is based on ionising energy losses (IEL), when electron-hole pairs produced in SiO_2 due to ionisation. Part of e-h pairs have large chance to recombine and this recombination depends on the type of radiation and its energy (Moll 1999). The mobility of the holes

in the oxide is lower than for electrons, so the holes are trapped on the SiO_2/Si interface by oxygen vacancies causing positive charges in the oxide until it reaches saturation at a high dose. This positive built in charge can affect the sensitivity of the diode.

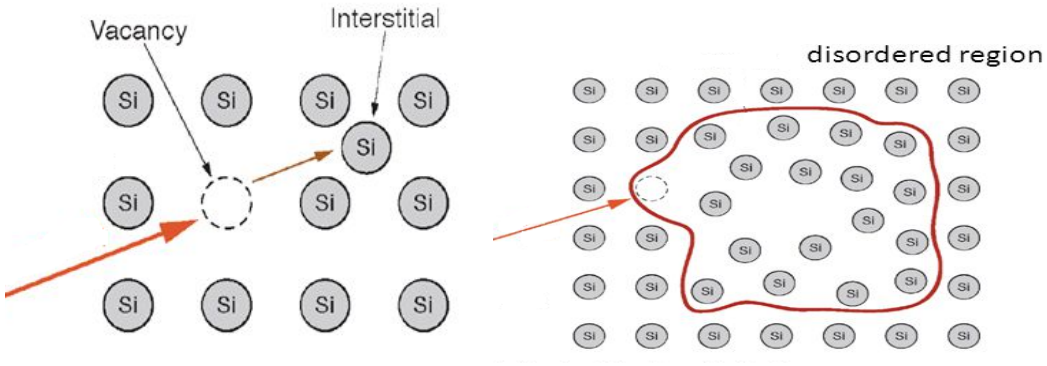

(a) (b)

Figure 2.8: Types of bulk radiation damage, (a) single damage, (b) cluster damage.

2.7.4 Commercial silicon detectors

2.7.4.1 SRS MapCheck™ (Sun Nuclear Corporation, Melbourne, FL)

MapCheck™ is a 2-D array designed especially for SRS patient specific QA and end-to-end test. It can replace the film dosimetry in the small field dosimetry. It can provide both absolute and relative dose measurements. It consists of 1013 diode detectors in an array, covering an area of 77 x 77 mm^2. The detector resolution is about 0.48 mm diameter and detector spacing of 2.47 mm. It is designed to insert into StereoPHAN and runs on SNC Patient software (Guo FQ 2006).

2.7.4.2 MapCheck 2 (Sun Nuclear Corporation, Melbourne, FL)

This is a 2D array, consisting of 1527 n-type diodes that can measure up to 32 x 26 cm^2. The active detector area is 0.64 mm^2 and volume of 0.019 mm^3 with 7.07 mm detector uniform spacing. It has been approved as an effective tool for VMAT QA and it showed

a good agreement with the treatment planning system for 6, 8, 10 and 15 MV photon beams, while there has been no consistency in the gamma passing rate in terms of energy (Jin, Jesseph et al. 2014, Keeling, Ahmad et al. 2014). The authors have compared MapCheck 2 with TPS (BrainLab iPlan version 4.5 and Varian Eclipse version 8.9) using AAA with 2 x 2 x 2 mm^3. The 2D and 3D Gamma passing rates (1%/1 mm, 2%/2 mm and 3%/3 mm) were used for different sites, where 3%/3 mm gamma passing rates were passed above 95%. Also, MapCheck 2 showed a large angular response reaching up to 25% for 6 MV, especially at gantry angles 90^0 and 270^0 (Keeling, Ahmad et al. 2013, Jin, Jesseph et al. 2014, Jin, Keeling et al. 2014).

2.7.4.3 ArcCheck (Sun Nuclear Inc, Melbourne, FL)

ArcCheck is a 4D QA measurement array designed especially for the modern radiotherapy delivery techniques. It contains 1386 diode detectors with 1 cm detector spacing, whilst facing the beam all the time. The detectors are placed in spiral geometry of 21 cm diameter cylindrical phantom of 21 cm length. There is a 15 cm cavity diameter, to allow the use of different detectors and tissue equivalent inserts. It has a real time electrometer measuring every pulse. The entry and exit doses are measured for every angle ($\pm 1^0$). ArcCheck showed excellent dose linearity and reproducibility, low field size and dose rate dependence within 0.5% and 1%, respectively. The angular dependence of ArcCheck was within 3% as compared with TPS for both 6FF and 6FFF MV photon beams. When used for clinical VMAT and IMRT cases, it showed good agreement with TPS in terms of 3% / 3 mm gamma passing rates (Chaswal, Weldon et al. 2014, Thiyagarajan, Nambiraj et al. 2016).

2.7.4.4 Delta^4 (ScandiDos Inc, Uppsala, Sweden)

Delta^4 consist of 1069 p-type diodes arranged on two orthogonal boards in 22 cm diameter PMMA cylindrical phantom. The spatial resolution is 5 mm at the interior (6 x 6 cm^2) and 10 mm exterior (20 x 20 cm^2). It is synchronized with the LINAC pulses, so provides a fast accurate response. The gantry angle and the delivery sequence are stored for each data point. Therefore, the required correction factors can be applied at the segment level. Delta^4 has an analysis software system, allows easy and quick plan analysis and compares with TPS in terms of dose deviation, distance to agreement and gamma index. The basic characterisation of Delta^4 was found to be good in terms of short-term reproducibility, dose linearity, dose rate dependence, angular response and absolute calibration accuracy (Sadagopan, BenComo et al. 2007, Zhang, Norrlinger et al. 2009, Feygelman, Opp et al. 2011). However, it is not suitable for small field dosimetry due to the large resolution of the detector (> 2 mm) (Bedford, Lee et al. 2009, Fredh, Scherman et al. 2013).

2.7.5 The silicon detectors developments

Many groups are working these days on silicon array detectors (Manolopoulos, Wojnecki et al. 2009, Bocci, Cortés-Giraldo et al. 2012, Bisello, Menichelli et al. 2015); taking advantage of their excellent spatial resolution and small size compared to ion chambers, their real time measurements compared to EBT3 and TLDs and their high sensitivity compared to EBT3. In addition, they are less expensive than diamond detectors and they have reasonable uniformity compared to gel dosimetry. On the other hand, silicon detectors response is dose rate and angular dependent that require their characterization to derive correction factors.

The Centre for Medical Radiation Physics (CMRP) is working to develop silicon detectors that are suitable for small field dosimetry QA. The CMRP has developed different high spatial resolution monolithic silicon detectors such as the 1D Dose Magnifying Glass (DMG) (Wong, Carolan et al. 2010, Wong, Knittel et al. 2011), 2D Magic Plate (MP121 & MP512) that are widely published (Aldosari, Petasecca et al. 2014, Petasecca, Newall et al. 2015, Alrowaili, Lerch et al. 2017). The MP 512 has 2 mm spatial resolution and it was concluded that for SRS small field dosimetry, a detector with better spatial resolution is required to accurately reproduce the penumbra. Recently, the CMRP has developed an innovative monolithic silicon array detector, DUO (Shukaili, Petasecca et al. 2017) and OCTA (Porumb, Aldosari et al. 2016), to be used in SRS/SRT for real time dosimetry as a logical incremental step forward in the clinical application of monolithic Magic Plate detector technology for improvement of small radiation field dosimetry. The next chapters will give details of these two detectors and their electrical and clinical performance characterisations for small field dosimetry.

2.8 Conclusion

Recently, with new radiotherapy treatment techniques such as stereotactic radiotherapy (SRS/SRT), intensity modulated radiation therapy (IMRT) and image guided radiation therapy (IGRT), the use of small radiation fields in clinical practice has increased. The small field is not easily defined because it depends on the quality of the beam, the size of the source (focal spot), the type of collimation and the density of the irradiated media. Small field dosimetry is challenging due to the existence of lateral charge disequilibrium, partial blocking of the beam source and the detector size. Therefore, the quality assurance of small field treatment requires specific dosimetry tools that ideally should be (i) tissue equivalent, (ii) of small volume, (iii) dose rate, energy and

directionally independent, (iv) of high spatial resolution and real-time readout and (v) capable of 2D mapping. In addition, the density of the material surrounding the sensitive volume (SV) of the detector (extracameral volume) is important.

Until now, there is no ideal detector that has all those characteristics. Hence, there are recommendations to use more than two detectors in order to compare the results of small beam parameters. Radiochromic films have been used widely for two-dimensional dosimetry in SRS because they have good spatial resolution; they are energy independent, tissue equivalent and self-developing. The main disadvantages of radiochromic films are the post irradiation waiting time and the long processing, which may further increase the uncertainty of measurements.

Silicon diode detectors are the most widely used dosimeters in SRS dosimetry because of their small sensitive volume. Usually, they are not subject to volumetric effects, energy dependence in MV photon fields and can be compensated for temperature dependence. Some commercial dosimetry QA devices using silicon detectors are Delta4 (Scandidose, Sweden), SRS MapCheck, MapCheck2 and ArcCheck (Sun Nuclear, Melbourne, USA). Unfortunately, these commercial tools don’t have enough spatial resolution for SRS/SRT QA where sub-millimetre spatial resolution is required in the penumbral region. Therefore, the Centre for Medical Radiation Physics (CMRP) has been working to develop silicon detectors that are suitable for small field dosimetry QA.

CHAPTER 3: Description of the proposed instrumentation

3.1 Introduction

The aim of this chapter is to describe in detail the detectors that will be used in this thesis (DUO and OCTA), with their electric connections and their software programmes. The rotatable phantom and the inclinometer used will be also be described in this chapter.

3.2 Hardware

3.2.1 DUO detector

DUO detector (figure 3.1) is a monolithic silicon detector designed by the Centre of Medical Radiation Physics (CMRP) at the University of Wollongong (UOW). The pixels are arranged in two linear orthogonal arrays with 253 pixels for each arm, implemented on a 470 μm thick p-type bulk silicon substrate, which has low resistivity (10 Ω.cm) and N_A about 1.358 x 10^{15} cm^{-3}. The size of the central pixel is 180 x 180 μm^2, the four other central pixels are 160 x 200 μm^2 and the remaining pixels have a size of 40 μm in the direction of the linear array axis and 800 μm in the orthogonal direction (figure 3.2). The detector pitch is 200 μm to provide the required spatial resolution for measurements of the sharp fall off penumbra regions. The total array area is 52 x 52 mm^2. DUO is placed between two 5 mm thick PMMA slabs in order to protect it from mechanical damage. The diodes operate in passive mode (no voltage applied between the n-p junctions). Moreover, DUO was pre-irradiated with a dose of 140 kGy using Co-60 gamma source to stabilize its response. After pre-irradiation, the

sensitivity of the DUO was stable and within 2% for any subsequent 1 kGy irradiation. Radiation degradation of the DUO's sensitivity due to photo-neutrons from 18 MV medical LINAC was measured to be 2% for 65 Gy of dose delivered at d_{max} (Aldosari 2015). The DUO detector is placed on a thin printed circuit board (PCB-500 µm thick), and connected to the fast DAQ system.

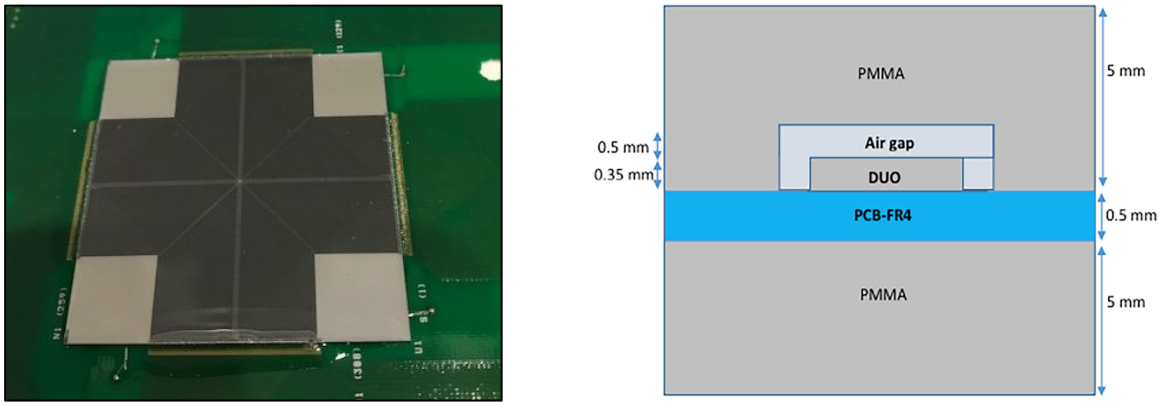

(a) (b)

Figure 3.1: a) DUO detector mounted on a PCB, b) Schematic of the DUO packaging (not to scale).

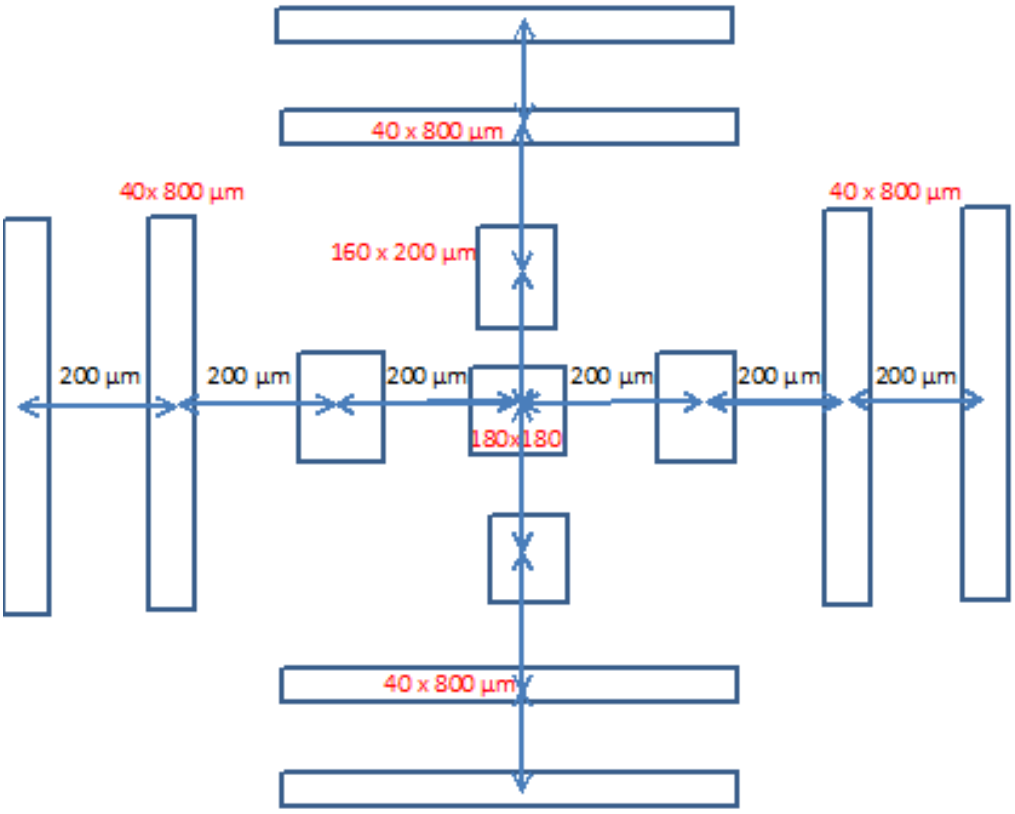

Figure 3.2: A diagram of DUO central pixels arrangement and sizes (not to scale).

3.2.2 OCTA detector

OCTA detector (figure 3.3) is likewise a monolithic silicon detector designed by CMRP at UOW. It contains 512 pixels arranged in four linear arrays, two crosses of two orthogonal arrays, each 45^0 with respect to one another, intersecting at the centre (figure 3.4). OCTA has been manufactured on p- type silicon (100 Ω.cm) 38 µm thick epitaxial layer. The central pixels form 3 x 3 square and total area of 920 x 920 μm^2 with pixel size of 160 x 200 μm^2, except the central one in which the size is 180 x 180 μm^2. The other pixels are 40 x 800 μm^2, with overall detector size of 40.2 x 40.2 mm^2. The pitch size is 300 µm in the orthogonal arrays and 430 µm in the other diagonal arrays. OCTA also like DUO, is placed on PCB board and placed between two 5 mm thick PMMA slabs with an air gap of 1.0 cm above it. It also works in passive mode.

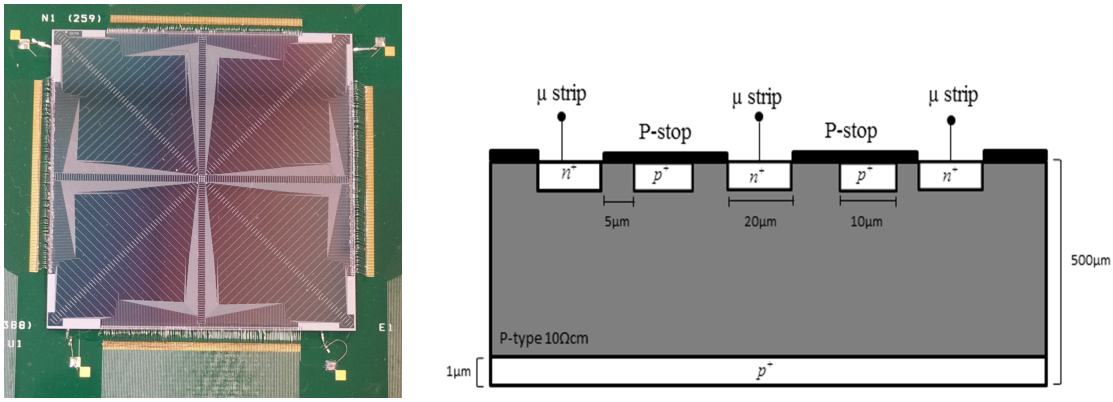

(a) (b)

Figure 3.3: (a) OCTA detector on PCB, (b) A simplified topology fragment of OCTA detectors based on a bulk substrate.

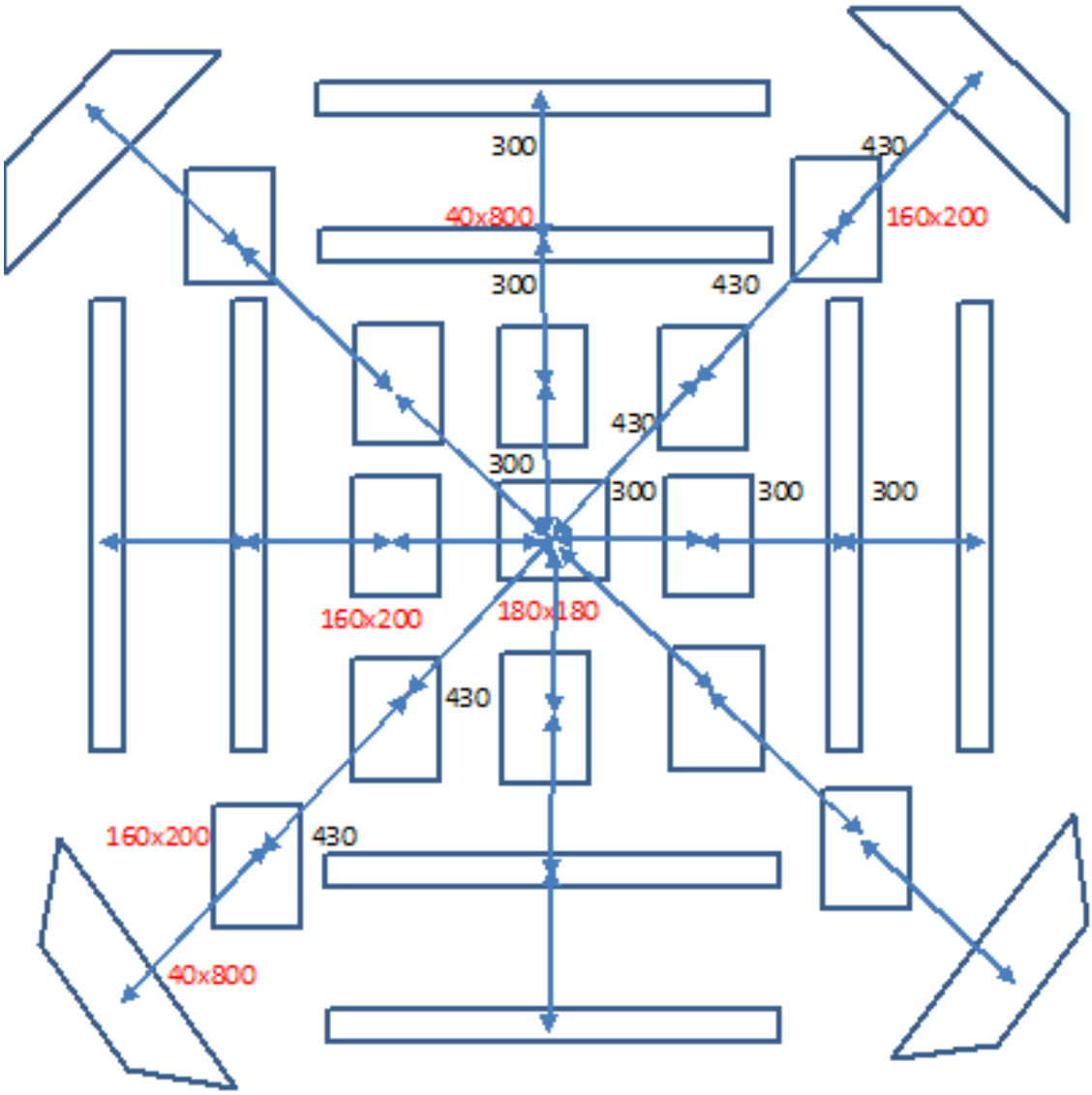

Figure 3.4: A diagram of OCTA central pixels arrangement and sizes, all measurement units in µm (not to scale).

3.3 Software

3.3.1 Data Acquisition System

The data acquisition system (DAQ) is an essential tool for the readout of pixelated detectors. Its purpose is to convert the electric signal originated in the detector into digital values for analysis processing. In this study both detectors, DUO and OCTA, are

sharing the same DAQ. It is designed by CMRP and is based on a commercial analogue front end named AFE0064 (Texas Instruments). AFE0064 chips consist of 64 channels which each provides an analogue differential output proportional to the charge accumulated in the capacitor during a determined time frame. The sensitivity of the chip (gain) can be adjusted electronically by varying the amount of charge that is stored on the capacitor in 7 steps up to 9.6 pC, with 16-bit resolution for each integrator and less than 0.1% non-linearity. In order to have high signal-to-noise ratio, the AFE provides a correlated double sampling of the analogue output to subtract the low frequency noise and base line from the input signal.

For both DUO and OCTA, the DAQ uses eight AFE0064 chips, for the total of 512 channels. They readout in parallel by using four analogue to digital converters (ADCs). Field Programmable Gate Array (FPGA) controls both AFEs and ADCs. This FPGA is used to provide the clocks and sync circuits for synchronisation to manage the signal trigger from the LINAC to synchronise the acquisition when the beam is on. A coaxial cable is used to connect the LINAC to the FBGA DAQ. The digital data is then sent from the FPGA to the computer via USB 2.0 cable for data viewing, by using graphical user interface software (designed by the CMRP) and data storage.

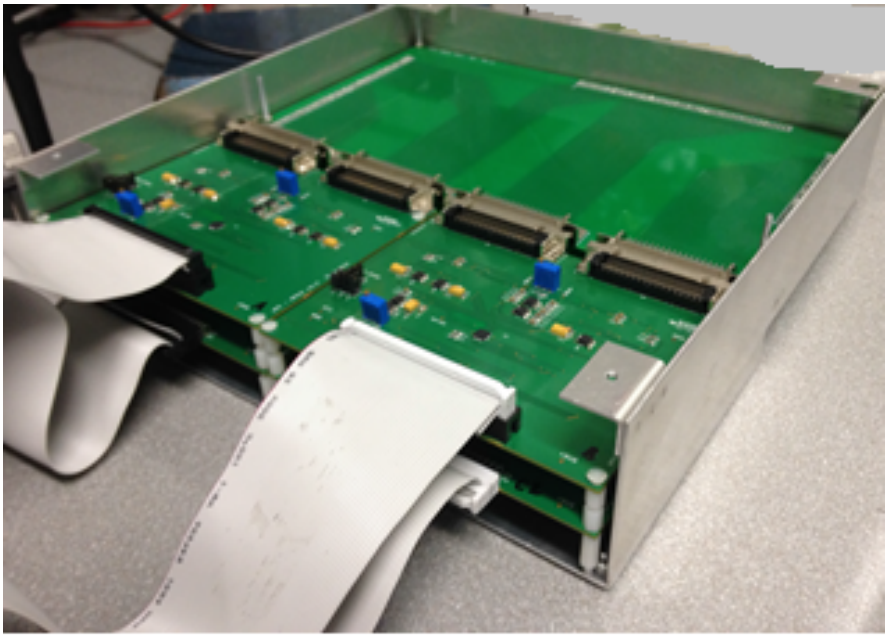

Figure 3.5: The DAQ system used for DUO and OCTA detectors.

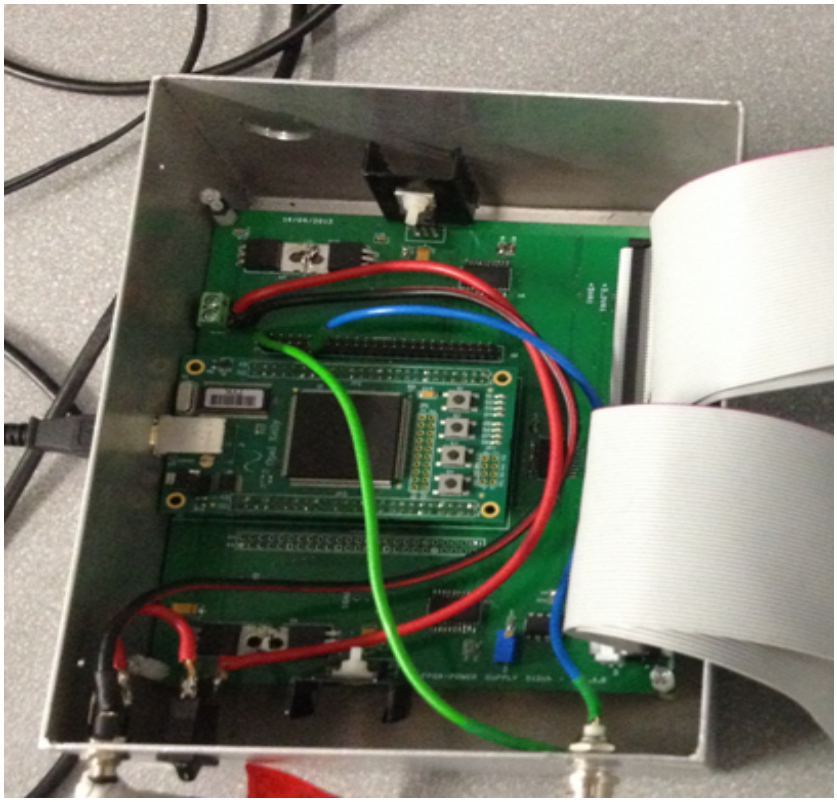

Figure 3.6: The FPGA board.

3.3.2 Interface software

To acquire the measurements, the user has to connect the electronics of the detector (FPGA) to the computer and power on the graphical user interface (GUI) software. GUI is the tool that is used for real-time visualisation and post processing. When it is on, it informs the user if the device is connected and it prompt the user to load the firmware in the FPGA.

The software has two main windows: the acquisition mode and off-line data analysis mode. In this research, two GUIs designed by the CMRP at the UOW are used, Romulus for DUO and AFE Magic Suite for OCTA.

3.3.2.1 Romulus

Romulus is versatile software, used for different CMRP detectors. It has been developed by using C++. In this research, the discussion of Romulus software (version 3.81) is focused on its use in combination with DUO detector. More details about this software can be seen in (Porumb 2016)

In the Romulus acquisition window (as in figure 3.7), there are four main areas:

1. Menu options at the top of the window: the user can load the firmware suitable for the detector, setup the required gain, select internal or external trigger and can choose which graph layout to use: frame-by-frame or integral response.
2. Real time data plots: displays the reading of the detector normalised dose
3. The user input parameters: for the user to input the specifications of the detector (integration width, duration of measurements and number of channels) and the required parameters for the graphical visualisation zones as well as the file name for saving.

4. Status notification: provides feedback for the user such as decoding status and confirmations of the use of equalisation factors.

In the Romulus data analysis window, off-line data analysis is possible on a per-pixel basis. Once the acquisition is done, the software saves the files as a .txt_le where readings are stored per pixel and per frame (for 512 channels). By knowing the correspondence between the channels list and the physical position of the pixels (as they are not in order in the PCB board), the readings can be associated to the proper channel.

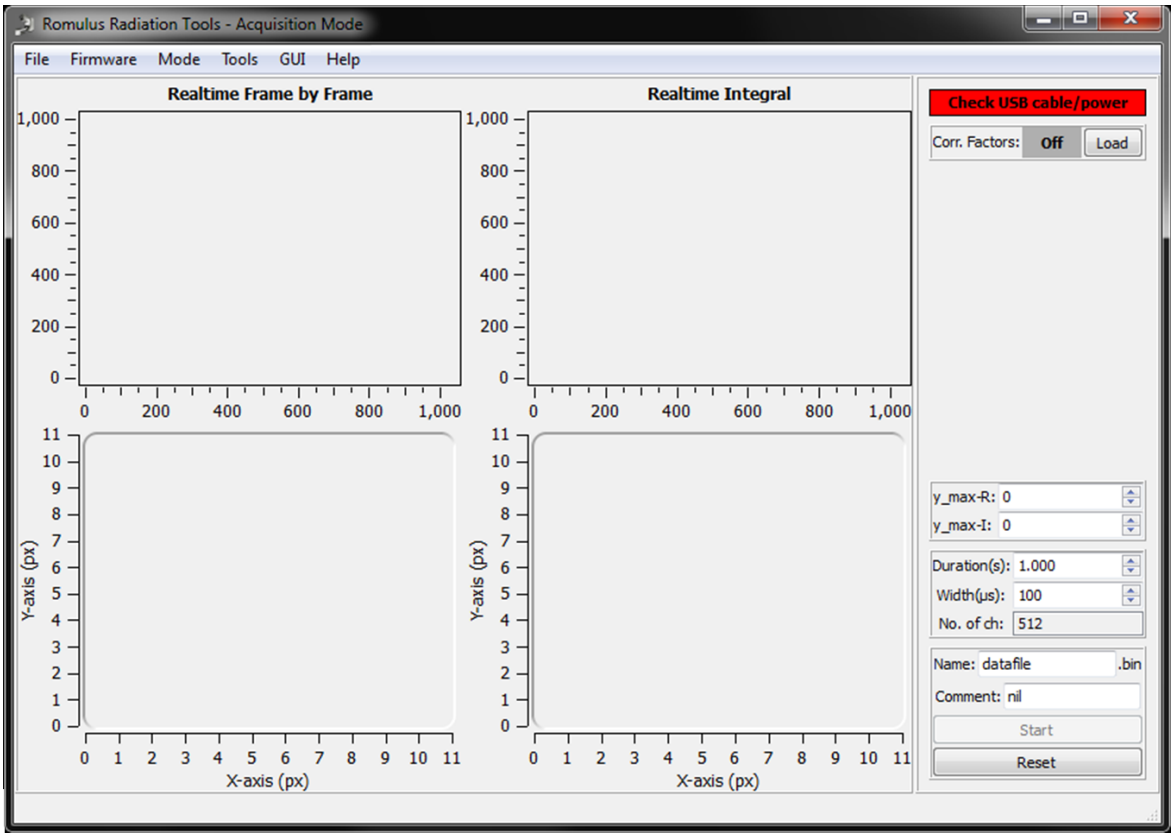

Figure 3.7: A screen shot of Romulus interface software.

3.3.2.2 AFE Magic Suite

AFE Magic Suite software is designed by the CMRP and is an upgrade of Romulus interface software. It has two main windows for visualisation and data analysis, as shown in figure 3.8.

In the visualisation window, the user can select the required parameters for the detector and setup the measurements. This window has two main functional modes: alignment and acquisition. The alignment mode selection allows confirming the correct alignment of the detector before starting the measurements in all axes of each detector. In the acquisition mode, the user can visualise in real time the 2D map of instantaneous and integral detector responses. The normalised response of individual axis can be seen by selecting the axis in the 2D map.

The silicon detector array consists of many pixels, which are connected to multichannel electronic readouts. The response of each channel on the array could differ from the others, as it is a function of the sensitivity of each pixel and the gain of its corresponding preamplifier readout channel. To solve this issue, the per-pixel correction factors need to be obtained to produce uniform response of the DUO detector. This procedure is called equalisation (Wong, Fuduli et al. 2012). Therefore, the array detector is irradiated in a flat radiation field in order to find the per-pixel factor. This can be done automatically before the experimental measurements by selecting the equalisation mode in the acquisition window. Then in the analysis mode, select to apply the equalisation factor to the measurements.

Then, the user can decode the file, load the files and read the log. More details about decoding the files can be seen in a PhD thesis by Claudiu Porum (Porumb 2016). In the read log, by double clicking on the file the final detector response is calculated and saved in files (which can be opened in excel) as

1. File.dat: raw data
2. File_decoded.txt: the response of each channel as a function of time frame.

3. File_decoded_integral.dat1: the sum of the response for each channel overall the irradiation time without mapping.
4. File_decoded_integral_map.dat1: The sums of the response for channel overall the irradiation time with mapping as per pixel order in the array.
5. File_decoded_integral_map_map_baselinesubstract.dat3: the sum of the response for channel overall the irradiation time with mapping as per pixel order in the array corrected by using the equalisation factors.

In the analysis window, the user can see the detector response of each channel in terms of acquisition time by selecting the channel view as example shown in figure 3.9.

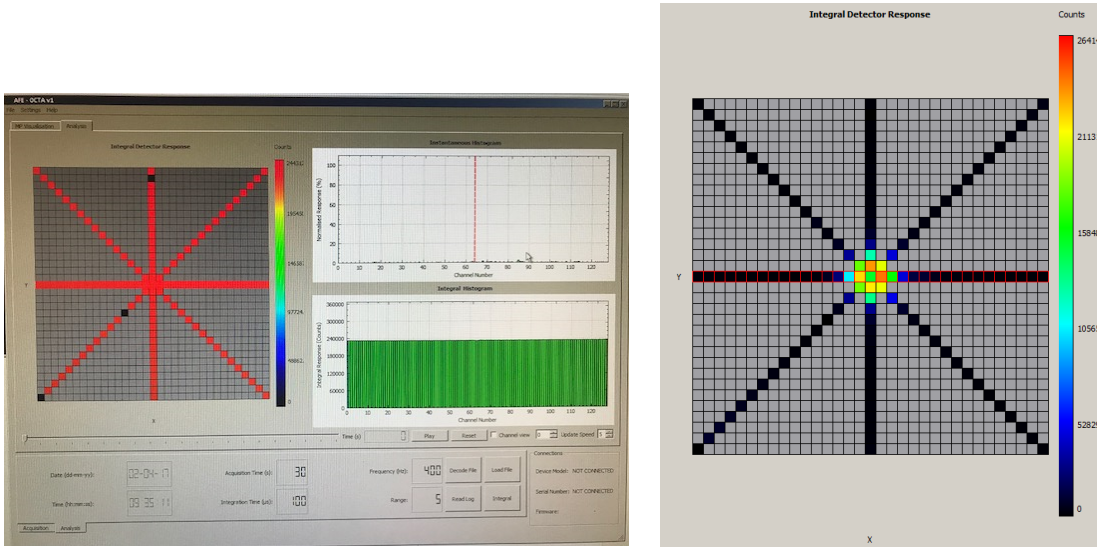

(a) (b)

Figure 3.8: A screen shot of Magic Suite software for OCTA, (a) equalisation measurement (20 x 20 cm^2 flat field), (b) small field measurements.

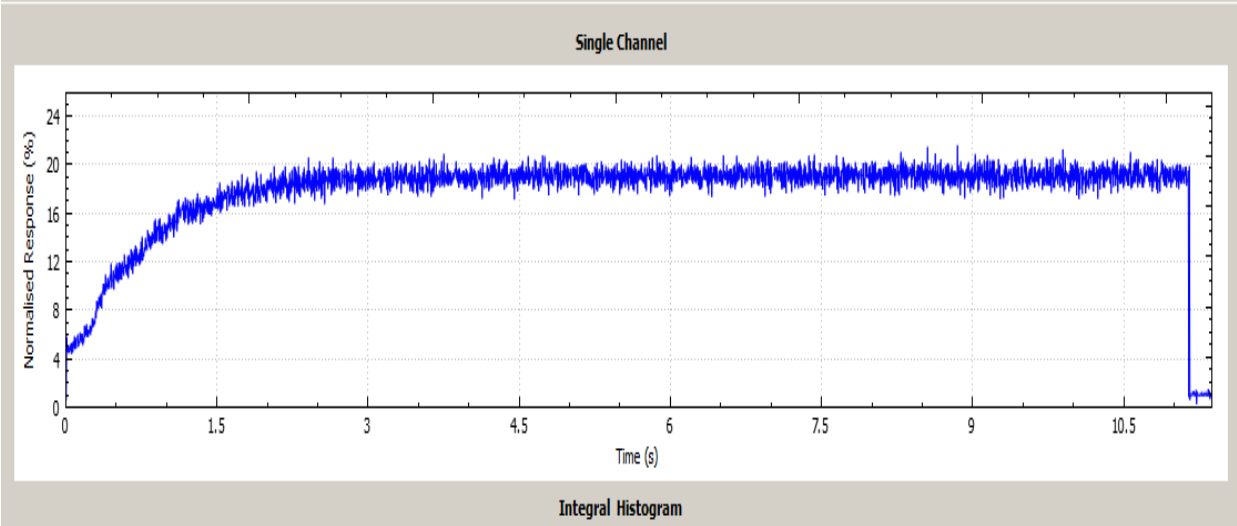

Figure 3.9: An overview of the single channel response per time.

3.4 Detectors mapping

The 512 channel detectors, DUO and OCTA, have different pixel positions on the detector as their PCB wiring is optimised in order to reduce the long distance between the pixel and its readout electronics, which results in complicated correspondence (routing) between the pixels and the readout channel numbers. Hence, to find the corresponding readout channel number for each pixel is required. The routing for DUO and OCTA detectors was created to correlate all pixels with AFE readout channels. To check this correlation, a focused laser beam and an optic system were used. A green laser was collimated by using lens and mirrors to get a spot beam that was large enough to stimulate around a few pixels of the detector. By using a 2D stepper motor table, which can move in steps smaller than the pitch size between the pixels, the laser spots have been moved between neighbouring pixels and the corresponding channel detected in the Romulus software and visualized in 2D view (figure 3.10). Each detector has its own routing of correspondence of readout channels to pixels.

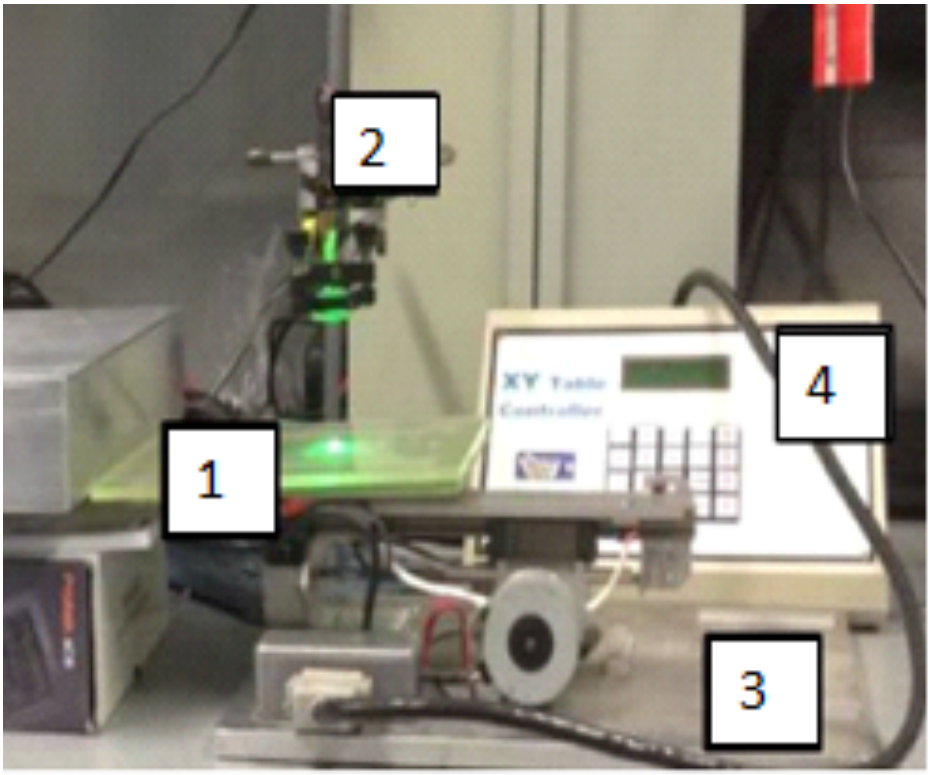

Figure 3.10: Experimental setup to verify the mapping of DUO detector, (1) DUO detector, (2) laser system, (3) sliding table, (4) controller for the sliding table.

3.5 Rotatable cylindrical phantom

A rotatable cylindrical phantom has been designed and manufactured by CMRP at UOW, in order to allow the detector to rotate in an angular range of $\pm 180^0$ $\pm 0.25^0$ with movement controlled automatically or manually. The phantom is made of PMMA (density 1.17 g/cm^3) in cylindrical shape of 30 cm diameter and 40 cm length, with rectangular cavity of 20.5 x 17.5 x 5.1 cm^3 at the centre to insert the detector array. The weight of the phantom is 35 kg. DUO was sandwiched between two 2.5 cm thick PMMA slabs, and placed on the centre of the phantom.

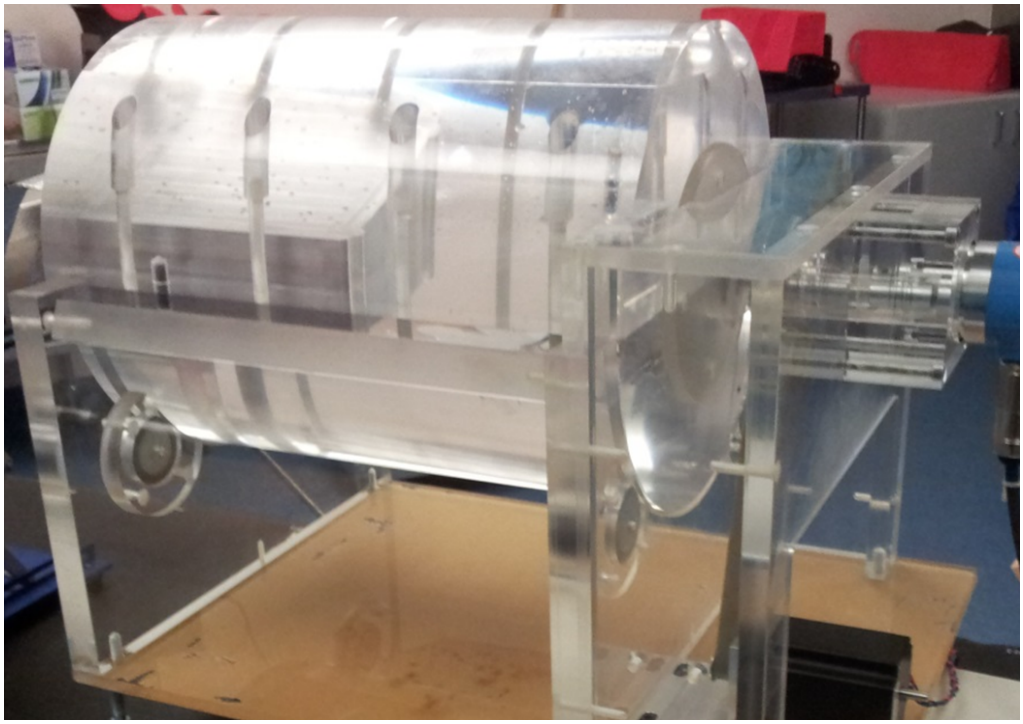

Figure 3.11: The rotatable cylindrical phantom.

3.6 Inclinometer

Attached to the LINAC head, the inclinometer allows reading of the gantry angle by using the software interface. It is a 12-bit digital gyroscope ADIS16209 by ANALOG DEVICES (Norwood, MA, USA). It works in single axis operation $\pm 180^0$ and double axis operation $\pm 90^0$, with measurement step of 0.043^0. The inclinometer is about 9.2 x 9.2 x 3.9 mm^3 and it can work at the temperature range between -40 and 125 ^0C.

3.7 Conclusion

This chapter provided a description of the different experimental instrumentations used to complete this work. Two monolithic silicon detector arrays, DUO and OCTA, their data acquisition system and rotatable cylindrical phantom were described. DUO has two orthogonal arrays each having 253 diodes with 0.2 mm pitch size, while OCTA has two orthogonal and two diagonal arrays with each having 128 diodes. The pitch size in the

orthogonal arrays is 0.3 mm and in the diagonal arrays is 0.43 mm. The data acquisition system used for both detectors is the same and it is based on AFE0064. The DAQ is connected to FPGA in one side and to the detector on the other side. There are two interfaces software used in this work, Romulus and AFE magic suite; both are designed by CMRP. The characterisation of these detectors to be used for small field dosimetry, especially SRS/SRT dosimetry, is presented in the following chapters.

CHAPTER 4: Optimizing the 2D monolithic silicon detector array (DUO) for OF measurements

4.1 Introduction

The increased use of stereotactic radiotherapy, involving field sizes smaller than the ones described in the current dosimetry protocols, led to the implementation of small field dosimetry formalism. Hence, IAEA and AAPM groups jointly proposed the use of correction factors $K_{Q_{clin},Q_{msr}}^{f_{clin},f_{msr}}$ for small field dosimetry to extend the recommendations given in conventional CoP for clinical reference dosimetry based on absorbed dose to water (Alfonso, Andreo et al. 2008). These correction factors must be calculated for a combination of detectors, beam energies and field sizes and they are sensitive to the detector position and angles for the LINAC model. These are difficult to use. Hence, a much more preferable option is to design a detector without correction factors necessary for small field dosimetry. Some researchers have focused their studies on how to design detectors suitable for small field dosimetry with a minimum of correction required. Scott, Kumar et al. (2012), (Benmakhlouf and Andreo 2017) have studied the effect of density and atomic composition of different detectors in small radiation fields by calculating the density correction factors by using Monte Carlo. They have found that the density effect is depending not only on the mass density, but also on both the electron density and on the square of I-value of the medium, and hence on the stopping power rations. The differences in the detector response in small field dosimetry are related to the incomplete interpretation of the physics gathering in the interaction processes that happen. They showed that the ideal detector has to have small active

volume and water-like density. (Charles, Crowe et al. 2013, Charles, Cranmer-Sargison et al. 2014, Charles, Cranmer-Sargison et al. 2014) and (Underwood, Winter et al. 2013, Underwood, Winter et al. 2013, Underwood, Thompson et al. 2015) had showed how different detectors can be modified by using the principle of mass density composition. Air gaps are known to cause dose reduction downstream in megavoltage dosimetry, which then re-builds the electronic equilibrium. Therefore, those researchers used air gaps to compensate the over response of detectors in small field dosimetry, especially in the output measurements and beam profiles. The thickness of the air gap depends on the type and design of the detector. Hence, the aim of this chapter is to study the effect of the introduction of an air gap upstream of the monolithic silicon detector array DUO. Different sizes of air gaps have been used to measure the output factors and beam profile parameters (FWHM and (20-80) % penumbra width). These results were then compared with suitable detectors, radiochromic^{TM} EBT3 films and MO*Skin*, in order to select the optimum air gap thickness above DUO to compensate for the over-response of the silicon array. As such, no correction factors will be required in performing small field dosimetry.

4.2 Materials and Methodology

DUO detectors (as prescribed at 3.2.1) have been used with electronic and Romulus software interface (section 3.3.2.1). Different PMMA cover phantoms have been used (designed at the UOW), with built-in air gap sizes of 0.5, 1.0, 1.5 and 2.0 mm. The DUO requires a minimum air gap of 0.5 mm above the silicon surface to avoid physical damage to the bonding wires, which are necessary to connect the detector pads to the flexible carrier. This air gap is produced by the plastic cover, which is protecting

detector. Also, this cover produce lateral air gaps about 2 mm surrounding DUO from each side. This plastic cover is a part of the phantom and shown in Fig. 4.1.

Figure 4.1: PMMA phantom to cover DUO detector with a built-in air gap

4.2.1 The effect of air gap on output factors measurements.

Measurements of output factors were done for square field sizes ranging from 0.5 x 0.5 cm^2 to 30 x 30 cm^2, defined by the jaws only. The measurements were performed using a 6 MV photon beam from Varian 2100EX LINAC at ICCC (Wollongong, NSW). The output factors were measured at source to surface distance (SSD) of 90 cm and 10 cm depth. The LINAC was set to deliver 100 MU at dose rate of 600 MU/min. To ensure the correct positioning of the detector, the central pixel of the DUO detector with size 0.18 x 0.18 mm^2 was aligned to the centre of the field and that was checked by irradiating DUO three times with 100 MU for 0.5 x 0.5 cm^2 field size to ensure that the response of the central pixels exhibited the maximum response. The measurements were repeated with different air gap sizes above the detector of 0.5, 1.0, 1.5 and 2.0 mm. The

OF was calculated as the ratio of the average response of the central pixels (five central pixels) at a specific field size to the same central pixels of the reference field size (10 x 10 cm^2) at the same depth. Then, the output factor for each field size was an average of three repeated measurements. The errors of the measurements were calculated as two standard deviations of the three measurements. The measurements of output factors were repeated by using radiochromic^{TM} EBT3 films and MO*Skin* in the exact same setup conditions.

4.2.2 The effect of air gap size on beam profiles.

To measure the effect of air gap thickness on beam profiles parameters, DUO was irradiated with 6 MV beam at 90 cm SSD and 10 cm depth for three air gap thicknesses (0.5, 1 and 2 mm). The multi-leaf collimator was completely retracted and the square field sizes, as defined by the jaws, were 0.5, 1, 2, 3, 4 and 5 cm. Responses of all pixels for each field size were normalized to the central pixel response. Each beam profile is an average of three repeated measurements. The dose reductions as a function of air gap thicknesses were calculated. The beam profile parameters (FWHM and (20-80) % penumbra) were calculated by using MATLAB software, to check the effect of the air gap with different thicknesses on small beam profiles.

4.3 Results

4.3.1 The effect of air gap on output factors measurements.

The output factors have been measured for different air gaps upstream the active volume of the DUO detector in order to compensate for the overestimation of the dose measured by a silicon detector. Figure 4.2 shows the measurements of the output factor measured at depth 10 cm in a 6 MV photon field, and SSD 90 cm with different air gaps from 0.5 to 2 mm size. The output factor was calculated as the response of the central

diodes of the DUO detector for each field size normalized to a 10 x 10 cm^2 field size and a particular air gap size. The results show that there is negligible change in the OF as a function of air gap for the normal field sizes (> 3 x 3 cm^2) and there is a higher effect at the smallest field size (0.5 x 0.5 cm^2). It is clearly seen from the figure that as the air gap decreases, the OF measured increases for small field sizes (< 3 x 3 cm^2). For square field of 0.5, 1 and 2 cm edges, the output factors increased by 8%, 5% and 1%, respectively when the air gap thickness decreased from 2 mm to 0.5 mm. For square field edges from 3 cm and above, the increase in the output factors were less than 0.5%.

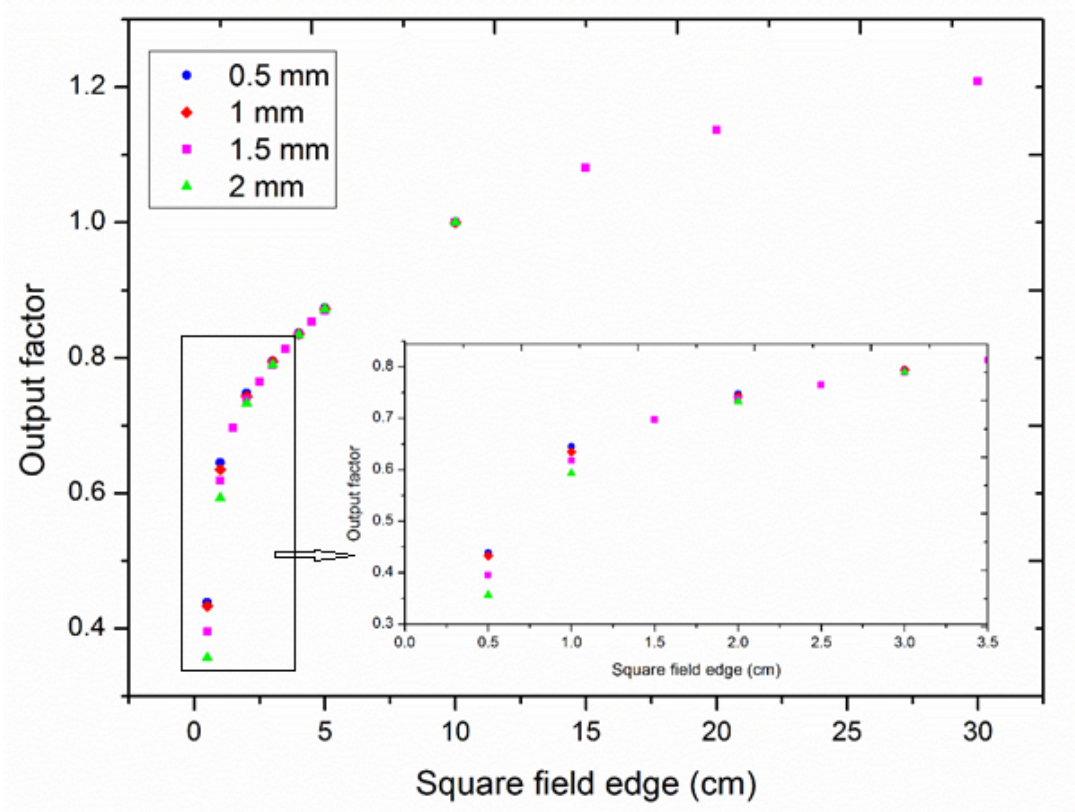

Figure 4.2: Output Factors for 6 MV photon fields of different sizes measured by DUO detector with different air gap sizes (0.5, 1, 1.5, 2 mm) and normalized to 10 x 10 cm^2 field.

DUO with an air gap of 0.5 mm shows the best agreement in the comparison of the

output factors as a function of field with EBT3 and MO*Skin* as shown in figure 4.3. The maximum percentage difference between them is for the small field sizes (0.5 and 1.0 cm field edge) and all data is within ±1.8%. The error bars calculated from DUO measurements represent two standard deviations and they are smaller than 0.04%.

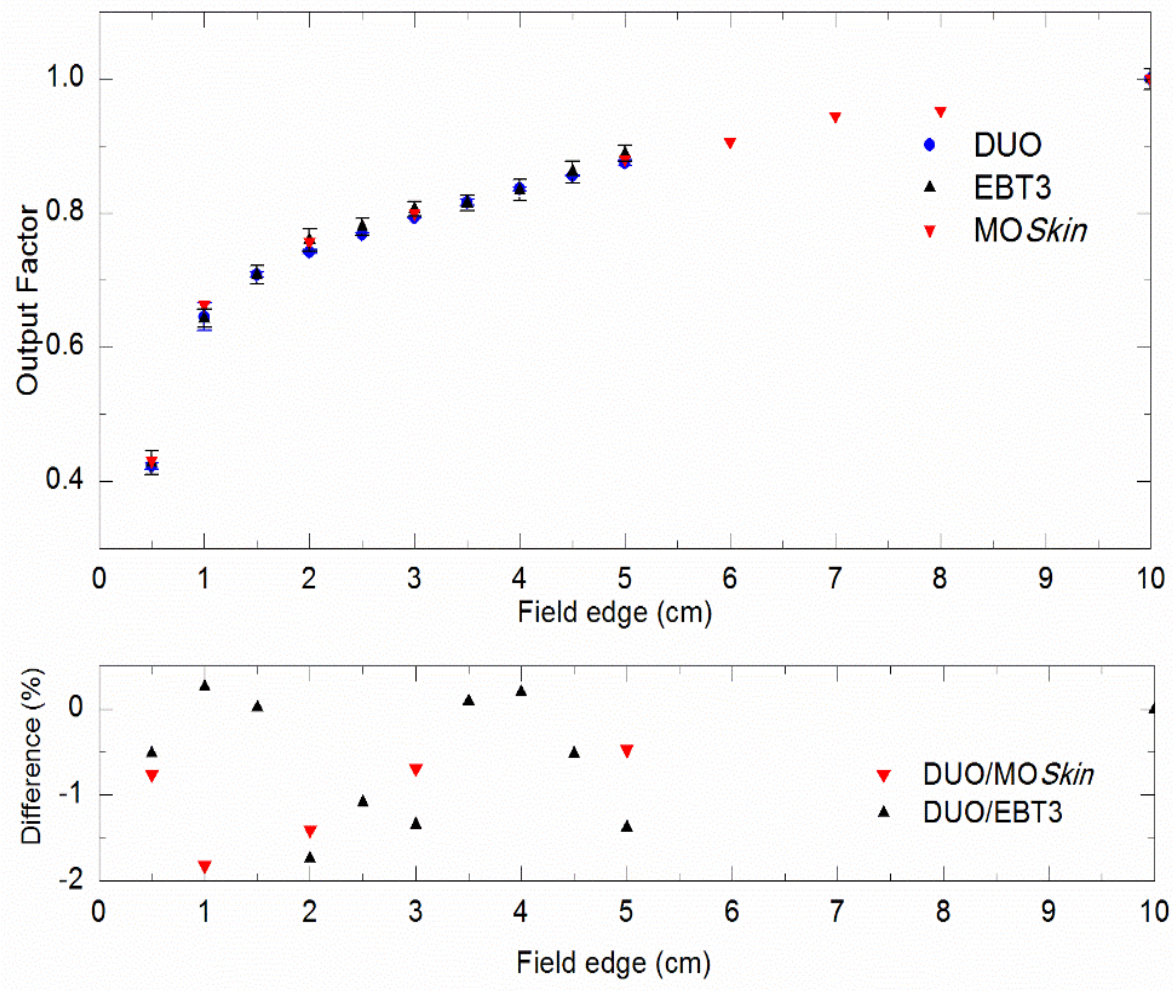

Figure 4.3: A comparison of OF at 6 MV photon beam measured by DUO with 0.5 mm air gap upstream with EBT3 films and MO*Skin* detector. Lower panel: the difference in percentage between DUO/EBT3 and DUO/MO*Skin*.

4.3.2 The beam profiles parameters as a function of different air gap thickness

The beam profiles for square field edges (0.5, 1, 2, 3, 4 and 5 cm) were measured by using different air gap thicknesses above the DUO detector (0.5, 1, 2 mm) at 90 SSD and 10 cm depth. The beam profiles of field edges 0.5 and 1 cm are shown in figure 4.4. From these figures, there is clearly response reduction as the function of air gap, so by increasing the air gap the response is reduced at the central pixels. The relative percentages in the response reduction measured by the central pixel were calculated relative (for the air gap thicknesses 1 and 2 mm) to the response of the same pixel with a 0.5 mm air gap are presented in figure 4.5. The results show that there is no measureable response reduction effect for both air gap sizes of 1 and 2 mm for the field sizes from 3 x 3 cm^2 and above. There were response reductions of 18%, 8%, 2% and 0.5% at 2 mm air gap normalised at 0.5 mm and air gap thickness for square field edges of 0.5, 1, 2 and 3 cm, respectively. The percentage of response reduction becomes less at the air gap size of 1 mm and was around 1.5%, 1% and 0.5% at square field edges of 0.5, 1 and 2 cm, respectively. The loss in electronic equilibrium that caused this dose reduction also caused a broadening of the beam profiles immediately beyond the air gap, as shown in figure 4.4 for square field edges of 0.5 and 1.0 cm at air gaps of 0.5, 1 and 2 mm. The FWHM and penumbra width (average of both ascending and descending penumbra) for each field size were calculated by using MATLAB software as a function of air gap thickness. The results showed by increasing the air gap thickness, the FWHM and penumbra widths increased. The effect of the 2mm air gap thickness is very high in comparison to 0.5 mm and 1 mm in the penumbra width. For a 5mm square field edge, the penumbra increased by 0.26 mm and the FWHM increased by 0.22 mm for an air gap increase from 0.5 to 2 mm.

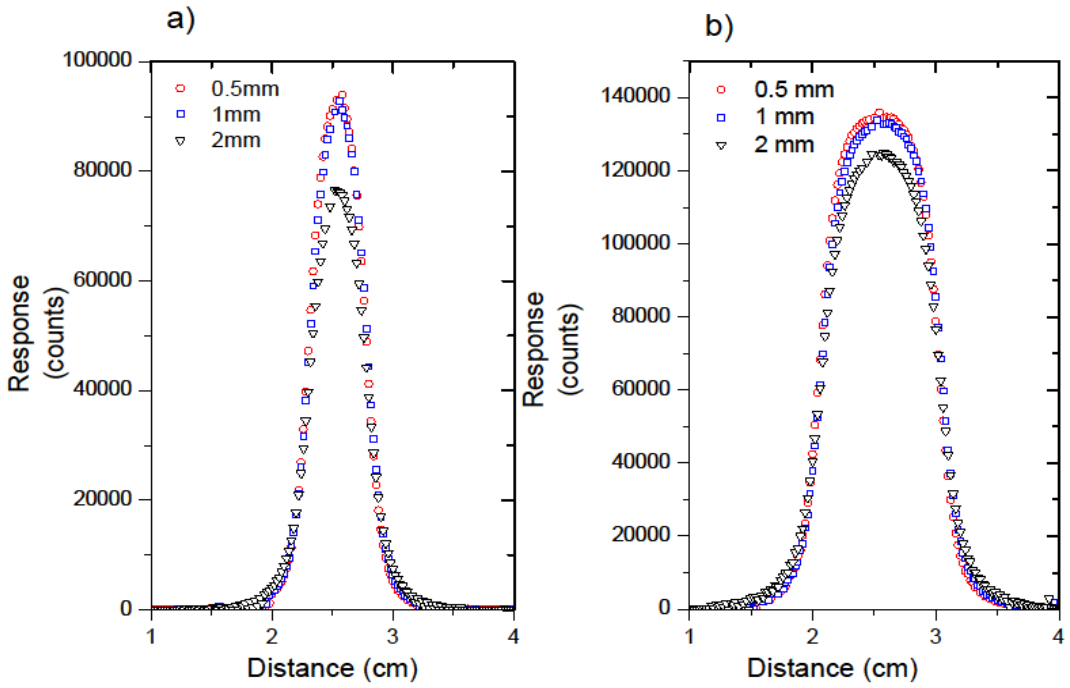

Figure 4.4: cross beam profiles measured by DUO detector as a function of air gap thickness a) for a 0.5 x 0.5 cm^2 field size and b) for a 1.0 x 1.0 cm^2 field size.

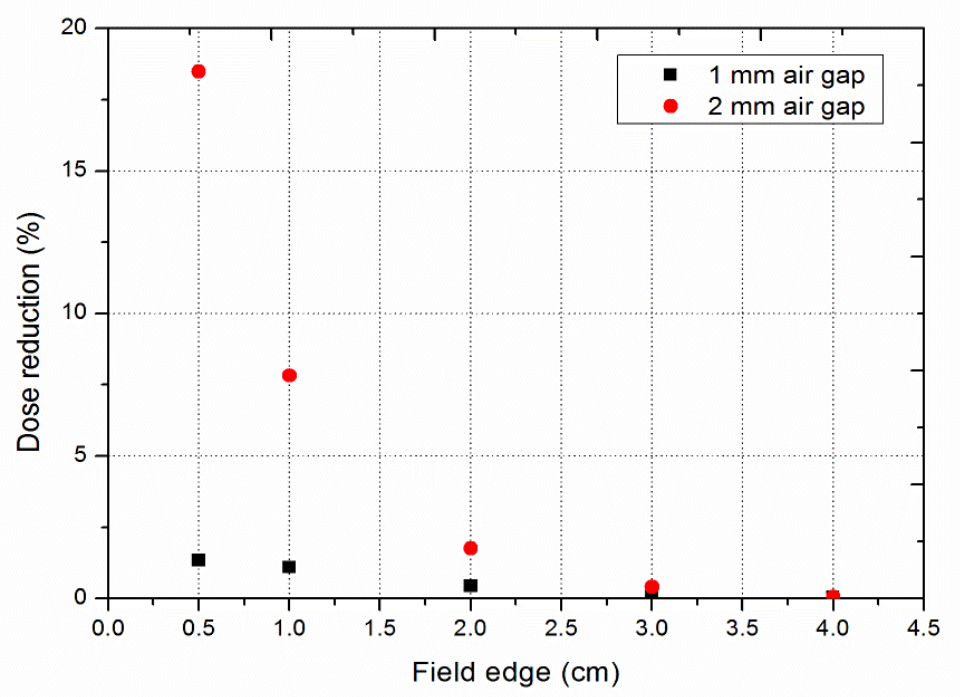

Figure 4.5: Dose reduction as a function of air gap thickness normalized to air gap thickness of 0.5 mm for different field sizes.

Table (4.1): (a) FWHM and (b) penumbra width: for square field sizes as a function of air gap thickness

Field edge	Air gap Thickness (mm)		
	0.5	1	2
5	4.86	4.9	5.08
1	9.65	9.68	9.7
2	19.37	19.52	19.55
3	29.59	29.62	29.67
4	39.54	40	40.03

(a) FWHM (mm)

Field edge	Air gap Thickness (mm)		
	0.5	1	2
5	1.76	1.85	2.03
10	2.27	2.31	2.68
20	2.56	2.76	3.33
30	2.61	2.93	3.58
40	2.97	3	3.69

(b) Penumbra width (mm)

4.4 Discussion

DUO detector response as most silicon diodes should be corrected for small field dosimetry by using air gap above detector. Different air gaps from 0.5 mm to 2.0 mm have been used to measure the output factors for square radiation fields. The results show that there isn't effect of air gap in the OF measurements for square fields larger than (30 x 30 mm^2). However, there is a very large effect for smaller field sizes. The OF increases with decreasing the air gap thickness at these field sizes. These reached up to 8% for 5 x 5 mm^2 when the air gap decreased from 2 mm to 0.5 mm. These results are in agreement with Charles (2014), as he found there is an increase in the output factors for 6 mm square field edge about (7.8%) by using 0.5 mm surrounding air gap on Landauer nanoDot OSLDs. The 0.5 mm air gap upstream DUO shows the best agreement with EBT3 and MO*Skin* measurements, where the percentage deviation is within ±1.8%.

DUO with different air gap thicknesses have been used to measure the beam profiles for square field edges (0.5, 1, 2, 3, 4 and 5 cm). There is negligible dose reduction at the central pixel for square field sizes from 3 x 3 cm^2 and above as a function of different air gap thickness, which is also seen by Charles (2014) for a single diode. While there is a dose reduction up to 18% for 5 x 5 mm^2 when an air gap of 0.5 mm increased to 2.0 mm. The percentage of reduction reduced to 1.5% when the 1.0 mm air gap was used. These findings are similar to other researcher's results (Solberg, Holly et al. 1995, Rustgi, Samuels et al. 1997, Charles, Crowe et al. 2013). Also, FWHM and penumbra widths are increasing by increasing the air gap thickness, especially for smaller field sizes. Similar results were demonstrated by others (Solberg, Holly et al. 1995, Charles, Crowe et al. 2013). For a 10 mm square field edge, the penumbra increased by 0.41 mm and the FWHM increased by 0.05 mm for an air gap increase from 0.5 to 2 mm. These results agree with those of Rustgi, Samuels et al. (1997) who found that the FWHM increased by 0.4 mm and the penumbra width increased by 2.1 mm for 12.5 mm circular collimator when the air gap increased from 0 mm to 3 mm.

4.5 Conclusion

Many researchers have used the approach of "mass density compensation" to modify the detector response in small field geometries by using appropriate materials to match the response of the detector to nearby water equivalent materials (Bouchard, Kamio et al. 2015, Bouchard, Seuntjens et al. 2015). They have studied the effect of using small air gaps on small field dosimetry, which causes an over-response in the output factors and a dose reduction immediately downstream and re-establishes the electronic equilibrium. The loss in electronic equilibrium that caused dose reduction also caused a widening of the beam profiles immediately beyond the air gap.

In this study, an air gap has been introduced immediately above the monolithic silicon array, DUO. The air gap thickness was varied in order to quantify the effect of different air gap thicknesses on the OF and beam profiles. It was confirmed that the introduction of an air gap upstream of DUO has a significant effect on small field dosimetry. The optimum air gap of 0.5 mm for the best agreement with EBT3 for smallest field size 0.5 cm was evaluated. The effect of air gap for central pixel in DUO is similar to a single diode that is explained by stronger lateral disequilibrium for small fields. The next step is to study the possibility of charge sharing effect on DUO monolithic silicon detector array.

CHAPTER 5: Charge sharing effect on the monolithic high spatial resolution silicon detector array (DUO)

5.1 Introduction

The new advances in the silicon technology enable the design and fabrication of pixelated monolithic detectors. The introduction of these types of detectors in radiation therapy provides unique opportunities for high spatial resolution dosimetry of small radiation fields. The advantages of the outstanding spatial resolution of the DUO detector has been demonstrated for small square field dosimetry on a LINAC and can be used for SRS/SRT dosimetry (Shukaili, Petasecca et al. 2017).

However, they can be affected by charge the sharing effect due to the charge generated between pixels as a result of the small pitch size (Zheng, Cheng et al. 2016). In order to provide more accurate dosimetry in steep dose gradient fields and utilize all of the advantages of pixelated silicon detectors, corrections associated with this charge sharing effect should be considered if needed.

Charge sharing effect is well studied in silicon strip and pixelated detectors and well considered in the case of energy deposited by particles incident between diodes (strips) (Atkinson, Ahlbin et al. 2011, Livingstone, Prokopovich et al. 2012). They can be used for the accurate determination of the coordinates of incident particles with micron spatial resolution and its deposited energy simultaneously as was demonstrated in the case of alpha particles incident on silicon strip detector (Rosenfeld, Pugatch et al. 1993) and coordinate of minimum ionizing particle (m.i.p) in high energy physics vertex detectors for each single event (Livingstone, Prokopovich et al. 2013).

In case of application of pixelated monolithic silicon detectors for dosimetry of continuous radiation field between pixels, the effect of charge sharing on measured steep dose gradient should be considered and if necessary to be corrected. Therefore, the aim of this chapter is to study the possible effect of charge sharing in pixelated monolithic detectors (Bulk DUO and Epitaxial OCTA) on measured steep dose gradient typical for penumbral small radiation field in MV X-ray therapy.

5.2 Methodology

5.2.1 The physics of charge sharing effect

When a silicon pixel detector is irradiated by an x-ray photon, it will cause the production of numbers of electron-hole pairs that depend on the energy of the irradiated photon. Then the electrons and holes will flow to the anode and cathode of the detector due to the electric field. If the x-ray photon irradiated the centre of the pixel in the detector, the corresponding electrode will collect the generated charge. In this case the readout signal of each channel is proportional to the corresponding irradiated pixel (Knoll 2010). But if the irradiated photon hits the neighbouring area of the pixel's edge, the resulting charges may be collected by two or more neighbouring pixels. This is called the charge-sharing phenomenon as shown in figure 5.1 (Maj, Baumbaugh et al. 2012, Maj, Grybos et al. 2013, Maj, Szczygieł et al. 2015).

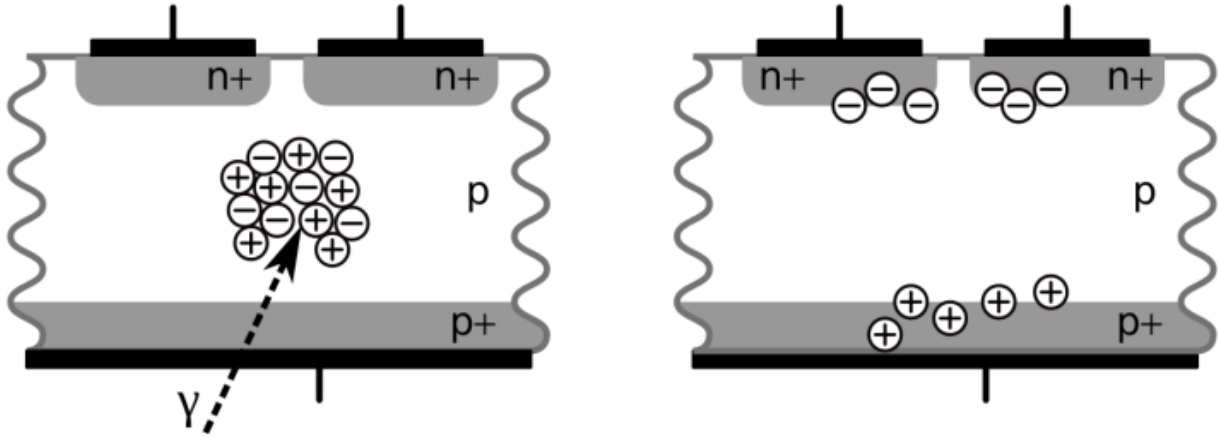

Figure 5.1: charge sharing effect in pixelated detectors (Maj, Szczygieł et al. 2015).

This phenomenon depends on the geometry of the pixels, so as the distance between the pixels (pitch) and/or the pixel size become smaller, the charge sharing effects increases significantly (Veale, Bell et al. 2011, Zheng, Cheng et al. 2016).

Therefore, both Bulk DUO and Epitaxial OCTA have a small pitch size of 200 and 300 μm respectively, part of the charge produced between two neighbouring pixels may drift to the neighbouring pixel. This sharing of charge may potentially affect accuracy of the penumbra shape measurement that may affect the FWHM of the measured beam profile.

5.2.2 Theoretical model of charge sharing effects on DUO detector

We consider the X-ray radiation field with dose gradient "m" incident on the linear array of the DUO detector. Figure 5.2 shows fragments of DUO linear array of pixels with 4 neighbour strips. It is assumed that the charge created in a region between strips with thickness dx between two (left and right) strips where sharing between them is in the ratio $Q_R/ Q_L= x / L-x$ as demonstrated in (Rosenfeld, Pugatch et al. 1993). A mathematical consideration is done as described in Appendix A to investigate if charge sharing exists at the penumbra region.

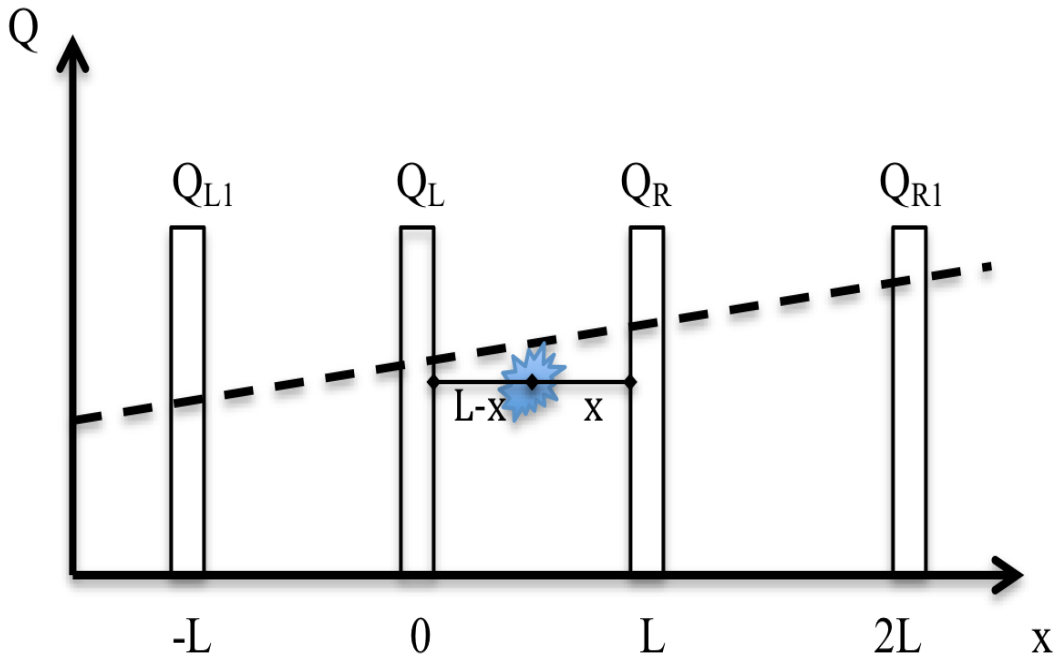

Figure 5.2: A diagram of charge sharing events in pixelated detector by linear gradient.

From this consideration, it is clear that charge sharing in case of the constant dose gradient "m" does not change the gradient and signal measured from pixels that represent correct dose distribution along the linear pixel array. It is important to mention that consideration was done under assumption of point pixels and constant dose gradient. The pixel width and length should be considered in relation to pitch and can affect accurate measurement in very steep and very slow dose gradient as happened in different part of penumbra.

5.2.3 Verification of approach

- **Experimental setup**

The charge sharing effect on Bulk DUO and Epitaxial OCTA detectors were examined experimentally by irradiating it with 6 MV photon beam and using a physical wedge of 60^0 to provide high dose gradients in a phantom. The detector was irradiated with wedge field at d_{max} with field size of 10 x 10 cm^2 and SSD 100 cm. The detector was irradiated

by 100 MU and dose rate of 600 MU/min. The same setup was used for Markus ion chamber (PTW) to compare the dose profiles obtained by DUO and the ionization chamber at the same depth.

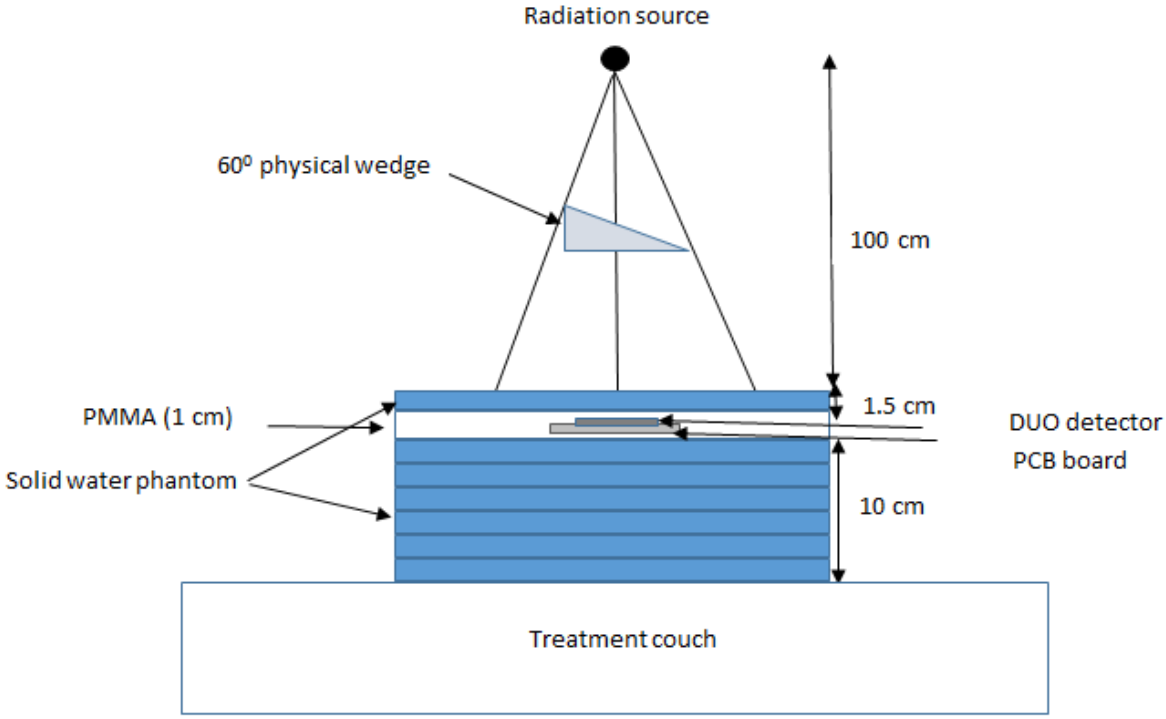

Figure 5.3: The experimental setup.

5.3 Results

6.3.1 Experimental results

The dose profiles were measured by Bulk DUO and Epitaxial OCTA detectors compared with the dose profiles measured by IC. Then the profiles were linearly fitted as shown in figure 5.5. Bulk DUO shows slightly higher slope of the dose profile than measured with ionization chamber suggesting effect of charge sharing between the neighbouring pixels. The effect of charge sharing on Bulk DUO was calculated as a ratio of slopes measured with Bulk DUO and IC, resulting in correction factors (CF)= 0.077/0.067 =1.15; while Epitaxial to IC slope ration is about 1.03. This means that the

charge sharing effect is not changing the dose gradient measured by the Epitaxial OCTA. The profile measured by Bulk DUO was then corrected by increasing the distance between the pixels by a factor of 15%, while the response of each pixel remains as measured t. The corrected Bulk DUO profile was compared to the IC profile as shown in figure 5.5. The resulted slope of Bulk DUO profile after applying the correction factor was the same as the Markus ion chamber.

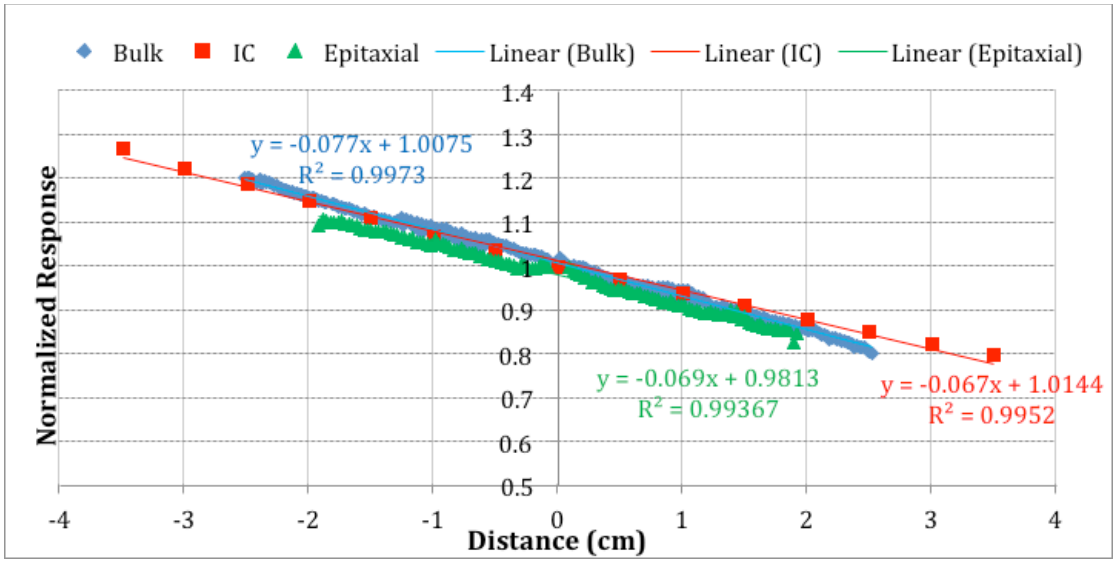

Figure 5.4: The response of Bulk and Epitaxial DUO detector compared with ion chamber (IC) for 10 x10 cm^2 field by using 60^0 physical wedge and 6 MV at 100 SSD and 1.5 cm depth (normalized to the centre).

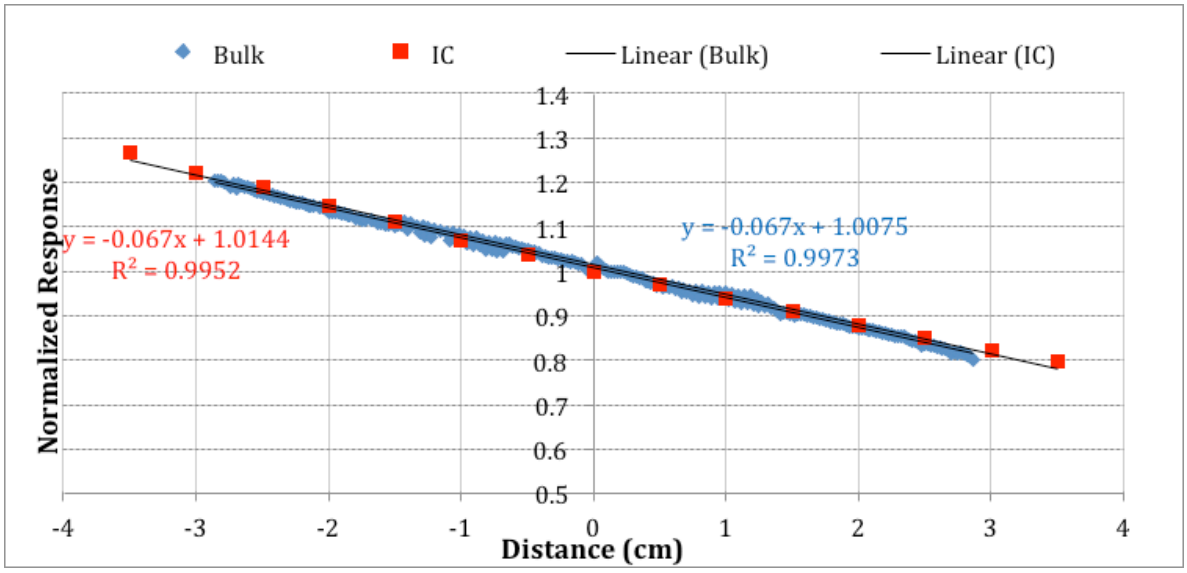

Figure 5.5: The response of Bulk DUO detector after applying the charge sharing correction factor (15%) to the pitch size, compared to ion chamber.

6.3.2 The generic method of charge sharing on DUO profiles (MATLAB software)

To check the effect of charge sharing on beam profiles, several square radiation field beam profiles were measured on Varian LINAC and ELEKTA SRS cone by using Bulk DUO and compared with EBT3. To apply the correction factors associated with charge sharing effects to the beam profiles measured on ELEKTA LINAC was equipped with a circular cone collimator. Firstly the first derivative of the Bulk DUO response for each cone size was calculated by using MATLAB^{TM} software in order to determine the gradient area. Then, from the first derivative of the response, the channels that have to be corrected for the charge sharing effects (penumbra region) were determined. The penumbra profiles were corrected by changing the pitch size for 230 µm instead of 200 µm without changing the pixel response values.

6.3.3 The effect of applying charge sharing corrections on beam profiles (FWHM & penumbra)

The beam profiles for several square radiation fields and SRS cone collimators for sizes from 5 to 50 mm that were measured with DUO, were compared with EBT3 films profiles with and without the charge sharing corrections. The profiles were normalised at 50%, to see clearly the behaviour at the penumbra region. The distance to agreement (DTA) has been calculated as the difference in the normalised response at the same distance from the centre between the two profiles as shown in figures 5.6 and 5.7, for square radiation fields and SRS cone collimators respectively. The DTA becomes smaller after applying the corrections for all small SRS cone collimator data, especially for small cone sizes. On the other hand, charge sharing corrections work inversely for square field edges, as the corrections makes the fields wider in comparison to EBT3 profiles.

The SRS cone beam profile parameters (FWHM and (20-80) % penumbra) were analysed by using MATLAB for Bulk DUO with and without the correction as shown in figure 5.10 for average penumbra. Then these were compared with the EBT3 measurements, where the differences were calculated as shown in tables 5.1 for the SRS cone collimator.

There was a significant effect on the SRS cone data, where the difference in the FWHM between DUO and EBT3 was high up to -13% and -6% before applying the charge sharing CF for cones 5 and 7.5 mm, respectively. After correction, the differences were reduced within 1% for all cone sizes. The difference in the both penumbra widths (20-80) % before applying the corrections was more than 1 mm; which was reduced after applying the correction to be within 0.6 mm.

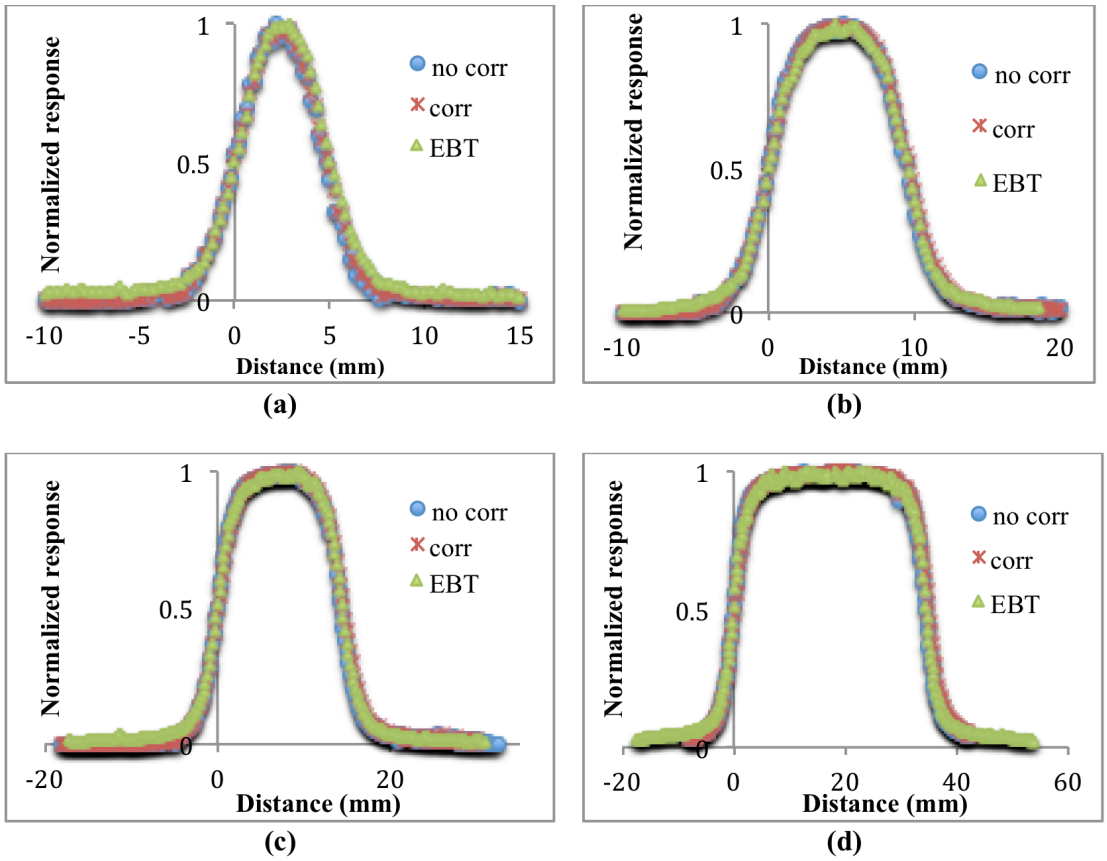

Figure 5.6: Beam profiles for square radiation fields of edges 5, 10, 15 and 35 mm comparison between Bulk DUO with no corrections, Bulk DUO with charge sharing corrections applied and EBT3.

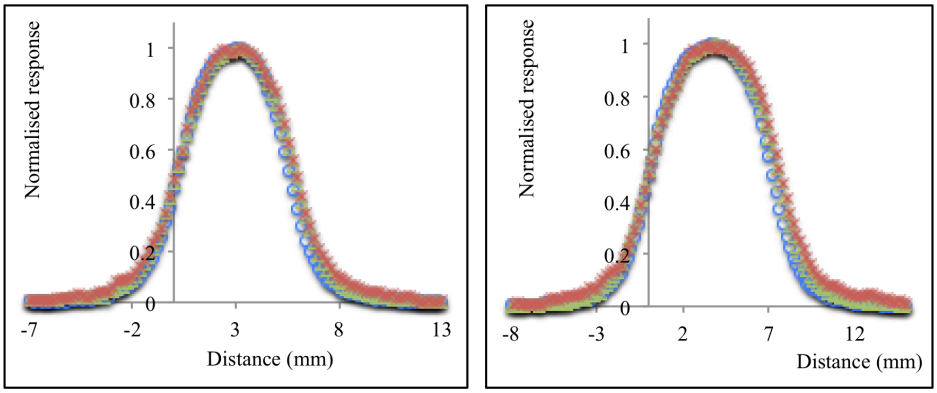

(a) (b)

(c) (d)

Figure 5.7: Beam profiles of cone diameters 5, 7.5, 10 and 30 mm comparison between Bulk DUO with no corrections (circle), Bulk DUO with charge sharing corrections applied (cross) and EBT3 (triangle).

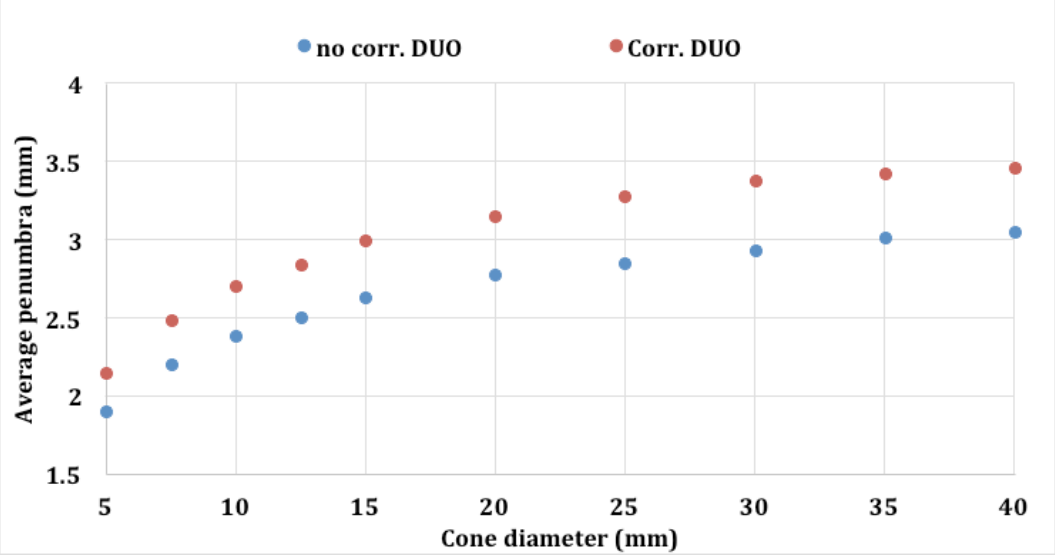

Figure 5.8: The average penumbra of cross-line SRS cone beam profiles measured by Bulk DUO with and without charge sharing correction compared to EBT3.

Table 5.1: The difference in the FWHM and penumbra width for radiation fields produced by the SRS cones and measured with Bulk DUO and EBT3.

	FWHM		Average penumbra	
Cone Size	no corr.	corr.	no corr.	corr.
mm	%		mm	
5	-13.01	0.64	-0.21	0.04
7.5	-6.04	-0.96	-0.40	-0.10
10	-2.89	0.89	-0.46	-0.14
12.5	-2.42	0.85	-0.62	-0.29
15	-2.70	-0.70	-0.66	-0.30
20	-2.10	0.29	-0.58	-0.21
25	-0.58	0.91	-0.68	-0.25
30	-1.83	0.50	-1.02	-0.56
35	-1.05	0.35	-0.81	-0.40
40	-1.19	0.05	-0.95	-0.54

5.4 Discussion

The size of the sensitive volume (SV) of the detector plays an important role in small field dosimetry. A detector with small pitch size and small SV is required for small field dosimetry in order to detect the penumbra width accurately with high spatial resolution. However, some other effects can affect the measured profiling such as volume averaging and charge sharing effects.

The charge sharing effect is dependent on the pitch size and charge collection efficiency between pixels. The chance of charge sharing to happen is increased by reducing the

pitch size. Hence, it is important to test Bulk DUO (where the pitch size is 0.2 mm) and Epitaxial OCTA (where the pitch size is 0.3 mm) for charge sharing effect. The analytical consideration of charge sharing between two neighbour pixels in assumption of point pixels, constant dose gradient and absence of charge carriers recombination shows that charge sharing between pixels do not affect the measured dose gradient (see Appendix A). On the other hand, for very small field size (e.g. 5-10 mm cones) the penumbral region is small (about 2 mm) and approximation of constant gradient within several pixels placed in (20-80) % is not always correct. This means the dose gradient can't be considered as constant over all the penumbra width. The experimental measurements done by using both Bulk DUO and Epitaxial OCTA detectors demonstrate that there is steeper dose gradient for profiles measured by Bulk DUO in comparison with the ionization chamber, while Epitaxial OCTA is in agreement with IC within measurements error. Therefore, charge sharing is affected by the type of Si substrate. Bulk DUO detector has been fabricated on low resistivity silicon which is about 10 Ω cm and N_A about 1.358 x 10^{15} cm^{-3} that is leading to lower diffusion length in comparison to Epitaxial substrate in addition to the larger thickness of the detector (about 470 μm) that provides larger sensitive volume associated with each pixel from which charge is collecting and more charge recombination and associated with that deterioration of measured penumbra. Epitaxial OCTA has been manufactured on p-Si 38 μm thick epitaxial layer with resistivity about 100 Ω cm (N_A is about 1.33 x 10^{14} cm^{-3}). Increased diffusion length and much smaller sensitive volume from which charge is collected in Epitaxial OCTA in comparison with Bulk DUO is leading to much less or the absence of charge collection deficit due to recombination and as result much more accurate penumbra measurements by Epitaxial OCTA. It is in agreement with theoretical consideration (Appendix A), which is not considering charge recombination.

Charge sharing effect has been analysed for Bulk DUO by profile measurements of small square radiation fields and SRS cone collimated fields. The correction factor for measured penumbra has been applied as described above. When the square radiation field was used, the charge sharing correction factors did not improve the DTA between Bulk DUO and EBT3 films, especially for large field sizes (> 10 x 10 mm^2). While in the case of circular beam profiles such as SRS cone profiles, the charge sharing correction works better and DTA becomes smaller overall the cone sizes. This could be due to both charge sharing and volume averaging effects of Bulk DUO where partial contributions of each of them is different in the case of square and cone radiation fields. Both of these effects should be taken into account for interpretation of the Bulk DUO response in small radiation fields.

Fig 5.9 and 5.10 show the isodose lines for small square and cone fields and sensitive areas of the single pixel (not to scale). It is obvious that for cone fields (Fig 5.10) the sensitive volume of the pixel is exposed to non-uniform radiation fields in the direction along the long side of the pixel (longitudinal direction) additionally to orthogonal (radial direction). This is leading to volume averaging effect in both longitudinal and radial directions, i.e. measured signal is relatively less than relative dose at this point. This effect will be more pronounced with increasing of the dose gradient when the pixel is moving to the steepest part of the penumbra. From consideration above, it is clear that while the size of the pixel in the radial direction is very small (40 μm) in comparison to longitudinal direction (800 μm) it cannot be considered as a point pixel in a very steep radial field. This effect is leading to the relative appearance of increasing of the gradient of measured penumbra in comparison with it's true value and will be more pronounced with the increasing size of the pixels in either longitudinal of radial direction but with different weighting.

In the case of the small square field (Fig 5.9) this effect is manifested by the radial size of the pixel only as the dose is not changing along the longitudinal direction within 800 μm of the pixel length. In both cases ideal correction of apparent increasing of slope of the penumbra will be impossible based on dose profile measurements with Bulk DUO in the well-known wedge field if the gradient of this field is not exactly the same as in penumbra. However, the correction developed in a wedge field will improve agreement with the EBT film that was observed in the case of the Bulk DUO.

The volumetric effect considered above would be more pronounced in Bulk DUO than in Epitaxial OCTA where the effective sensitive volume is better confined to the geometric pixel size due to the small thickness (38 μm) of Epitaxial layer. However in Bulk DUO, this effective sensitive volume associated with each pixel can be much larger due to the thickness of the Bulk DUO detector (470 μm) is 13 times larger in comparison with Epitaxial OCTA detector that provide more pronounced volumetric effect.

In case of square field is impossible to expect the same degree of agreement of corrected penumbra measured by Bulk DUO with penumbra measured by EBT3 film as for the cone field based on the correction coefficient derived in arbitrary wedge field because apparent increasing of penumbra is driven by volumetric effect in direction perpendicular to the longer side of the pixel additionally to not full charge collection especially with increasing size of the field. This is confirmed by experimental data (Fig 5.8 and Table 5.2).

In light of this consideration of the Bulk DUO response in high gradient field it became clear why Epitaxial OCTA is in good agreement with EBT3 film (Table 5.3) and with wedge field measured with IC.

It is known that the dose gradient is much steeper at the radial direction than the longitudinal direction. Therefore, the width size of the pixel in the radial axis has higher effect at the penumbra region in terms of volume averaging effect. Bulk DUO with a pixel size of 0.04 x 0.8 mm^2 would be able to predict the penumbra more accurately than detectors with a larger pixel size. However, the contribution to the pixel response is from radiation 2D field which has a different gradient in the direction of the measured profile (radial penumbra, pixel size 0.04 mm) and in orthogonal direction (longitudinal direction, pixel size 0.8mm) the radial penumbra can be detected more accurately than the longitudinal penumbra as the width at the radial direction is 0.04 mm, which means there is less volume averaging that would happen, while this could take place in the transverse direction where the length of the pixel is 0.8 mm. Figure (5.9) shows an example of the % isodose lines for square field size and one pixel of Bulk DUO detector (not in scale). The % dose line that cuts the pixel is almost the same overall the size of the pixel. Hence, the dose measured by the Bulk DUO pixel isn't affected by volume averaging effect that much. However, in the circular beam profiles, Bulk DUO's pixels could cut two or more iosdose lines as shown in the example of figure (5.10). This leads to higher volume averaging effect measured by Bulk DUO in SRS cone collimator. Therefore, the resulted penumbra would be sharper than expected.

Table 5.2: The difference in the FWHM and penumbra width for radiation fields produced by small square field and measured with Bulk DUO and EBT3.

	FWHM		Penumbra	
Field edge	No corr.	Corr.	No corr.	Corr.
mm	%		mm	
5	0.92	4.27	-0.03	0.42
10	-0.68	0.69	-0.04	0.01
15	-1.15	2.95	0.23	0.41
20	-0.91	-0.73	0.26	0.39
25	1.06	1.51	0.31	-0.51
30	-0.44	2.33	0.37	-1.08
35	0.02	1.21	0.36	1.83
40	-0.02	1.29	0.39	0.40
45	-0.05	1.51	0.44	-0.63

Table 5.3: The difference in the FWHM and penumbra width for radiation fields produced by the SRS cones and measured with Epi OCTA and EBT3.

Cone	FWHM	Penumbra
mm	%	mm
5	1.7	0.0
7.5	0.0	-0.2
10	0.0	0.0
12.5	1.6	-0.1
15	1.0	-0.5
20	1.0	-0.1
25	0.8	-0.7
30	0.0	-0.7
35	1.1	-0.7
40	0.0	-0.7

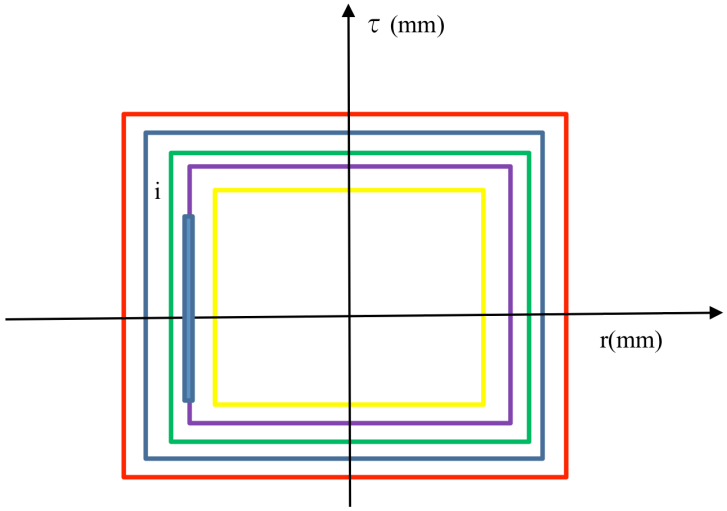

Figure 5.9: An example of the isodose lines for square radiation field, i is the DUO's pixel.

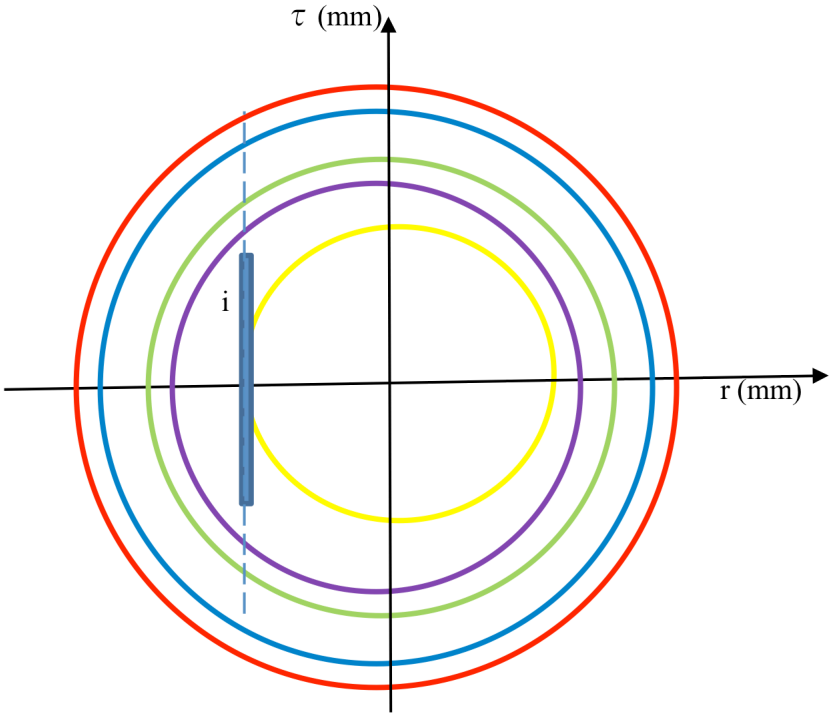

Figure 5.10: An example of the isodose lines for square radiation field, i is the DUO's pixel.

5.5 Conclusion

The effect of charge sharing and effective pixel size on measured dose profile in small photon fields with steep penumbrae with Bulk DUO and Epitaxial OCTA monolithic silicon detectors has been studied. It was demonstrated analytically that charge sharing between pixels generated by radiation field under assumption of constant gradient, point pixels and absence of recombination between pixels should not change dose gradient measured by pixelated detectors based on pixel values.

The increasing of apparent slope of the penumbra as measured by Bulk DUO is mostly the result of volumetric effect, which is composed of longitudinal and radial volumetric effects, and their partial contributions that depend on 2D dose distribution of small radiation fields. From this point of view, not corrected Bulk DUO is demonstrating

stronger disagreement in penumbra measured with EBT film (gold standard) due to its effective longitudinal and radial pixel size that is larger than geometrical 0.04 x 0.8 mm^2 size due to thick 0.47 mm silicon substrate from which charges are collected. For Epitaxial OCTA, the sensitive volume is much better confined to geometrical pixel size due to thin 0.038 mm epitaxial layer from which charge is collected. It is reflected in almost perfect agreement in wedge field gradient measured by Epitaxial OCTA and IC as well as in steep penumbrae measured with Epitaxial OCTA and EBT film.

These presented findings are only confirmation of how difficult a small field dosimetry with sub-millimetre spatial resolution using monolithic detectors with geometric spatial resolution 0.2-0.3 mm and pixel size 0.04x0.8 mm^2. It is a clear recommendation that for optimal spatial resolution in small field dosimetry, an epitaxial substrate should be used for manufacturing of the monolithic detectors like DUO and OCTA. For thinner an epitaxial substrate and less size of the pixel the penumbra and related FWHM of the small beams will be measured more accurately, which is trade off with Signal/Noise ratio.

CHAPTER 6: Evaluation of DUO silicon detector array for small square radiation field

6.1 Introduction

Small field dosimetry requires detectors like diodes that have specific features including excellent spatial resolution in order to resolve the sharp penumbra, small sensitive volume to minimize the volume averaging effects, on-line measurements to be used as pre-treatment dosimetry tool and provide 2D measurements to enhance the accuracy of measurements by using different points in the treatment fields. However, diodes need to be corrected for their perturbation, which is mainly due to the density of the detector and extra-cameral components. This study uses a 2D silicon detectors designed by CMRP at UOW. In the previous chapters, an air gap has been introduced upstream of the DUO detector, and the output factors as well as the beam profiles parameters and dose reduction have been studied as a function of different air gap thicknesses. DUO with an air gap of 0.5 mm has been selected to be the optimal air gap size, in comparison with the OF with EBT3 and MO*Skin*. Also, DUO was tested for charge sharing effect and the correction factor has been derived to correct the sharp gradient at the penumbra region. In this chapter, DUO has been fully characterised as a small field dosimetry tool by using small square fields, including:

- Uniformity
- Beam profiles
- Dose per pulse
- Percentage depth dose

6.2 Methodology

6.2.1. Uniformity

The DUO detector was irradiated with 6 MV photon beam by using a large field size, 20 x 20 cm^2 at 100 cm SSD and 10 cm depth, in Solid Water^{TM} phantom. The expected result is that not all pixels would have the same response due to the difference in the sensitivity of the pixel and its electronics' gain from each other, which is called uniformity. To calculate the correction factors, the response for each channel is calculated as the sum response during the all irradiated time, X_i where X is the sum response of a channel and i is the channel number. There were some dead channels (not responding), which could be due to the imperfect connection on the PCB circuit board. These channels were removed before the start of the analysis. Then the average response over the all channels is calculated as (X_{avr}). Hence, the equalisation correction factor is calculated per pixel as:

$$F_{equ,i} = \frac{X_i}{X_{avr}}$$

Then the equalised responses ($R_{equ,i}$) for any DUO measurements using the same electronics have been calculated as

$$R_{equ,i} = \frac{X_i}{F_{equ,i}}$$

The uniformity is calculated as the percentage deviation of the $R_{equ,i}$ from the central pixel's $R_{equ,centre}$.

6.2.2. Beam profiles measurements

To measure the beam profiles, DUO was irradiated by 6 MV at 100 cm SSD and 10 cm depth for an air gap thickness of 0.5 mm. The square field edge ranged from 0.5 cm to 10 cm collimated by the jaws, by increments of 0.5 cm step. Responses of all pixels for each field size were normalized to the central pixel response. Each beam profile is an average of three repeated measurements and the uncertainty is a two-standard deviation of each three measurements.

6.2.3. EBT3 film measurements

The beam profiles measured with the DUO detector were compared to Gafchromic^{TM} EBT3 films irradiated under the same conditions. The films were cut into different sizes to match the field sizes used for the DUO detector and scanned in transmission mode with an EPSON expression 10000XL using a 48-bit RGB, at a resolution of 72 dpi. All films were pre-scanned and post-scanned in a consistent orientation and read out without colour or sharpness corrections. Eight films of size 3.0 x 3.0 cm^2 were used to get the calibration conversion factors, irradiated from 50 to 600 MU. Two additional films were not irradiated to get the initial optical density at 0 cGy. The time between the irradiation and the post scan of films were about 48 hours, to ensure the stabilization of the film response. The analysis was done by using Image J (version 1.47v) and MATLAB software tools. The red channel was used for the analysis, based on the largest change in the optical density and dose. The films were irradiated to 400 MU.

6.2.5. Dose per pulse response

The radiation dose from the Varian LINAC is delivered with short 3 μs pulses at frequency of 360 Hz and the dose per pulse dependence is related to the variation in the

dose rate delivered in pulsed beams. The dose delivered in each pulse is high enough to affect the sensitivity of silicon detector response (Wilkins, Li et al. 1997). Therefore, it is necessary to characterize silicon detectors dose rate responses in terms of the dose per pulse (Jursinic and Nelms 2003). For the DUO detector, the dose per pulse dependence (DPP) measurements were carried out in a Solid Water^{TM} phantom of size of 30 x 30 cm^2 by using 6 MV photon beam. The dose rate was fixed at 600 MU/min, irradiated 10 x 10 cm^2 field size at depth 1.5 cm with changing SSD from 100 to 366 cm, corresponding to a dose per pulse range from 2.78 $x10^{-4}$ to $2.1x10^{-5}$ Gy/pulse. The measurements were repeated by using CC 13 (IBA dosimetry Wellhofer Scanditronix, Germany) ion chamber as a reference. More details on this method can be found elsewhere (Wong, Knittel et al. 2011, Aldosari, Petasecca et al. 2014). No change in DUO response was observed for different LINAC nominal dose rate in a range (100-600) MU/min at any depth in a phantom.

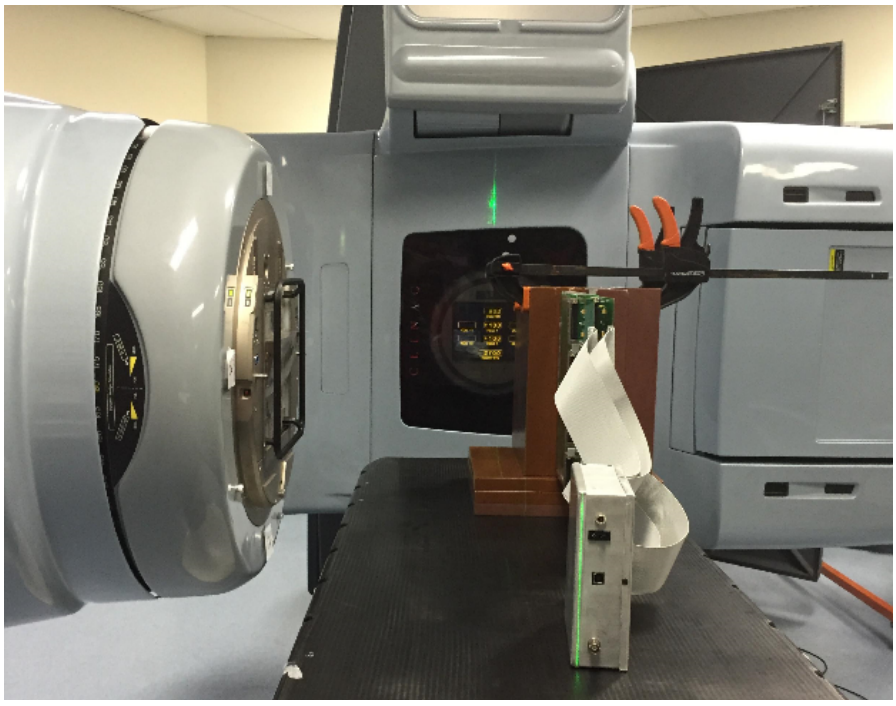

Figure 6.1: Dose per pulse measurement setup.

6.2.6. Percentage depth dose

The DUO detector was placed above a 10 cm Solid Water^{TM} phantom of size 30 x 30 cm^2 to provide the required back scattering conditions and Solid Water^{TM} slabs with different thickness were used to measure the depth doses from 0 up to 25 cm depth for 10 x 10 cm^2. The PDD were measured for 6 MV photon beam at 100 cm SSD. The LINAC was set to deliver 100 MU at 600 MU/min dose rate. Under the same conditions, a Markus ionization chamber (PTW Freiburg – Germany, Model N23343) was used to compare the PDD measurements. Markus chamber has been used instead of CC13 because it requires less correction factors for PDD measurements (Apipunyasopon, 2012).

6.3 Results

6.3.1. Uniformity

DUO detector was tested for uniformity over all its channels. Figure 6.2 represents the calculated equalisation corrected factors (CF) for each channel connected to DUO array. The CFs are within ±0.1% over all the array. Figure 6.3 shows a comparison in the normalised response at the central pixel to 1, between the raw data and equalised data (CF applied). The error bars are calculated from two standard deviations of three measurements and they are all less than 0.2%. In the raw data, the variation coefficient between the channels was within ±1.8% and in the equalised data (after uniformity correction applied), the variation between channels reduced to < ±0.1%. It is important to apply the equalisation correction factors for all the measurements using DUO detector.

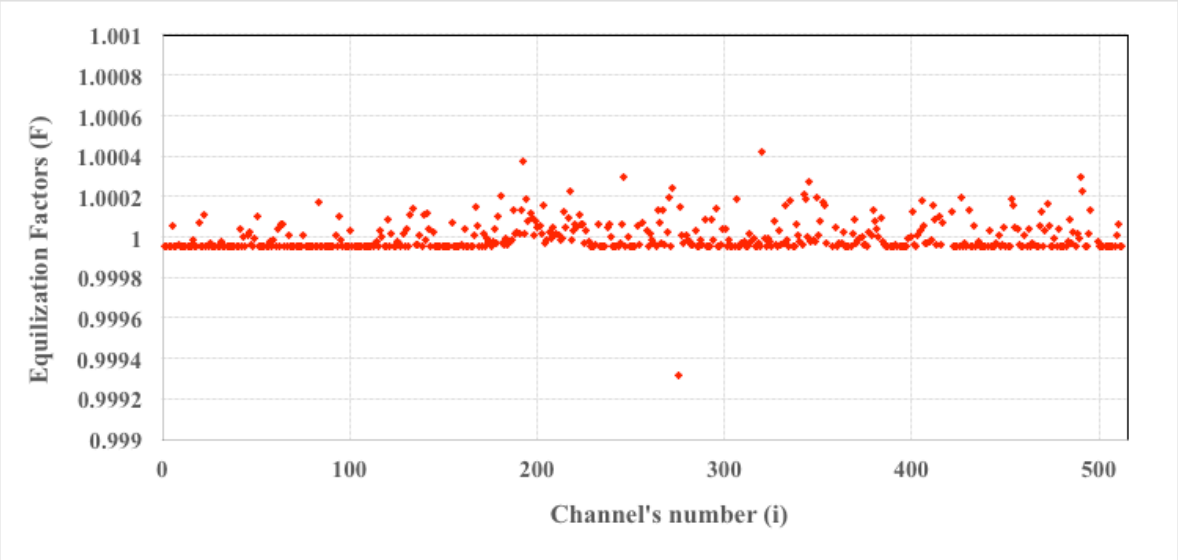

Figure 6.2: The calculated equalisation CF for DUO array as a function of channel number.

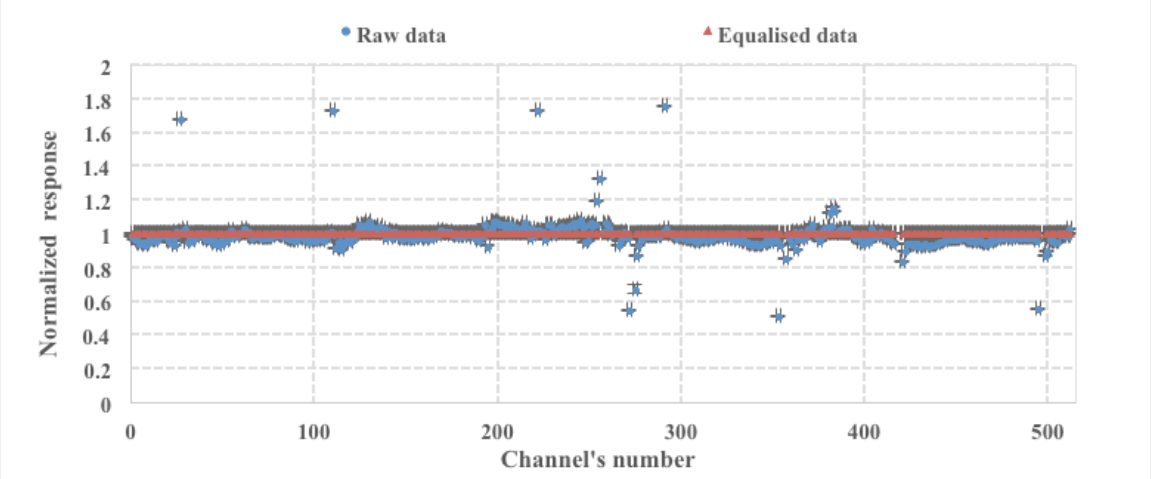

Figure 6.3: The DUO normalized response as a function of channel number with and without applying the equalisation factors.

6.3.2. Beam profiles

The beam profiles measured by using EBT3 films are an average of the central area depending of the field size used, for example for field size 2 x 2 cm^2, five pixels were used in the direction of the profile measured (X- and Y- profiles) as shown in figure 6.4.

Then the beam profiles for 6 MV photon beam at 90 cm SSD and 10 cm depth were measured by using the DUO with a 0.5 mm air gap and EBT3 films for field sizes ranging from 0.5 x 0.5 cm^2 to 5.0 x 5.0 cm^2 in both the X and Y-directions which are shown in figures 6.5 and 6.6, respectively. It is very clear that DUO has a lower response than EBT3 at the out-of-field region reached up to 4%. This is due to the dose rate dependence of DUO detector.

Table 6.1 shows the FWHM and penumbra (80- 20) % for X-profile of both the EBT3 films and the DUO. The data has been analysed by using an interpolation-shape preserving fit with accuracy of 0.01 mm in the Curve Fitting Toolbox available in MATLAB™. The difference in the FWHM between EBT3 and DUO calculated as

$$\text{Difference in FWHM (\%)} = \frac{DUO - EBT3}{EBT3} \times 100\%$$

The differences in the FWHM in the range of field sizes listed were 1%, demonstrating good agreement. The (80-20) % penumbra measured by the DUO gives a wider penumbra than the EBT3 film for field sizes larger than 1 x 1 cm^2. However, the largest absolute value of the discrepancy in measured penumbra is 0.44 mm for 4.5 x 4.5 cm^2 field. Hence, it is still acceptable for clinical use, considering that the general criterion for the plan verification in small field therapies is approximately 1 mm distance to agreement. The same beam profile was observed in the Y-direction but it is not presented in a Table 6.1.

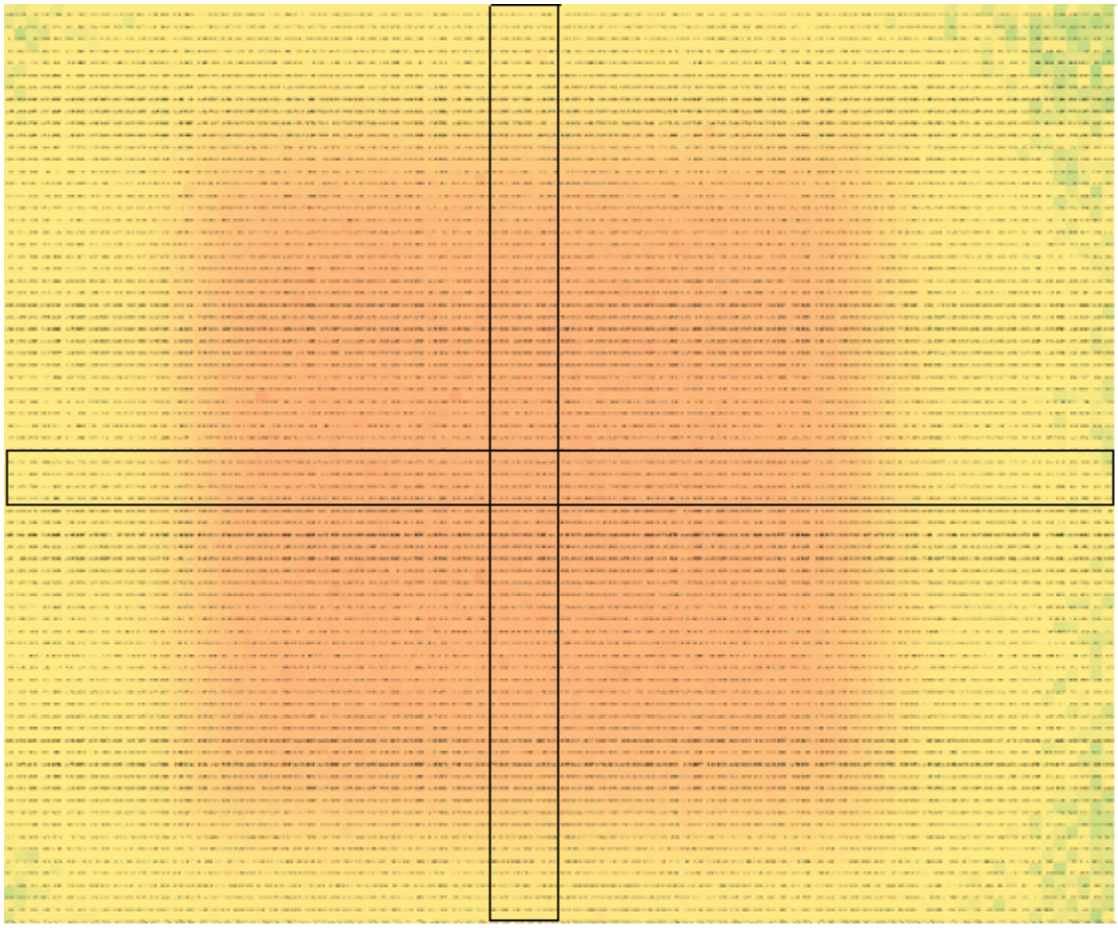

Figure 6.4: Screenshot of EBT3 dose map in excel for field size of 2 x 2 cm^2. The small rectangles represent the central pixels that were used to plot the profiles (not in scale).

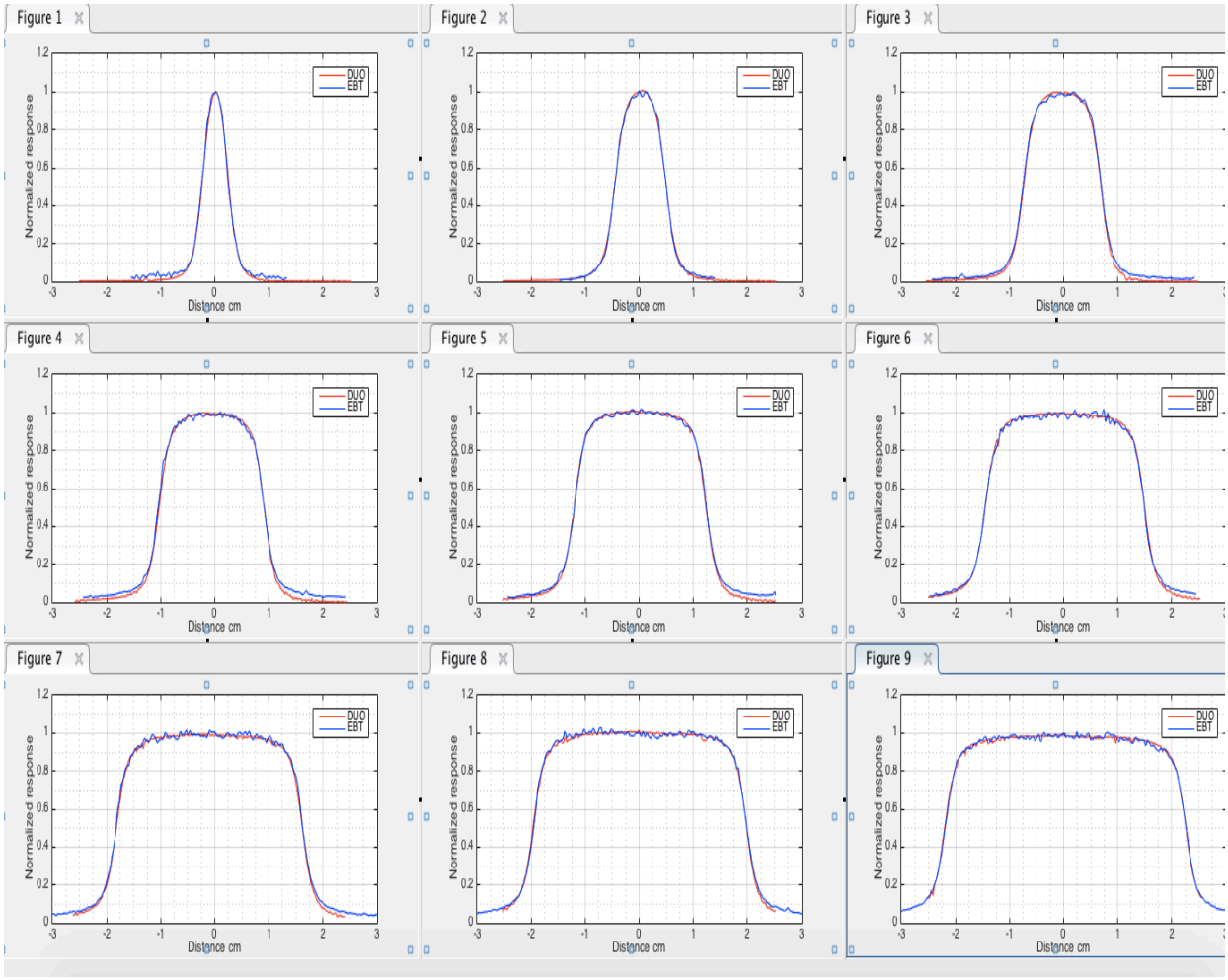

Figure 6.5: Beam profiles of 6MV photon fields measured by the DUO and EBT3 films at isocentre SAD=100 cm and depth 10 cm in the X-direction square fields edges of: figure1) 0.5 cm, 2) 1 cm, 3) 1.5 cm, 4) 2.0 cm, 5) 2.5 cm, 6) 3.0 cm, 7) 3.5 cm, 8) 4.0 cm, 9) 4.5 cm.

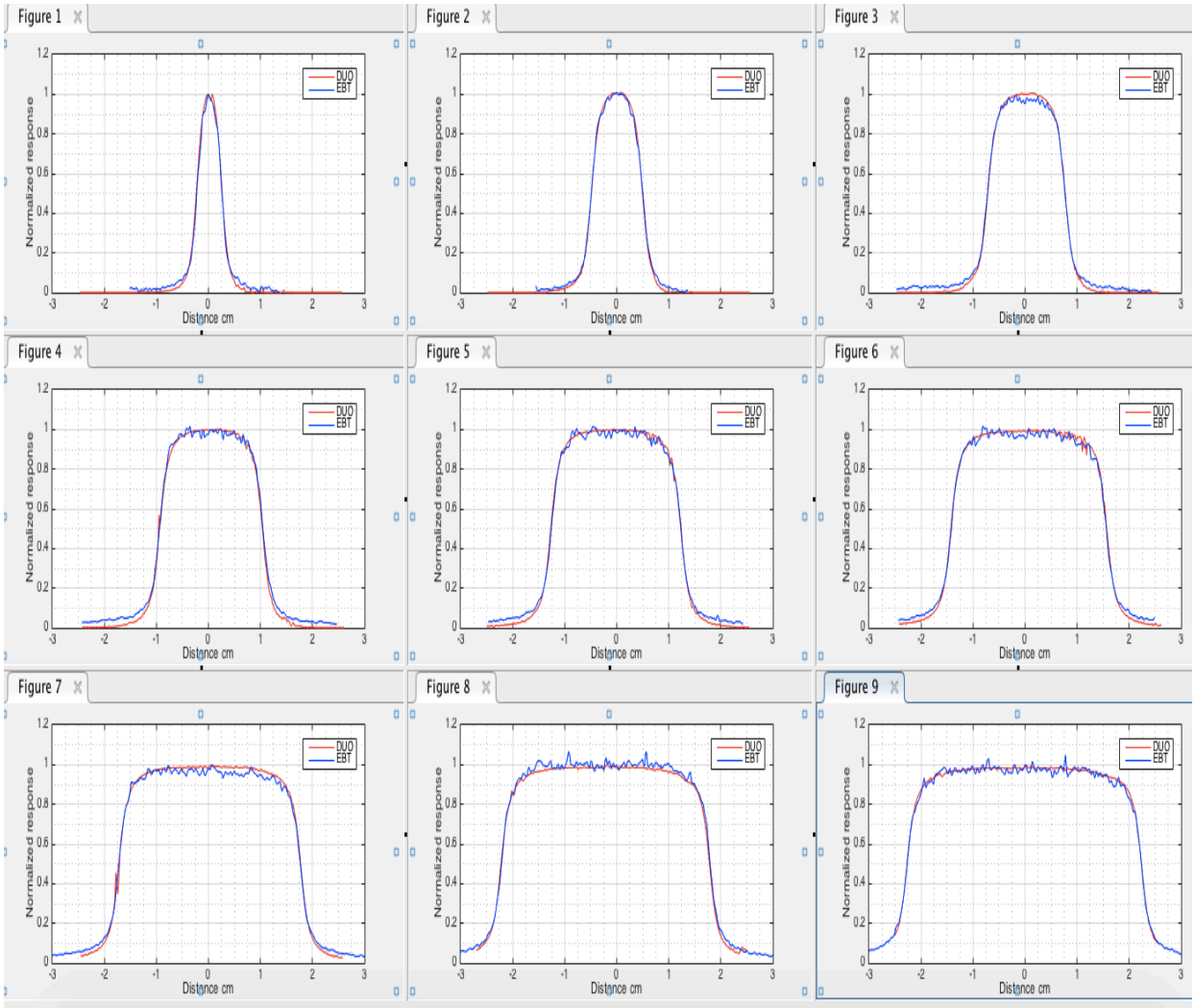

Figure 6.6: Beam profiles of 6MV measured by DUO and EBT3 films at isocentre SAD=100 cm and depth 10 cm in the Y-direction for square fields edges of: figure1) 0.5 cm, 2) 1 cm, 3) 1.5 cm, 4) 2.0 cm, 5) 2.5 cm, 6) 3.0 cm, 7) 3.5 cm, 8) 4.0 cm, 9) 4.5 cm.

Table 6.1: FWHM and penumbra (80% to 20%) of both EBT3 films and DUO detector in the X-profiles.

Field size (cm)	EBT3 (X-profiles)		DUO (X-profiles)		DUO_EBT3 differences		
	FWHM (cm)	Penumbra (cm)	FWHM (cm)	Penumbra (cm)	ΔFWHM (%)	ΔPenumbra (%)	ΔPenumbra (mm)
0.5	0.502	0.232	0.506	0.229	0.917	-1.293	-0.03
1	0.961	0.266	0.954	0.262	-0.677	-1.504	-0.04
1.5	1.452	0.297	1.436	0.32	-1.15	7.744	0.23
2	1.969	0.312	1.952	0.338	-0.909	8.333	0.26
2.5	2.436	0.325	2.461	0.356	1.055	9.538	0.31
3	2.951	0.332	2.938	0.369	-0.441	11.145	0.37
3.5	3.446	0.348	3.446	0.384	0.02	10.345	0.36
4	3.939	0.355	3.939	0.394	-0.02	10.986	0.39
4.5	4.46	0.357	4.458	0.401	-0.045	12.325	0.44

6.3.3. Dose per pulse dependence

Figure 6.7 shows the DPP dependence of the DUO detector for 6 MV photons and field size 10 x 10 cm^2. The error bars were calculated from three measurements of the DUO detector as two standard deviations. It can be seen that the DUO detector has dose per pulse dependence with the response changing within 23% for a DPP variation of 2.78 $x10^{-4}$ to $2.1x10^{-5}$ Gy/pulse. A 3rd order polynomial fit was used to get the DPP correction factors as on a Fig 5.7. The DPP response of the DUO detector presented in Fig.5.7 vs DPP ratio (DPP) normalized to the DPP 2.78 x 10^{-4} Gy/pulse corresponding

to measurements at d_{max} and SSD =100 cm, was approximated by the polynomial f(DPP). The corrected PDD at depth X in a phantom was obtained from the numerical solution of the equation M(X) = PDD f(PDD), where f(PDD) is f(DPP) normalized to one in both the vertical and horizontal axes and where the value one corresponds to PDD at d_{mac} and M(X) was measured by the DUO value at a depth X and normalized to the value at d_{max}.

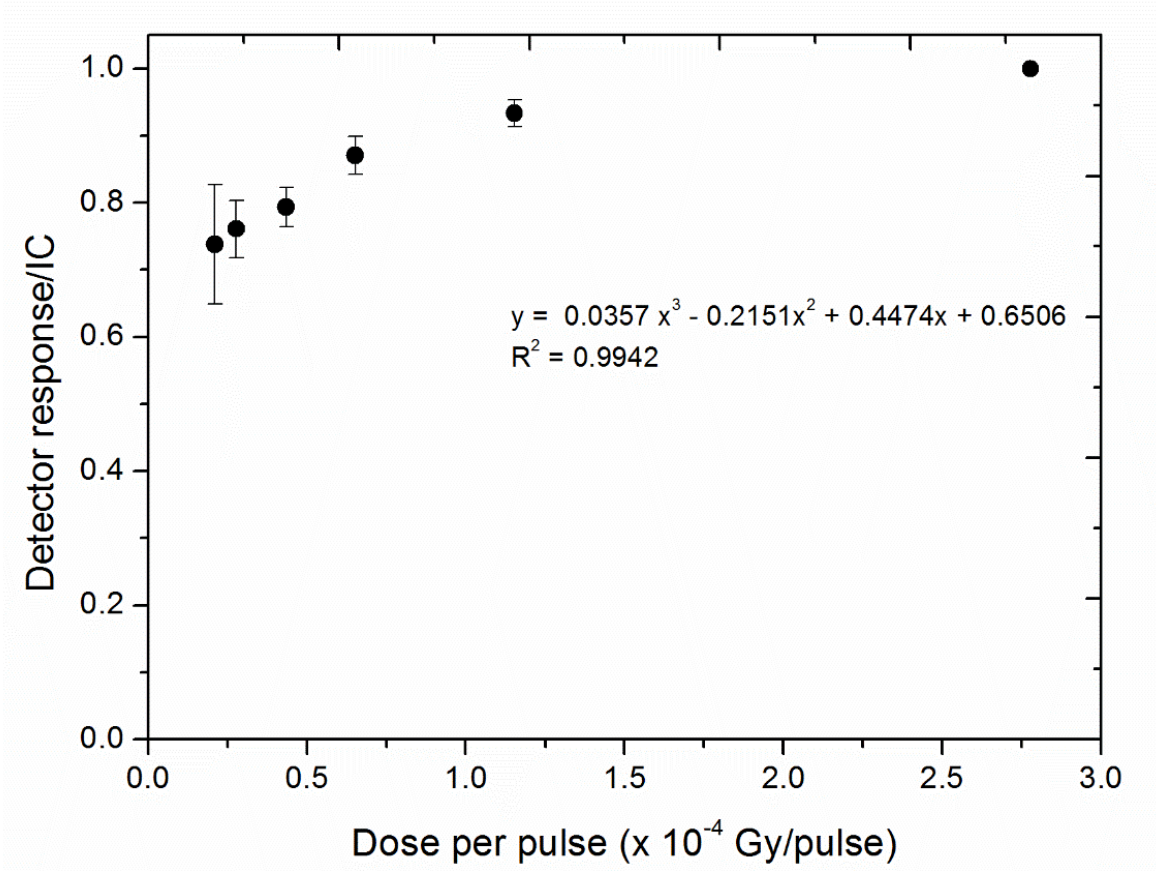

Figure 6.7: Dose per pulse response for the DUO normalized to the dose per pulse 2.78 $x10^{-4}$ Gy/pulse corresponding to the depth of 1.5 cm and SSD of 100 cm. All measurements were carried out at a 600 MU/min nominal LINAC dose rate.

6.3.4. Percentage depth dose

The PDD was measured by using the average reading of the central pixel of the DUO detector and correcting it using the DPP correction factors at each depth as described

above. It is compared with the PDD of a Markus ionization chamber, as shown in figure 6.8. The measurements were done from 0 mm to 25 cm depths in Solid Water™ and then corrected to water equivalent depths. The percentage difference was calculated and found to be within 1.5% for depths beyond the surface. Difference in PDD measured by IC and DUO in a build-up region and on the phantom surface in particular is related to different water equivalent depth (WED) of IC and DUO. The WED of IC is about 50 μm due to the thin entrance window of IC while WED of DUO made of silicon thickness about of 400 μm is about 1 mm. Due to steep gradient in a build-up region it corresponds to 17% and about 30% PDD measured on a surface of the phantom corresponding to IC and DUO, respectively. The error bars calculated represent two standard deviations over the central channels of the detector as determined from two repeated measurements.

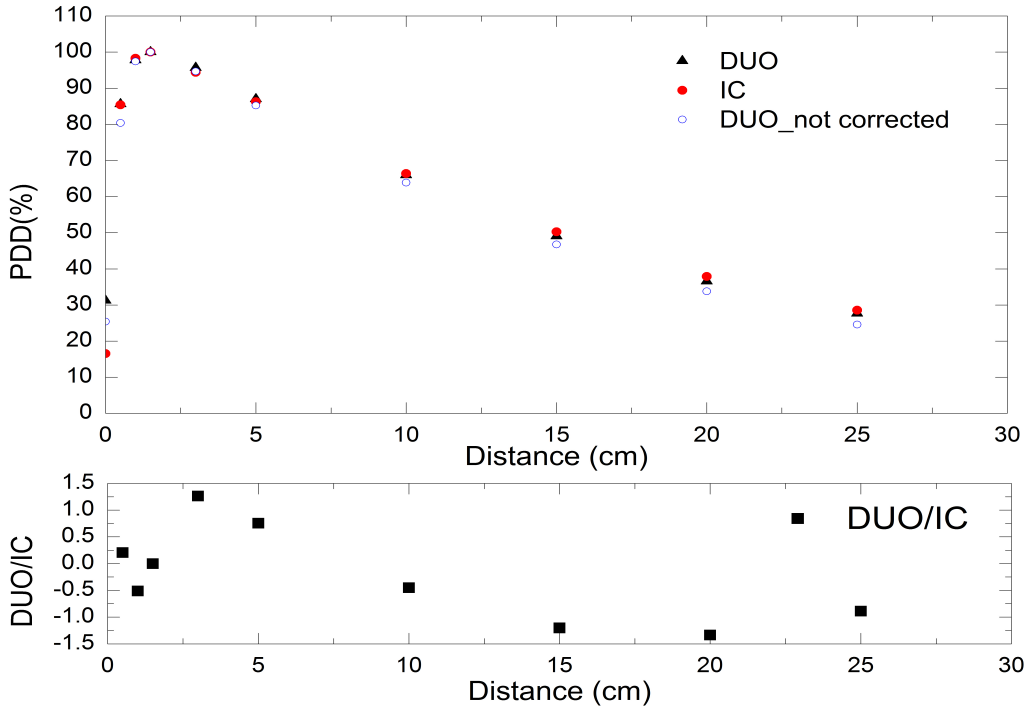

Figure 6.8: PDD of 6MV at the isocentre for a field size of 10 x 10cm^2 measured by the DUO silicon detector. Lower panel: percentage difference between DUO and ionization chamber measurements.

6.4 Discussion

DUO has been fully characterized for square field sizes in terms of uniformity, beam profile, dose per pulse and percentage depth dose. DUO non-uniformity has been studied among all its pixels/ readout channels. There was a non-uniformity within 1.8%, which reduced by using the non-uniformity correction factors to 0.1%. In terms of dose beam profile measurements, DUO agrees well with EBT3 profiles and provides an acceptable agreement in the FWHM and (20-80) % penumbra measurements. The difference in the FWHM and penumbra width measured by DUO and EBT3 are within 1% and 0.5 mm, due to the high spatial resolution. While DUO profiles agree with EBT3 within the accepted criteria in terms of FWHM and penumbra width, DUO shows under-response of dose at the 'out-field' region. This results in around 4%, which could be due to the dose rate dependence of DUO detector. DUO detector has dose per pulse dependence within 23% for a DPP variation from 2.78 $x10^{-4}$ to 2.1$x10^{-5}$ Gy/pulse. Therefore, correction factors were calculated in order to correct the percentage depth dose.

The percentage difference was calculated and found to be within 1.5% for depths beyond the surface. The difference in the PDD on the phantom surface is related to higher water equivalent depth (WED) measured by DUO in comparison to Markus ionization chamber.

6.5 Conclusion

The DUO is a monolithic pixelated detector with 2 orthogonal 1D diode arrays produced using ion implanted p-type silicon technology and has been characterized in a 6 MV small photon field environment. Characterization of the DUO for phantom dosimetry QA in small field applications was demonstrated. The DUO shows a good uniformity after applying the equalization factors, less than ±0.1%. DUO shows a dose per pulse dependence within 5% down to 1.2×10^{-4} Gy/pulse, while it shows approximately 23% at the lowest DPP of 2.8×10^{-5} Gy/pulse. The DPP corrected percentage depth dose measurements of the DUO were compared to those made with Markus ionizing chamber and agreed to within ±1.5% for the depths up to 25 cm and beyond the phantom surface. The normalized beam profile distributions for square field edges between 0.5 and 5 cm were measured with the DUO and compared to Gafchromic™ EBT3 film. The very good agreement in small field profiling was demonstrated by the FWHM agreement with the EBT3 within 1% and the 20-80% penumbra within 0.5 mm.

In this chapter we demonstrated that monolithic silicon detector DUO with a total size 52 x 52 mm^2 containing the two orthogonal arrays of 1D high spatial resolution pixels is suitable for fast QA of small radiation field dose profiling with a size typical in SRS/SRT. Further work will be to characterize DUO by using cone SRS collimator.

CHAPTER 7: A monolithic silicon detector array for small field dosimetry in Stereotactic Radiotherapy

7.1 Introduction

In this chapter, the accuracy of the DUO silicon detector array as a QA tool for SRS cone collimators is investigated. All the measurements were performed in the radiation oncology department of Prince of Wales hospital (Randwick, NSW, Australia) by using 6 MV flattened photon beams from an ELEKTA Axesse^{TM} linear accelerator with a retrofitted Agility head (Elekta AB, Stockholm, Sweden), adapted for stereotactic treatment by using an additional gantry mounted ELEKTA cone collimators system. The cone collimators diameter varied from 5 to 50 mm, every 2.5 mm up to 20 mm and then every 5 mm. In this study, three detectors were used for the measurements; two detectors were available commercially: EBT3 Gafchromic^{TM} films and IBA Stereotactic Field Diode (SFD), and the third used detector was DUO. The tested parameters were:

1. Output factors
2. Beam profiles
3. Percentage depth dose

7.2 Methodology

7.2.1 Detectors

The detectors used in this study were DUO silicon detector array (section 3.2.1), EBT3 radiochromic^{TM} films (section 2.6.2.1) and IBA SFD. The IBA stereotactic field diode SFD (IBA dosimetry, Nuremberg, Germany) is a p-type unshielded low resistivity silicon diode. It has an active volume of 0.017 mm^3 with 0.06 mm thickness and 0.6

mm diameter. Its sensitivity is 6 nC/Gy (Lechner, Palmans et al. 2013). Morales, Crowe et al. (2014) have studied the dose rate dependence of SFD by measuring the PDD for field size 10 x 10 cm^2 and compared it with the ionization chamber. The results have showed an agreement within 0.5%. Therefore, IBA SFD doesn't exhibit any dose rate dependence. However, many authors have published correction factors for IBA SFD detectors to compensate for the over-response due to the non-water equivalent materials used in the diode construction and the volume averaging effect, for different LINACs and at different depths (Ralston, Liu et al. 2012, Benmakhlouf, Sempau et al. 2014, Liu, Suchowerska et al. 2014). In this paper, we have used the CF provided by Ralston, Liu et al. (2012) to overcome the over-response of IBA SFD detectors in the OF measurements.

7.2.2 Measurements

7.2.2.1 Uniformity

The uniformity of DUO array was performed by an irradiated DUO array with 6 MV as described in section 5.2.1. The equalisation factors were calculated to apply them for all of the measurements of DUO array.

7.2.2.2 Beam profiles and output factors (OF)

To characterize the performance of the DUO detector in radiation fields collimated by ELEKTA SRS circular cones, profiles of radiation fields from the cones with size 5, 7.5, 10, 12.5, 15, 20, 25, 30, 35 40 and 50 mm were measured at 10 cm depth in Solid Water^{TM} phantom (Gammex RMI 457, Middleton, USA). The X MLC and Y jaw position were set as in table 7.11, for all measurements with these circular cones. The phantom size is 30 x 30 cm^2 to provide the proper scattering conditions with a 10 cm slab used for the backscatter. The DUO detector was irradiated by 6 MV photon beam

with 100 MU at 90 cm SSD, taken three measurements for every settings. The beam profiles were measured in both X (cross-plane) and Y (in-plane) profiles simultaneously. These data were compared with EBT3 films data that were taken under the exact same experimental conditions. Also, IBA SFD was used to measure the beam profiles at the same setup, except the water phantom was used instead of Solid Water^{TM} phantom.

The dose profiles were measured in 0.2 mm steps with DUO, corresponding to its pixels pitch, while EBT3 films measured dose points every 0.35 mm, as determined by the resolution of the scanner, 72 dpi. The SFD diode data were obtained by scanning in a water phantom with a step of 0.3 mm. The profiles measured by EBT3 films and IBA SFD diode were interpolated by using MATLAB^{TB} software to 0.2 mm by using cubic shape preserving function. The FWHM and penumbra width were calculated by using a code function in MATLAB^{TB} software.

The OFs were calculated as the ratio of the dose response at the central pixels of DUO detector for each SRS cone size at 10 cm depth to the dose response at the same central pixels of 50 mm SRS cone size at the same depth. These OF are compared to the OF taken by SFD and EBT3 films. For IBA SFD diode, the OF were calculated with and without applying the published correction factors.

Table 7.1: The field sizes used for each circular cone diameter.

Circular cone diameter (mm)	Field size (mm)
5, 7.5, 10	30 x 30
12.5, 15, 17.5, 20	40 x 40
25, 30	50 x 50
35, 40, 50	60 x 60

7.2.2.3 Percentage depth dose (PDD)

To investigate the performance of DUO at each depth for different SRS cone sizes, the percentage depth dose (PDD) was measured in Solid Water™ at 90 cm SSD (figure 1). Solid Water™ slabs were placed on the bottom (10 cm) for backscattering purposes. The PDD was measured for cone sizes from 5 to 40 mm at depths from 0.5 to 25 cm. The measurements were repeated three times for each setting in order to calculate the error from the standard deviation. Corresponding measurements were performed with EBT3 for comparison. IBA SFD was used also to measure the PDD in water phantom at 90 cm SSD, for all cone sizes. It should be noted that the PDD measured by DUO was corrected for the dose per pulse (DPP) variation as calculated in section 5.3.4.

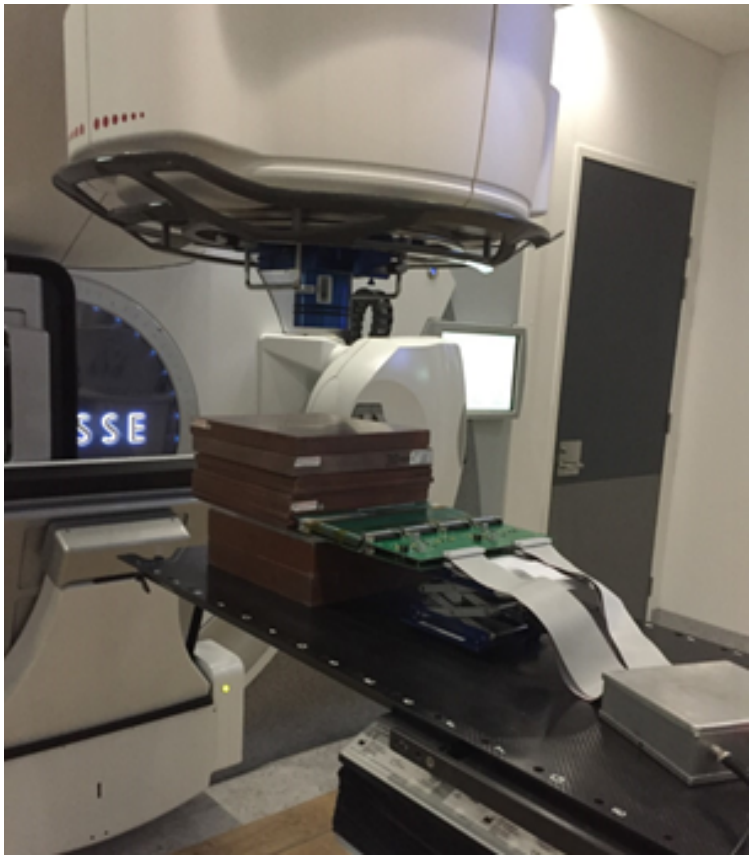

Figure 7.1: Setup for PDD measurements using DUO detector with Solid Water™ slabs for Elekta SRS circular cone collimator at 90 cm SSD.

7.2.2.4 EBT3 film measurements

Gafchromic™ EBT3 films were used to compare the profiles, OF and PDD obtained for SRS cones with the DUO detector. Ten EBT3 calibration films were cut into 3 x 3 cm^2 to get the calibration curve, irradiated from 50 to 600 MU. The measurement films were cut into sections so that it is larger than each SRS cone size by 2 cm in order to measure the beam profiles and PDD. The films were pre-scanned and post-scanned with an Epson scanner (10000 XL), where the post-scan was performed 48 hours after the irradiation. The films were scanned in transmission mode using 48-bit RGB color mode with 72 dpi scan resolution. Films were scanned at the center of the scanning area by using a template to reduce the optical non-uniformity and in one fixed direction to avoid

film induced change in pixel values. The EBT3 films were placed between Solid Water^{TM} slabs in an orientation perpendicular to the beam central axis (CAX). The analysis was performed by using MATLAB and the red channel pixel values were used to calculate the optical density. The films were irradiated with 500 MUs. The dose calibration curve was fitted using a third-order polynomial function. The dose maps were calculated using MATLAB and the center of the cone was determined in order to calculate the OF, PDD and beam profiles in two dimensions. An example for cone 5 mm at 10 cm depth is presented in figure 7.2.

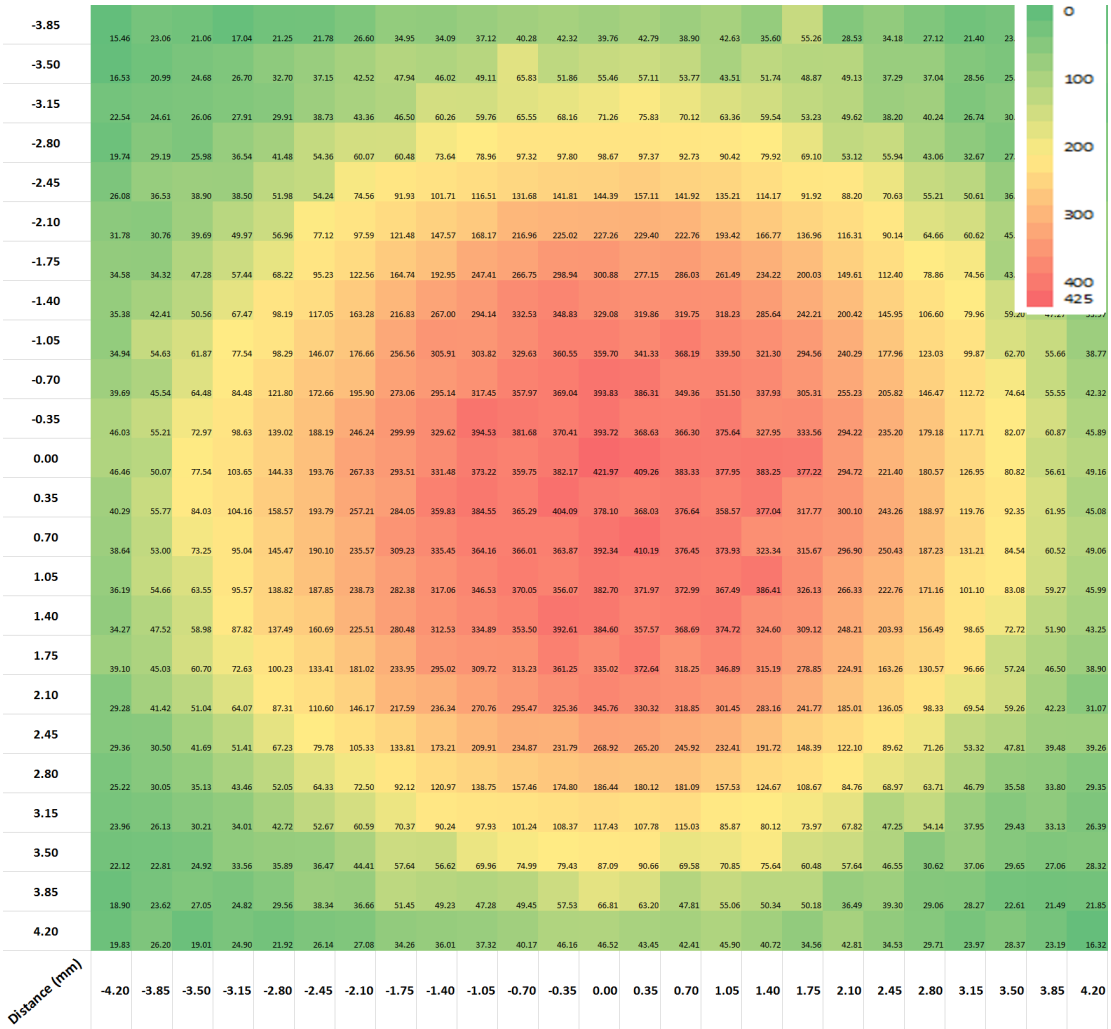

Figure 7.2. 2D dose map for 5 mm cone diameter at 10 cm depth, the scale is the dose in cGy.

7.3 Results

7.3.1 Uniformity

Figure 8.5 shows the DUO response before applying the equalisation factors and after it. There was a variation in the response between the pixels up to 2.1%. This percentage decreases to less than 0.25% after applying the equalisation factors.

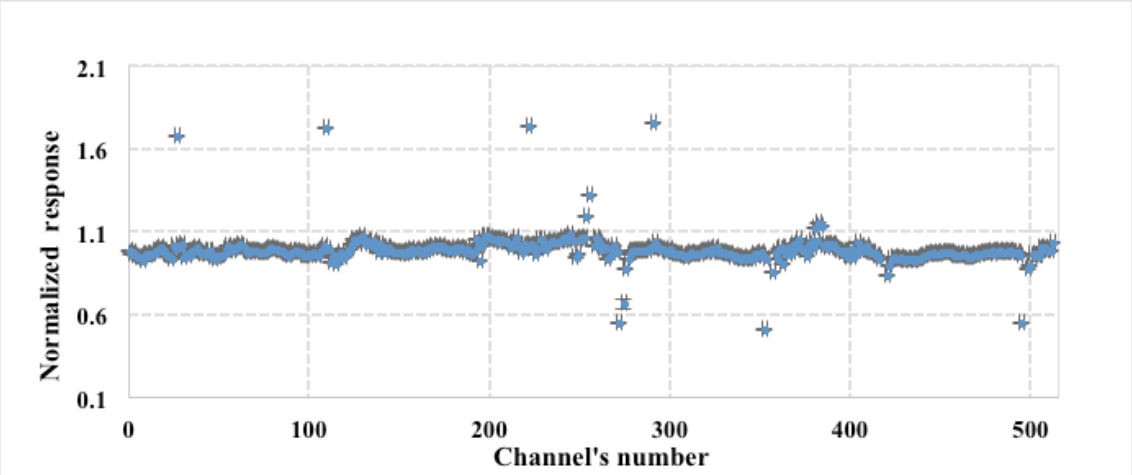

(a)

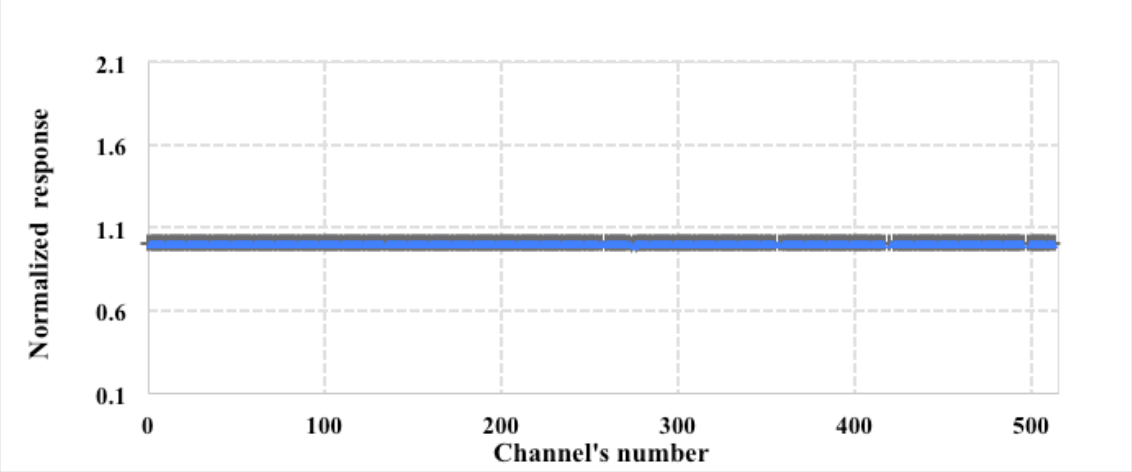

(b)

Figure 7.3: Detector response (a) before and (b) after applying equalisation factors.

7.3.2 Beam profiles

Both cross-plane and in-plane beam profiles of all cone sizes were measured by using DUO, SFD and EBT3 films as shown in figure 7.3 and 7.4, respectively. DUO profiles were corrected for charge sharing effect as discussed in chapter 5, where the pitch size becomes 0.23 mm at the penumbra region. The beam profiles were normalized to 1 at the center. In general, there is an agreement between the three detectors in both X- and Y- profiles.

The beam profile parameters (FWHM and penumbra width (20-80) % were calculated for each cone size in the cross-plane and in-plane directions for the three detectors, by using an interpolation-shape preserving fit with accuracy of 0.01 mm in the Curve Fitting Toolbox available in MATLAB^{TM}. The (20-80) % penumbra width is calculated as the average between the (20-80) % ascending and descending parts on the beam profiles.

The measurements depend on both the pitch size and the detector volume. The comparisons of these parameters as measured by DUO, EBT 3 film and SFD are shown in tables 7.2 - 7.4. There is a good agreement between DUO, EBT3 film and SFD within ±0.5 mm for FWHM. The (20-80) % penumbra widths showed a good agreement within ±0.7 mm for all cone sizes. By comparing the profile parameters between X-profiles and Y-profiles, there were differences up to 0.3, 0.6 and 0.8 mm in FWHM measured by DUO, EBT3 and SFD, respectively. In terms of penumbra width, the differences between X-profiles and Y-profiles were high up to 0.5, 0.6 and 1.0 mm, measured by DUO, EBT3 and SFD, respectively.

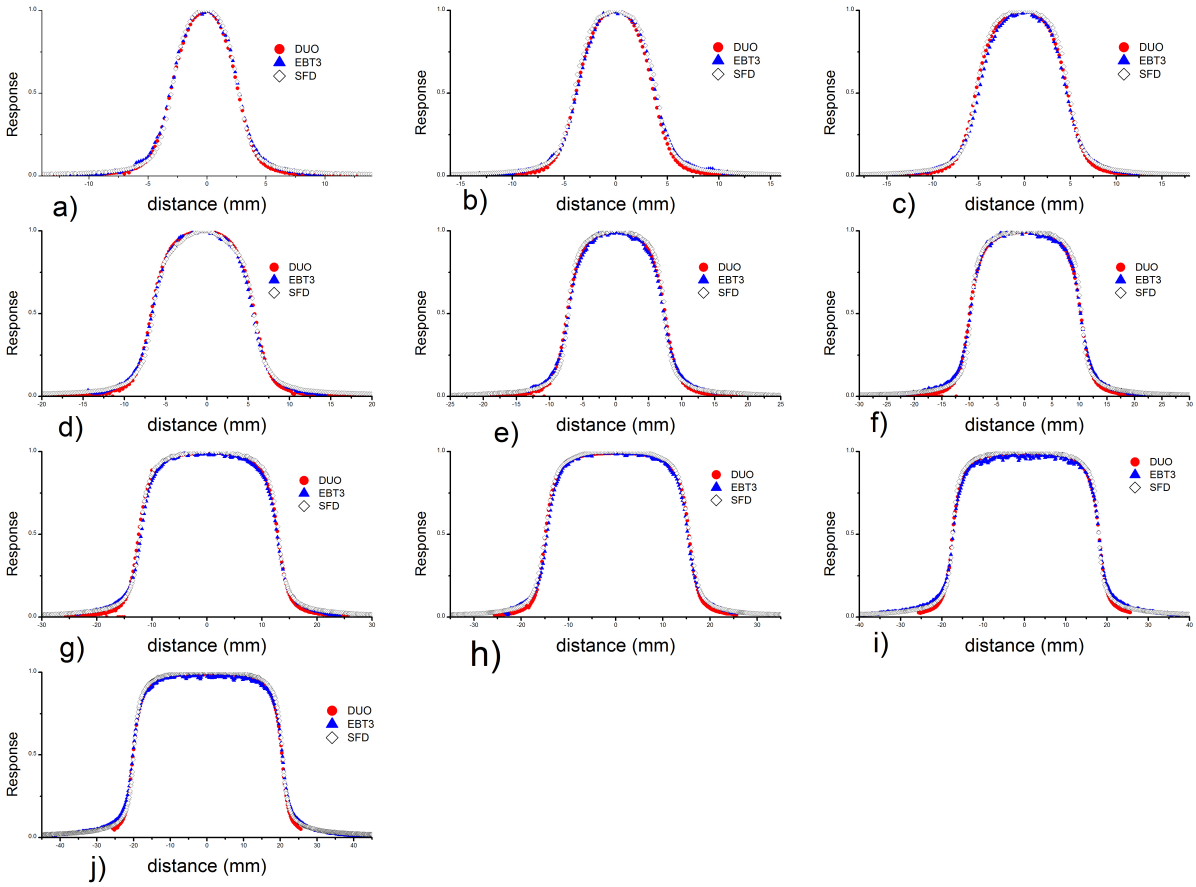

Figure 7.4: Cross-plane profiles measured by DUO, EBT3 and SFD at 90 cm SSD, for cone sizes: (a) 5 mm, (b) 7.5 mm, (c) 10 mm, (d) 12.5 mm, (e) 15 mm, (f) 20 mm, (g) 25 mm, (h) 30 mm, (i) 35 mm and (j) 40 mm.

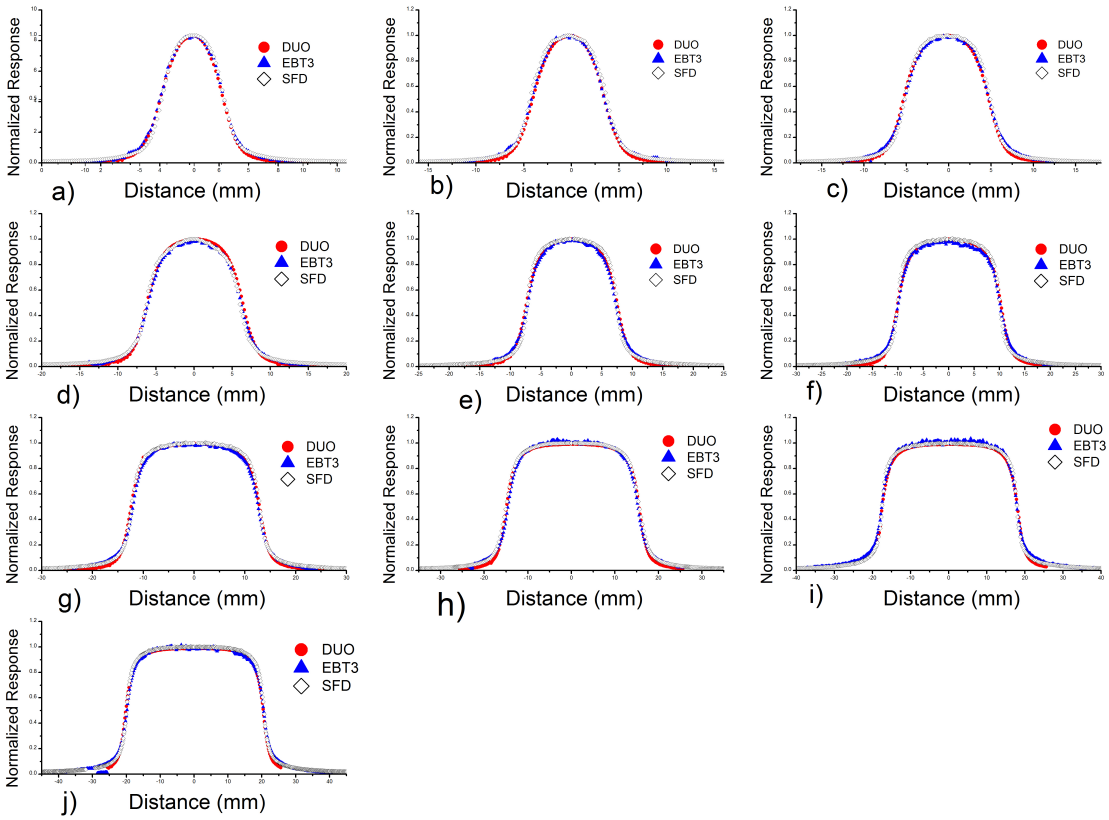

Figure 7.5: In-plane profiles measured by DUO, EBT3 and SFD at 90 cm SSD, for cone sizes: (a) 5 mm, (b) 7.5 mm, (c) 10 mm, (d) 12.5 mm, (e) 15 mm, (f) 20 mm, (g) 25 mm, (h) 30 mm, (i) 35 mm and (j) 40 mm.

Table 7.2: FWHM measured by DUO, EBT3 and SFD in both X-profiles and Y-profiles.

	FWHM (mm)						Differences (mm)			
Cone	X-profile			Y-profile			DUO/EBT3		DUO/SFD	
(mm)	DUO	EBT3	SFD	DUO	EBT3	SFD	X-profile	Y-profile	X-profile	Y-profile
5	6.13	6.2	6	5.87	5.8	5.8	-0.07	0.07	0.13	0.07
7.5	7.6	8	7.8	7.53	7.6	7.4	-0.4	-0.07	-0.27	0.13
10	10.16	10.4	10.2	10.16	10	9.8	-0.24	0.16	-0.04	0.36
12.5	12.85	13	12.8	12.76	12.6	12.4	-0.15	0.16	0.05	0.36
15	15.05	14.8	15.4	14.79	14.8	14.6	0.25	-0.01	-0.35	0.19
20	20.25	20.4	20.6	20.19	19.8	20.6	-0.15	0.39	-0.35	-0.41
25	25.51	25.4	25.6	25.68	25.4	25.4	0.11	0.28	-0.09	0.28
30	30.71	30.2	30.8	30.68	30.4	30.8	0.51	0.28	-0.09	-0.12
35	35.57	35.2	36	35.68	35.8	35.8	0.37	-0.12	-0.43	-0.12
40	40.83	40.4	41	40.91	40.6	40.8	0.43	0.31	-0.17	0.11

Table 7.3: Penumbra measured by DUO, EBT3 and SFD in both X-profiles and Y-profiles.

	Penumbra (mm)						Differences (mm)			
Cone	X-profile			Y-profile			DUO/EBT3		DUO/SFD	
(mm)	DUO	EBT3	SFD	DUO	EBT3	SFD	X-profile	Y-profile	X-profile	Y-profile
5	2.04	2	1.6	1.81	1.8	1.8	0.04	0.01	0.44	0.01
7.5	2.5	2.6	2.2	2.27	2	1.9	-0.1	0.27	0.3	0.37
10	2.5	2.8	2.2	2.5	2.2	1.8	-0.3	0.3	0.3	0.7
12.5	2.96	3	2.6	2.47	2.6	2.2	-0.04	-0.13	0.36	0.27
15	2.96	3.2	2.5	2.5	2.8	2.2	-0.24	-0.3	0.46	0.3
20	2.5	3.2	2.8	2.73	3.2	2.2	-0.7	-0.47	-0.3	0.53
25	3.19	3.4	3	2.96	3.2	3	-0.21	-0.22	0.19	-0.04
30	3.42	3.6	3.3	3.19	3.2	3.6	-0.18	-0.01	0.12	-0.41
35	3.65	3.8	3.6	3.19	3.8	2.6	-0.15	-0.61	0.05	0.59
40	3.65	4	3.3	3.19	3.8	3.1	-0.35	-0.61	0.35	0.09

Table 7.4: The differences in FWHM and penumbra between X-profiles and Y-profiles measured by DUO, EBT3 and SFD, calculated as (X-profile – Y-profile).

Cone	FWHM (mm)			Penumbra (mm)		
mm	DUO	EBT3	SFD	DUO	EBT3	SFD
5	0.26	0.4	0.2	0.23	0.2	0.2
7.5	0.07	0.4	0.4	0.23	0.6	0.3
10	0	0.4	0.4	0	0.6	0.4
12.5	0.09	0.4	0.4	0.49	0.4	0.4
15	0.26	0	0.8	0.46	0.4	0.3
20	0.06	0.6	0	0.23	0	0.6
25	-0.17	0	0.2	0.23	0.2	0
30	0.03	-0.2	0	0.23	0.4	0.3
35	-0.11	-0.6	0.2	0.46	0	1
40	-0.08	-0.2	0.2	0.46	0.2	0.2

7.3.1 Output factors

Figure 7.5 shows the OF for different cone sizes normalized to 50 mm cone size as measured by DUO, SFD and EBT3 films and their percentage deviations. The error bars were calculated as 2 SD of three DUO measurements under the same setting. The results show a good agreement between DUO and EBT3 within ±0.7% for all cone

sizes. IBA SFD shows an over response of up to 5.7% before applying the correction factors. After applying the over-response correction factors provided by Ralston, Liu et al. (2012) for SFD, the average difference between SFD and EBT3 output factors was 1% with the maximum difference of 2% for 5 mm cone.

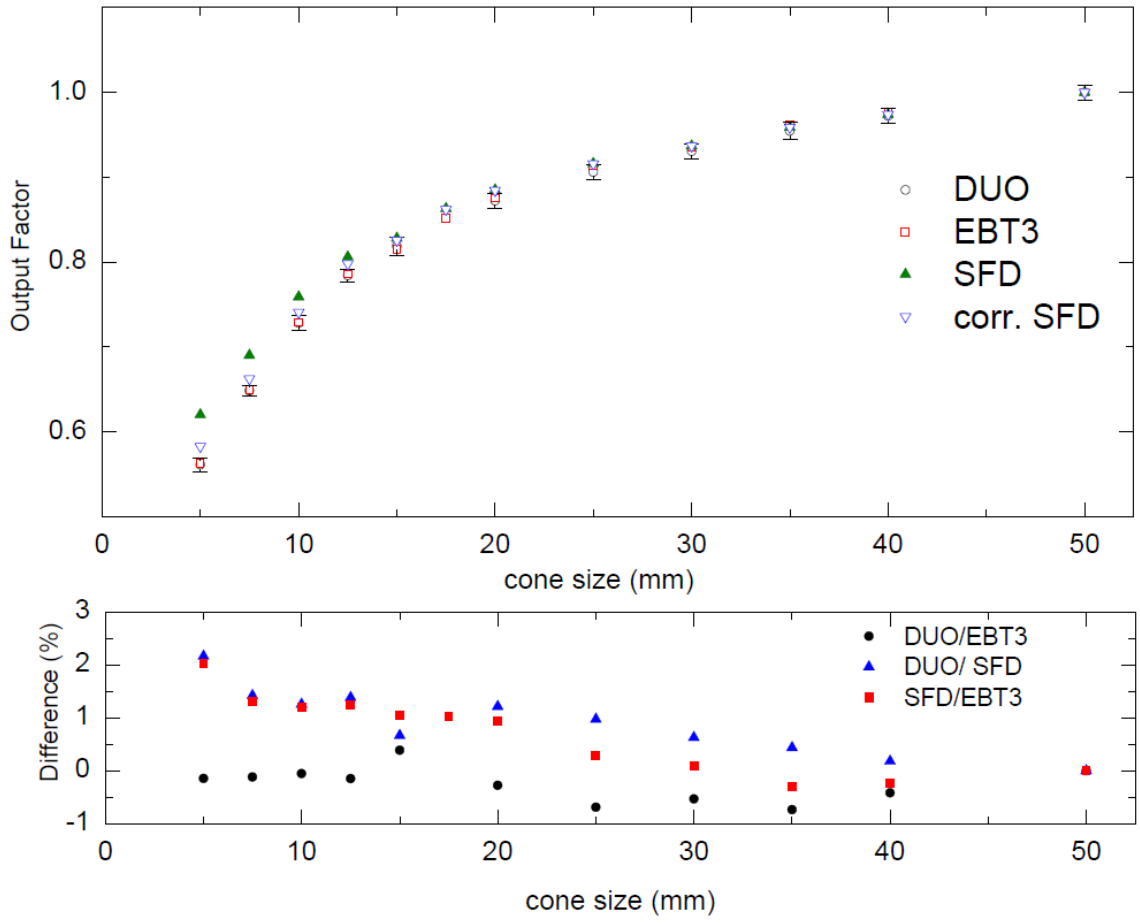

Figure 7.6: the output factors (OF) normalized to cone 50 mm diameter by using DUO, EBT3 and SFD, lower panel: the DUO/EBT3, DUO/SFD and SFD/EBT3 percentage difference (%).

7.3.3 Percentage depth dose

Figures 7.6 and 7.7 show the PDD measured by using DUO, SFD and EBT3 films for cone sizes of 5, 7.5, 10, 12.5, 15, 20, 25, 30 and 40 mm at depths up to 25 cm, and the

percentage deviations between the detectors, respectively. The water equivalent depths were calculated by applying the depth dependence correction factor (C_p) taking into account that measurements with EBT film and DUO detector were carried out in a Solid Water^{TM} phantom while measurements with SFD were done in water. The depth of maximum dose (d_{max}) was different at each cone size by using DUO, SFD and EBT3, therefore the data was normalized at a 10 cm depth in order to facilitate comparison between them. Actually, the depth of maximum dose is around 12.2 mm for 5 mm cone size and it increases to around 15.2 mm for 40 mm cone size. The error in the DUO measurements was calculated as two standard deviations from three sets of measurements at the same setup (error bars are not clear in the figure as they are very small). The error bar in the EBT3 measurements represents two standard deviations of the central dose area from the average dose for each cone diameter.

The comparison of depth dose measured by the three detectors in all the cone sizes showed overall average agreement of ±0.5%; with maximum differences of ±2% between all three detectors; with maximum differences within ±2% for DUO/EBT3 and SFD/EBT3.

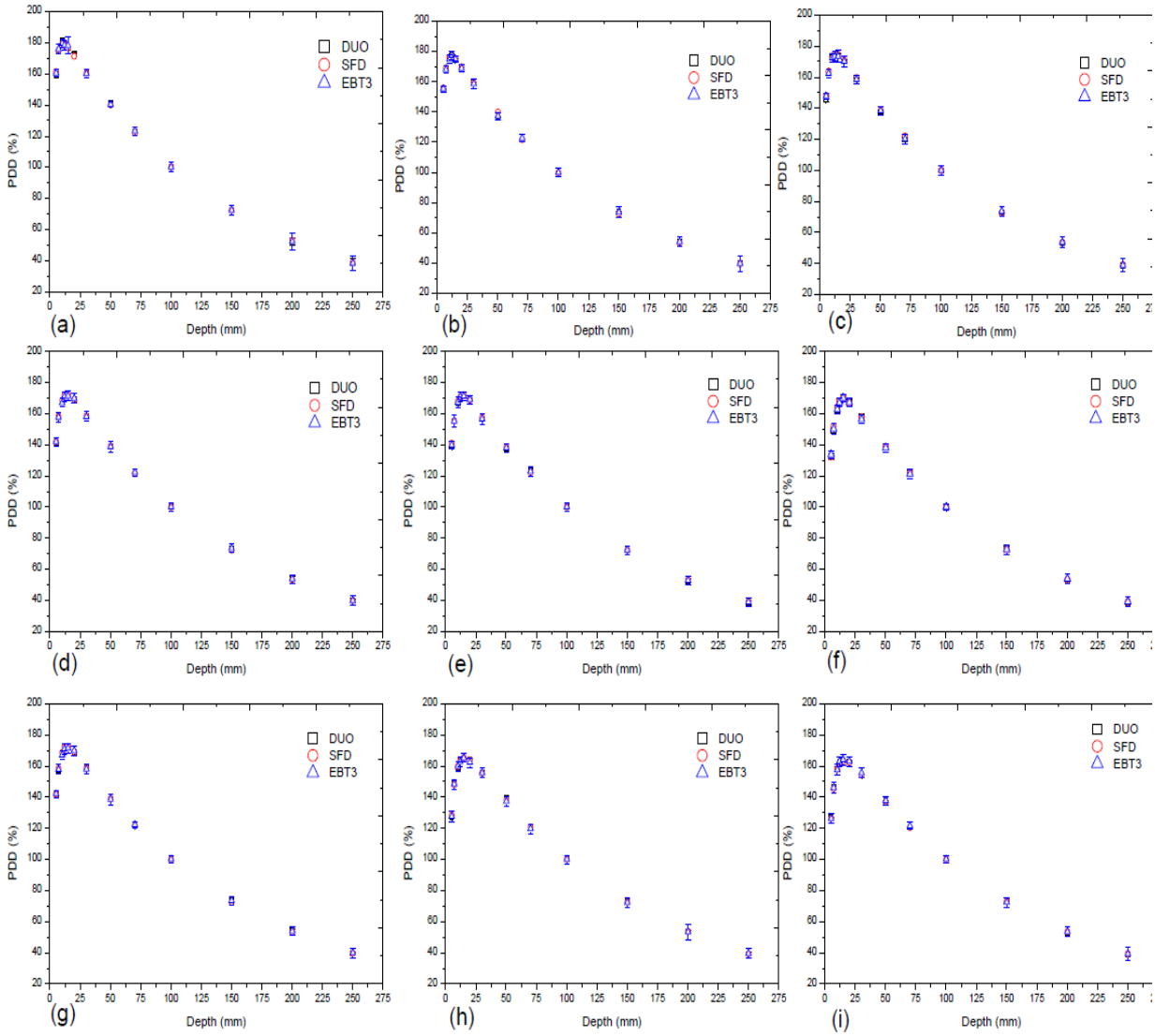

Figure 7.7: Percentage depth dose (PDD) for different cone diameters measured by DUO, SFD and EBT3 at SSD 90 cm for cone sizes: (a) 5 mm, (b) 7.5 mm, (c) 10 mm, (d) 12.5 mm, (e) 15 mm, (f) 20 mm, (g) 25 mm, (h) 30 mm and (i) 40 mm.

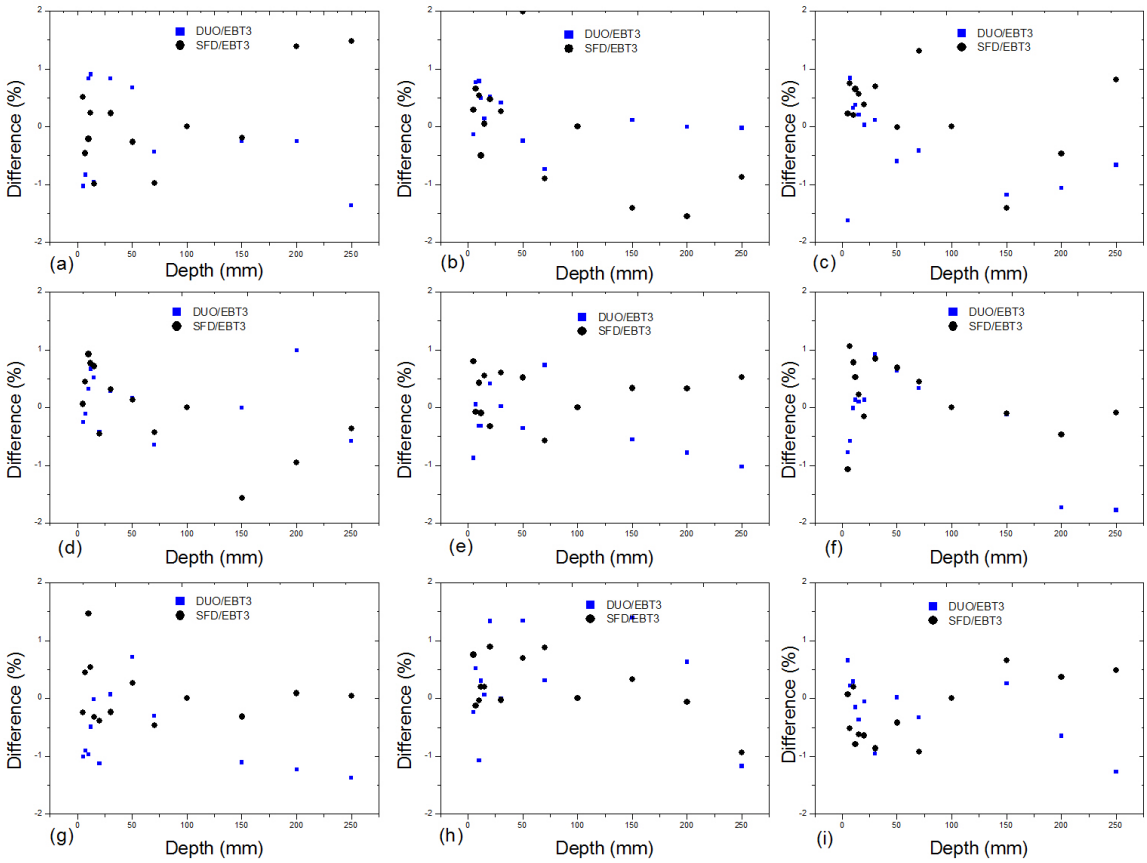

Figure 7.8: The differences in the PDD between DUO/ EBT3 and SFD/EBT3; for cone sizes: (a) 5 mm, (b) 7.5 mm, (c) 10 mm, (d) 12.5 mm, (e) 15 mm, (f) 20 mm, (g) 25 mm, (h) 30 mm and (i) 40 mm.

7.4 Discussion

In this study, three detectors were used to measure the beam profiles, output factors and PDD for ELEKTA SRS cone collimators. One of these detectors is water-equivalent and has sufficient spatial resolution for small field dosimetry (EBT3) and two are diodes (DUO 2D high spatial resolution monolithic diode array and a single diode IBA SFD), which required correction for the non-water equivalence and/or volume averaging effects.

7.4.1 Beam profiles

By comparing the beam profiles of the SRS cone collimators, DUO shows good agreement with the EBT3 films in the 'in-field' area after applying the charge sharing correction factors, but slightly lower dose in the 'out-field' area for all the cone sizes. This could be due to the dose rate dependence of DUO for very low dose rate.

The normalized response measured by IBA SFD shows higher drop off in the penumbra region than DUO and EBT3 for cone sizes smaller than 20 mm, as shown in figure 7.8. (Tyler, Liu et al. 2013) also found this. The same behaviour was found in the comparison of Y-profiles. This could be due to the large sensitive volume and high Z extra-cameral material that has been explained in more detail by Benmakhlouf and Andreo (Benmakhlouf and Andreo 2017) . It could be also improved by using the deconvolution method, which has been developed to obtain beam profiles independent of the detector size (Poppe, Stelljes et al. 2011) . However, this method is complicated if done manually and is not practical in a clinical setting as a large number of profiles require long post processing time (Das, Cheng et al. 2008). The results depend on both the pitch size (and spatial sampling in case of SFD) and the size of the sensitive volume of the detector. DUO shows good agreement in comparison with EBT3 and IBA SFD diode in both FWHM and penumbra width, for both X- and Y- profiles. However, all three detectors show differences between X- and Y- profiles in terms of FWHM and (20-80) % penumbra widths (table 7.4). X-profile parameters were higher than Y-profile parameters, which could be due to the elliptical shaped focal spot of the ELEKTA Axesse LINAC source. Different groups have studied the shape and size of the x-ray source and found that it depends on the LINAC model, with mostly the elliptical shape (Wang and Leszczynski 2007, Seco and Verhaegen 2013, Herwiningsih and Fielding 2016) .

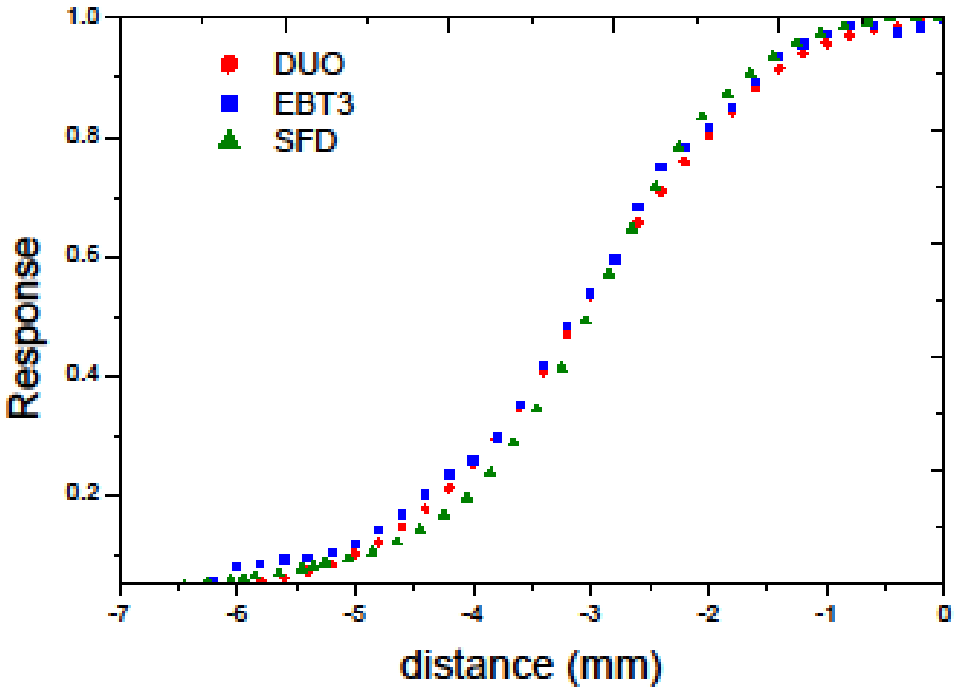

Figure 7.9: Penumbra comparison between DUO, SFD and EBT3 for 5 mm SRS cone diameters.

7.4.2 Output factors

A number of studies reported that diode over-response in small fields is due to the density of silicon and the extra-cameral materials surrounding the detector. However, it has been recently clarified that electron density, rather than the density as a fundamental characteristic of the material, is driving the diode response through density effect in mass stopping power of electrons and ionization potential of silicon (Benmakhlouf and Andreo 2017). In this study, the DUO silicon detector was corrected by using a 0.5 mm air gap above the detector as studied earlier (chapter 4). This correction provides an overall agreement in the output factors for cone sizes from 5 to 50 mm, between DUO and EBT3 within ±0.7%.

Different scientific papers have focused on finding proper correction factors to minimize the over-response of the IBA SFD by studying their response for different

beam qualities, field sizes and types of LINACs in comparison with EBT3 and Monte Carlo simulation. In this work, IBA SFD diode was corrected by using the correction factors provided by Ralston *et al.* for IBA SFD at depth 10 cm (Ralston, Liu et al. 2012). This led to better agreement in the OF measurements between IBA SFD and EBT3, where the difference reduced from 5.7% to 2% for the 5 mm cone size. The average agreement in the OF for all cone sizes is about ±0.8% after applying the correction factors for the IBA SFD.

Recently published AAPM practice guidelines recommends SRS-SBRT annual QA for the OF and the tolerance is ±2% from the baseline for >1.0 cm apertures, and ±5% from the baseline for ≤ 1.0 cm apertures (Halvorsen, Cirino et al. 2017). Our results showed a good agreement between the three detectors indicating that DUO could be a suitable candidate for stereotactic cones regular QA. Its practicality and online reading would make it the preferred option over the other 2 detectors in clinical settings.

7.4.3 Percentage depth dose

In the PDD measurements, the depth of the maximum dose (d_{max}) was changed as a function of the cone diameter and it was difficult to detect the exact d_{max} as it depends on the available phantom thickness and the resolution of the detector. Therefore, all PDD measurements were normalized to 100 mm depth.

The comparison of PDDs between DUO, EBT3 and IBA SFD show an agreement within ±2% for small cone sizes up to 20 mm, and then the agreement increased to ±1.5% for the larger cones.

7.5 Conclusion

It was recommended in the IPEM report 103 to avoid the use of ion chamber for the small beam profile measurements due to different issues such as their large volume,

which cause volume averaging effects, therefore artificially broadening in the penumbra region and increasing the FWHM of the measured beam profile. In addition, the use of small air filled ionization chambers cause under response to the dose due to the low mass density of air (Scott, Kumar et al. 2012). Thus, the use of EBT3 Gafchromic^{TM} films and diodes were recommended. To facilitate small field dosimetry and propose an alternative to time consuming films and single diode water tank measurements, CMRP designed a monolithic silicon detector DUO with 0.2 mm spatial resolution for SRS dosimetry. The effect of the high density of silicon on the output factor measurements was successfully compensated by introducing an air gap of 0.5 mm above it. The charge sharing effect on the DUO detector was corrected in the beam profile measurements. The DUO detector was characterized for circular cones mounted on an ELEKTA axesse by measuring the beam profiles, output factors and PDD for cone diameters ranging from 5 to 50 with EBT3 better than SFD in terms of beam profiles and output factors. The good agreement between DUO and EBT3 in the profiles shows a difference less than ±0.5 mm in the FWHM and ±0.7 mm in the (20-80) % in the penumbra width. The output factors show very good agreement between DUO and EBT3 for all cone sizes within ±0.7%. IBA SFD detector agrees with the EBT3 and DUO measurements of output factors after applying the dose over-response correction factors which shows an average agreement of ±1%, with maximum difference about 2% for a 5 mm cone. In the percentage depth dose curves, there is a good agreement between DUO, SFD and EBT3 for all depths of all measured cone diameters; with the average difference within 0.5% and maximum of ±2%.

In conclusion, DUO is a suitable detector for SRS/SRT dosimetry as it has excellent resolution (0.23 mm) in a direction of the steepest dose gradient, real time data analysis and it provides both in-plane and cross-plane measurements simultaneously. The good

agreement with EBT3 films measurements confirms its accuracy and precision for SRS/SRT measurements; which is one of the treatment modalities where small field dosimetry is paramount and DUO can be applied successfully. The next step is to deliver real plan measurements by using the same SRS cones by using DUO and EBT3 and then comparing them with the treatment planning system (TPS).

CHAPTER 8: Potential clinical applications of monolithic silicon detector array DUO for pre-treatment QA

8.1 Introduction

Stereotactic radiotherapy delivers higher dose per fraction in smaller volumes compared to conventional radiotherapy treatment, which means errors in the treatment delivery will have a higher radiobiological effect on the patient. Therefore, patient pre-treatment quality assurance is usually done before the start of the treatment to ensure that the plan and its related dosimetry are accurate. Hence, a dosimeter, which has real time measurements, is easy to use and has high resolution, is required to perform such pre-treatment QA for the SRS patient's plan.

The previous chapters discussed the suitability of using the DUO detector as QA tools for small field dosimetry by using small square fields (by using jaw collimators) and SRS cone collimators in terms of output factors, beam profiles and percentage depth dose. The aim of this chapter is to perform a clinical application of DUO by delivering SRS cone plans and comparing it with the treatment planning system and EBT3 films. Hence, treatment plans were generated and delivered to DUO in order to verify its use as patient pre-treatment QA dosimetry for SRS cone collimators by using a cylindrical phantom designed by CMRP.

8.2 Methodology

To perform pre-treatment QA for SRS/SRT treatment, a phantom is required to deliver the patient plan in order to check that the correct dose will be delivered to the patient by

using a suitable detector. The SRS/SRT treatment aims to treat small lesions surrounded by critical normal tissues. The verification procedure consists of re-calculating the dose delivered by the patient's fields onto the QA phantom by using the treatment planning system and then delivering the patient's plan in the phantom and measuring the dose by using a suitable detector for ultimately comparing it with the calculated dose distribution.

In this study, a cylindrical phantom is used (as described in section 3.5). It is designed to be suitable for SRS/SRT treatment with a 30 cm diameter and 40 cm length (similar to the head shape). It is made of water equivalent material (PMMA) and it is machined to be suitable to use with the DUO detector.

8.2.1 X-ray CT for the rotatable cylindrical phantom

The cylindrical phantom with the DUO detector inserted was scanned by using a CT simulator scanner (Aquilion, LB, Toshiba). The imaging protocol used was the clinical one used for stereotactic treatment, with a tube potential of 120 kV_P a slice thickness of 0.5 mm and a large Field of view to fully include the couch. Two scans were performed, one with the detector in the horizontal position and the second with the detector rotated at 90^0, in vertical position. These CT images were sent to the treatment planning system (TPS).

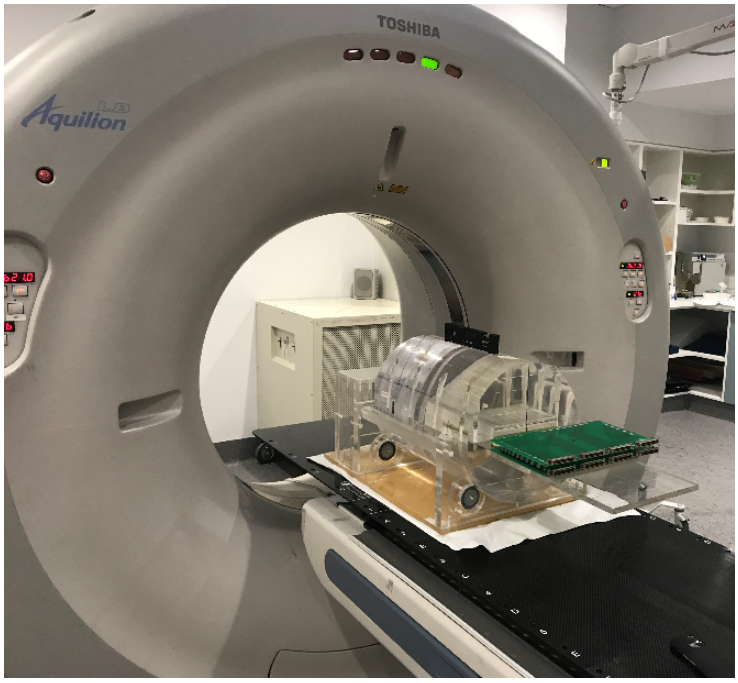

Figure 8.1: CT of the rotatable phantom with DUO placed horizontally at the centre of the phantom.

8.2.2 Treatment planning

The treatment planning was performed by using the Monaco 5.11.01 Monte Carlo TPS (ELEKTA, Sweden). The CT images of the rotatable cylindrical phantom were imported and treatment plans were created for the 2 detector positions, horizontal and vertical, in order to have more information in four directions where DUO can provide two profiles in each position. Each plan consisted of eight beams, one for each cone with diameters of 5, 7.5, 10, 12, 15, 20, 25 and 30 mm. The energy was selected as 6MV photon beam, each isocentric beam centred on the central pixel of the DUO detector and delivering a fixed dose of 1000 MU through an arc for gantry angles from 245^0 to 115^0 to prevent collisions of the cone collimators with the couch (the plan report is shown in Appendix B). The TPS is based on the Monte Carlo photon algorithm (version 1.6) set with 0.5% statistical uncertainty per control point. The grid spacing was selected to be 0.1 cm. The machine model selected was ELEKTA Agility version 5,

Prince Of Wales Hospital (POWH), Sydney. Doses were calculated in the medium, the high-densities area of the DUO detector were overridden to 1 in order to calculate doses in water in the plane of the array, matching the array dose calibration in water. The resulted data was then opened by using excel file (as the example is shown in figure 8.3). The horizontal and vertical beam profiles were extracted from these data as an average of three central pixels. Then, the profiles were interpolated by using MATLAB into 0.2 mm in order to compare it with DUO profiles.

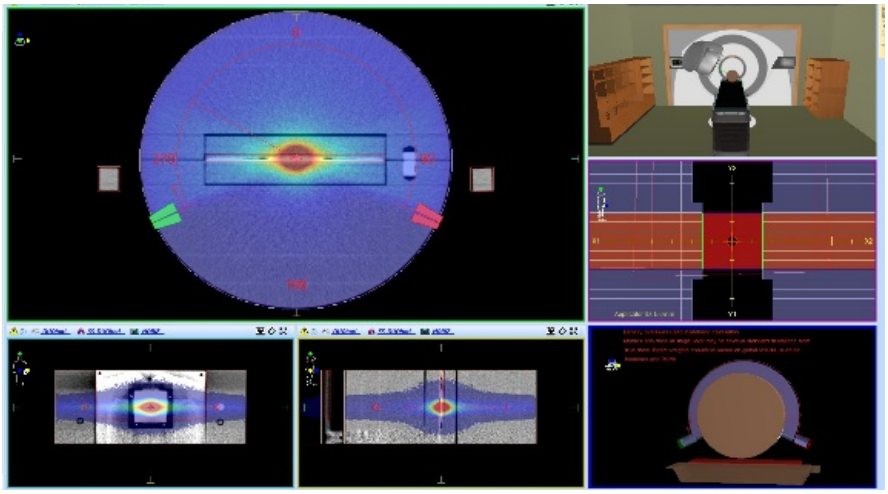

(a)

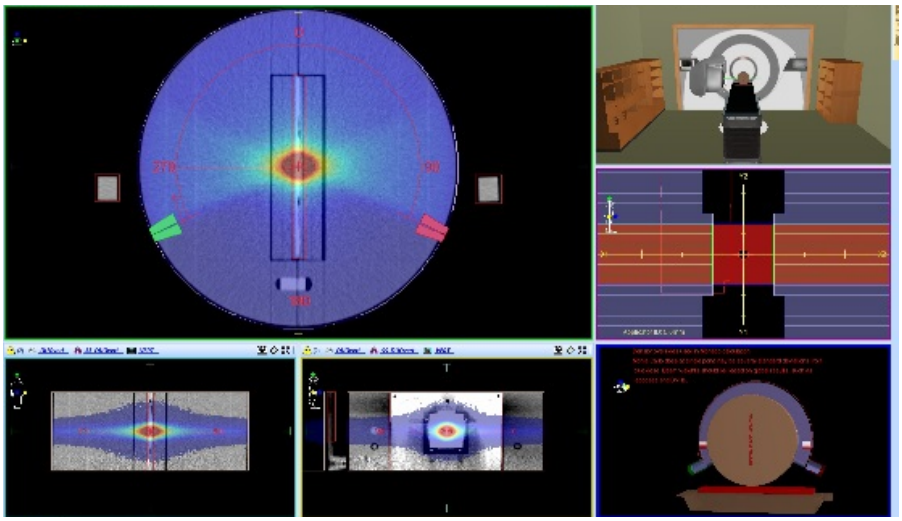

(b)

Figure 8.2: Screenshots of the Monaco planning system software, where the rotatable phantom was set with DUO detector in (a) horizontal (plan 1) and (b) vertical (plan 2) position.

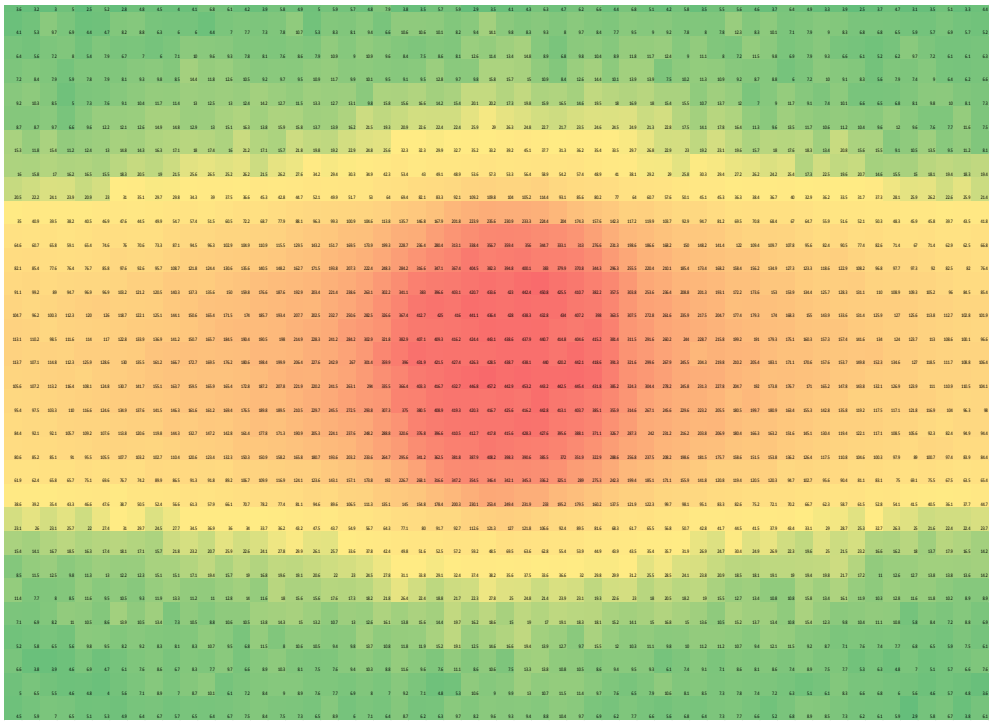

(a)

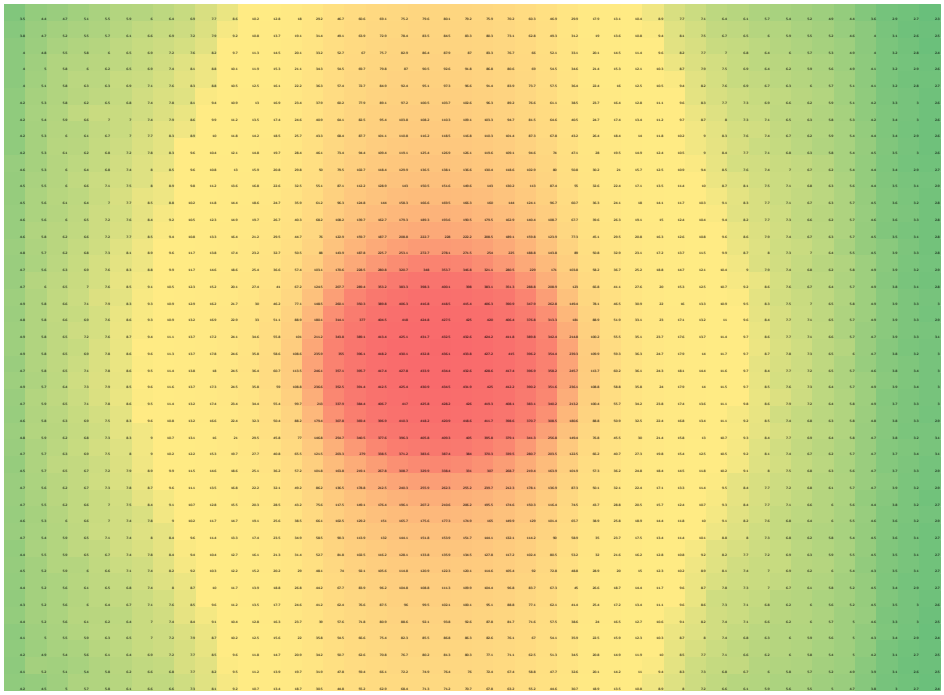

(b)

Figure 8.3: Dose map calculated by the TPS for 12.5 mm cone diameter, when DUO is positioned (a) horizontally, (b) vertically. Colour scale indicates doses in cGy.

8.2.3 EBT3 films preparation

Since EBT3 film dosimetry was a good detector to be used in the SRS dosimetry until now, its use to compare with DUO and TPS is necessary. The same procedure as in section 7.2.3.3 was followed to prepare the films. For the calibration, ten EBT3 films of 3 x 3 cm^2 were pre-scanned and irradiated for doses from 0 to 700 MU. For the treatment plans verification, 18 films of 5 x 5 cm^2 were prepared in order to be used in the same phantom holder of DUO.

The calibration films were analysed to calculate the calibration equation and the red channel was used. Then the films that were used to measure the profiles for each beam delivery in both phantom directions were analysed and calibrated by using MATLAB™ software. Finally, the resulted doses mapped were used to extract the beam profiles for each cone collimator in two directions, horizontal and vertical. Then, the profiles were interpolated to 0.2 mm.

8.2.4 Experimental setup

8.2.4.1 Calibration

To convert the counts number measured by the DUO array detector to dose in cGy, a calibration was performed. At the standard condition at d_{max} in Solid Water™ phantom, 100 MU equals to 100 cGy for SSD 100cm and a 10x10 cm^2 field size. So, DUO was irradiated by a 6 MV photon beam with a dose of 100 MU. DUO was set up above the 10 cm Solid Water™ phantom (for backscatter) and 1.5 cm depth (d_{max}) at 100 cm SSD for 10 x 10 cm^2. Therefore, the calibration factors were calculated by dividing 100 by charge response to convert it to dose in cGy, for each pixel in the array. An array of calibration factors was generated to be used in the plan delivery measurements (multiply the charge response of each pixel by its corresponding calibration factor).

8.2.4.2 Plan delivery

The cylindrical phantom was laterally centered on the couch with DUO aligned with the center of the 5 mm SRS cone, previously adjusted to the mechanical collimator center of rotation with a split-field test method as per standard departmental procedure. The inclinometer was attached to the gantry head, and it was set as 0^0 when the gantry is at 0^0. The CBCT was used to precisely position the DUO detector in the phantom to the LINAC isocenter. The first treatment delivery was according to the first TPS plan, where the phantom was set up horizontally. Then EBT3 films replaced the DUO detector with the same setup. These two steps were repeated for the phantom placed vertically.

The resulting profiles from DUO were corrected to take into account the angular dependence of the DUO detector. The angular dependence correction factors for the DUO array were calculated following the method prescribed by Stansook, Utitsarn et al. (2017) for gantry angle rotation from -180^0 to 180^0 in step of 15 degrees. Then the individual beam profiles were compared with EBT3 and TPS results. The distance to agreement between them was calculated by using MATLAB™.

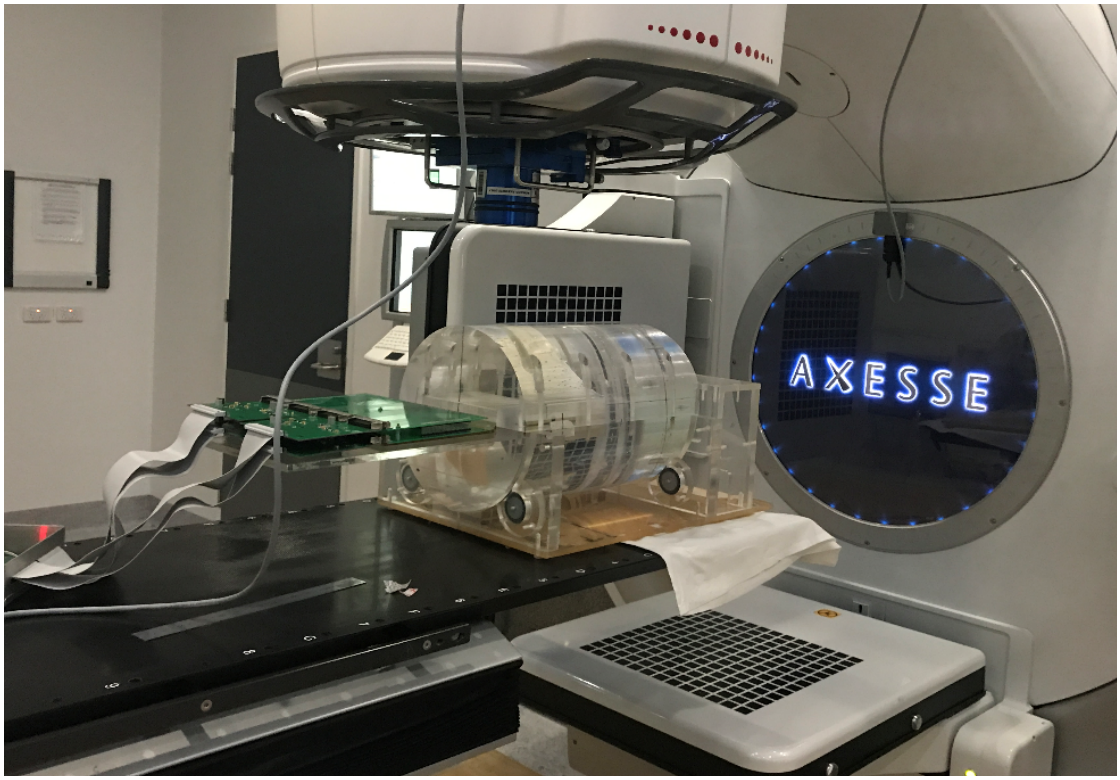

Figure 8.4: The experimental setup of the SRS plan delivery with DUO inserted at the center of the phantom. The inclinometer is attached to the LINAC gantry drum.

8.2.4.3 Data acquisition and analysis

The data acquisition was set up by selecting range 5 (corresponding to a factor of 4.8 pC) at 100 μs integration time and 120 seconds of acquisition time. The frequency was set up at 400 Hz (similar to ELEKTA LINAC setup).

The angular dependence of the DUO detector study (it has been established at CMRP outside the current research), the correction factors for the angular dependence of DUO (as shown in figure 8.5) were interpolated in step of 1 degree by using piecewise cubic hermit interpolation polynomial (PCHIP) function on MATLAB software. Then by using the real plan angles measured by the inclinometer, new correction factors were calculated for each beam delivery depending on its real gantry angle during the measurements per pixel (Appendix C). The response measured by DUO has been

corrected for the angular dependence correction factors as per pixel. Then the response was equalized and converted into dose (cGy) (the function used in MATLAB is presented in Appendix D), end with two profiles (horizontal and vertical), which are finally corrected for the charge sharing effect.

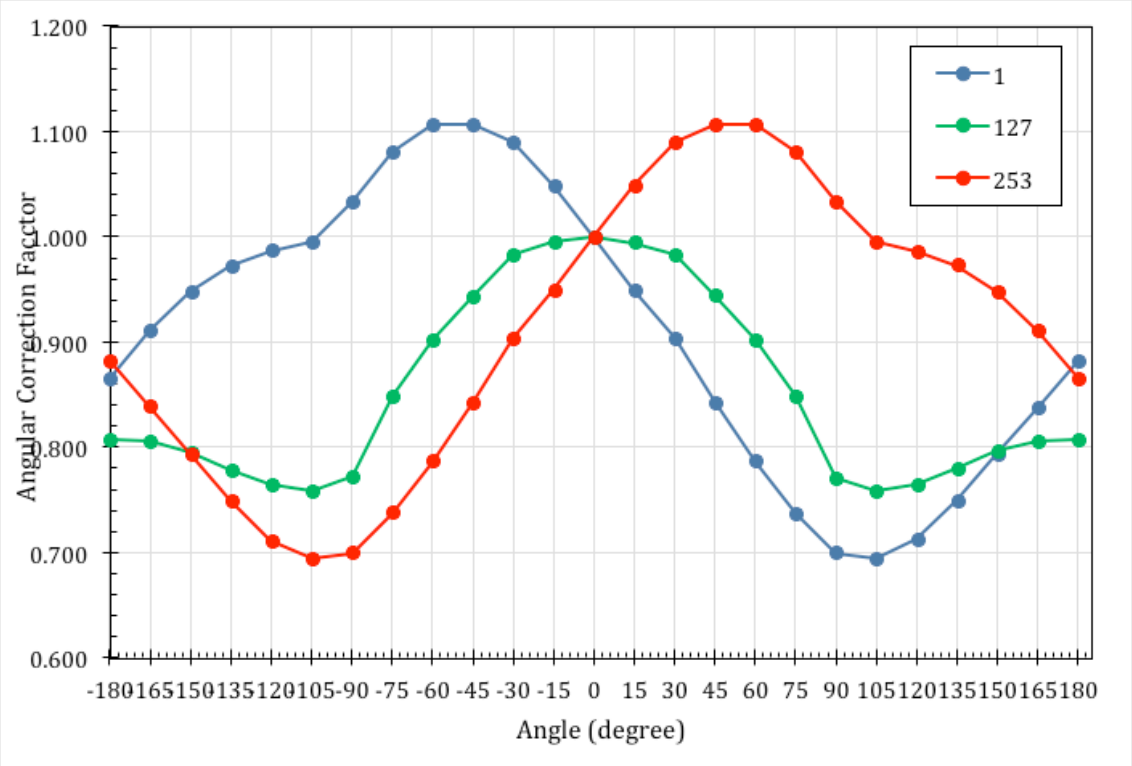

Figure 8.5: Angular correction factors of DUO detector for three pixels: first (blue), central (green) and last (red) in the horizontal linear array.

8.3 Results

8.3.1 The mechanical isocentre shift on ELEKTA LINAC

To check the mechanical isocentre shift, the beam profiles measured by DUO at angles 0^0, 90^0 and -90^0 in both phantom positions were extracted from the data measured by using a cone 5 mm in diameter. Figure 8.6 shows the horizontal and vertical beam profiles measured at different angles in the phantom position horizontally and vertically, centred at the maximum dose measured at 0^0 gantry angle in the horizontal beam (X-

profiles) when the phantom positioned horizontally. The mechanical isocentre shift is calculated as the shift in the maximum dose in each beam profile. Table (8.1) shows the mechanical isocentre shift of ELEKTA LINAC as measured by DUO detector in this experimental setup.

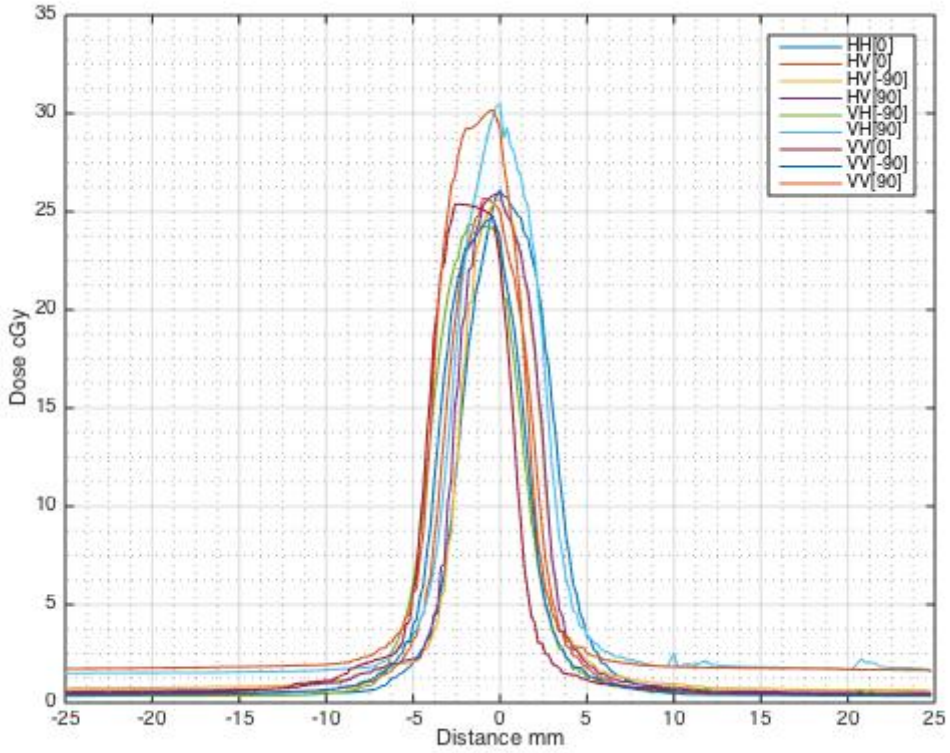

Figure 8.6: Beam profiles for 5 mm cone collimator at gantry angles 90^0 and -90^0, (a): horizontal (X-profile) and (b): Vertical (Y-profile). H is Horizontal and V is vertical, where the first letter refers to the phantom position and the second letter refers to the profile axes. The number in the bracket refers to the gantry angle. Example HH [0] refers to horizontal phantom, horizontal profile at gantry angle 0^0.

Table 8.1: The mechanical isocentre shift of LINAC as a function of gantry rotation. The difference is relative to the gantry 0^0 at the horizontal phantom position in the horizontal axis.

Mechanical isocentre offset				
Phantom	Horizontal		Vertical	
Axis / Gantry	Horizontal	Vertical	Horizontal	Vertical
Degree	mm	mm	mm	mm
0	0	-1		-0.2
-90		0	-0.8	-1
90		-0.2	0	-1

8.3.2 Cone movements when interchange the cones

DUO has been set up by using the smallest cone diameter (5 mm) and then larger cone collimators (7.5, 10, 12.5, 15, 20 & 30 mm) were inserted in the stereotactic collimator mount without changing the phantom and DUO setup. To check the cone centre movement with interchanging the cone collimators, beam profiles measured by DUO when the phantom was positioned horizontally, were centred at the maximum response for 5 mm cone diameter and compared as shown in figure 8.7 (a & b) for horizontal and vertical profiles, respectively. The beam profiles were normalized to distance 0 mm at to 50% dose measured by 5 mm cone collimator. The FWHM were calculated for each beam profile and the central of the beam is calculated as the mid-point from the FWHM of each profile (cone collimator). The cones offset shifts were calculated by finding the difference in the distance of the central beam between the 5 mm cone and the other

cones. The results are tabulated as shown in tables 8.1 and 8.2 for horizontal and vertical profiles, respectively.

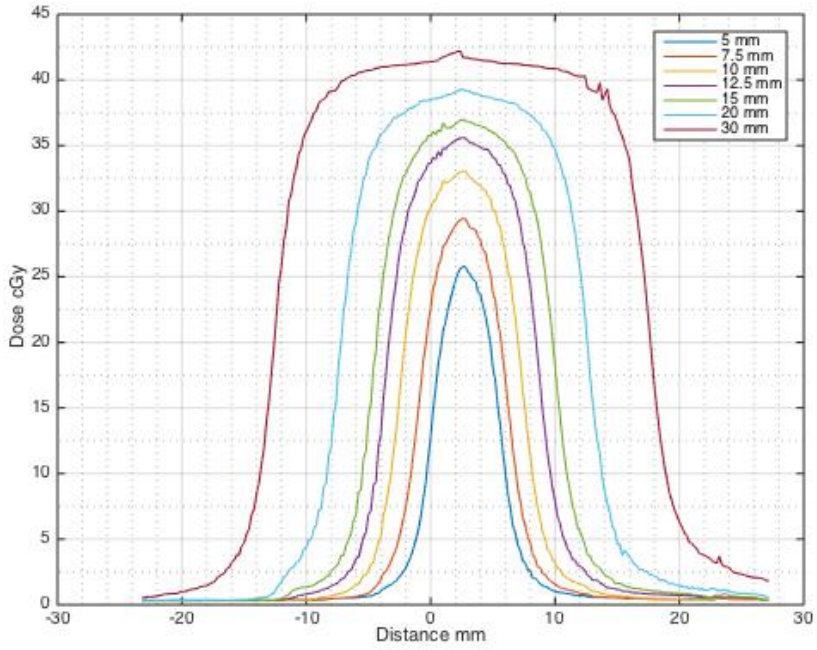

(a)

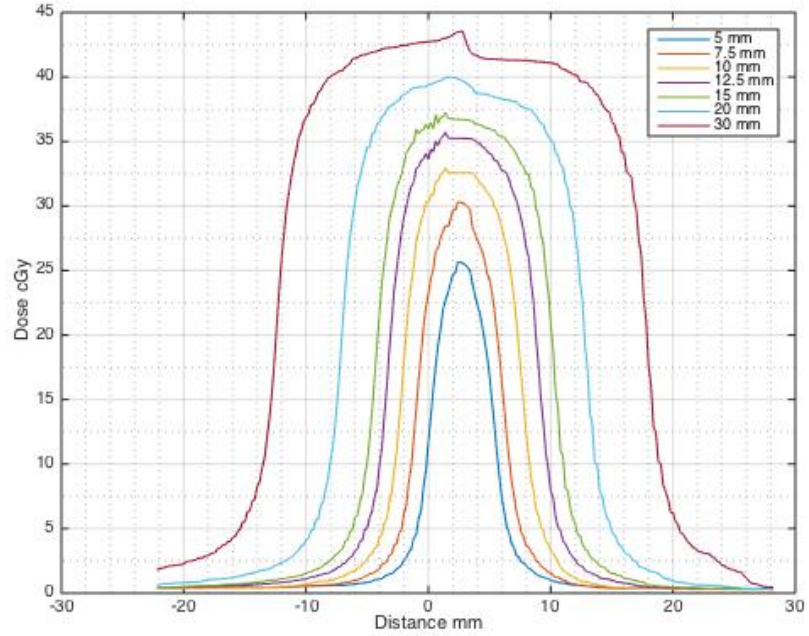

(b)

Figure 8.7: The beam profiles measured by DUO detector for cone diameters (5, 7.5 10, 12.5, 15, 20 & 30 mm) and centred at the maximum response for 5 mm cone collimator, (a) horizontal and (b) and vertical.

Table 8.2: The cone centre offset when the phantom positioned horizontally in both the horizontal and vertical profiles for different cone sizes.

Cone centre offset		
axis / Cone	Horizontal	Vertical
mm	mm	mm
5	0	0
7.5	0.4	0.2
10	0.6	-0.2
12.5	0.4	-0.4
15	0	-0.2
20	0.2	-0.2
30	0.4	0.2

8.3.3 Beam profiles

Finally, the beam profiles measured by using DUO were compared with TPS and EBT3 films. The percentage dose differences at each position were calculated for each beam profile in comparison to TPS. Figures 8.8 and 8.9 shows the horizontal and vertical profiles at the horizontal position of the phantom, while figures 8.10 and 8.11 are for the vertical position of the phantom. The gamma index has been calculated as a function of dose limit within ±3% for two sets of dose profiles, horizontal phantom horizontal profiles and vertical phantom horizontal profile as shown in tables 8.3 and 8.4, respectively.

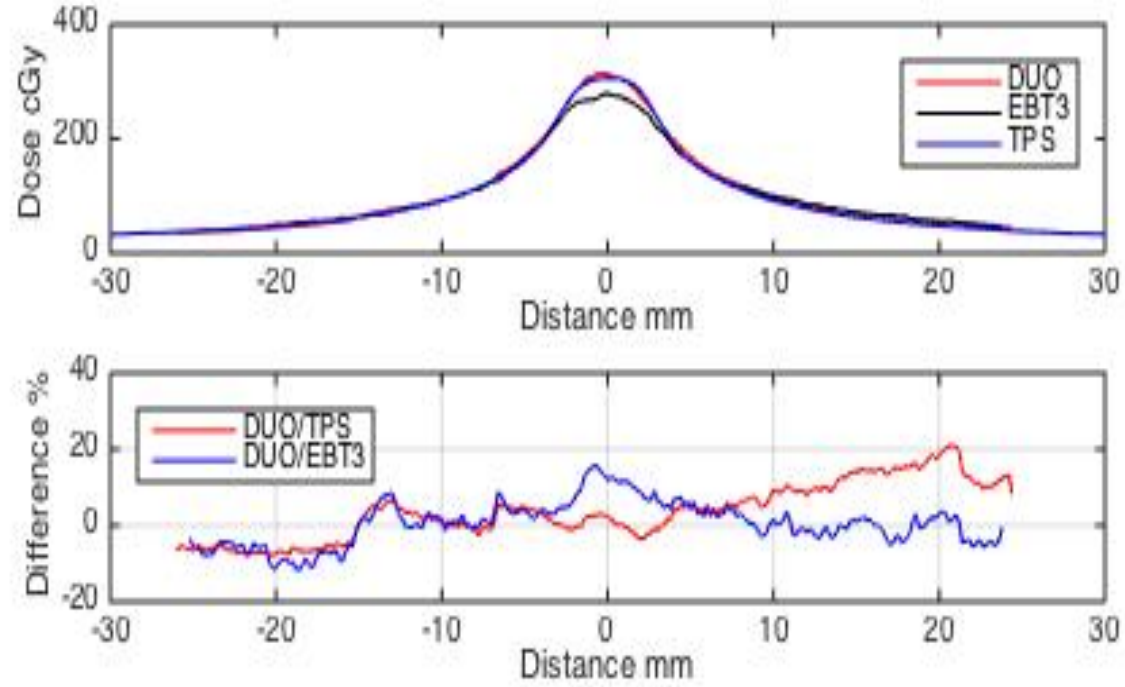
Dose cGy
400
200
0
-30
-20
-10
0
10
20
30
Distance mm
DUO
EBT3
TPS
Difference %
40
20
0
-20
DUO/TPS
DUO/EBT3
Distance mm

(a)

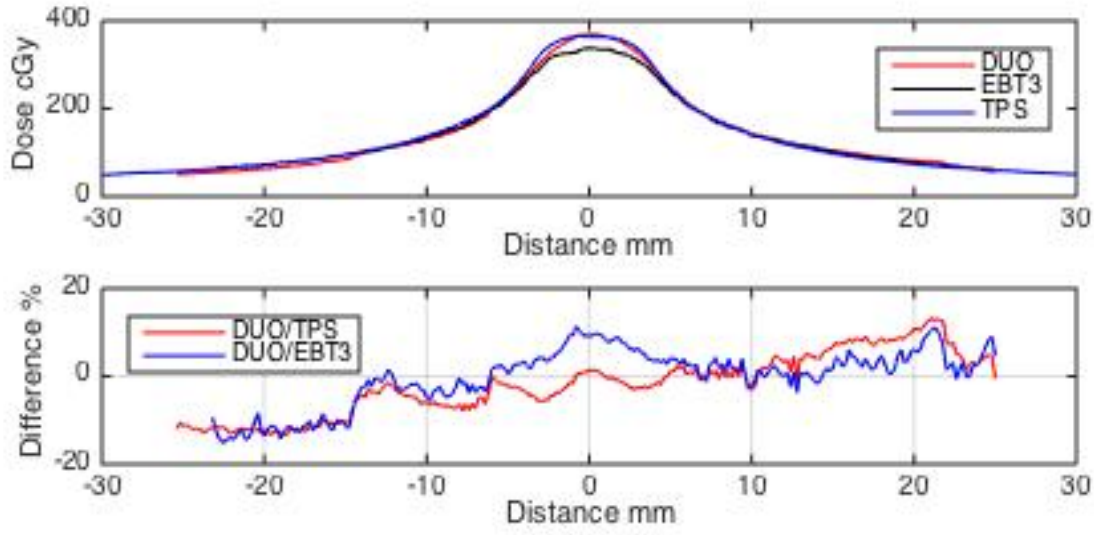
Dose cGy
400
200
0
-30
-20
-10
0
10
20
30
Distance mm
DUO
EBT3
TPS
Difference %
20
0
-20
DUO/TPS
DUO/EBT3
Distance mm

(b)

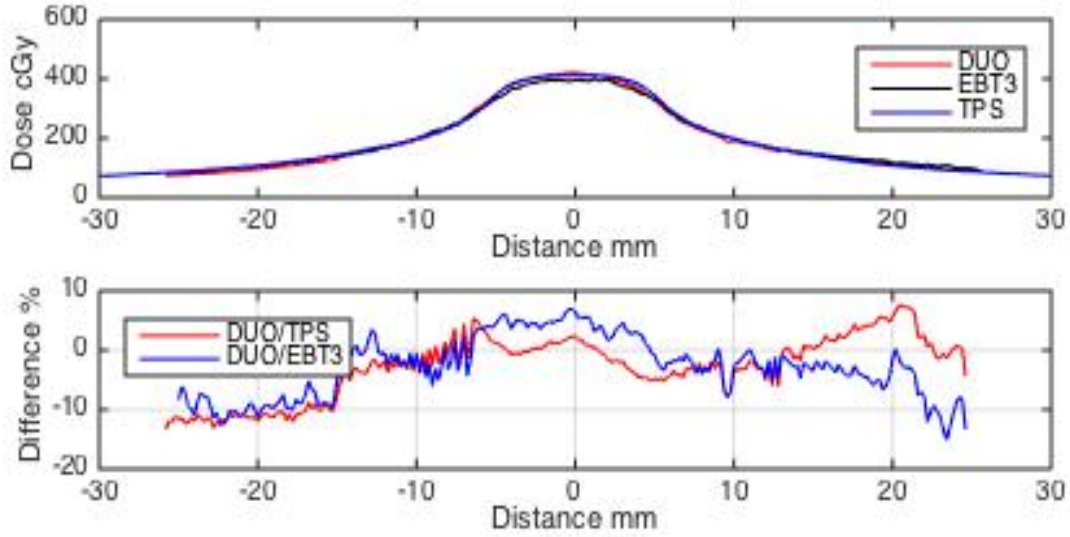
Dose cGy
600
400
200
0
-30
-20
-10
0
10
20
30
Distance mm
DUO
EBT3
TPS
Difference %
10
0
-10
-20
DUO/TPS
DUO/EBT3

(c)

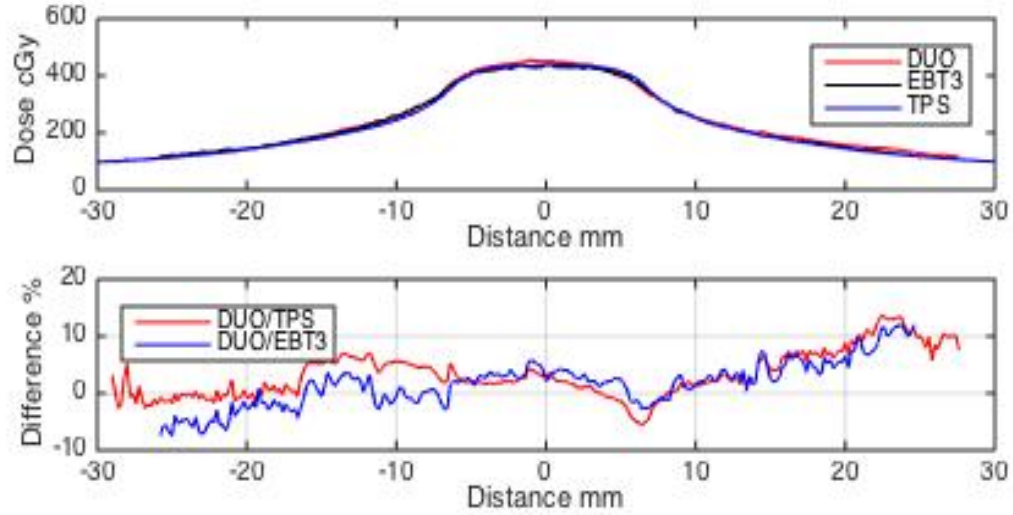
Dose cGy
600
400
200
0
-30
-20
-10
0
10
20
30
Distance mm
DUO
EBT3
TPS
Difference %
20
10
0
-10
DUO/TPS
DUO/EBT3

(d)

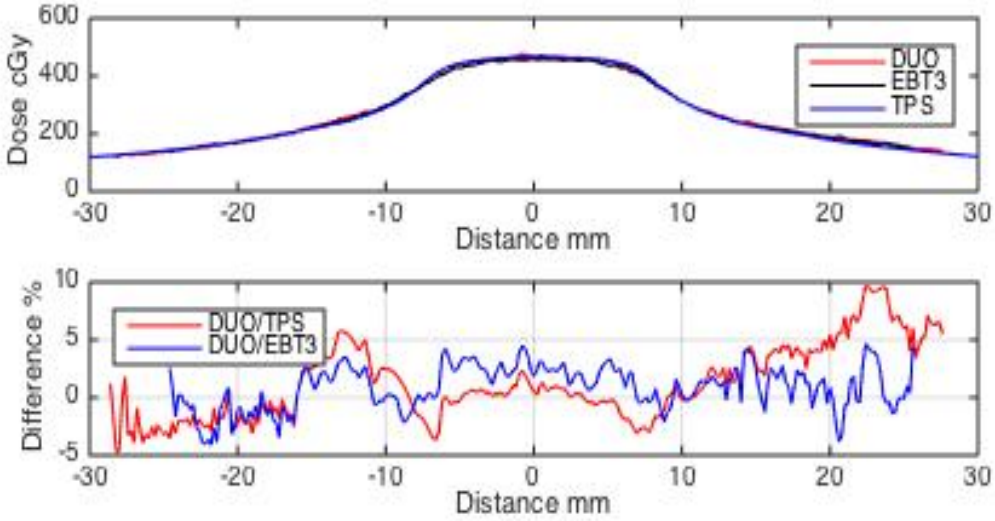
Dose cGy
600
400
200
0
-30
-20
-10
0
10
20
30
Distance mm
DUO
EBT3
TPS
Difference %
10
5
0
-5
DUO/TPS
DUO/EBT3
Distance mm

(e)

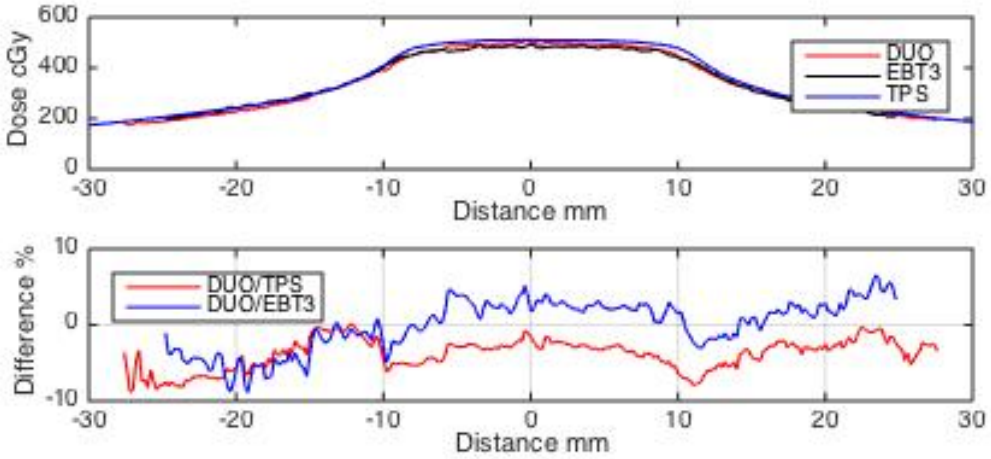
Dose cGy
600
400
200
0
-30
-20
-10
0
10
20
30
Distance mm
DUO
EBT3
TPS
Difference %
10
0
-10
DUO/TPS
DUO/EBT3
Distance mm

(f)

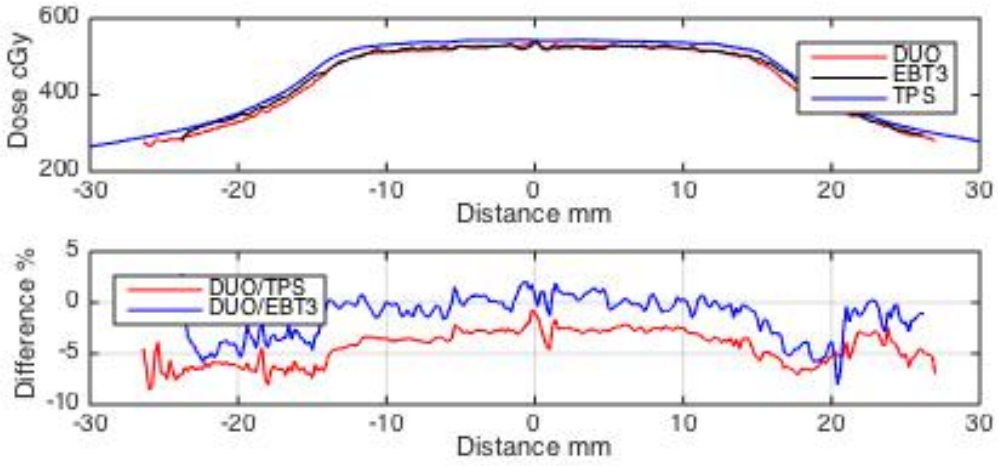

(g)

Figure 8.8: The horizontal beam profiles at phantom position horizontally for cone diameters: (a) 5, (b) 7.5, (c) 10, (d) 12.5, (e) 15, (f) 20 and (g) 30 mm.

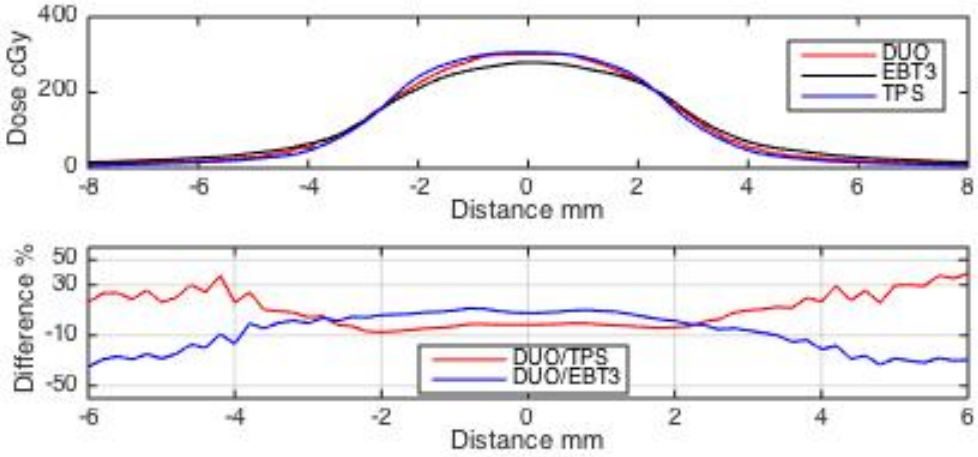

(a)

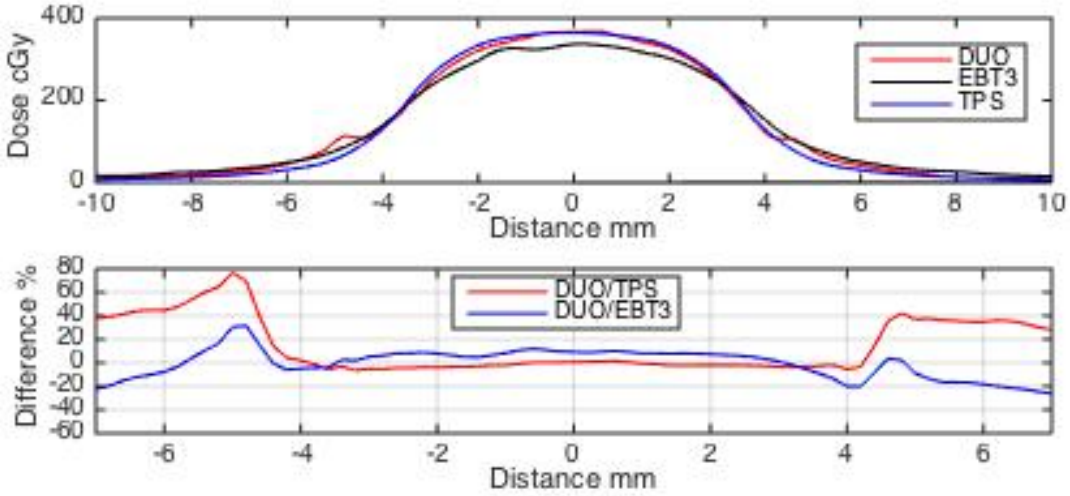
Dose cGy
400
200
0
-10
-8
-6
-4
-2
0
2
4
6
8
10
Distance mm
DUO
EBT3
TPS
Difference %
80
60
40
20
0
-20
-40
-60
-6
-4
-2
0
2
4
6
Distance mm
DUO/TPS
DUO/EBT3

(b)

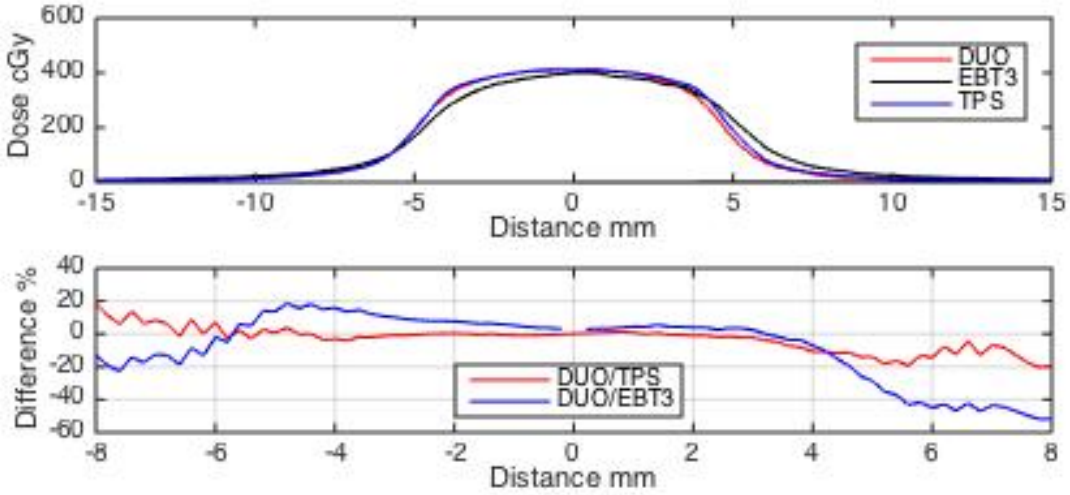
Dose cGy
600
400
200
0
-15
-10
-5
0
5
10
15
Distance mm
DUO
EBT3
TPS
Difference %
40
20
0
-20
-40
-60
-8
-6
-4
-2
0
2
4
6
8
Distance mm
DUO/TPS
DUO/EBT3

(c)

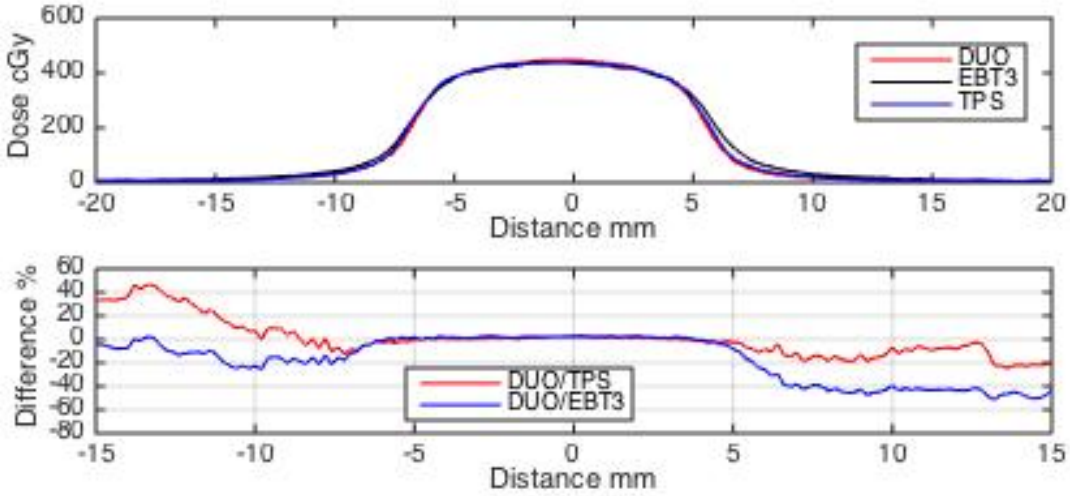
Dose cGy
600
400
200
0
-20
-15
-10
-5
0
5
10
15
20
Distance mm
DUO
EBT3
TPS
Difference %
60
40
20
0
-20
-40
-60
-80
-15
-10
-5
0
5
10
15
Distance mm
DUO/TPS
DUO/EBT3

(d)

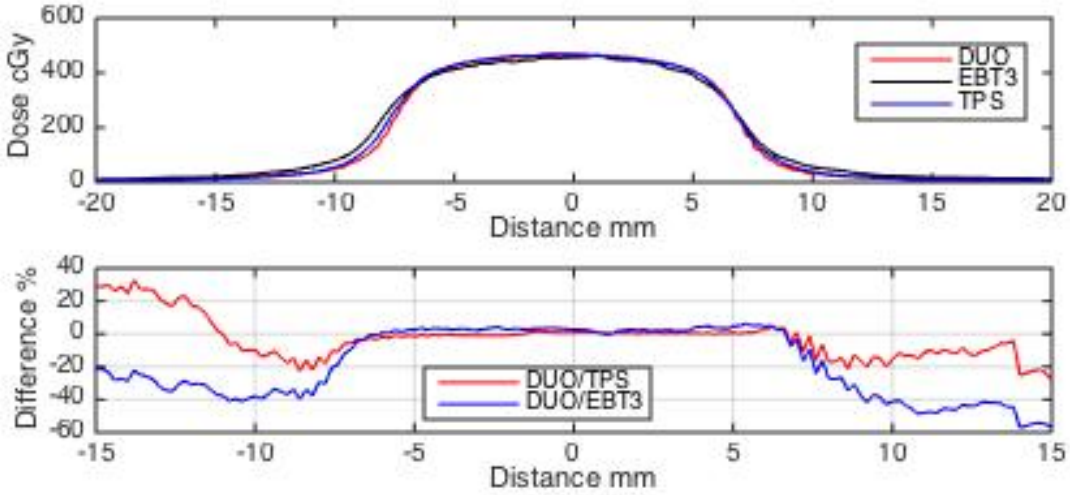
Dose cGy
600
400
200
0
-20
-15
-10
-5
0
5
10
15
20
Distance mm
DUO
EBT3
TPS
Difference %
40
20
0
-20
-40
-60
-15
-10
-5
0
5
10
15
Distance mm
DUO/TPS
DUO/EBT3

(e)

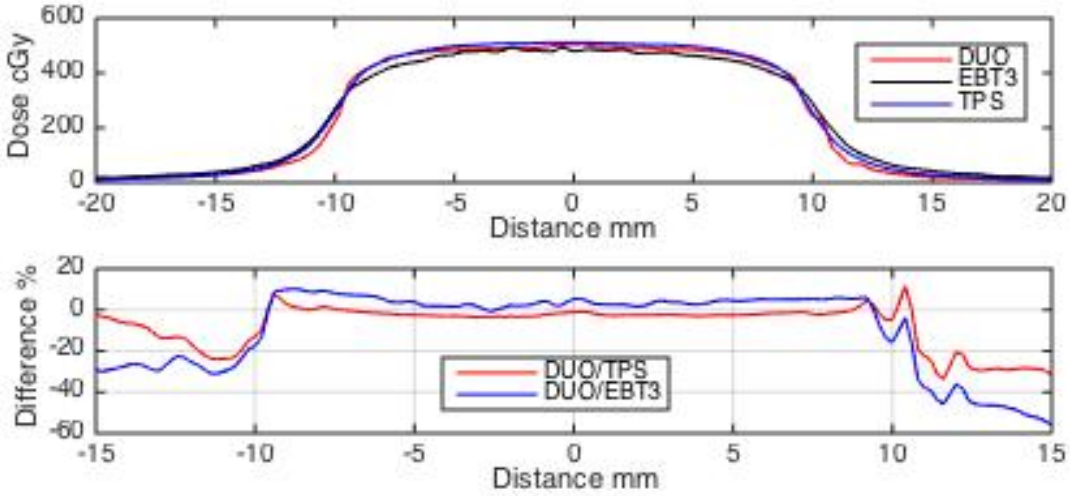

(f)

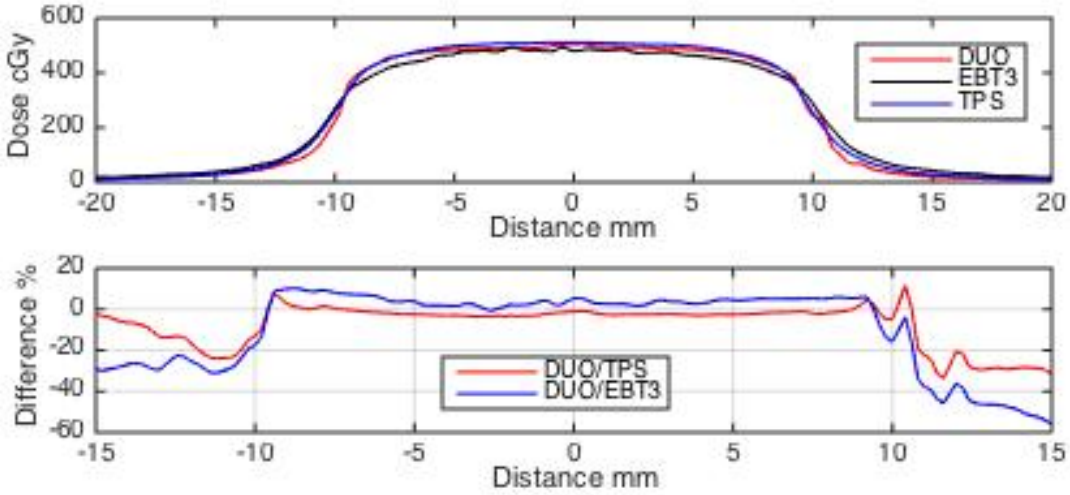

(g)

Figure 8.9: The Vertical beam profiles at phantom position horizontally for cone diameters: (a) 5, (b) 7.5, (c) 10, (d) 12.5, (e) 15, (f) 20 and (g) 30 mm.

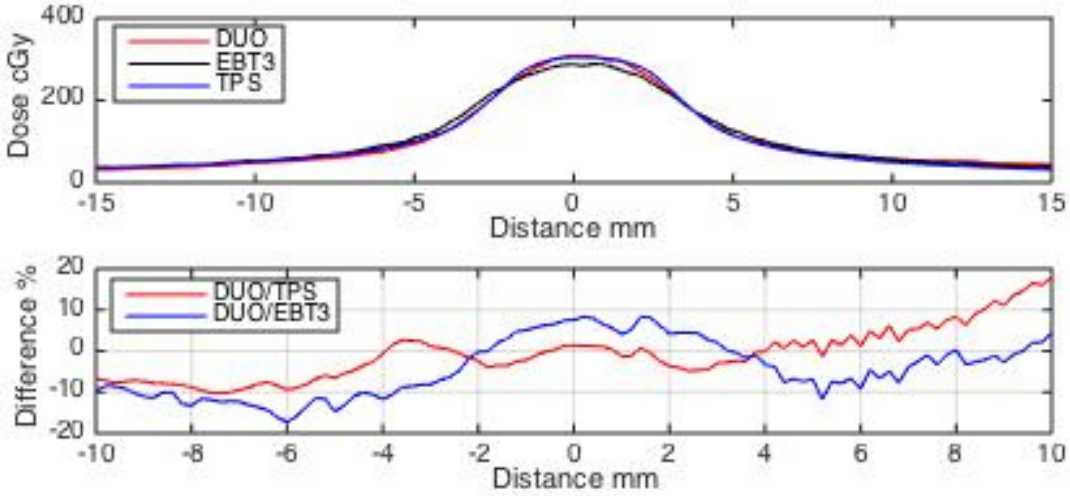
Dose cGy
400
200
0
DUO
EBT3
TPS
-15
-10
-5
0
5
10
15
Distance mm
Difference %
20
10
0
-10
-20
DUO/TPS
DUO/EBT3
-10
-8
-6
-4
-2
0
2
4
6
8
10
Distance mm

(a)

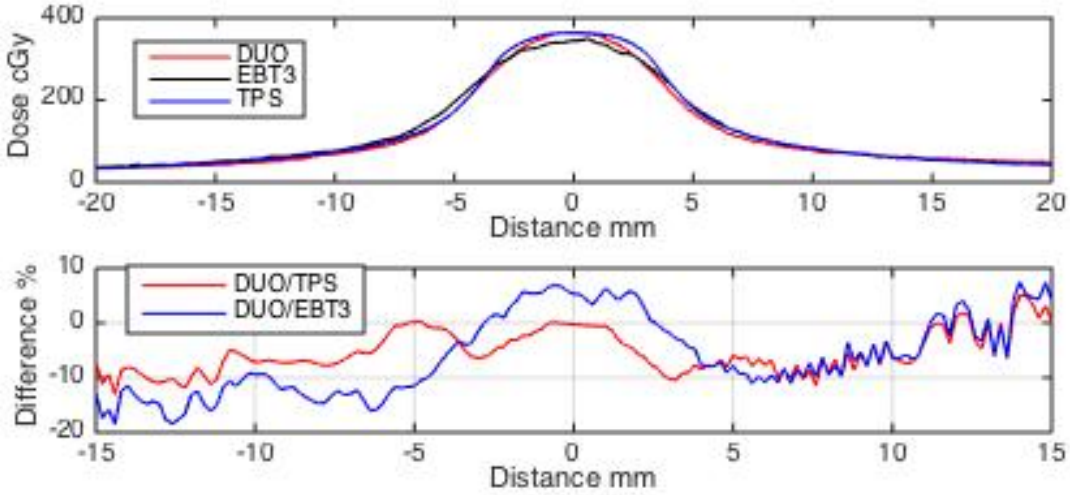
Dose cGy
400
200
0
DUO
EBT3
TPS
-20
-15
-10
-5
0
5
10
15
20
Distance mm
Difference %
10
0
-10
-20
DUO/TPS
DUO/EBT3
-15
-10
-5
0
5
10
15
Distance mm

(b)

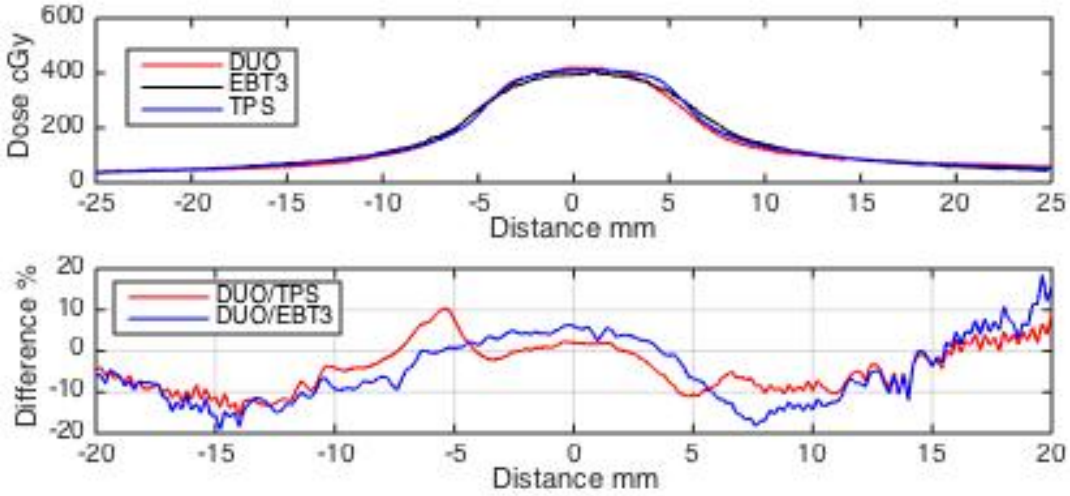
Dose cGy
DUO
EBT3
TPS
Distance mm
Difference %
DUO/TPS
DUO/EBT3
Distance mm

(c)

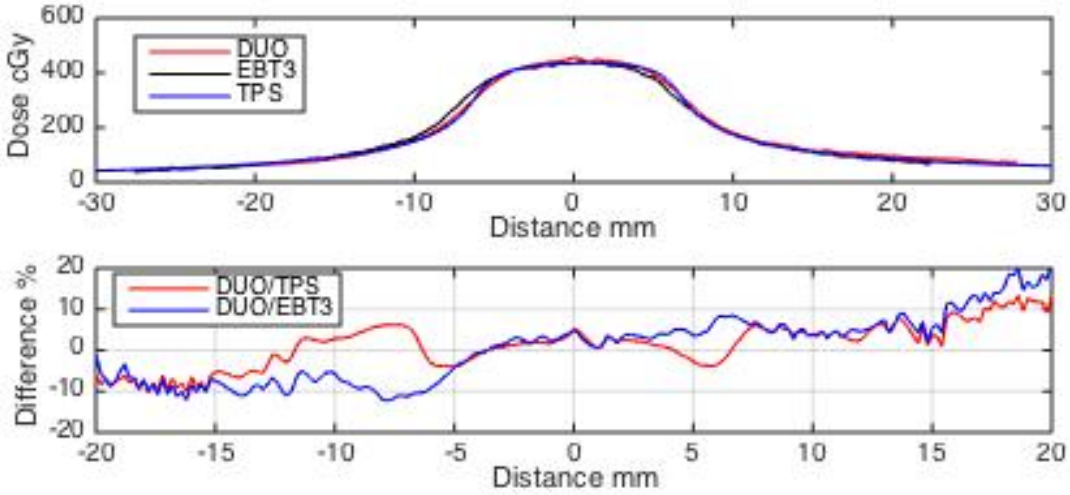
Dose cGy
DUO
EBT3
TPS
Distance mm
Difference %
DUO/TPS
DUO/EBT3
Distance mm

(d)

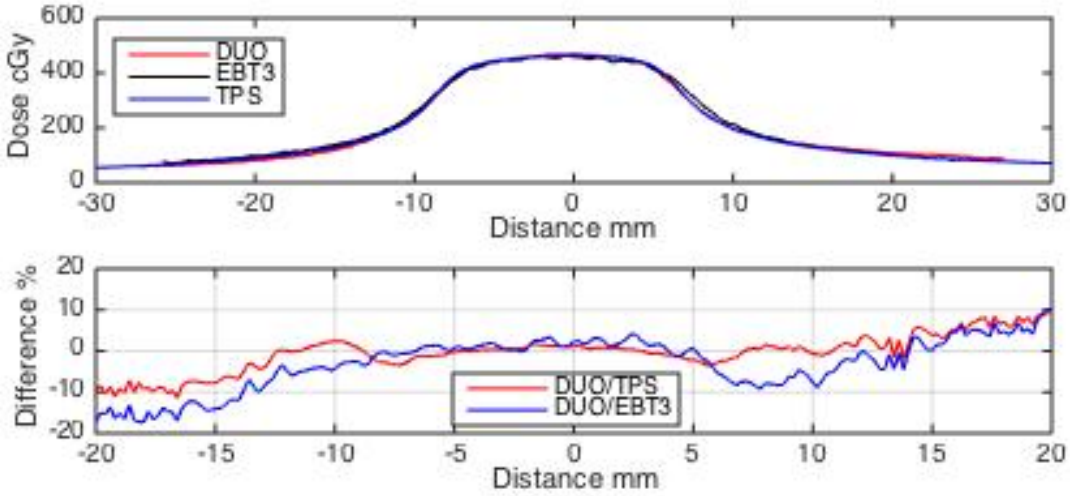
Dose cGy
600
400
200
0
DUO
EBT3
TPS
-30
-20
-10
0
10
20
30
Distance mm
Difference %
20
10
0
-10
-20
DUO/TPS
DUO/EBT3
-20
-15
-10
-5
0
5
10
15
20
Distance mm

(e)

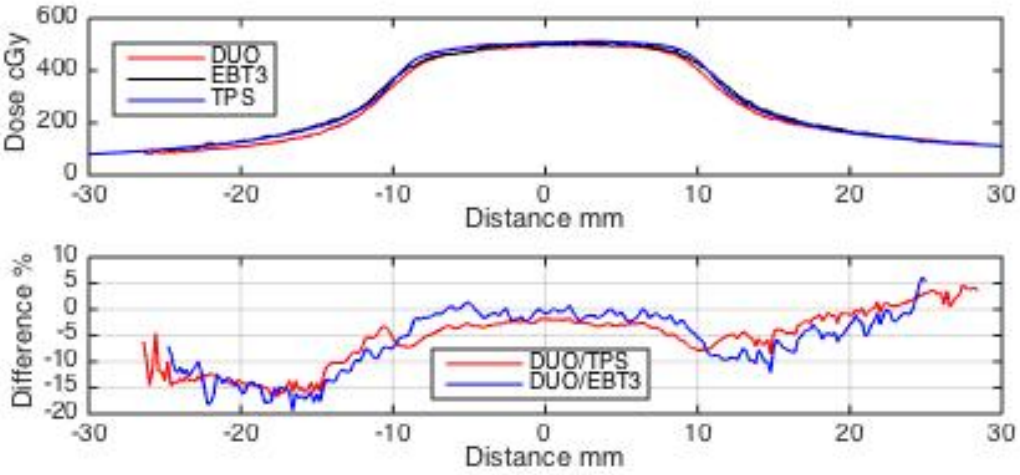
Dose cGy
600
400
200
0
DUO
EBT3
TPS
-30
-20
-10
0
10
20
30
Distance mm
Difference %
10
5
0
-5
-10
-15
-20
DUO/TPS
DUO/EBT3
-30
-20
-10
0
10
20
30
Distance mm

(f)

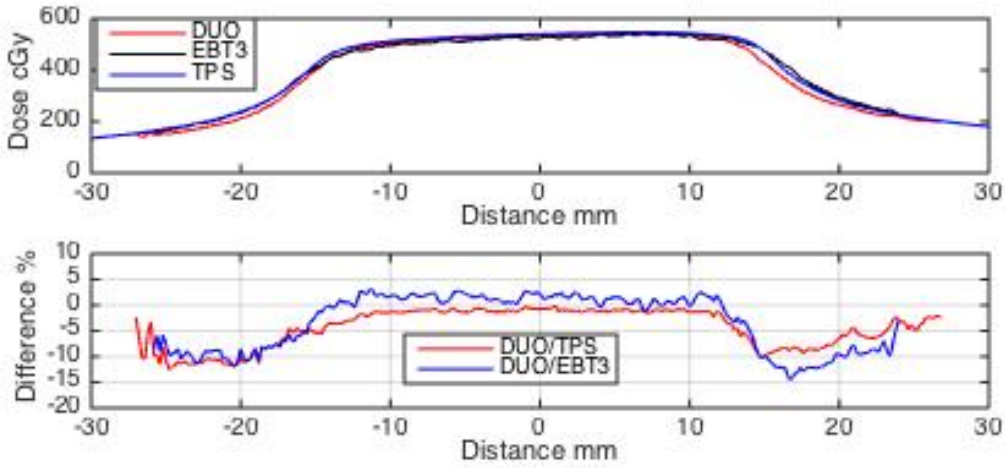

(g)

Figure 8.10: The horizontal beam profiles at phantom position vertically for cone diameters: (a) 5, (b) 7.5, (c) 10, (d) 12.5, (e) 15, (f) 20 and (g) 30 mm.

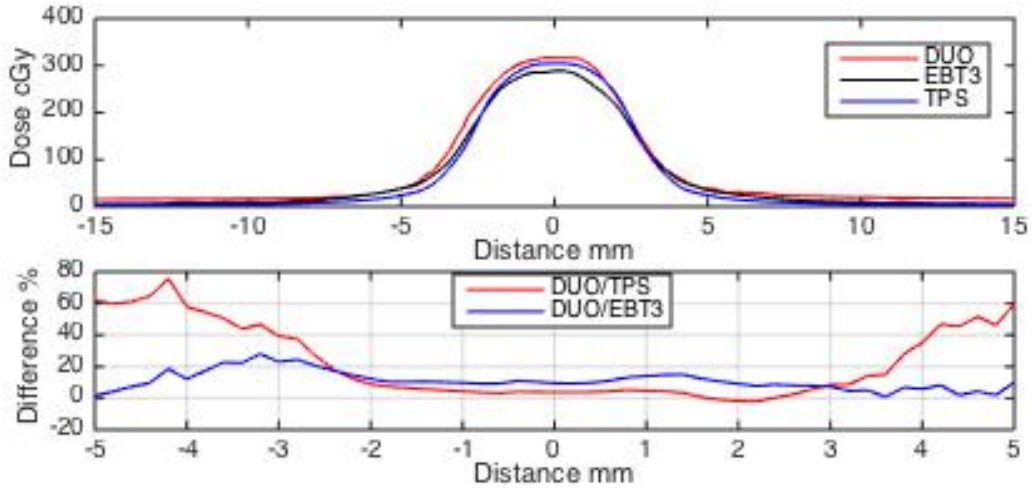

(a)

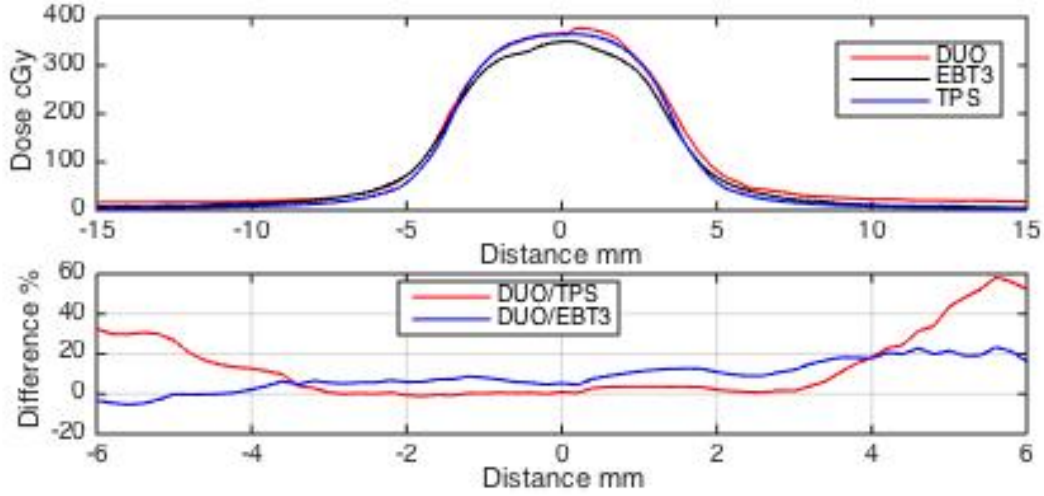
Dose cGy
Distance mm
DUO
EBT3
TPS
Difference %
DUO/TPS
DUO/EBT3
Distance mm

(b)

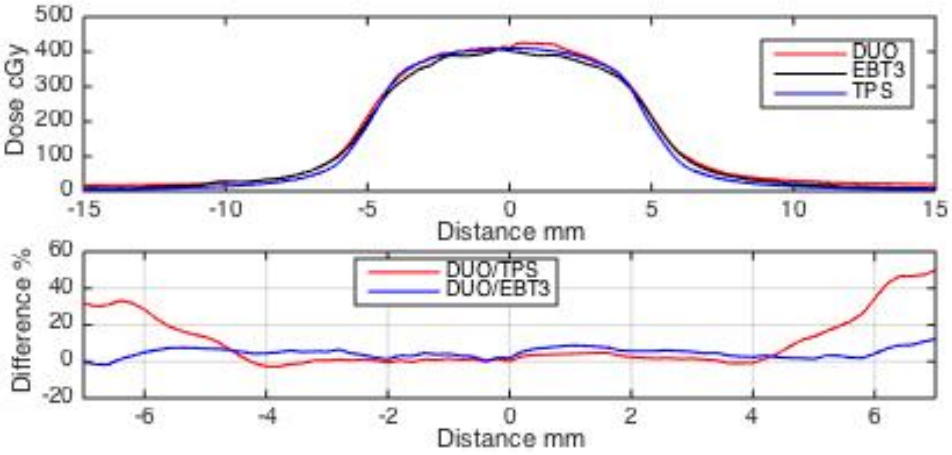
Dose cGy
Distance mm
DUO
EBT3
TPS
Difference %
DUO/TPS
DUO/EBT3
Distance mm

(c)

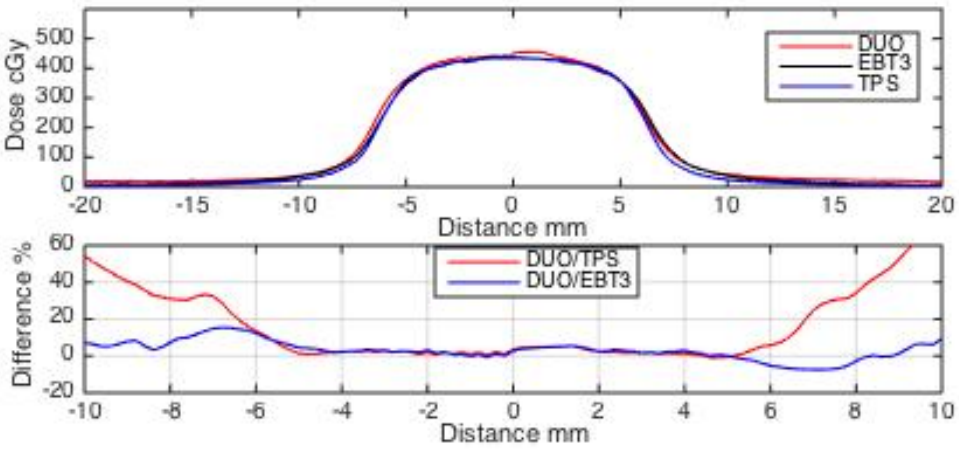
Dose cGy
Distance mm
DUO
EBT3
TPS
Difference %
DUO/TPS
DUO/EBT3
Distance mm

(d)

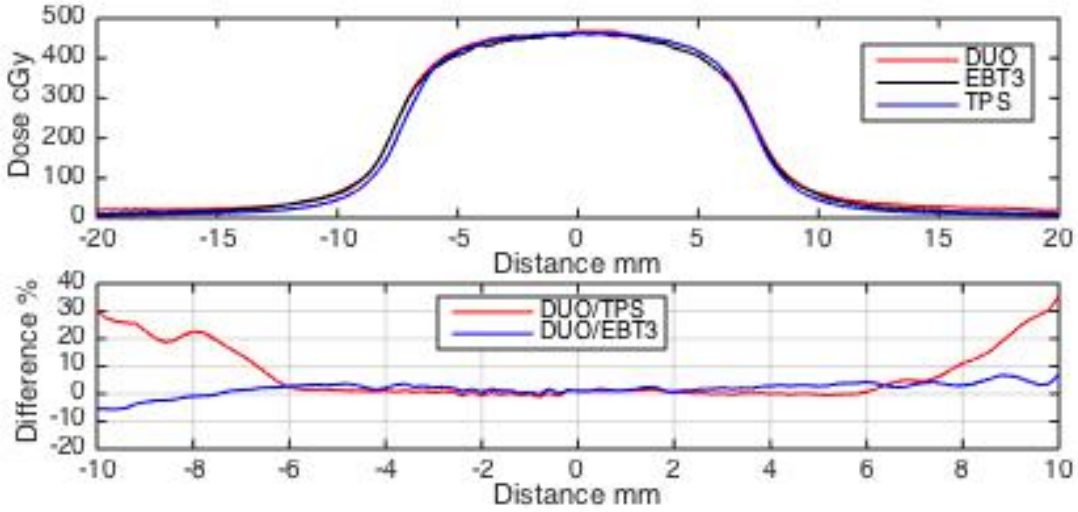
Dose cGy
Distance mm
DUO
EBT3
TPS
Difference %
DUO/TPS
DUO/EBT3
Distance mm

(e)

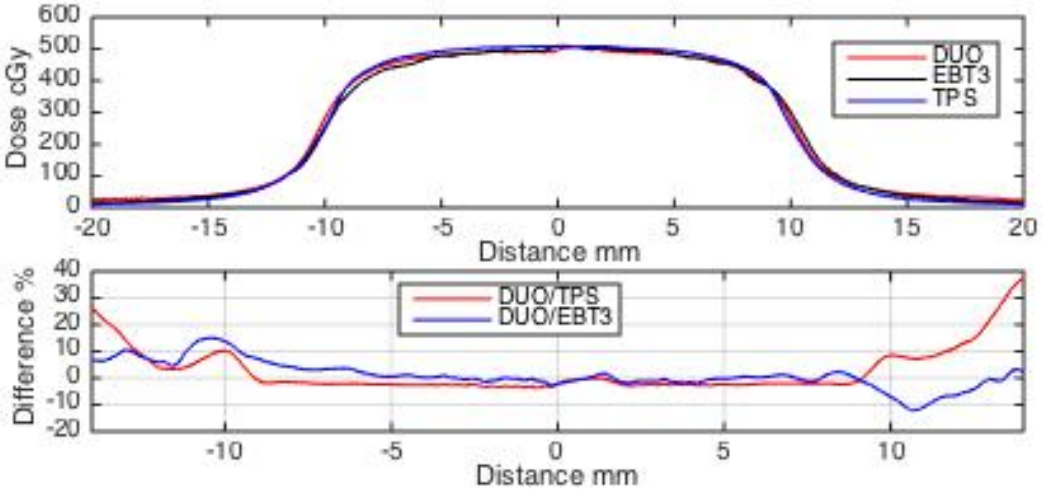
Dose cGy
Distance mm
DUO
EBT3
TPS
Difference %
DUO/TPS
DUO/EBT3
Distance mm

(f)

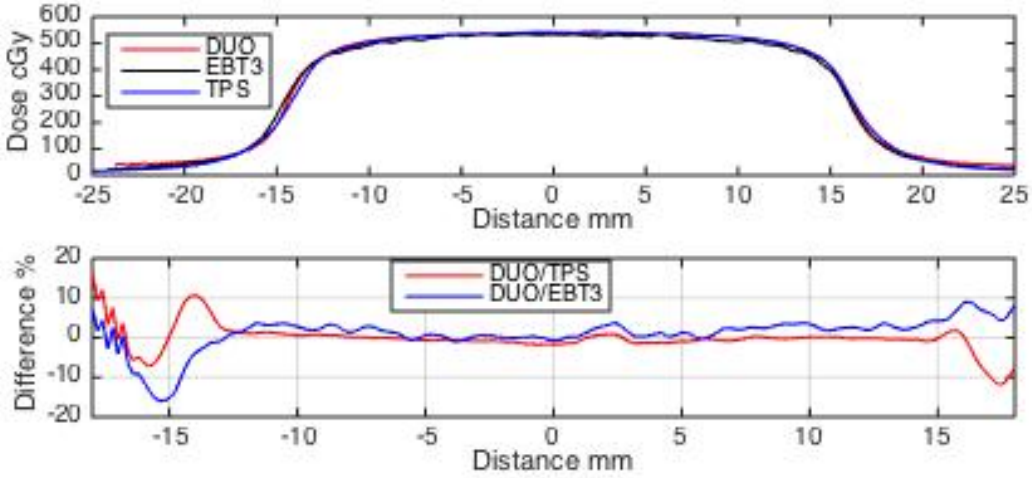

(g)

Figure 8.11: The Vertical beam profiles at phantom position vertically for cone diameters: (a) 5, (b) 7.5, (c) 10, (d) 12.5, (e) 15, (f) 20 and (g) 30 mm.

Table 8.3: Gamma calculation for (3%, 0 mm) in the horizontal dose profiles when the phantom is positioned horizontally.

Gamma	3% dose difference	
cone	DUO/EBT	DUO/TPS
5	83	95
7.5	90	96
10	98	98
12.5	99	99
15	100	99
20	100	100
30	100	100

Table 8.4: Gamma calculation for (3% / 0 mm) in the horizontal dose profiles when the phantom is positioned vertically.

Gamma	3% dose difference	
Cone	DUO/EBT	DUO/TPS
5	82	79
7.5	97	77
10	97	81
12.5	95	89
15	100	95
20	100	96
30	100	100

8.4 Discussion

One source of uncertainty in the SRS/SRT treatment system is the exact position of the target relative to the LINAC mechanical isocenter during the beam delivery (Treuer, Hoevels et al. 2000). Ideally, the mechanical isocenter is defined as the intersection between the gantry, collimator and couch rotation axis. However, the isocenter moves with the gantry, collimator or couch rotation due to the mechanical limitation of the LINAC. Therefore, it is very important to check the mechanical shift of the LINAC. In this chapter, the data gathered by using the DUO detector for cone 5 mm at horizontal and vertical phantom positions were used to study the mechanical isocenter shift. DUO shows that there is about -1 mm shift between the horizontal and vertical profiles at gantry 0^0 measured at the horizontal phantom position, while there is a very small shift within -0.2 mm at gantry angles 90^0 and -90^0. When the phantom rotated in a vertical

position, the horizontal dose profile shifted up to -0.8 mm at gantry -90^0 and there was a negligible shift at gantry angle 90^0. The vertical beam profiles were shifted up to -1 mm at gantry angles 90^0 and -90^0, but -0.2 mm for gantry angle 0^0. This isocenter shift of LINAC has reached the tolerance limit. These isocentric shifts are within the tolerance for the QA equipment, where the tolerance is ±1 mm for complete gantry rotation (Halvorsen, Cirino et al. 2017).

Also, the differences in the cones centering were instantaneously noticeable with DUO when interchanging the cones using the smallest 5 mm cone as reference for the setup. In order to evaluate the shifts due to differences in cones centering, the beam profiles were measured when the phantom was positioned horizontally by using DUO and compared by using the mid-point in the FWHM of the beam profiles. The results showed that there are shifts for other cones within ±0.4 mm except for cone 10 mm where the shift was up to 0.6 mm at the horizontal profile. By gathering the mechanical shift and the cone offset, the isocenter beam shifted up to 0.9 mm for all cone sizes except cone 10 mm where the shift reached the limited tolerance of 1 mm. Therefore, it is very important to check the isocenter shift as a result of cone interchanging and it is better to isocenter each cone separately. Actually, some patients are treated by using cone in cone techniques (more than one cone size), hence DUO could ultimately help pre-treatment QA by centering cones in an average position where Winston Lutz tests should still be passed.

The beam profiles measured by using DUO and EBT3 have been compared with the calculated profiles by using treatment planning system (TPS) in two phantom positions, horizontal and vertical. For the smaller cone sizes (5 & 7.5 mm diameter), there are underestimates in the dose at the centre of the beam profiles measured by using EBT3 in comparison with DUO and TPS, for all four directions (as shown in the figures 8.8-

8.11). The underestimated dose measured by EBT3 films was high up to 12%, 7%, and 3% for the profiles of 5, 7.5 and 10 mm cone diameter respectively. For the larger cone sizes, EBT3 beam profiles were matched TPS and DUO within 2% at the isocenter dose area. The dose reduction could be due to the air gap upstream EBT3. The effect of the air gap above the detector was tested and showed its effect on the small field sizes, where it reached to 11.5% / mm for 6 mm square field size by using OSLD detector based (Charles, Crowe et al. 2013, Shukaili, Petasecca et al. 2017). The holder creates around 0.7 mm air gap above EBT3 films. This lower density of air causes a lower response at the centre and a wider penumbra on the small field sizes dosimetry (Scott, Kumar et al. 2012). DUO agrees with TPS at the in-field region in all four directions of dose profiles within ±5%. However, there is a large divergence at the out-field area (dose profile tail), especially when the dose is very low (as in the horizontal phantom vertical profiles, vertical phantom, vertical profiles) where the differences reached high to ±80% for small field sizes. These differences could be due to the dose rate dependence of the DUO detector at very low doses. On the other hand, DUO shows better agreement with EBT3 than TPS at the out-field dose profiles. This could be due to the spatial resolution of detectors (DUO and EBT3) compared to TPS where the resolution of calculation is 1 mm. DUO shows a very good agreement with TPS in terms of gamma index (3% dose limit at 0 mm) from 95% to 100% for all cone sizes when position the phantom horizontally and use the horizontal dose profiles (normal incidence of the beam).

8.5 Conclusion

DUO has been tested for real plan delivery by using different SRS/SRT ELEKTA cone collimators. It was compared with TPS, which is based on Monte Carlo algorithm, and

with EBT3 films. DUO shows an isocentric ELEKTA LINAC shift within ±1 mm between 0^0 and 90^0 gantry angles in both directions. This amount of shift is within the tolerance limit (±1 mm). The DUO detector is also used to check the movement of the cones when interchanging the cone as a function of the 5 mm cone collimator. The centre shift of all cone sizes at the four beam profile directions shows a shift within ±0.4 mm, except the 10 mm cone which results in 0.6 mm shift. Therefore, it is recommended to center each cone separately, in order to reduce the isocenter shift of the dose profiles.

Finally, DUO shows a good agreement with TPS in terms of beam profiles (cGy), except at the very low doses. This agreement results in good gamma index above 95% for ±3% dose limit. However, in SRS/SRT treatments the dose profiles area at the very low doses are not very important as there is a high fall off dose at the penumbra region. EBT3 films shows lower responses for the smaller cone sizes (5, 7.5 and 10 mm diameters) due to the air gap above it in the DUO holder. However, EBT3 shows good agreement for the larger cone sizes with TPS and DUO detectors.

Chapter 9: Radiation response and characterisation of OCTA silicon detector array on Stereotactic Radiosurgery

9.1 Introduction

This chapter introduces a new generation of monolithic silicon detector arrays called, OCTA. This detector has been designed by CMRP at UOW for radial unsymmetrical cylindrical field as it has four arrays with high spatial resolution and small active volume (more details in section 3.2.2). Therefore, OCTA provides special features to be used as a dosimetry tool for circular cone collimators. Hence, this chapter focuses on characterising OCTA by studying the pre-irradiation electrical effects (I-V and C-V), the radiation hardness and radiation damage. Moreover, this chapter also aims to apprehend OCTA's potential clinical usefulness for SRS/SRT small field dosimetry using cones, by characterizing it in terms of:

1. Uniformity
2. Linearity
3. Output factors
4. Beam profiles
5. Percentage depth dose
6. The centre shift as gantry rotation

9.2 Methodology

9.2.1 Current-Voltage characterisation

I-V measurements were done by using Keithley 230 programmable voltage source, to apply the reverse bias, coupled with a Keithley 199 System DMM/scanner and Keithley 614 electrometer, used to measure the current. The detector was placed in a dark aluminium container at room temperature, in order to protect the detector from the ambient light that can generate photocurrent. The p^+ diode (one of the bias pins available in each side of the OCTA detector) was connected to the voltage source and the n^+ diode (selected from different sides across the detector) to the electrometer. Different n^+ diodes were used to check the effect of the current leakage across the detector array. The negative voltage applied ranged from 0 to –30 V, with incremental steps of -1 V. The delay time between the applied voltage and the readout current was kept at 1000 ms, to reach the current stabilization. These parameters were setup by using a LabView interface and then saved for analysis.

The current-voltage measurements were repeated again after every step of irradiation to check the effect of the accumulated dose on it. The same diodes were used in order to compare them as a function of the accumulated dose.

9.2.2 Capacitance-Voltage characterization

The C-V test was performed to check the depletion bias of the detector. Ideally, increasing the voltage on a detector will cause a reduction on the capacitance until fully depleted. If more voltage is applied after that, the depletion width will not change.

$$C \propto \frac{1}{\sqrt{V}}$$

It is important to know the C-V of the detector array to determine the small signal behaviour and its effect on the pre-amplifier noise. The C-V for the real silicon detector isn't as simple as in the ideal p-n silicon detectors, due to the existence of multiple depletion steps, which happen between the diodes junctions.

This C-V test was done by measuring the capacitance against a range of reverse voltages by using a Boonton 7200 capacitance meter. The reverse voltage applied to diodes was from 0 to -20 V, with -0.5 incremental steps and 2000 ms delay time. OCTA was placed in a dark aluminium container at room temperature and parameters were selected and data saved by using LabView software. Before changing the pixel, the capacitance meter was set to zero.

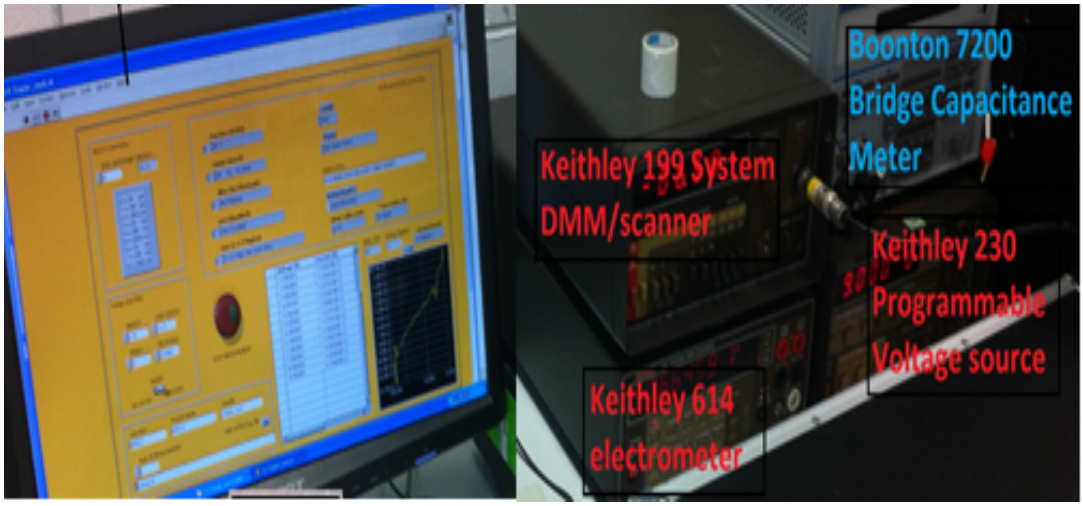

Figure 9.1: I-V and C-V measurement setup.

9.2.3 Radiation hardness characterisation

Radiation hardness is an important characteristic for the dosimeter to avoid the change in its performance with the accumulated dose. Therefore, the response of the OCTA detector was checked before the ^{60}Co irradiation (at the Australian Nuclear Science and Technology Organisation) and after every step (20 kGy) of ^{60}Co irradiation, up to 160 kGy. The response of OCTA was performed at Illawarra Cancer Care Centre (ICCC) by

using Varian 2100C LINAC. The OCTA detector was set at 100 cm SSD and 1.5 cm depth with jaw opening of field size 10 x 10 cm^2. It was irradiated by using 6 MV photon with 100 MU at 600MU/min dose rate. Five measurements were taken to calculate the standard deviation. The average responses of all diodes (505) was measured and normalised to the pre-irradiation response.

9.2.4 Uniformity

The uniformity of OCTA detector was performed by irradiating OCTA with a flattened 6 MV photon beam, at 100 cm SSD. OCTA was placed above a 10 cm Solid Water^{TM} phantom and at a depth of 10 cm. A field size of 15 x 15 cm^2 was used to deliver 100 MU at a dose rate of 600 MU/min. The same procedure that was used for DUO (section: 5.2.1) was used to calculate the equalisation factor and get the uniformity of OCTA.

9.2.5 Dose linearity

The dose linearity measurements were performed by irradiating OCTA with 6 MV photon beam at 100 cm SSD. The field size used was 10 x 10 cm^2 at 1.5 cm depth in the Solid Water^{TM} phantom. OCTA was irradiated in a range of doses from 50 to 500 cGy. Three measurements were taken for each MU irradiation, to calculate the standard deviation of measurements.

9.2.6 Beam profiles and Output factors (OF)

To characterize the performance of the OCTA detector for ELEKTA SRS circular cone collimators, profiles of the cone sizes 5, 7.5, 10, 12.5, 15, 20, 25, 30, 35, 40 and 50 mm were measured at 10 cm depth in the Solid Water^{TM} phantom. The same setup as DUO was used (section: 5.2.2). The beam profiles were measured in four arms X, Y, SWNE (south-west to north-east) and NSWE (north-south to west-east). These data were

compared with EBT3 films; data that was taken under the same experimental conditions.

The output factors (OF) were calculated as the ratio of the dose response at the average of the nine central pixels of the OCTA detector for each SRS cone size at 10 cm depth to the dose response at the same central pixels of 50 mm SRS cone size at the same depth. The same setup was used to measure the output factors by using MO*Skin*; for comparison.

9.2.7 Percentage depth dose

The percentage depth dose (PDD) was measured at SSD 90 cm. The same setup was used as DUO experiments (section: 5.2.5). The cone diameters used to measure PDD was 5, 7.5, 10, 12.5, 15 and 20 mm.

9.2.8 Centre of rotation (COR)

The centre of orientation (COR) and positioning uncertainty of the LINAC due to the gantry, collimator or/and couch rotation is important to be verified by changing one of these parameters (gantry, collimator, couch) and keep the others the same.

In this study, the centre of rotation was checked by using a 5 mm diameter cone collimator. The gantry was rotated from 0^0 to 180^0, while keeping the couch and collimator at the same angle position. By using the OCTA detector, the centre shift was determined in four directions.

9.3 Results

9.3.1 I-V

Figure 9.2 shows the results of I-V of the OCTA detector by using different channels at 0 kGy (pre-irradiation test) plotted in a logarithmic scale. All diodes followed the

predicted trend, where increasing the reverse bias causes an increase in the leakage current. However, there is a difference in the value of the leakage current between different pixels; where all are in the range of nA and the breakdown reverse voltage will be after 30 V.

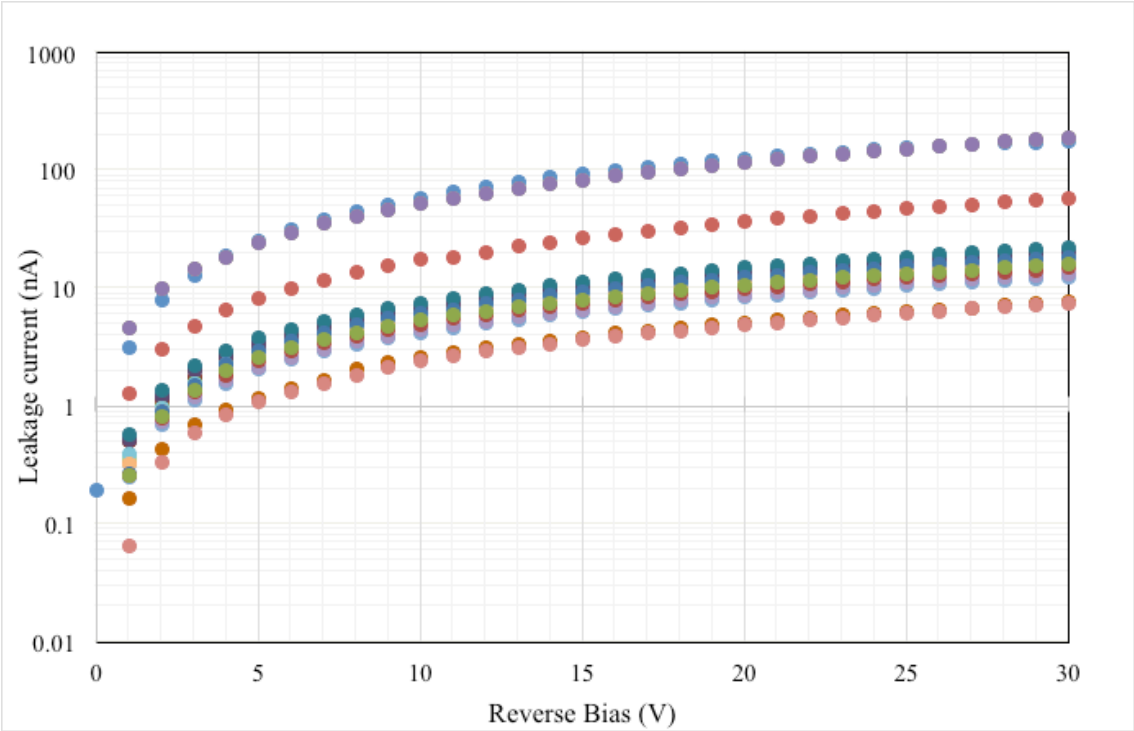

Figure 9.2: I-V of different diodes in OCTA detector before the irradiation (0 kGy).

9.3.2 C-V

Figure 4 shows the C-V of different pixels in the OCTA array. To show the behaviour more clearly, two pixels were detected as in figure 5. The capacitance decreases as the reverse bias increases, which follows the predicted trend of C-V for silicon detector. For a reverse bias applied from 0 to 20 V, the capacitance decreases in a range of pF.

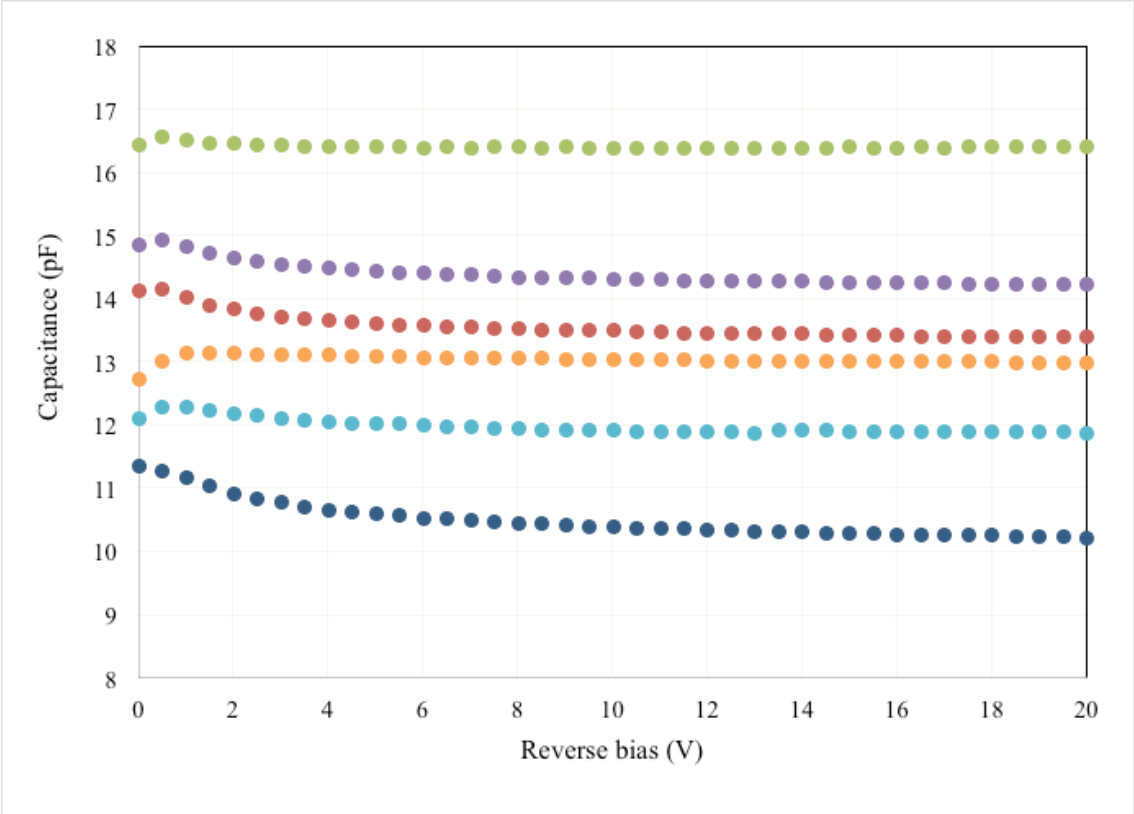

Figure 9.3: C-V of OCTA measured from different pixels.

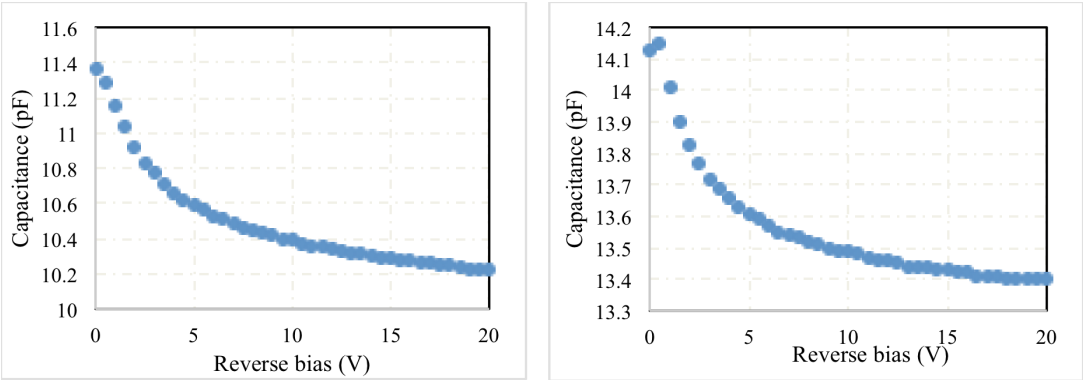

(a) (b)

Figure 9.4: C-V curves measured by two pixels of OCTA detector at 0 kGy; a: #36 and b: #15.

9.3.3 Radiation Hardness

Figure 9.5 shows the relative sensitivity of OCTA detector after ^{60}Co irradiation. This result was expected for a silicon detector, where the sensitivity decreases after irradiation. This is due to the change in the carrier lifetime as a function Generation and Recombination centers (GRCs) at the depletion region.

The stability of OCTA was achieved at 120 kGy ^{60}Co irradiations, because of its small sensitive volume that have short carrier lifetime. Moreover, the sensitivity of the detector is affected by the diffusion length, which decreases with the accumulated dose. This shows that OCTA should be irradiated before its use in clinical dosimetry and has to be used in a passive mode. The error bars represent a two standard deviation from five repeated measurements.

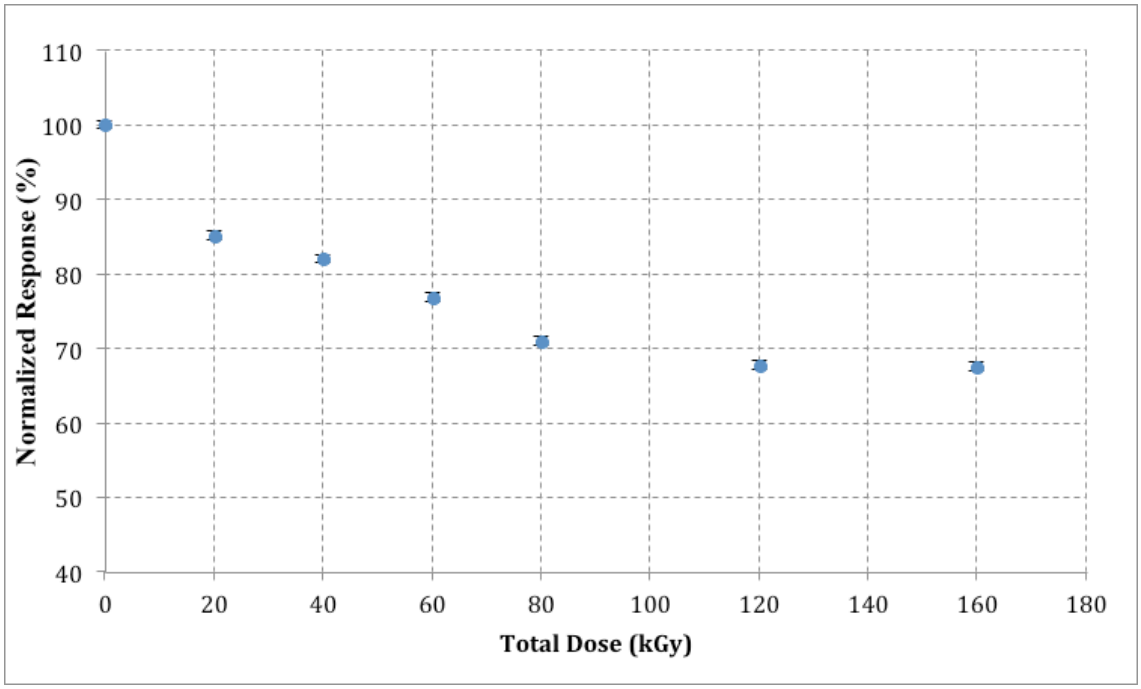

Figure 9.5: The relative sensitivity of OCTA as a function of pre-irradiation dose, the error bars represent two standard deviation but they are very small to be seen.

9.3.4 Uniformity

Figure 9.6 shows the OCTA response before applying the equalisation factors and after it. There was a variation in the response between the 512 channels up to 2.5%. This percentage decreases to less than 0.5% after applying the equalisation factors.

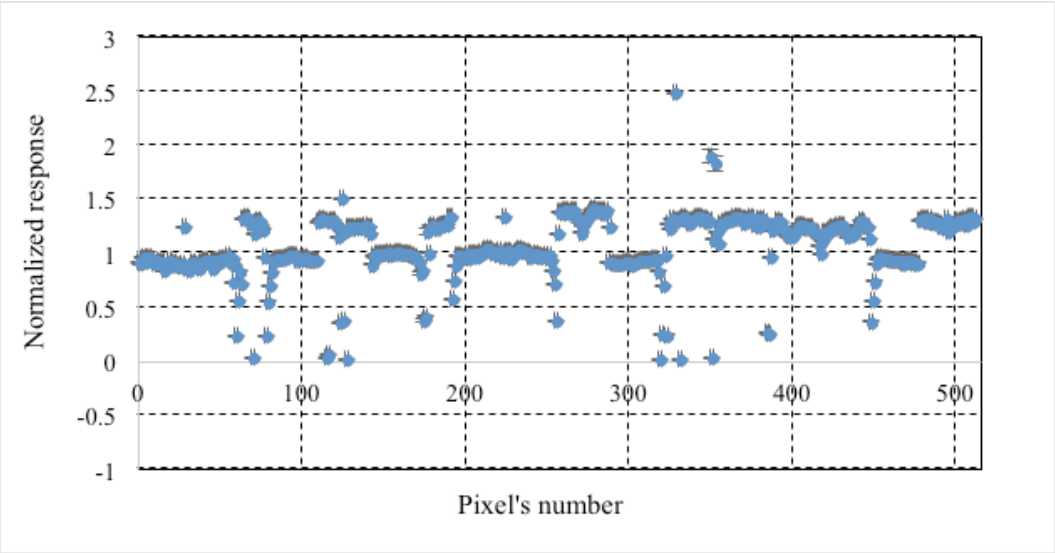

(a) Raw response

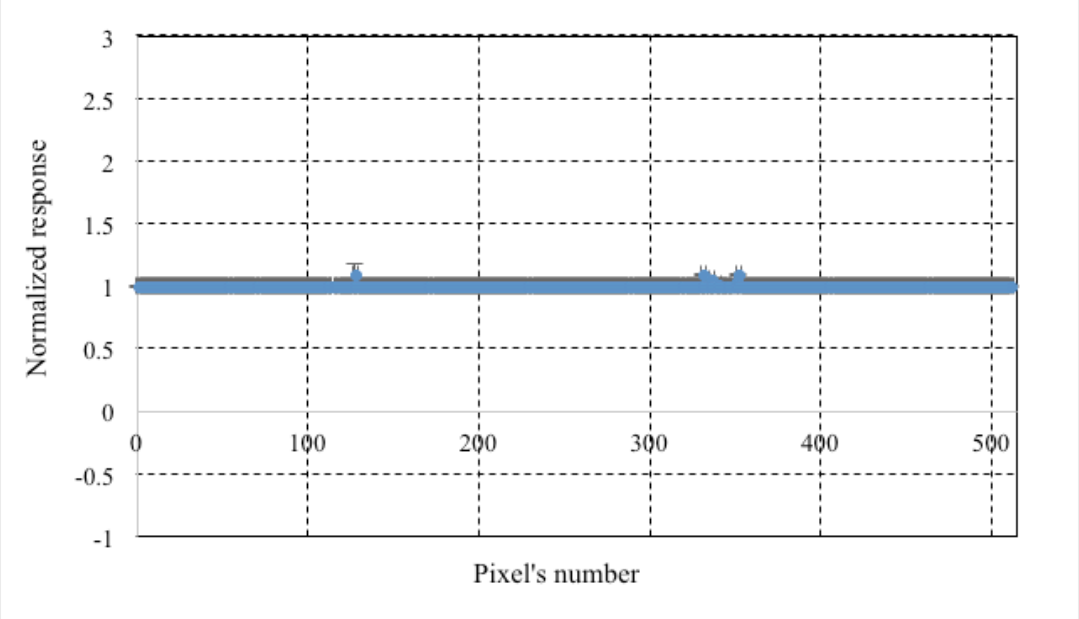

(b) Uniformity corrected

Figure 9.6: Detector response (a) before and (b) after applying equalisation factors.

9.3.5 Dose Linearity

The dose linearity of OCTA was tested in the range from 50 to 500 cGy, in step of 50 cGy. Figure 9.7 shows the excellent linearity of OCTA with R^2=1. The error bars were calculated as two standard deviation over three measurements for each dose point, but they are hard visibly because they are so small.

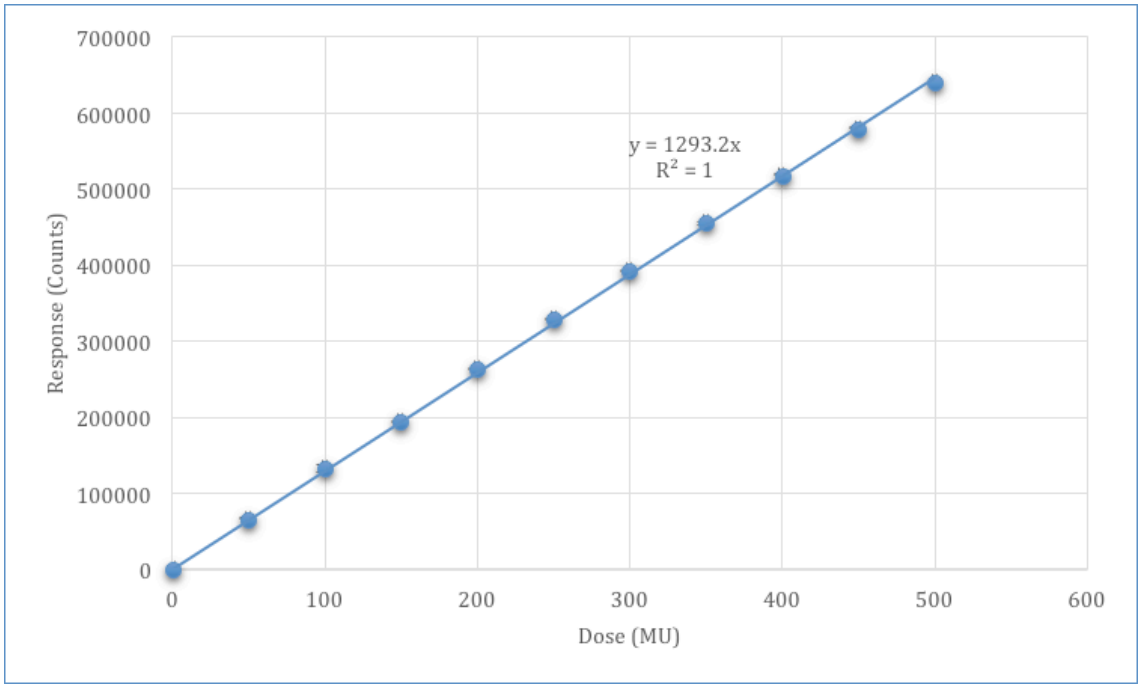

Figure 9.7: The linearity of OCTA at the central pixels.

9.3.6 Output Factors

Figure 9.8 shows a comparison of the output factors measured by OCTA, MO*Skin* and EBT3 films as a function of ELEKTA cone diameter size at 10 cm depth, for 6 MV photon beam. They all agree within 2% overall the cone sizes. However, OCTA agrees with EBT3 within 1.5% and with MO*Skin* within <1%. This shows that OCTA has no volume averaging effects or perturbations that affects its response.

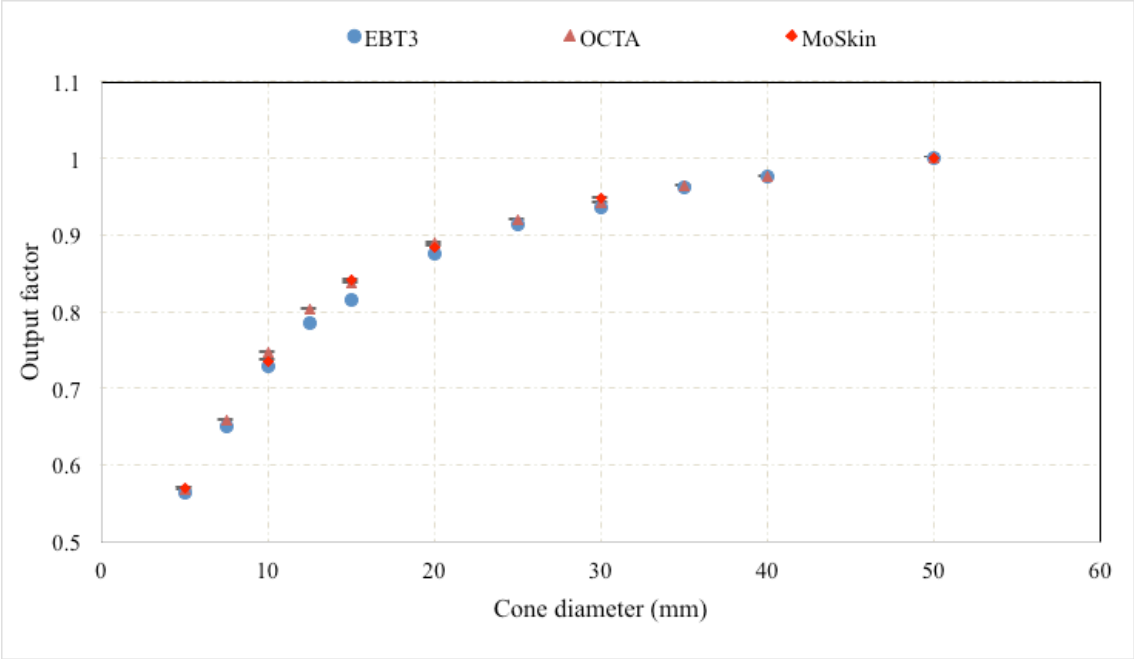

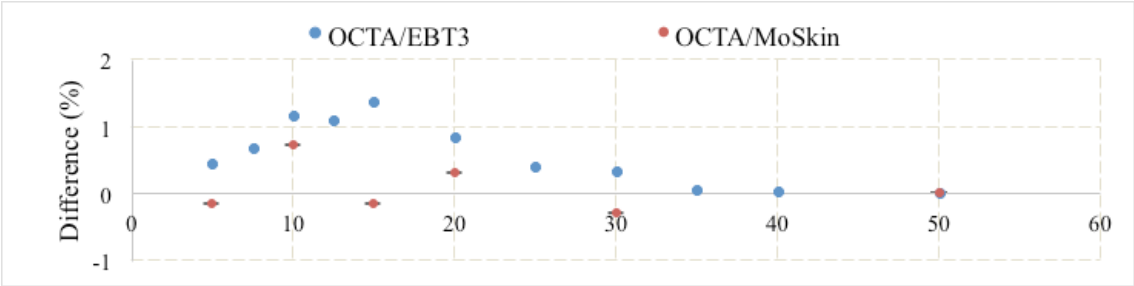

Figure 9.8: Comparison of the output factors measured by OCTA, MO*Skin* and EBT3.

9.3.7 Beam Profiles

Figures from 9.9 and 9.12 show the measurements of the beam profiles for ELEKTA cone collimators ranging from 5 to 50 mm diameter, compared with the EBT3 measurements (results from chapter 7). OCTA provides profiles in four directions; horizontal, vertical and two orthogonal profiles at 45^0 from the centre in both directions. The resolution of the horizontal and vertical profiles is 0.3 mm, while it is 0.42 in the two orthogonal profiles. However, the resolution is still very good and even higher than EBT3 films resolution at 72 dpi. The profiles are all interpolated to 0.2 mm resolution by using MATLAB and normalised to 50% of the dose. In addition, the charge sharing

effects in the orthogonal arms were corrected by using the same methodology that was used for DUO detector (chapter 6).

To calculate the orthogonal profiles measured by EBT3 films, MATLAB have been used. First find the right diagonal profiles in an average area of 2 x 2 cm^2 around the centre by using function of (diag). Then by using the flip MATLAB function, the left diagonal also calculated as an average of 2 x 2 cm^2 diagonal profiles around the centre. The resolution of the diagonal profiles is calculated and found to be 0.49 mm. The EBT3 profiles were interpolated by using MATLAB to 0.2 mm, for a comparison with OCTA profiles.

The FWHM and penumbra width (20-80) % were evaluated and compared between OCTA and EBT3 in the four directions as shown in tables 9.1 and 9.2 for OCTA and EBT3 films, respectively. The maximum difference between OCTA and EBT3 in terms of FWHM is 0.4 mm among the four directions, while the difference in the (20-80 %) penumbra is within 0.3 mm in the orthogonal beams and within 0.7 mm in the diagonal beams.

Table 9.1: FWHM and penumbra width measured for cones by using OCTA.

	FWHM				(20 - 80 %) Penumbra width			
Cone	X-profiles	Y-profiles	SWNE	NSWE	X-profiles	Y-profiles	SWNE	NSWE
mm	mm	mm	mm	mm	mm	mm	mm	mm
5	6	5.8	6	6	2.2	1.8	2	2
7.5	7.6	7.6	7.6	7.6	2.5	2	2.4	2.2
10	10	10	10	10	2.7	2.4	2.6	2.6
12.5	12.6	12.6	12.6	12.6	2.9	2.5	2.8	2.7
15	15	14.8	14.6	14.8	3	2.6	2.8	2.5
20	20.2	20.2	20.2	20.2	3.2	3	3.1	3
25	25.4	25.2	25.2	25.2	3.3	3	3.2	3.1
30	30.4	30.4	30.4	30.4	3.4	3.2	3.3	3.2
35			35.4	35.6			3.4	3.4
40			40.4	40.6			3.6	3.4

Table 9.2: FWHM and penumbra width measured for cones by using EBT3.

	FWHM				(20 - 80 %) Penumbra width			
Cone	X-profiles	Y-profiles	SWNE	NSWE	X-profiles	Y-profiles	SWNE	NSWE
mm	mm	mm	mm	mm	mm	mm	mm	mm
5	6.2	5.8	5.8	5.8	2.2	1.8	2	2
7.5	8	7.6	7.4	7.6	2.6	2	2.3	2.4
10	10.4	10	10.2	10	2.8	2.3	2.8	2.6
12.5	13	12.6	12.4	12.4	3.1	2.6	2.9	2.8
15	14.8	14.8	14.6	14.8	3.2	2.9	3	3
20	20.4	19.8	20.2	20	3.3	3.1	3.4	3.1
25	25.4	25.4	25.2	25	3.3	3.2	3.8	3.8
30	30.2	30.4	30.2	30.4	3.7	3.3	3.9	3.9
35	34.6	35.8	35.2	35.2	3.8	4.0	3.6	4.1
40	40.4	40.6	40.2	40.6	4.0	4.0	4.1	4.1

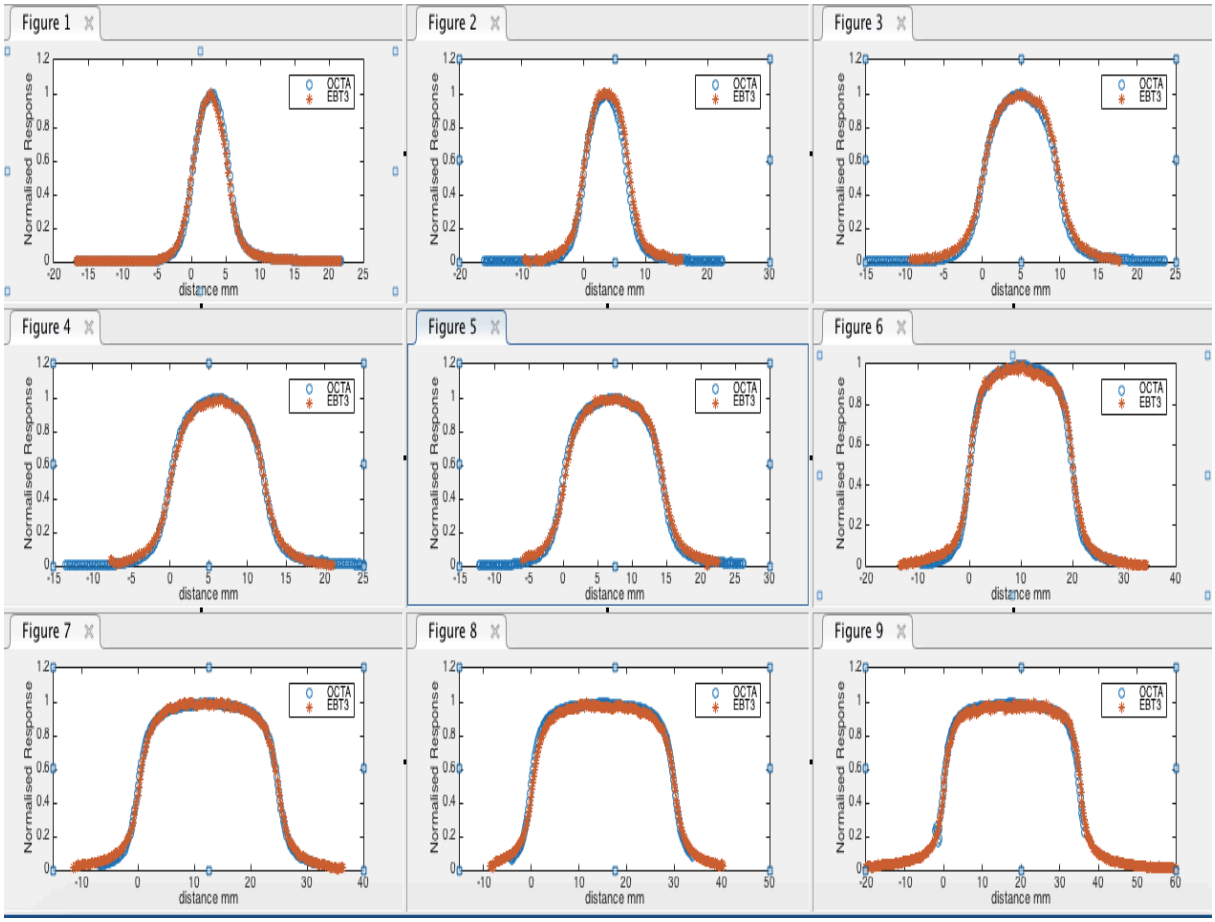

Figure 9.9: Horizontal beam profiles comparisons between OCTA and EBT3 for SRS cone diameters: figure 1) 5, 2) 7.5, 3) 10, 4) 12.5, 5) 15, 6) 20, 7) 25, 8) 30 and 9) 35 mm.

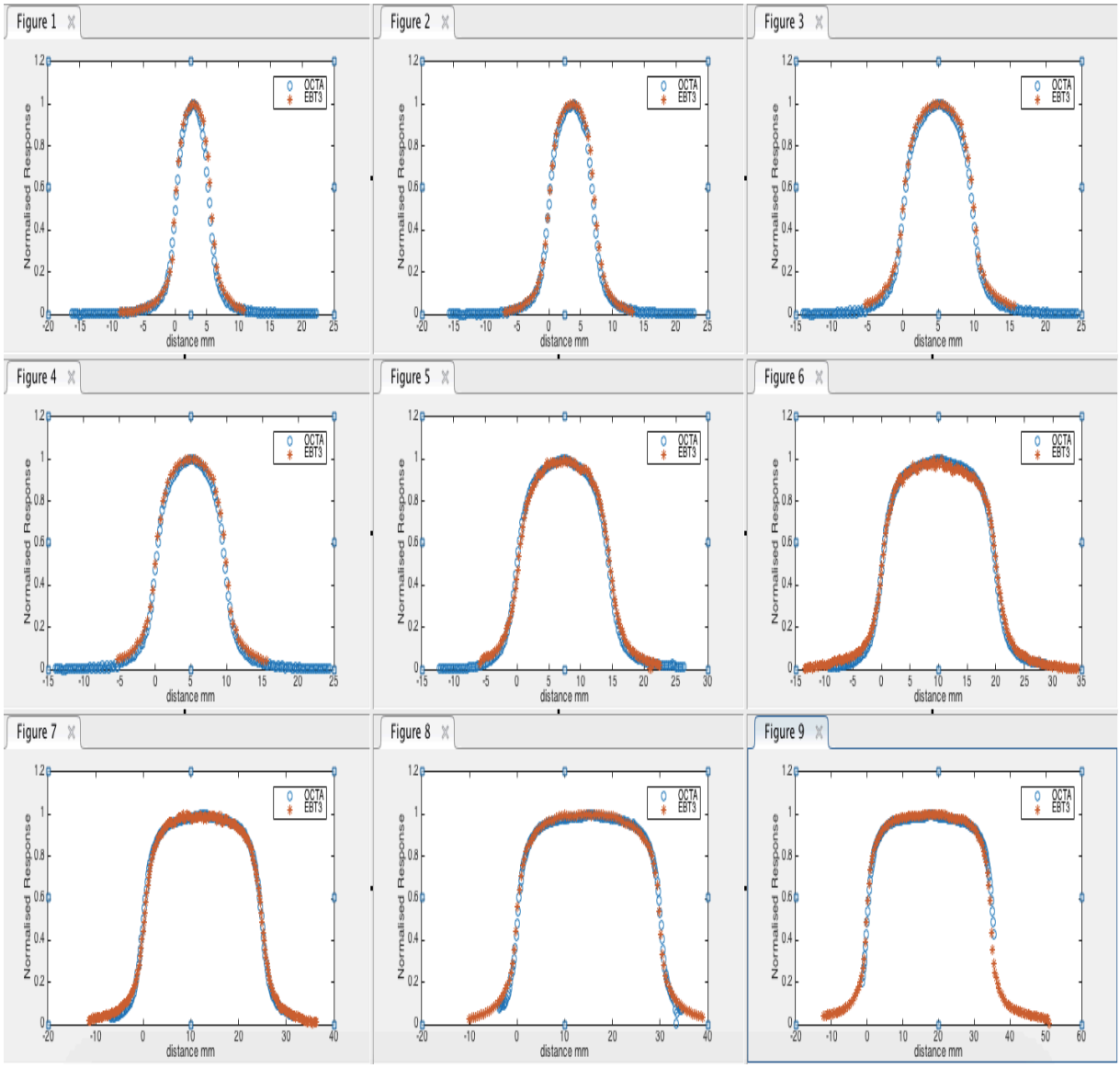

Figure 9.10: Vertical beam profiles comparisons between OCTA and EBT3 for SRS cone diameters: figure 1) 5, 2) 7.5, 3) 10, 4) 12.5, 5) 15, 6) 20, 7) 25, 8) 30 and 9) 35 mm.

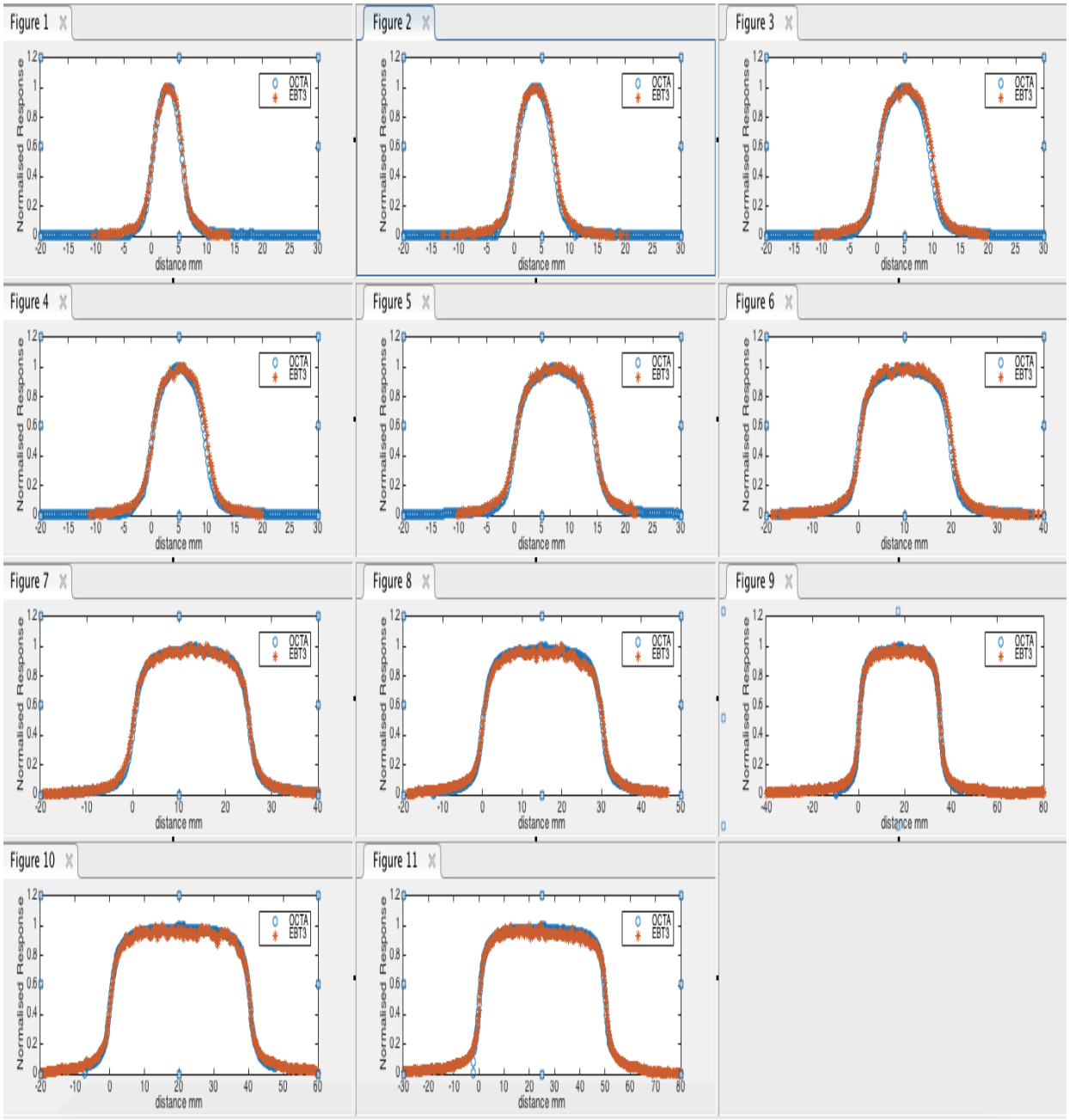

Figure 9.11: SWNE beam profiles comparisons between OCTA and EBT3 for SRS cone diameters: figure 1) 5, 2) 7.5, 3) 10, 4) 12.5, 5) 15, 6) 20, 7) 25, 8) 30 and 9) 35 mm.

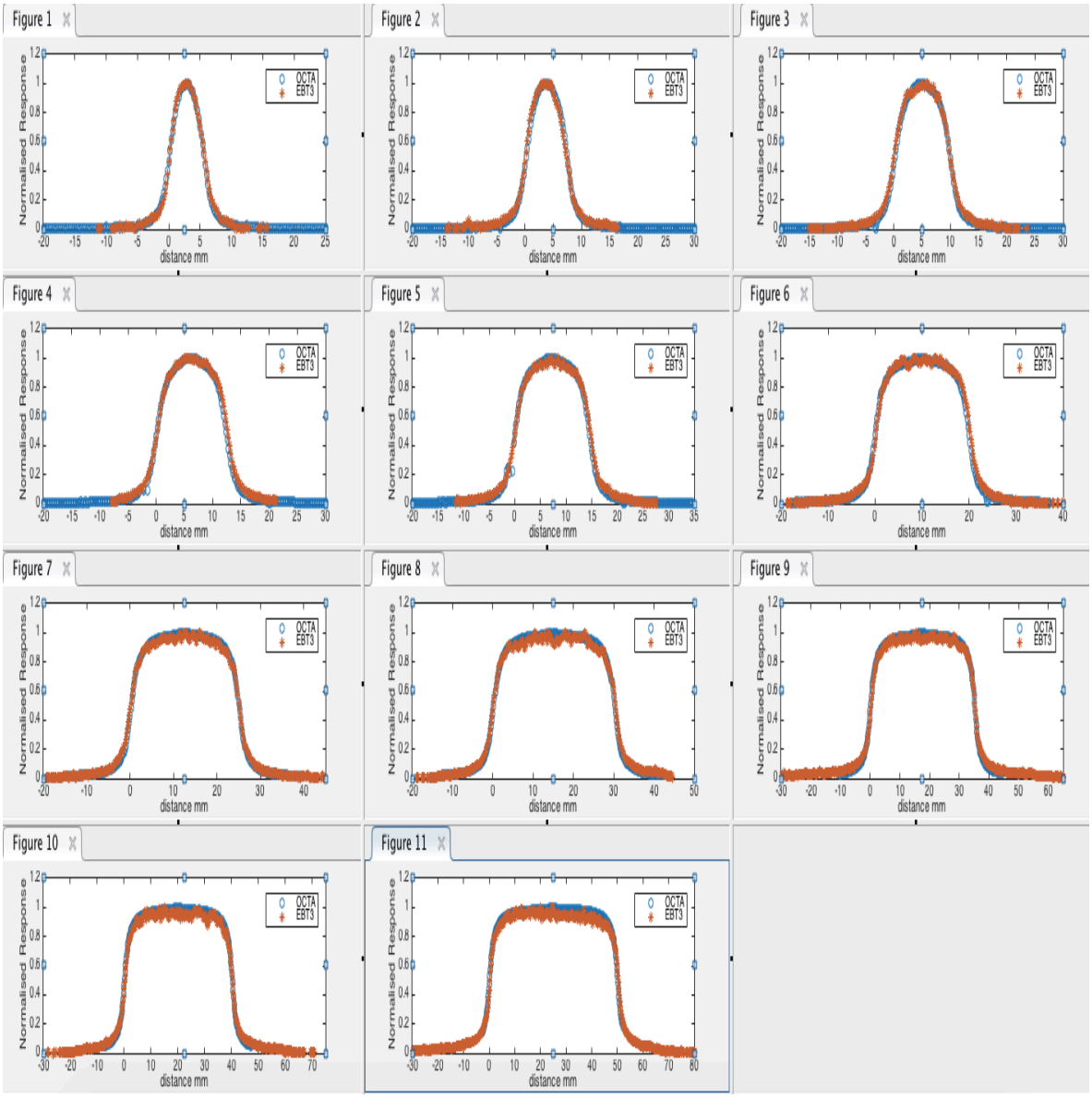

Figure 9.12: NSWE beam profiles comparisons between OCTA and EBT3 for SRS cone diameters: figure 1) 5, 2) 7.5, 3) 10, 4) 12.5, 5) 15, 6) 20, 7) 25, 8) 30 and 9) 35 mm.

9.3.8 Percentage depth Dose

Figure 9.13 shows the percentage depth dose measured by OCTA and compared with EBT3 films. As the phantom cover above OCTA was 1.0 mm PMMA, the minimum depth used was 5.2 mm water equivalent depth. The PDD measured with OCTA was in

a good agreement with the EBT3 within 4% for all cone diameters measured beyond 5.2 mm.

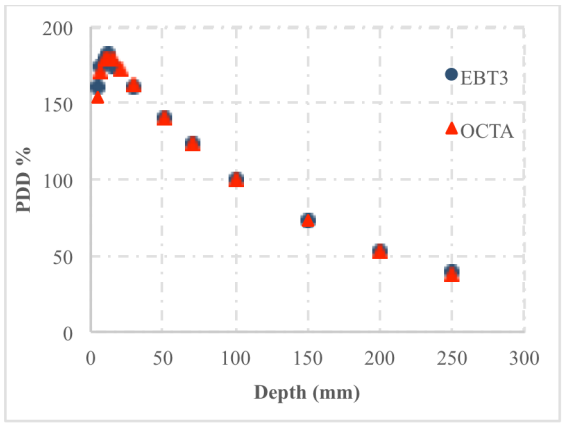

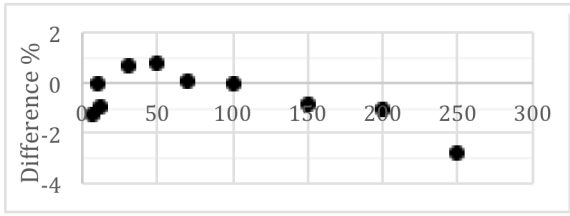

(a)

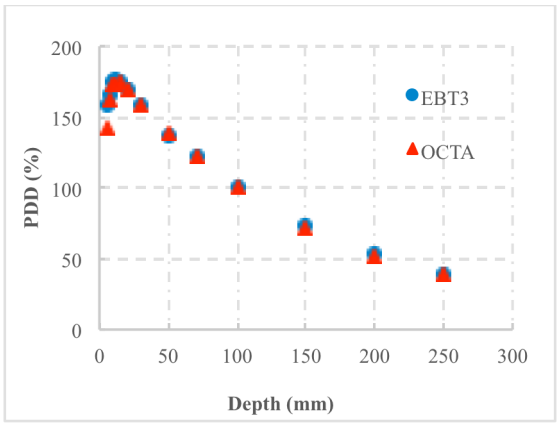

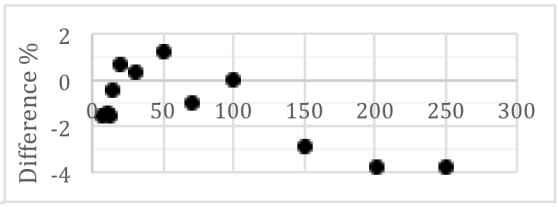

(b)

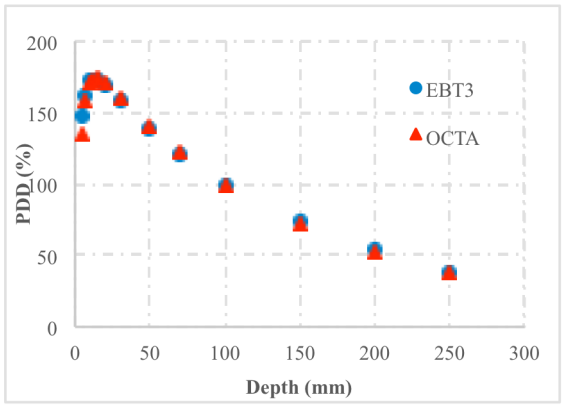

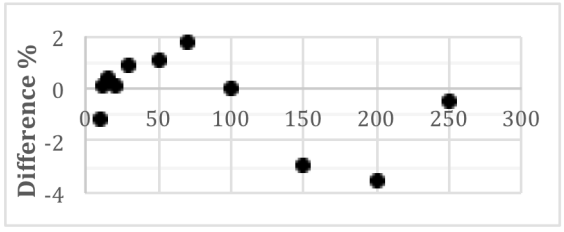

(c)

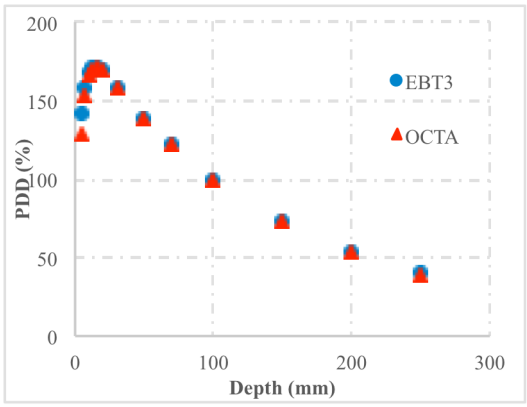

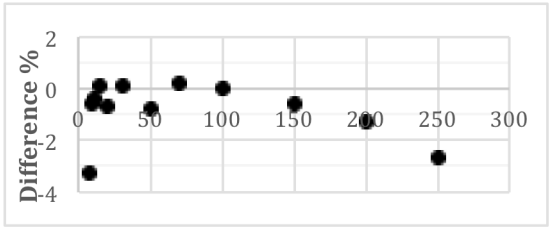

(d)

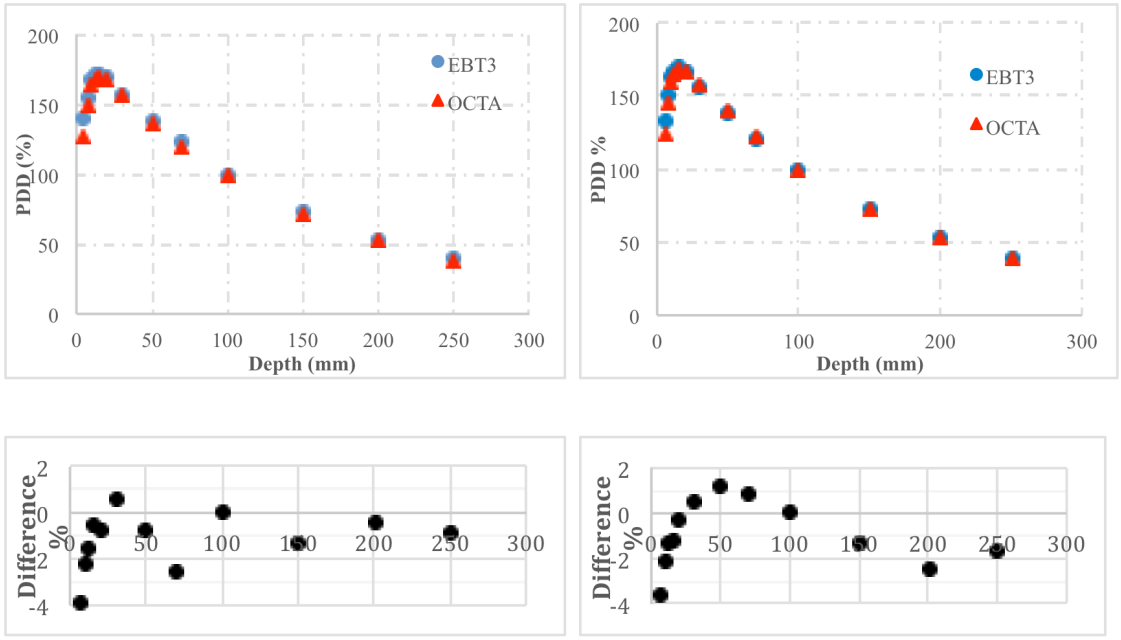

(e) (f)

Figure 9.13: PDD measured by OCTA and compared with EBT3 for SRS cone diameters (a) 5, (b) 7.5, (c) 10, (d) 12.5, (e) 15 and (f) 20 mm.

9.3.9 Determination of the mechanical centre rotation (COR)

The centre of rotation was checked by changing the gantry angle from 0^0 to 180^0, while keeping the couch and collimator at the same angle position. By using the OCTA detector, the centre shift was determined in four directions as shown in figure 9.14. The data was normalized to one at the maximum response (peak) at gantry angle 0^0, for each direction, to clearly see the effect of gantry rotation on the centre position and response. There was a dose reduction and offset shift in the position when the gantry rotated from 0^0 to 180^0 as shown in table 9.3, which is because the attenuation through the couch at the 180^0 gantry angle and DUO detector package.

This test is part of the Winston Lutz test, that is used to measure the central axis offset due to the LINAC components rotation (Rowshanfarzad, Sabet et al. 2011). There are

also different techniques and procedures that have been used to check the COR similar, but all have advantages and disadvantages as discussed by Rowshanfarzad, Sabet et al. (2011). Therefore, OCTA is a very useful tool to determine the COR easily positioning and on-time profile measurements in four directions, which is very important for the alignment of the SRS cone collimators.

1. Vertical

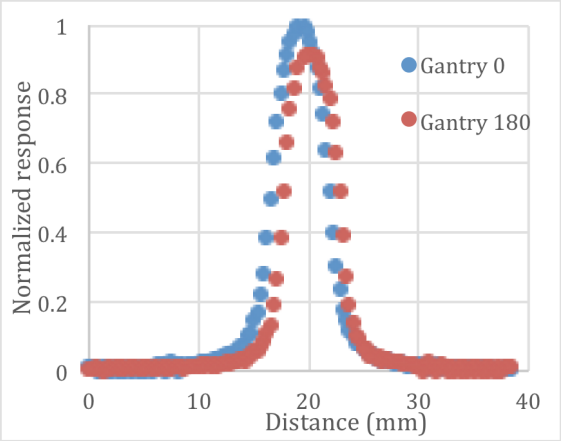

2. Horizontal

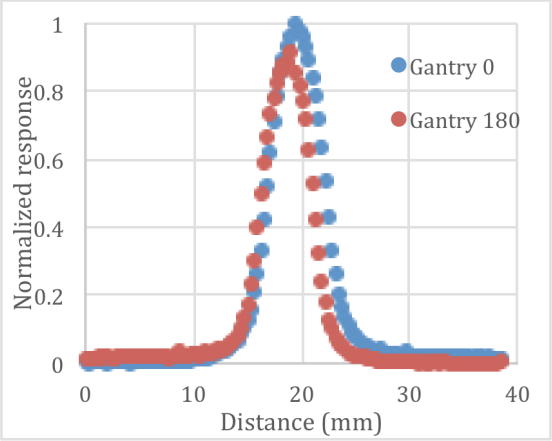

3. SWNE

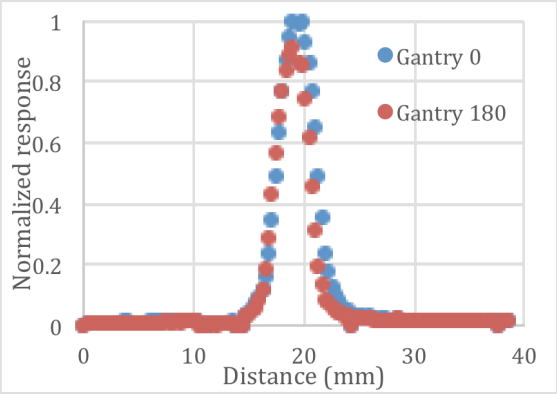

4. NWSE

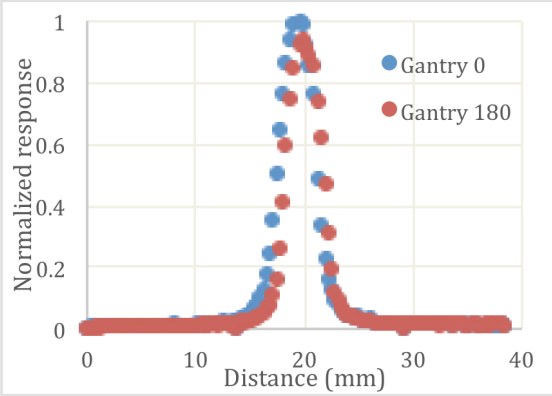

Figure 9.14: The centre of axis shift with the gantry rotation in (a) vertical, (b) horizontal, (c) SWNE and (d) NWSE directions.

Table 9.3: The dose reduction and offset shift between gantry angles 0^0 and 180^0 for 5 mm cone diameter.

Array	Dose reduction	Offset shift
	%	mm
Vertical (G-T)	8.24	-0.3
Horizontal (A-P)	8.67	0.6
SWNE	8.65	0.9
NWSE	5.91	0.9

9.4 Discussion

OCTA detector has been introduced by CMRP for SRS/SRT dosimetry as a development of monolithic silicon detectors developed for small field dosimetry. In this chapter, OCTA has been characterized in terms of electrical and clinical properties. In terms of electrical characterisation, OCTA has been tested in terms of I-V and C-V. OCTA followed the predicted trend in terms of I-V, where increasing the reverse bias caused an increase in the leakage current. The capacitance decreased as the reverse bias increased, which followed the predicted trend of C-V for the silicon detector. OCTA tested in terms of its sensitivity after irradiation. This is done by irradiating OCTA by using ^{60}Co beams and it shows stability in sensitivity at 120 kGy. The sensitivity of OCTA reduced by about 30% after the pre-irradiation. The variation in the response among all pixels of OCTA after equalisation applied gives good uniformity within 0.5%. OCTA was tested for dose linearity and the results in shows that OCTA has ideal trend of dose linearity with Response (counts) = 1293.2 x MU delivered. The beam profiles, OF and PDD were measured by using SRS cone collimators provided by

ELEKTA LINAC. The results were compared with EBT3 and MO*Skin* for OF. The OF shows a good agreement with EBT3 and MO*Skin* within 1.5%. The beam profiles are in a good agreement with EBT3 in four directions ends with an agreement in the FWHM and penumbra width up to 0.4 and 0.7 mm, respectively. The PDD measured by OCTA for cone diameters from 5 to 20 mm show a good agreement with EBT3 within 4%. The higher percentages in PDD differences were due to the dose per pulse effect on the silicon detector. Higher resistivity diode detectors are more effected by dose per pulse dependence, leading to underestimates of the PDD curve at the tail after applying the normalization (Wilkins, Li et al. 1997). Hence, PDD measured by OCTA has to be corrected for dose per pulse dependence (DPP) as DUO detector. OCTA has been used to test the mechanical shift of ELEKTA LINAC isocenter. The results show that there is an offset shift within ±0.9 mm in all four directions when the gantry was rotated from 0^0 to 180^0. There was a dose reduction when the beam delivered at gantry 180 compared to gantry 0^0. This reduction is due to the couch (where the attenuation reached to 3%) and OCTA design (including the 1 mm air gap above it).

9.5 Conclusion

In this chapter, the electrical and clinical characterisation of OCTA silicon detector array was presented. OCTA consists of four linear arrays in, horizontal, vertical, SWNE and NWSE direction, with 128 pixels each. Electrical characterisation of OCTA in terms of I-V and C-V shows that OCTA is following the expected trend as for p-silicon diodes. The radiation damage study shows the stability response of OCTA from 120 kGy pre-irradiation from ^{60}Co. In addition, OCTA has been tested by using clinical LINAC and the results showed that OCTA has acceptable characteristics in terms of

uniformity, linearity, OF, beam profiles and PDD, which could provide a new monolithic silicon detector suitable for small circular beam dosimetry.

In conclusion, OCTA provides data in four directions with high spatial resolution and on-line data analysis, where these extra features could be of importance for SRS pre-treatment QA, especially for SRS adapted LINACs with a non-negligible mechanical isocentre size where the strict SRS treatment tolerances requirements are sometimes difficult to meet and deserves special attention, demanding numerous quality controls before patients treatments can be delivered.

Chapter 10: Conclusion

The aim of the work of this thesis is to develop a dosimetry tool for SRS/SRT quality assurance by using monolithic silicon detector arrays with high spatial resolution. This has been achieved by testing two silicon detectors designed especially for SRS/SRT QA, called DUO and OCTA. They were optimized for the output factor measurements by using a suitable air gap upstream and they were characterised in terms of charge sharing effects, in order to apply the required correction factors at the penumbra region. Then they were tested as potential QA tools by using ELEKTA SRS cone collimators. This chapter outlines the main works and findings regarding DUO and OCTA silicon detector arrays. In addition, this chapter discusses the future of this research.

1. DUO

DUO is a monolithic silicon detector designed by the Centre of Medical Radiation Physics (CMRP) at the University of Wollongong (UOW). It is manufactured by using low resistivity Bulk silicon substrate. The pixels are arranged in two linear orthogonal arrays with 253 pixels for each arm. The five central pixels are with size of 0.18 x 0.18 mm^2 each, and the remaining pixels have size of 0.04 x 0.8 mm^2. The detector pitch is 0.2 mm to provide the required spatial resolution for measurements of the sharp fall of the penumbra regions. The total array area is 52 x 52 mm^2. DUO is placed between two 5 mm thick PMMA slabs in order to protect it from mechanical damage. DUO was pre-irradiated with a dose of 140 kGy using Co-60 gamma source to stabilize its response. After pre-irradiation, the sensitivity of the DUO was stable and within 2% for a 1 kGy further irradiation. In chapter 4, DUO was optimised for the OF measurements by testing the use of the air gap with different thicknesses above it and then compared with EBT3 and MO*Skin* measurements for small field sizes by using collimator jaws from

Varian LINAC. In addition, the beam profile parameters were studied as a function of the air gap thickness. The air gap above DUO shows a large effect in the OF measurements for field sizes smaller than 3 x 3 cm^2, and small air gaps of 0.5 mm were the best to match EBT3 OF. The output factors matched the EBT3 measurements within 1%. There was a dose reduction of about 18% for square field edge of 0.5 cm for air gaps changed from 2 mm to 0.5 mm upstream of DUO. The FWHM and penumbra widths increased as air gap thicknesses increased.

Then Bulk DUO was tested for the charge sharing effect due to the Si substrate type and pitch size (chapter 5). The mathematical analysis shows that charge sharing between pixels generated under the assumption of constant gradient, point pixels and absence of recombination, doesn't exist. The experimental results showed there is a higher gradient at the penumbra region that is mostly due to volumetric effect.

In chapter 6, DUO was evaluated for small field dosimetry by using square field sizes. DUO shows good uniformity after applying equalisation factors, within ±0.5%. The beam profiles measured by DUO agrees with EBT3, provides a good agreement in the FWHM and penumbra width within 1% and 0.6 mm, respectively. DUO exhibits dose per pulse dependence with the response changed up to 23% in the range from 2.78 x 10^{-4} to 2.1 x 10^{-5} Gy/pulse, so correction factors were calculated to correct the PDD from the effect of DPP dependence. After applying the corrections, PDD agrees with the ionisation chamber measurements for 6MV within 1.5%.

In chapter 7, DUO has been used to characterise SRS cone collimators provided by ELEKTA LINAC. It was used to measure the beam profiles, OF and PDD for cones from 5 mm to 50 mm and compared with one water equivalent detector (EBT3) and one diode (IBA SFD). The results showed DUO can be used to measure OF provided by SRS cones as it agrees with EBT3 film measurements within ±0.7% and with IBA SFD

diode within ±2% (after applying the correction factors). The SRS cone profiles measured by DUO were corrected for charge sharing effects and compared with EBT3 and SFD. The profiles were agreed and resulted in an agreement in the FWHM and penumbra width within 1% and ±0.7 mm in both X-profiles and Y-profiles. By comparing the X-profiles and Y-profiles, where X-profiles have wider penumbra in all cone sizes; which could be due to the source shape in the ELEKTA LINAC. PDD measurements for all SRS cone collimators showed an overall agreement between DUO, EBT3 and SFD within ±2% for depths from 0.5 to 25 cm.

Finally DUO was used to verify the delivery of SRS cone collimator treatments in two positions, vertical and horizontal, each position tested with eight SRS cones as in chapter 8. The DUO dose profiles were compared with EBT3 and TPS, which is based on Monte Carlo algorithm and it resulted in a good agreement with average gamma (3%, 0 mm) within 95% except at the very lower doses at the profile tails. DUO was used to test the mechanical isocentre ELEKTA LINAC shift and the cone offset when interchanging the cones. The results showed there is about 1 mm and 0.4 mm shift for mechanical isocentre shift and cone interchanging, respectively. It was faster and easier to test the amount of shift than EBT3, which is required as pre-treatment QA.

Therefore, the recommendations of this work are to replace Bulk DUO by Epitaxial DUO for more accurate measurements, as it is better in terms of radiation damage. Then, the new Epitaxial DUO has to be characterized with different modalities for small field dosimetry in different types of LINACs. Also, DUO needs to be examined to use with FFF SRS cone collimators and other FFF modalities. In addition, Epitaxial DUO can be used to characterise profiles with Calypso systems to study moving targets in radiotherapy.

2. OCTA

OCTA detector is likewise a monolithic silicon detector designed by Centre of Medical Radiation Physics (CMRP) at University of Wollongong (UOW). It is fabricated on a p-Si Epitaxial layer with high resistivity 100 Ω cm. It contains 512 pixels arranged in four linear arrays; two orthogonal crosses with two other arrays each 45^0 with respect to one another, intersecting at the centre. The central pixels form 3 x 3 mm^2 square with pixel size of 160 x 200 μm^2 and total area of 920 x 920 μm^2. The other pixels are 40 x 800 μm^2, with overall detector size of 40.2 x 40.2 mm^2. The pitch size is 300 μm in the orthogonal arrays (Horizontal & vertical) and 430 μm in the other diagonal arrays (SWNE & NSWE). OCTA is placed on a PCB board and sandwiched between two 5 mm thick PMMA slabs providing 1 mm air gap upstream its active volume. The final aim of this study was to characterise the OCTA detector in terms of electrical, radiation hardness and clinical properties in order to evaluate its use as a QA dosimeter for stereotactic radiotherapy treatments. Chapter 9 discussed the works done by using OCTA array. Firstly, I-V and C-V analysis were performed and showed an ideal trend of p-n silicon diodes. Secondly, irradiating OCTA using ^{60}Co showed that the response is stable at 120 kGy irradiation. Then OCTA's uniformity was tested by using the equalisation method and it showed uniformity within 0.5% after applying the equalisation factors. The dose linearity measured by OCTA provides ideal linear trend with a correlation of 1. Charge sharing effects have been studied in OCTA detector and there was negligible effect on it, due to the Epitaxial substrata. Furthermore, OCTA was used clinically to characterise ELEKTA SRS cone collimators in terms of beam profiles, OF, PDD and COR. The OF showed a good agreement with MO*Skin* and EBT3 within ±1%. The agreement in the beam profiles between EBT3 and OCTA provides an agreement in the FWHM and penumbra width up to ±0.4 mm and ±0.7 mm

in all four arms. In terms of PDD, OCTA agrees with EBT3 within ±4% for all cones up to 20 mm diameter for depths down to 25 cm, without DPP corrections. By using OCTA, the centre of axis rotation was tested when rotating the gantry from 0^0 to 180^0, which provides data in four directions. The results indicate that there is a centre offset shift up 0.9 mm, respectively. Therefore, OCTA is a powerful tool that can replace other methods used to determine the COR for pre-treatment QA, as it can be positioned easily and can provide on-time profile measurements; both which are very important for the alignment of the SRS cone collimators. To conclude, OCTA provides data in four directions with high resolution and on-line data analysis without charge sharing corrections, which required for pre-treatment SRS QA.

Future works on OCTA to complete its full clinical characterisation is to test its angular dependence and dose per pulse dependence. Then, OCTA has to characterize by using different modalities and LINACs for small field dosimetry. Furthermore, OCTA has to be used with FFF mode in small field dosimetry. Moreover, this detector can be tested with a movable phantom.

APPENDIX A

It is important to investigate whether charge-sharing effects between pixels in case of constant gradient filed is affecting measured dose field gradient with monolithic pixelated detector DUO. Charge sharing effects in pixel array is considered under the assumption that the dose gradient (or produce charge gradient of which is proportional to dose gradient in a detector) is constant along the linear pixel array. Additionally assumed that charge sharing happens between neighbouring pixels only, no charge recombination between pixels and size of the pixel is infinitely small (i.e. point pixel).

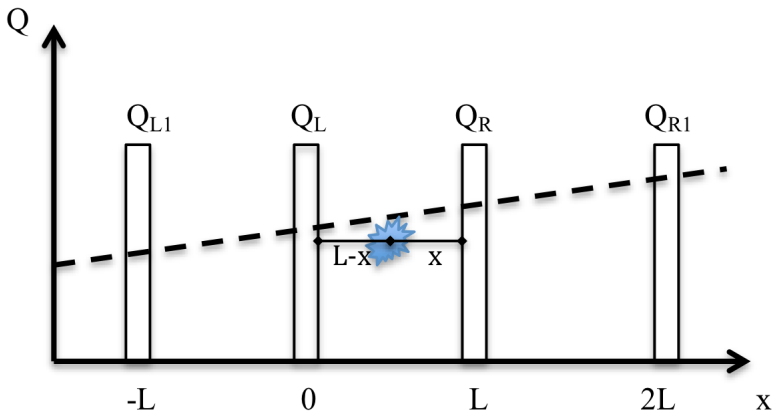

Assuming the amount of induced charge along the linear pixel array is proportional to the dose delivered and can be written as Q = a + mx, where m is a dose gradient and "a" is the cut off corresponding to the origin where the pixel (i) was placed. Fig 1 shows the charge distribution along the linear pixel array along with the position of 4 consecutive pixels i-1, i, i+1 and i+2 with pitch L. In this case the partial charge dQ deposited within dx length of an array is represented as dQ = (a + mx). dx/L, where x is the distance between the deposited charge dQ and pixel i..

The charge collected by the pixel i is calculated over the distance L on a right from the pixel i is:

$$\boldsymbol{Q_i = \int_0^L \frac{x}{L}\left(\frac{a+mx}{L}\right)dx}$$

$$\boldsymbol{= \frac{1}{L^2}\int_0^L (ax + mx^2)dx}$$

$$\boldsymbol{= \frac{1}{L^2}\left(\frac{ax^2}{2} + \frac{mx^3}{3}\right)\Big]_0^L}$$

$$\boldsymbol{= \frac{L^2}{L^2}\left[\frac{a}{2} + \frac{m}{3}L\right]}$$

$$\boldsymbol{= \left[\frac{a}{2} + \frac{m}{3}L\right]}$$

Similarly, the charge collected by the pixel i+1, where the distance between the deposited partial charge and the right pixel is (L-x), is calculated as:

$$\boldsymbol{Q_{i+1} = \frac{1}{L}\int_0^L \left(\frac{a+mx}{L}\right)(L-x)dx}$$

$$\boldsymbol{= \frac{1}{L^2}\int_0^L (aL - ax + mxl - mx^2)\ dx}$$

$$\boldsymbol{= \frac{1}{L^2}\left[aLx - \frac{ax^2}{2} + \frac{mLx^2}{2} - \frac{mx^3}{3}\right]_0^L}$$

$$\boldsymbol{= \frac{1}{L^2}\left[aL^2 - \frac{aL^2}{2} + \frac{mL^3}{2} - \frac{mL^3}{3}\right]}$$

$$\boldsymbol{= \left[a - \frac{a}{2} + \frac{mL}{2} - \frac{mL}{3}\right]}$$

$$= [\frac{\mathbf{a}}{\mathbf{2}} + \frac{\mathbf{mL}}{\mathbf{6}}]$$

$$= [\frac{\mathbf{a}}{\mathbf{2}} + \frac{\mathbf{mL}}{\mathbf{6}}]$$

Similarly charge collected by pixel i+1 due to charge sharing between pixels i+1 and i+2 is:

$$Q_{i+1}^{R} = \frac{1}{L}\int_{L}^{2L}\left(\frac{a+mx}{L}\right)(x-L)dx$$

$$= \frac{1}{\mathrm{L}^2}\int_{\mathrm{L}}^{2\mathrm{L}}(\mathrm{ax} - \mathrm{al} + \mathrm{mx}^2 - \mathrm{mxl})\mathrm{dx}$$

$$= \frac{1}{\mathrm{L}^2}[\frac{\mathrm{ax}^2}{2} - \mathrm{aLx} + \frac{\mathrm{mx}^3}{3} - \frac{\mathrm{mLx}^2}{2}]_{\mathrm{L}}^{2\mathrm{L}}$$

$$= \left(\frac{\mathrm{a}}{2} + \frac{5\mathrm{m}}{6}\mathrm{L}\right)$$

Similarly charge collected to the pixel i due to charge sharing between pixels i and i-1 can be presented as:

$$\boldsymbol{Q_i^L = \int_0^{-L} \frac{x}{L}\left(\frac{a+mx}{L}\right)dx}$$

$$\mathbf{= \frac{1}{L^2}[\frac{ax^2}{2} + \frac{mx^3}{3}]_0^{-L}}$$

$$= [\frac{\mathbf{a}}{\mathbf{2}} - \frac{\mathbf{mL}}{\mathbf{3}}]$$

By adding the charge collected to the pixel i as a result of charge sharing from the left and from the right of pixel, the total charge is calculated as:

$$\mathbf{Q_i + Q_i^L} = \left[\frac{\mathbf{a}}{\mathbf{2}} + \frac{\mathbf{mL}}{\mathbf{3}}\right] + \left[\frac{\mathbf{a}}{\mathbf{2}} - \frac{\mathbf{mL}}{\mathbf{3}}\right]$$

$$= \mathbf{a}$$

By adding the charge collected from the left and from the right of the pixel i+1, the total charge collected by pixel i+1 is calculated as:

$$\mathbf{Q_i + Q_{i+1}^R} = \left[\frac{\mathbf{a}}{\mathbf{2}} + \frac{\mathbf{mL}}{\mathbf{6}}\right] + \left[\frac{\mathbf{a}}{\mathbf{2}} + \frac{\mathbf{5mL}}{\mathbf{6}}\right]$$

$$= \mathbf{a + mL}$$

The gradient is calculated as:

$$\frac{\mathbf{\Delta Q}}{\mathbf{L}} = \frac{[(\mathbf{a + mL}) - \mathbf{a}]}{\mathbf{L}} = \mathbf{m}$$

APPENDIX B

PLAN REPORT

StudySet Information

Studyset ID: DUOvert **# of Slices:** 121 **Pixel Size:** 0.14 **Scan Orientation:** Head First Supine

Plan Information

Treatment Orientation: Head First Supine

Max Dose in Plan (cGy): 3548.1

Max Dose Location (cm): X = 0.00 Y = 0.00 Z = 0.00

Grid Information

Grid Spacing (cm): 0.10 **Assigned CTtoED File:** DICOM3.v1NormalCTED

Calculate Dose Deposition to: Medium **# of Calculation Points:** 25393302

Force entire volume to be treated as water: No

Prescription Information: [A]

Rx Site	Prescribe To:	Rx Dose (cGy)	Fractional Dose (cGy)	Number of Fractions
	Plan Isocenter	1800.0	1800.0	1

Actual Dose(cGy): 3548.1

Rescale: No user normalization applied

Algorithm: Monte Carlo Photon

Statistical Uncertainty (%) per Control Point: 0.50

Delivery Mode: 3D Static Arc

Beam Information

Scan Reference Coordinates (cm): No Scan Reference Point has been selected

Seq.	Description	Treatment Unit	Modality	Energy	Gantry (deg)	Coll. (deg)	Couch (deg)	Isocenter X(cm)	Y(cm)	Z(cm)	# of Segs	MU/Fx
1	Cone5	ElektaSRSV01	Photon	6.0 MV	245.0/230.0	0.0	0.0	0.00	0.00	0.00	0	1000.00
2	Cone7	ElektaSRSV01	Photon	6.0 MV	245.0/230.0	0.0	0.0	0.00	0.00	0.00	0	1000.00
3	Cone10	ElektaSRSV01	Photon	6.0 MV	245.0/230.0	0.0	0.0	0.00	0.00	0.00	0	1000.00
4	Cone12	ElektaSRSV01	Photon	6.0 MV	245.0/230.0	0.0	0.0	0.00	0.00	0.00	0	1000.00
5	Cone15	ElektaSRSV01	Photon	6.0 MV	245.0/230.0	0.0	0.0	0.00	0.00	0.00	0	1000.00
6	Cone20	ElektaSRSV01	Photon	6.0 MV	245.0/230.0	0.0	0.0	0.00	0.00	0.00	0	1000.00
7	Cone25	ElektaSRSV01	Photon	6.0 MV	245.0/230.0	0.0	0.0	0.00	0.00	0.00	0	1000.00
8	Cone30	ElektaSRSV01	Photon	6.0 MV	245.0/230.0	0.0	0.0	0.00	0.00	0.00	0	1000.00

Approved by:

Name:_____ Signature:_____ Date:_____

Page 1 of 9

APPENDIX C

```
% angle: is the measured gantry angle from 180 to 180 in steps of 15
degree
% data: is the measured correction factors in compare with EBT3 per
pixel
% at each angle
% linear interapolate of angle in step of 1 degree
angle1=min(angle):1:max(angle);


% interapolate the correction factors by using pchip function
for a=1:253
    CF(a,:)=pchip(angle,data(a,:),angle1);
end


% CF1: is an array of new CF for the real plan angle
CF1=zeros(length(plan_angle),253);


% plan_angle 1: is an integer number rounded from the plan_angle of
% delivery
plan_angle1= round(plan_angle);
for i=1:length(plan_angle1)
    for j=1:length(angle1)
```

```
        if plan_angle1(i) == angle1(j)
            for m=1:253
                CF1(i,m) = CF(m,j);
            end
         end
    end
end
```

APPENDIX D

```
% Equ: is the equilisation factors for 512 pixels

% map the equalisation factos into vertical and horizantal arm as a

% function of mapped pixel numbers


% EquX: the equlisation factors for the horizantal arm in order

for i=1:length(Equ)

    for j=1:length(Xmap)

        if Xmap(j)==i

            EquX(j)=Equ(i);

        end

    end

end


%EquY: the equlisation factors for the vertical arm in order

for k=1:length(Equ)

    for m=1:length(Ymap)

        if Ymap(m)==k

            EquY(m)=Equ(k);

        end

    end

end
```

```
% CalibX: the calibration factors for the horizantal arm in order
for i=1:length(Calib)
    for j=1:length(Xmap)
        if Xmap(j)==i
            CalibX(j)=Calib(i);
        end
    end
end

% CalibX: the calibration factors for the horizantal arm in order
for k=1:length(Calib)
    for m=1:length(Ymap)
        if Ymap(m)==k
            CalibY(m)=Calib(k);
        end
    end
end

% Net_Vert is the sum of response corrected by angular CF in the
vertical
% arm per pixel
% Net_Charge_Vert: the sum response converted into charge
```

```
% Equ_Resp_Vert is the vertical net charge equilized


Net_Vert=sum(corr_Vert_data(:,:));

Net_Charge_Vert=Net_Vert./(65536/4.8);

Equ_Res_Vert= Net_Charge_Vert./ EquY;


% Net: is the sum of response corrected by angular CF in the
horizantal

% arm per pixel

% Net_Charge: the sum response converted into charge

% Equ_Resp: is the horizantal net charge equilized

Net = sum(corr_data(:,:));

Net_Charge=Net./(65536/4.8);

Equ_Res= Net_Charge./ EquX;

% the equlized response converted into dose by using calibration
factors

for i=1:253

Calib_Res(i) = Equ_Res(i) * CalibX(i);

end

for c=1:253

Calib_Res_Vert(c) = Equ_Res_Vert(c) * CalibY(c);

End
```

REFERENCES

Ahmed, S. N. (2007). Physics and engineering of radiation detection, Academic Press.

Aland, T., et al. (2011). "Evaluation of a Gafchromic EBT2 film dosimetry system for radiotherapy quality assurance." Australasian physical & engineering sciences in medicine **34**(2): 251-260.

Alashrah, S., et al. (2010). "Characterization of a 2D ionization chamber array for IMRT plan verification." Nuclear Instruments and Methods in Physics Research Section A: Accelerators, Spectrometers, Detectors and Associated Equipment **619**(1): 181-185.

Aldosari, A., et al. (2014). "A two dimensional silicon detectors array for quality assurance in stereotactic radiotherapy: MagicPlate-512." Medical physics **41**(9).

Aldosari, A. H. A. (2015). "Innovative silicon detectors for dosimetry in external beam radiotherapy."

Alfonso, R., et al. (2008). "A new formalism for reference dosimetry of small and nonstandard fields." Medical physics **35**(11): 5179-5186.

Almond, P. R., et al. (1999). "AAPM's TG-51 protocol for clinical reference dosimetry of high-energy photon and electron beams." Medical physics **26**(9): 1847-1870.

Alrowaili, Z., et al. (2017). Effect of scattered electrons on the 'Magic Plate'transmission array detector response. Journal of Physics: Conference Series, IOP Publishing.

Amerio, S., et al. (2004). "Dosimetric characterization of a large area pixel-segmented ionization chamber." Medical physics **31**(2): 414-420.

Andreo, P., et al. (2002). "Protocols for the dosimetry of high-energy photon and electron beams: a comparison of the IAEA TRS-398 and previous international Codes of Practice." Physics in Medicine & Biology **47**(17): 3033.

Aspradakis, M., et al. (2010). IPEM Report 103: Small field MV photon dosimetry.

Atkinson, N. M., et al. (2011). "Effect of transistor density and charge sharing on single-event transients in 90-nm bulk CMOS." IEEE Transactions on Nuclear Science **58**(6): 2578-2584.

Attix, F. H. (2008). Introduction to radiological physics and radiation dosimetry, John Wiley & Sons.

Baldock, C., et al. (2010). "Polymer gel dosimetry." Physics in medicine and biology **55**(5): R1.

Beddar, A. (2006). "Plastic scintillation dosimetry and its application to radiotherapy." Radiation Measurements **41**: S124-S133.

Beddar, A., et al. (1992). "Water-equivalent plastic scintillation detectors for high-energy beam dosimetry: I. Physical characteristics and theoretical considerations." Physics in medicine and biology **37**(10): 1883.

Bedford, J. L., et al. (2009). "Evaluation of the Delta4 phantom for IMRT and VMAT verification." Physics in medicine and biology **54**(9): N167.

Benedict, S. H., et al. (2014). Stereotactic radiosurgery and stereotactic body radiation therapy, CRC Press.

Benedict, S. H., et al. (2010). "Stereotactic body radiation therapy: the report of AAPM Task Group 101." Medical physics **37**(8): 4078-4101.

Benmakhlouf, H. and P. Andreo (2017). "Spectral distribution of particle fluence in small field detectors and its implication on small field dosimetry." Medical physics **44**(2): 713-724.

Benmakhlouf, H., et al. (2014). "Output correction factors for nine small field detectors in 6 MV radiation therapy photon beams: a PENELOPE Monte Carlo study." Medical physics **41**(4).

Bisello, F., et al. (2015). "Development of silicon monolithic arrays for dosimetry in external beam radiotherapy." Nuclear Instruments and Methods in Physics Research Section A: Accelerators, Spectrometers, Detectors and Associated Equipment **796**: 85-88.

Bocci, A., et al. (2012). "Silicon strip detector for a novel 2D dosimetric method for radiotherapy treatment verification." Nuclear Instruments and Methods in Physics Research Section A: Accelerators, Spectrometers, Detectors and Associated Equipment **673**: 98-106.

Bouchard, H., et al. (2015). "Detector dose response in megavoltage small photon beams. II. Pencil beam perturbation effects." Medical physics **42**(10): 6048-6061.

Bouchard, H., et al. (2015). "Detector dose response in megavoltage small photon beams. I. Theoretical concepts." Medical physics **42**(10): 6033-6047.

Brady, L. W., et al. (2013). Perez & Brady's principles and practice of radiation oncology, Lippincott Williams & Wilkins.

Buranurak, S., et al. (2013). "Temperature variations as a source of uncertainty in medical fiber-coupled organic plastic scintillator dosimetry." Radiation Measurements **56**: 307-311.

Butson, M. J., et al. (2010). "Energy response of the new EBT2 radiochromic film to x-ray radiation." Radiation Measurements **45**(7): 836-839.

Charles, P., et al. (2014). "Design and experimental testing of air slab caps which convert commercial electron diodes into dual purpose, correction-free diodes for small field dosimetry." Medical physics **41**(10).

Charles, P., et al. (2014). "A practical and theoretical definition of very small field size for radiotherapy output factor measurements." Medical physics **41**(4).

Charles, P., et al. (2013). "The effect of very small air gaps on small field dosimetry." Australasian Physical and Engineering Sciences in Medicine **36**(1): 71-72.

Charles, P., et al. (2013). "Monte Carlo-based diode design for correction-less small field dosimetry." Physics in medicine and biology **58**(13): 4501.

Charles, P. H. (2014). Very small field dosimetry, Queensland University of Technology.

Chaswal, V., et al. (2014). "Commissioning and comprehensive evaluation of the ArcCHECK cylindrical diode array for VMAT pretreatment delivery QA." Journal of applied clinical medical physics **15**(4): 212-225.

Chung, J.-B., et al. (2016). "Comparison of dosimetric performance among commercial quality assurance systems for verifying pretreatment plans of stereotactic body radiotherapy using flattening-filter-free beams." Journal of Korean medical science **31**(11): 1742-1748.

Cosgrove, V., et al. (2000). "The reproducibility of polyacrylamide gel dosimetry applied to stereotactic conformal radiotherapy." Physics in medicine and biology **45**(5): 1195.

Cranmer-Sargison, G., et al. (2012). "Monte Carlo modelling of diode detectors for small field MV photon dosimetry: detector model simplification and the sensitivity of correction factors to source parameterization." Physics in medicine and biology **57**(16): 5141.

Cranmer-Sargison, G., et al. (2011). "Implementing a newly proposed Monte Carlo based small field dosimetry formalism for a comprehensive set of diode detectors." Medical physics **38**(12): 6592-6602.

Czarnecki, D. and K. Zink (2013). "Monte Carlo calculated correction factors for diodes and ion chambers in small photon fields." Physics in medicine and biology **58**(8): 2431.

Dalal, R., et al. (2014). "Combined effect of bulk and surface damage on strip insulation properties of proton irradiated n+-p silicon strip sensors." Journal of Instrumentation **9**(04): P04007.

Das, I., et al. (2013). "Small field dosimetry." Med. Phys. **40**(6): 465.

Das, I. J., et al. (2008). "Accelerator beam data commissioning equipment and procedures: Report of the TG-106 of the Therapy Physics Committee of the AAPM." Medical physics **35**(9): 4186-4215.

Das, I. J., et al. (2008). "Small fields: nonequilibrium radiation dosimetry." Medical physics **35**(1): 206-215.

Devic, S., et al. (2016). "Reference radiochromic film dosimetry: review of technical aspects." Physica Medica **32**(4): 541-556.

Dieterich, S., et al. (2011). "Report of AAPM TG 135: quality assurance for robotic radiosurgery." Medical physics **38**(6): 2914-2936.

Ding, G. X., et al. (2006). "Commissioning stereotactic radiosurgery beams using both experimental and theoretical methods." Physics in medicine and biology **51**(10): 2549.

Durmus, I. and E. Atalay (2017). Dosimetric comparison between 10MV-FFF and 6MV-FFF for lung SBRT. AIP Conference Proceedings, AIP Publishing.

Feygelman, V., et al. (2011). "Evaluation of a 3D diode array dosimeter for helical tomotherapy delivery QA." Medical Dosimetry **35**(4): 324-329.

Fraass, B., et al. (1998). "American Association of Physicists in Medicine Radiation Therapy Committee Task Group 53: quality assurance for clinical radiotherapy treatment planning." Medical physics **25**(10): 1773-1829.

Francescon, P., et al. (2008). "Total scatter factors of small beams: a multidetector and Monte Carlo study." Medical physics **35**(2): 504-513.

Francescon, P., et al. (1998). "Use of a new type of radiochromic film, a new parallel-plate micro-chamber, MOSFETs, and TLD 800 microcubes in the dosimetry of small beams." Medical physics **25**(4): 503-511.

Francescon, P., et al. (2011). "Calculation of kQclin, Qmsrfclin, fmsr for several small detectors and for two linear accelerators using Monte Carlo simulations." Medical physics **38**(12): 6513-6527.

Francescon, P., et al. (2012). "Monte Carlo simulated correction factors for machine specific reference field dose calibration and output factor measurement using fixed and iris collimators on the CyberKnife system." Physics in medicine and biology **57**(12): 3741.

Fredh, A., et al. (2013). "Patient QA systems for rotational radiation therapy: a comparative experimental study with intentional errors." Medical physics **40**(3).

Gagnon, J. C., et al. (2012). "Dosimetric performance and array assessment of plastic scintillation detectors for stereotactic radiosurgery quality assurance." Medical physics **39**(1): 429-436.

Griessbach, I., et al. (2005). "Dosimetric characteristics of a new unshielded silicon diode and its application in clinical photon and electron beams." Medical physics **32**(12): 3750-3754.

Grosu, A.-L., et al. (2006). "Stereotactic radiotherapy/radiosurgery." New Technologies in Radiation Oncology: 267-276.

Grusell, E. and G. Rikner (1986). "Evaluation of temperature effects in p-type silicon detectors." Physics in medicine and biology **31**(5): 527.

Guo FQ, W. C., Stern R, Luo C, Liu T, Shi J, Yang C, Purdy J. (2006). "Feasibility of Using a 2D Diode Array System for Clinical Electron Beam Measurements." Medical Physics **33**(6Part10): 2103-2104.

Halvorsen, P. H., et al. (2017). "Aapm-rss Medical Physics Practice Guideline 9. a. for Srs-sbrt." Journal of applied clinical medical physics **18**(5): 10-21.

Han, Z., et al. (2010). "Evaluation of MatriXX for IMRT and VMAT dose verifications in peripheral dose regions." Medical physics **37**(7): 3704-3714.

Haryanto, F., et al. (2002). "Investigation of photon beam output factors for conformal radiation therapy—Monte Carlo simulations and measurements." Physics in medicine and biology **47**(11): N133.

Hassani, H., et al. (2014). "A dosimetric study of small photon fields using polymer gel and Gafchromic EBT films." Medical Dosimetry **39**(1): 102-107.

Herwiningsih, S. and A. Fielding (2016). Focal spot estimation of an Elekta dedicated stereotactic linear accelerator Monte Carlo model. Journal of Physics: Conference Series, IOP Publishing.

Jang, K. W., et al. (2007). Measurement of two-dimensional photon beam distributions using a fiber-optic radiation sensor for small field radiation therapy. Nuclear Science Symposium Conference Record, 2007. NSS'07. IEEE, IEEE.

Jin, H., et al. (2014). "A comparison study of volumetric modulated Arc therapy quality assurances using portal dosimetry and MapCHECK 2." Progress in Medical Physics **25**(2): 65-71.

Jin, H., et al. (2014). "Interplay effect of angular dependence and calibration field size of MapCHECK 2 on RapidArc quality assurance." Journal of applied clinical medical physics **15**(3): 80-92.

Jursinic, P. A. (2007). "Characterization of optically stimulated luminescent dosimeters, OSLDs, for clinical dosimetric measurements." Medical physics **34**(12): 4594-4604.

Jursinic, P. A. and B. E. Nelms (2003). "A 2-D diode array and analysis software for verification of intensity modulated radiation therapy delivery." Medical physics **30**(5): 870-879.

Jursinic, P. A., et al. (2010). "MapCHECK used for rotational IMRT measurements: Step-and-shoot, Tomotherapy, RapidArc." Medical physics **37**(6): 2837-2846.

Jursinic, P. A. and C. J. Yahnke (2011). "In vivo dosimetry with optically stimulated luminescent dosimeters, OSLDs, compared to diodes; the effects of buildup cap thickness and fabrication material." Medical physics **38**(10): 5432-5440.

Kairn, T., et al. (2012). "Monte Carlo verification of gel dosimetry measurements for stereotactic radiotherapy." Physics in medicine and biology **57**(11): 3359.

Keeling, V. P., et al. (2014). "Dependency of planned dose perturbation (PDP) on the spatial resolution of MapCHECK 2 detectors." Journal of applied clinical medical physics **15**(1): 100-117.

Keeling, V. P., et al. (2013). "A comprehensive comparison study of three different planar IMRT QA techniques using MapCHECK 2." Journal of applied clinical medical physics **14**(6): 222-233.

Khan, F. M. (2010). The physics of radiation therapy, Lippincott Williams & Wilkins.

Knoll, G. F. (2010). Radiation detection and measurement, John Wiley & Sons.

Lalwani, K., et al. (2016). "Study the radiation damage effects in Si microstrip detectors for future HEP experiments." Nuclear Instruments and Methods in Physics Research Section B: Beam Interactions with Materials and Atoms **379**: 262-264.

Laub, W. U., et al. (1999). "A diamond detector in the dosimetry of high-energy electron and photon beams." Physics in medicine and biology **44**(9): 2183.

Lechner, W., et al. (2013). "Detector comparison for small field output factor measurements in flattening filter free photon beams." Radiotherapy and oncology **109**(3): 356-360.

Lee, B., et al. (2008). "Measurement of two-dimensional photon beam distributions using a fiber-optic radiation sensor for small field radiation therapy." IEEE Transactions on Nuclear Science **55**(5): 2632-2636.

Lee, B., et al. (2015). "Effects of temperature and X-rays on plastic scintillating fiber and infrared optical fiber." Sensors **15**(5): 11012-11026.

Lee, C., et al. (2014). "The use of normoxic polymer gel for measuring dose distributions of 1, 4 and 30mm cones." Radiation Physics and Chemistry **104**: 221-224.

Leksell, D. G. (1987). "Stereotactic radiosurgery: present status and future trends." Neurological research **9**(2): 60-68.

Li, Q., et al. (2010). "The angular dependence of a 2-dimensional diode array and the feasibility of its application in verifying the composite dose distribution of intensity-modulated radiation therapy." Chin J Cancer **29**(6): 617-620.

Li, Z. (2009). "Radiation damage effects in Si materials and detectors and rad-hard Si detectors for SLHC." Journal of Instrumentation **4**(03): P03011.

Lightstone, A., et al. (2005). "Intracranial stereotactic positioning systems: Report of the american association of physicists in medicine radiation therapy committee task group no. 68." Medical physics **32**(7): 2380-2398.

Lin, M. H., et al. (2015). "Robotic radiosurgery system patient-specific QA for extracranial treatments using the planar ion chamber array and the cylindrical diode array." Journal of applied clinical medical physics **16**(4): 290-305.

Liu, P., et al. (2011). "Plastic scintillation dosimetry: comparison of three solutions for the Cerenkov challenge." Physics in medicine and biology **56**(18): 5805.

Liu, P. Z., et al. (2014). "Can small field diode correction factors be applied universally?" Radiotherapy and oncology **112**(3): 442-446.

Livingstone, J., et al. (2012). "Large area silicon microdosimeter for dosimetry in high LET space radiation fields: Charge collection study." IEEE Transactions on Nuclear Science **59**(6): 3126-3132.

Livingstone, J., et al. (2013). "Charge collection in n-SOI planar microdosimeters." IEEE Transactions on Nuclear Science **60**(6): 4289-4296.

Low, D. A., et al. (2011). "Dosimetry tools and techniques for IMRT." Medical physics **38**(3): 1313-1338.

Low, D. A., et al. (2003). "Ionization chamber volume averaging effects in dynamic intensity modulated radiation therapy beams." Medical physics **30**(7): 1706-1711.

Lutz, G. (1995). "Silicon radiation detectors." Nuclear Instruments and Methods in Physics Research Section A: Accelerators, Spectrometers, Detectors and Associated Equipment **367**(1-3): 21-33.

Maj, P., et al. (2012). "Algorithms for minimization of charge sharing effects in a hybrid pixel detector taking into account hardware limitations in deep submicron technology." Journal of Instrumentation **7**(12): C12020.

Maj, P., et al. (2013). "18k Channels single photon counting readout circuit for hybrid pixel detector." Nuclear Instruments and Methods in Physics Research Section A: Accelerators, Spectrometers, Detectors and Associated Equipment **697**: 32-39.

Maj, P., et al. (2015). "Comparison of the charge sharing effect in two hybrid pixel detectors of different thickness." Journal of Instrumentation **10**(02): C02006.

Manolopoulos, S., et al. (2009). "Small field measurements with a novel silicon position sensitive diode array." Physics in medicine and biology **54**(3): 485.

Marinello, G. (2007). "Radiothermoluminescent dosimeters and diodes." Handbook of Radiotherapy Physics: 303-320.

Markovic, M., et al. (2014). "Characterization of a two-dimensional liquid-filled ion chamber detector array used for verification of the treatments in radiotherapy." Medical physics **41**(5).

Martens, C., et al. (2000). "The value of the PinPoint ion chamber for characterization of small field segments used in intensity-modulated radiotherapy." Physics in medicine and biology **45**(9): 2519.

Massillon-JL, G., et al. (2013). "Dosimetry for small fields in stereotactic radiosurgery using Gafchromic MD-V2-55 film, TLD-100 and alanine dosimeters." PloS one **8**(5): e63418.

Mayles, P., et al. (2007). Handbook of radiotherapy physics: theory and practice, CRC Press.

Metcalfe, P., et al. (2012). The physics of radiotherapy x-rays and electrons, Medical Physics Publ.

Miura, H., et al. (2016). "Gafchromic EBT-XD film: Dosimetry characterization in high-dose, volumetric-modulated arc therapy." Journal of applied clinical medical physics **17**(6): 312-322.

Moll, M. (1999). Radiation damage in silicon particle detectors: Microscopic defects and macroscopic properties, DESY.

Moll, M. and R. Collaboration (2006). "Radiation tolerant semiconductor sensors for tracking detectors." Nuclear Instruments and Methods in Physics Research Section A: Accelerators, Spectrometers, Detectors and Associated Equipment **565**(1): 202-211.

Moll, M., et al. (2000). "Investigation on the improved radiation hardness of silicon detectors with high oxygen concentration." Nuclear Instruments and Methods in Physics Research Section A: Accelerators, Spectrometers, Detectors and Associated Equipment **439**(2): 282-292.

Morales, J. E., et al. (2014). "Dosimetry of cone-defined stereotactic radiosurgery fields with a commercial synthetic diamond detector." Medical physics **41**(11).

Morin, J., et al. (2013). "A comparative study of small field total scatter factors and dose profiles using plastic scintillation detectors and other stereotactic dosimeters: the case of the CyberKnife." Medical physics **40**(1).

Moscatelli, F., et al. (2016). "Combined Bulk and Surface Radiation Damage Effects at Very High Fluences in Silicon Detectors: Measurements and TCAD Simulations." IEEE Transactions on Nuclear Science **63**(5): 2716-2723.

Niroomand-Rad, A., et al. (1998). "Radiochromic film dosimetry: recommendations of AAPM radiation therapy committee task group 55." Medical physics **25**(11): 2093-2115.

Pai, S., et al. (2007). "TG-69: Radiographic film for megavoltage beam dosimetry." Medical physics **34**(6): 2228-2258.

Pantelis, E., et al. (2008). "Dosimetric characterization of CyberKnife radiosurgical photon beams using polymer gels." Medical physics **35**(6): 2312-2320.

Pappas, E., et al. (2009). Stereotactic radiosurgery photon field profile dosimetry using conventional dosimeters and polymer gel dosimetry. Analysis and inter-comparison. Journal of Physics: Conference Series, IOP Publishing.

Pappas, E., et al. (2008). "Small SRS photon field profile dosimetry performed using a PinPoint air ion chamber, a diamond detector, a novel silicon-diode array (DOSI), and polymer gel dosimetry. Analysis and intercomparison." Medical physics **35**(10): 4640-4648.

Petasecca, M., et al. (2015). "MagicPlate-512: A 2D silicon detector array for quality assurance of stereotactic motion adaptive radiotherapy." Medical physics **42**(6): 2992-3004.

Podgorsak, E. (2005). "Radiation oncology physics." a handbook for teachers and students/EB Podgorsak.–Vienna: International Atomic Energy Agency **657**.

Podgorsak, E. (2008). "Radiation oncology physics: a handbook for teachers and students." Br J Cancer **98**: 1020.

Poppe, B., et al. (2011). "SU-E-T-131: Iterative Deconvolution of Dose Profile Measurements with Ionization Chambers Based on Lorentz-Type Lateral Response Functions of the Detectors." Medical physics **38**(6): 3516-3516.

Poppe, B., et al. (2013). "Performance parameters of a liquid filled ionization chamber array." Medical physics **40**(8).

Porumb, C. S. (2016). "Development of a multi-detector quality assurance instrument for intensity modulated radiotherapy."

Porumb, C. S., et al. (2016). "Characterisation of silicon diode arrays for dosimetry in external beam radiation therapy." IEEE Transactions on Nuclear Science **63**(3): 1808-1817.

Ralston, A., et al. (2012). "Small field diode correction factors derived using an air core fibre optic scintillation dosimeter and EBT2 film." Physics in medicine and biology **57**(9): 2587.

Ralston, A., et al. (2014). "Over-response of synthetic microDiamond detectors in small radiation fields." Physics in medicine and biology **59**(19): 5873.

Rikner, G. and E. Grusell (1985). "Selective shielding of a p-Si detector for quality independence." Acta Radiologica: Oncology **24**(1): 65-69.

Rikner, G. and E. Grusell (1987). "General specifications for silicon semiconductors for use in radiation dosimetry." Physics in medicine and biology **32**(9): 1109.

Rosenfeld, A., et al. (1993). "Strip detector for short-range particles." Nuclear Instruments and Methods in Physics Research Section A: Accelerators, Spectrometers, Detectors and Associated Equipment **326**(1-2): 234-238.

Rosenfeld, A. B. (2006). "Electronic dosimetry in radiation therapy." Radiation Measurements **41**: S134-S153.

Rowshanfarzad, P., et al. (2011). "Isocenter verification for linac-based stereotactic radiation therapy: review of principles and techniques." Journal of applied clinical medical physics **12**(4): 185-195.

Rustgi, A. K., et al. (1997). "Influence of air inhomogeneities in radiosurgical beams." Medical Dosimetry **22**(2): 95-100.

Sadagopan, R., et al. (2007). "Characterisation, commissioning and evaluation of Delta4 IMRT QA system." Medical physics **34**: 256.

Saini, A. S. and T. C. Zhu (2007). "Energy dependence of commercially available diode detectors for in-vivo dosimetry." Medical physics **34**(5): 1704-1711.

Sauer, O. A. and J. Wilbert (2007). "Measurement of output factors for small photon beams." Medical physics **34**(6): 1983-1988.

Scarboro, S. and S. Kry (2012). "Characterisation of energy response of Al2O3: C optically stimulated luminescent dosemeters (OSLDs) using cavity theory." Radiation protection dosimetry **153**(1): 23-31.

Schell, M., et al. (1995). TG-42 Report on stereotactic external beam irradiation, AAPM Report.

Scott, A. J., et al. (2012). "Characterizing the influence of detector density on dosimeter response in non-equilibrium small photon fields." Physics in medicine and biology **57**(14): 4461.

Seco, J. and F. Verhaegen (2013). Monte Carlo techniques in radiation therapy, CRC press.

Seimenis, I., et al. (2009). "The use of high field strength and parallel imaging techniques for MRI-based gel dosimetry in stereotactic radiosurgery." Journal of Instrumentation **4**(07): P07004.

Seuntjens, J. "IAEA/AAPM Code of Practice for the Dosimetry of Static Small Photon Fields."

Sharpe, M., et al. (1995). "Extrafocal radiation: A unified approach to the prediction of beam penumbra and output factors for megavoltage x-ray beams." Medical physics **22**(12): 2065-2074.

Shi, J., et al. (2003). "Modeling the instantaneous dose rate dependence of radiation diode detectors." Medical physics **30**(9): 2509-2519.

Shukaili, K. A., et al. (2017). "A 2D silicon detector array for quality assurance in small field dosimetry: DUO." Medical physics **44**(2): 628-636.

Solberg, T. D., et al. (1995). "Implications of tissue heterogeneity for radiosurgery in head and neck tumors." International Journal of Radiation Oncology* Biology* Physics **32**(1): 235-239.

Stansook, N., et al. "Angular dependence of a 2D monolithic silicon diode array for small field dosimetry." Medical physics.

Stasi, M., et al. (2005). "D-IMRT verification with a 2D pixel ionization chamber: dosimetric and clinical results in head and neck cancer." Physics in medicine and biology **50**(19): 4681.

Sze, S. M. and K. K. Ng (2006). Physics of semiconductor devices, John wiley & sons.

Tavernier, S. (2009). Interactions of particles in matter. Experimental techniques in nuclear and particle physics, Springer**:** 23-53.

Thiyagarajan, R., et al. (2016). "Analyzing the performance of ArcCHECK diode array detector for VMAT plan." Reports of Practical Oncology & Radiotherapy **21**(1): 50-56.

Treuer, H., et al. (2000). "On isocentre adjustment and quality control in linear accelerator based radiosurgery with circular collimators and room lasers." Physics in medicine and biology **45**(8): 2331.

Tyler, M., et al. (2013). "Characterization of small-field stereotactic radiosurgery beams with modern detectors." Physics in medicine and biology **58**(21): 7595.

Underwood, T., et al. (2015). "Validation of a prototype DiodeAir for small field dosimetry." Physics in medicine and biology **60**(7): 2939.

Underwood, T., et al. (2013). "Detector density and small field dosimetry: Integral versus point dose measurement schemes." Medical physics **40**(8).

Underwood, T., et al. (2013). "Mass-density compensation can improve the performance of a range of different detectors under non-equilibrium conditions." Physics in medicine and biology **58**(23): 8295.

Veale, M. C., et al. (2011). "An ASIC for the study of charge sharing effects in small pixel CdZnTe X-ray detectors." IEEE Transactions on Nuclear Science **58**(5): 2357-2362.

Wang, L. L. and K. Leszczynski (2007). "Estimation of the focal spot size and shape for a medical linear accelerator by Monte Carlo simulation." Medical physics **34**(2): 485-488.

WHO (2017). World's health ministers renew commitment to cancer prevention and control. http://www.who.int/cancer/media/news/cancer-prevention-resolution/en/.

Wilcox, E. E. and G. M. Daskalov (2007). "Evaluation of GAFCHROMIC® EBT film for CyberKnife® dosimetry." Medical physics **34**(6): 1967-1974.

Wilkins, D., et al. (1997). "The effect of dose rate dependence of p-type silicon detectors on linac relative dosimetry." Medical physics **24**(6): 879-881.

Wolff, T., et al. (1998). "Characterization and use of a commercial n-type diode system." The British journal of radiology **71**(851): 1168-1177.

Wolfsberger, L. D., et al. (2010). "Angular dose dependency of MatriXX TM and its calibration." Journal of applied clinical medical physics **11**(1): 241-251.

Wong, C., et al. (2009). "Small field size dose-profile measurements using gel dosimeters, gafchromic films and micro-thermoluminescent dosimeters." Radiation Measurements **44**(3): 249-256.

Wong, J., et al. (2010). "A silicon strip detector dose magnifying glass for IMRT dosimetry." Medical physics **37**(2): 427-439.

Wong, J., et al. (2012). "Characterization of a novel two dimensional diode array the “magic plate” as a radiation detector for radiation therapy treatment." Medical physics **39**(5): 2544-2558.

Wong, J., et al. (2011). "The use of a silicon strip detector dose magnifying glass in stereotactic radiotherapy QA and dosimetry." Medical physics **38**(3): 1226-1238.

Wootton, L. and S. Beddar (2013). "Temperature dependence of BCF plastic scintillation detectors." Physics in medicine and biology **58**(9): 2955.

Würfel, J. U. (2013). "Dose measurements in small fields." Med Phys **1**(1): 81-90.

Zhang, J. (2010). "SU-GG-T-247: A New Method to Compensate Angular Dependency of MapCheck Device in Intensity Modulated Arc Therapy." Medical physics **37**(6): 3242-3242.

Zhang, T., et al. (2009). "Poster—Wed Eve—31: Validation of the Delta4 Phantom for 3-D Dosimetry of IMRT Plans." Medical physics **36**(9): 4309-4309.

Zheng, X., et al. (2016). "Improving the spatial resolution in CZT detectors using charge sharing effect and transient signal analysis: Simulation study." Nuclear Instruments and Methods in Physics Research Section A: Accelerators, Spectrometers, Detectors and Associated Equipment **808**: 60-70.

Zhou, H. and C. Wu (2011). "SU-E-T-171: Quantitative Evaluation and Correction of the Gantry Angular Dependence of MapCheck2 for Patient QA Measurement." Medical physics **38**(6): 3525-3525.

Zhu, T. C. and B. E. Bjärngard (1994). "The head-scatter factor for small field sizes." Medical physics **21**(1): 65-68.